Operational Modelling of Geomagnetic Fields and Geomagnetically Induced Currents

Michael John Heyns

Supervisor:
Prof. C. T. Gaunt
Department of Electrical Engineering
University of Cape Town

Co-supervisor:
Dr. S. I. Lotz
SANSA Space Science
South African National Space Agency

Thesis Presented for the Degree of

DOCTOR OF PHILOSOPHY

in the Department of Electrical Engineering

University of Cape Town

February 2021

Declaration

This thesis/dissertation has been submitted to the Turnitin module (or equivalent similarity and originality checking software) and I confirm that my supervisor has seen my report and any concerns revealed by such have been resolved with my supervisor. Furthermore, I confirm that I understand the meaning of plagiarism and that it is wrong. All work presented in this thesis/dissertation is my own, unless otherwise acknowledged or deemed to be as part of the normal guidance offered by my supervisor.

Name:	Michael John Heyns
Student number:	HYNMIC005
Signature:	Signed by candidate
Date:	22/02/2021

Acknowledgements

As alluded to in the preamble, many theses take a scenic journey across many fields to make new discoveries. This is no exception. What started off as a relatively simple question became the basis of intense research over a number of years that uncovered some real nuggets of insight but also many more questions. Being able to pursue such an engaging topic can only happen when supported by an amazing team, who need to be acknowledged. Many more years can easily be spent working together and probing aspects further still, but there comes a time when the initial output needs to take the form of a thesis as was initially intended.

I would firstly like to acknowledge my supervisors, Prof. Trevor Gaunt at UCT and Dr. Stefan Lotz at SANSA. Similar to the multi-disciplinary nature of the GIC problem, this supervisory team is a perfect blend of engineering and space science. In particular, I would like to thank Prof. Gaunt for sharing his vast experience, which is by no means limited to GICs. His deep understanding of the field at large, has been critical in moulding the work into what it is. Dr. Lotz has been a pillar of support throughout the course of this work, often enduring barrages of ideas and picking out some of the more promising ones. His input in understanding the space science aspects and our conversations around the application of new approaches has been indispensable. Also at SANSA, and an active member of the larger SANSA-UCT GIC work group, I would like to thank Prof. Pierre Cilliers. His additional experience in dealing with the GIC problem and his contagious energy has lead to many stimulating conversations and insights. At UCT, further thanks goes to Dr. David Oyedokun for his collaboration.

With regards to institutions, I would like to thank the SANSA Space Science team in Hermanus for being a partner in my journey that started many years ago – well before entering as a university student. Further thanks goes to UCT for providing an opportunity to pursue a PhD and the NRF and Open Philanthropy Project for funding various aspects of the research.

Throughout the course of my research there has been the opportunity for international collaborations, some of which have materialised into formal outputs. My hope is to strengthen these collaborations in the future and follow up on some interesting questions uncovered – there is much work to be done. In no specific order, I would like to acknowledge the SWIGS group led by Alan Thomson (BGS), Anna Kelbert (USGS), Bob Weigel (GMU), Santi Marshal (Ebre), Chigo Ngwira (Astra), David Boteler (NrCAN) and Donald Danskin (NrCAN). In a similar vein, I would to acknowledge the different international GIC data providers from the US to Australia, Japan and the Kola peninsula. Thanks goes to Ian Grant from TVA and David Jacobson from Manitoba in North America, Ya Sakarov and Vyacheslav Vorobjev from PGI for Kola peninsula data, Greg Hesse from Powerlink in Australia and Dr. Shinichi Watari who facilitated in the sharing of data from Hokkaido Electric Power in Japan.

Last, but definitely not least, I would like to thank my support base back home. ***This one is for you!***

> “It ain’t what you don’t know that gets you into trouble. It’s what you know for sure that just ain’t so.”
>
> -Mark Twain

Abstract

Geomagnetically induced currents (GICs) have long been known to affect power systems adversely. Modelling these GICs usually involves consideration of a chain of coupled systems. The scope of the modelling chain spans multiple disciplines, from solar physics through to geophysics and power engineering. Most models split the chain into sequential and separate processes. Recent approaches focus on improving accuracy in the geophysical process and in network models to a transformer level. However, even complex models in the geophysical or engineering steps leave significant unmodelled uncertainties in the coupled systems.

The focus of this work is to use data-driven approaches to probe the uncertainties and provide a framework for operational estimation from the geomagnetic field to GIC. Although the empirical approaches chiefly link measurements of geomagnetic fields and GICs, measured geoelectric fields and magnetotelluric surface impedance responses are also employed. Analysis is done in both the time and frequency domains. Various aspects of this novel empirical approach have been tested using datasets from power networks in four mid-latitude countries, with consistent results found across the different contexts.

The novel empirical ensemble method shows improvements compared with previous empirical models, regardless of data fidelity or coverage. Frequency-related driving and filters are shown to have material effects on GIC modelling. The network parameters widely used to calculate GICs at nodes are shown to vary with the magnitude of the geomagnetic disturbance during an event. Modelling uncertainty can be quantified, and an operational level of modelling was possible across all cases.

For GIC modelling in networks with sparse magnetic field data coverage, the well-defined and often used planar spherical elementary current systems interpolation method is adapted to use low-cost variometers and describe mid-latitude current systems. For the first time, uncertainty is included in the results from this interpolation scheme.

This research has direct applications for power system operators in mid-latitude regions. The use of variometers and low-cost GIC monitors supports the feasibility of large-scale data collection. The empirical modelling methods developed can augment existing approaches and inform decisions regarding operations, maintenance, planning and risk assessment.

Contents

Preamble and Published Works VI

List of Tables VII

List of Figures IX

Acronyms and Abbreviations X

Indices X

1 Introduction to GICs 1
- 1.1 Resolving Complexity . . . 2
- 1.2 Coupled System Process Chain of GIC Driving . . . 3
  - 1.2.1 Solar and Solar Wind Processes . . . 3
  - 1.2.2 Magnetospheric Processes . . . 5
  - 1.2.3 Geomagnetic Storms . . . 7
  - 1.2.4 Geophysical Processes . . . 8
- 1.3 Problems of Coupled System Approach . . . 10
- 1.4 New Possibilities . . . 10
- 1.5 Hypothesis . . . 11
- 1.6 Research Questions . . . 11
- 1.7 Arrangement of Dissertation . . . 12

2 Literature Review 13
- 2.1 Operational Modelling Perspectives . . . 13
- 2.2 GIC Modelling . . . 14
  - 2.2.1 Network Modelling . . . 15
  - 2.2.2 Geophysical Modelling . . . 16
  - 2.2.3 Transfer Function Modelling . . . 17
- 2.3 Input Parameter Sensitivity . . . 18
- 2.4 Geomagnetic Field Interpolation . . . 19
- 2.5 Summary . . . 19

3 Theoretical Background 21
- 3.1 Induction Driving of GICs . . . 22
- 3.2 Spectral Characteristics . . . 28
- 3.3 Linking Spectral Characteristics with EMF Driving . . . 31
- 3.4 Modelling Nodal GICs . . . 34
- 3.5 Modelling the Geomagnetic Field . . . 35

4 Framework for Operational Model Development 39
- 4.1 Framework Overview . . . 39
- 4.2 Procedure for Analysis . . . 41
- 4.3 Data . . . 42
  - 4.3.1 Data Cleaning and Conversion . . . 46
  - 4.3.2 Data Cadence . . . 48
  - 4.3.3 Geoelectric Field Derivation . . . 48

5 Model Development 55
- 5.1 Frequency Response of GICs . . . 55
- 5.2 Considering the Use of Proxies . . . 59
- 5.3 Ensemble Methodology in the Time and Frequency Domains . . . 61

5.3.1 Ensemble Estimation of Network Parameters 63
5.3.2 Ensemble Estimation of Transfer Functions 69
5.4 Summary 72

6 GIC Modelling Results 74
6.1 An Ideal Case 76
6.1.1 Network Parameters in Different Contexts 76
6.1.2 Variation of Network Parameters 78
6.1.3 Directionality of Network Parameters 81
6.1.4 Frequency Domain Transfer Functions 83
6.1.5 Modelling Results 85
6.2 A Typical Case & Comparison with Previous Modelling 89
6.3 A Pathological Case 93
6.4 A Few Further Cases 95
6.4.1 Applications Down Under 95
6.4.2 A Complex Geological Case 100
6.5 Summary 102

7 Improved Interpolation of the Geomagnetic Field 104
7.1 dSECS: Including dB/dt Interpolation 105
7.2 Uncertainty in Interpolation 110
7.3 Correction of SECS Implementation in southern Africa 120
7.4 Summary 123

8 Discussion 125
8.1 Summary of Contributions to the Field 129

9 Concluding Remarks 131
9.1 Answers to the Research Questions 131
9.2 Validity of the Hypothesis 134
9.3 Implications of Hypothesis and Research Presented 135

Acknowledgement of Data Sources 136

Acknowledgement of Software Sources 136

References 138

Preamble and Published Works

As with many projects, an initial idea or interest can spark a cascade of further ideas or interests. Some may say these spin-off inquiries are distractions to be avoided. The wandering journey nevertheless has a crucial role to play in the pursuit of new knowledge and deeper understanding, whether personal or general to a field. In this spirit, various aspects of the research presented in this thesis have made their way into the public domain. For reference they are listed below:

Papers:

M. J. Heyns, S. I. Lotz and C. T. Gaunt, 'Geomagnetic Pulsations Driving Geomagnetically Induced Currents', *Space Weather*, 2020. doi: 10.1029/2020SW002557.

M. J. Heyns, C. T. Gaunt, P. J. Cilliers and S. I. Lotz, 'Data Driven Transfer Functions and Transmission Network Parameters for GIC Modelling', *Proceedings of the 21st Power Systems Computation Conference (PSCC 2020)*, Electric Power Systems Research (188), pp. 106546, 2020. arXiv:2004.08837, doi:10.1016/j.epsr.2020.106546.

Peer-reviewed Proceedings:

C. T. Gaunt, P. J. Cilliers, M. J. Heyns, S. I. Lotz, H. K. Chisepo, A. V. Adebayo, L. D. Borril, D. T. O. Oyedokun, 'Calculations leading to voltage stability and transformer assessment in the presence of geomagnetically induced currents', *CIGRE Session*, 2020.

M. J. Heyns, S. I. Lotz and C. T. Gaunt, 'Probabilistic Analysis of Power Network Susceptibility to GICs', *2020 International Conference on Probabilistic Methods Applied to Power Systems (PMAPS)*, IEEE, pp. 1–6, 2020. arXiv:2006.12205, doi: 10.1109/PMAPS47429.2020.9183597.

D. T. O. Oyedokun, M. J. Heyns, P. J. Cilliers and C. T. Gaunt, 'Frequency Components of Geomagnetically Induced Currents for Power System Modelling', *2020 International SAUPEC/RobMech/PRASA Conference*, IEEE, pp. 1–6, 2020. arXiv:1912.09367, doi: 10.1109/SAUPEC/RobMech/PRASA48453.2020.9041021.

M. J. Heyns, S. I. Lotz and C. T. Gaunt, 'dSECS : Including Variometers in Geomagnetic Field Interpolation', *The Proceedings of SAIP2018, the 63rd Annual Conference of the South African Institute of Physics, edited by Prof. Japie Engelbrecht (UFS/2018)*, pp. 212–217, 2018. ISBN: 978-0-620-85406-1, arXiv:1912.04743.

M. J. Heyns, S. I. Lotz, P. J. Cilliers, C. T. Gaunt, 'Ensemble Estimation of Network Parameters: A Tool to Improve the Real-time Estimation of GICs in the South African Power Network', *The Proceedings of SAIP2017, the 62nd Annual Conference of the South African Institute of Physics, edited by Prof. Japie Engelbrecht (SU/2017)*, pp. 270–275, 2017. ISBN: 978-0-620-82077-6, arXiv:1912.04742.

Posters and Other Outputs:

M. J. Heyns, S. I. Lotz and C. T. Gaunt, 'QuickView Presentation: Mid-latitude long-period pulsations and their implications for GIC modelling', *Virtual European Space Weather Symposium*, 2020.

M. J. Heyns, S. I. Lotz, C. T. Gaunt and P. J. Cilliers, 'Including Uncertainty Estimates and Spatial Characterisation in Practical Spherical Elementary Current Systems Interpolation', *IUGG General Assembly*, Montreal, Canada, 2019. doi: 10.13140/RG.2.2.21069.38881.

M. J. Heyns, S. I. Lotz, P. J. Cilliers and C. T. Gaunt, 'Dealing with Uncertainty in GIC Modelling: An Empirical Approach', *IAPSO-IAMAS-IAGA Joint Assembly*, Cape Town, South Africa, 2017. doi: 10.13140/RG.2.2.10583.62885.

M. J. Heyns, S. I. Lotz, P. J. Cilliers and C. T. Gaunt, 'Ensemble Estimation of Network Parameters', *NOAA/SWPC Space Weather Workshop*, Broomfield, CO., USA, 2017. doi: 10.13140/RG.2.2.20649.95849.

List of Tables

1 GIC data from power networks . . . 42
2 Network parameter spreads associated with different B-fields and conductivity profiles 77
3 Variation of network parameters with GIC magnitude . . . 81
4 Modelling results for the Paradise node in the TVA network . . . 87
5 Comparison of ensemble estimation results for the Grassridge substation with previous work . . . 92
6 Data coverage of variometers in southern Africa for SECS validation . . . 105
7 Comparison of measured B-field and results from SECS interpolation . . . 105

List of Figures

1 Flow of the coupled system process chain leading to GICs . . . 2
2 A representation of the complex nature of the solar magnetic field . . . 3
3 Images from different SOHO instruments of the events on the Sun relating to the Halloween Storm of 2003 . . . 4
4 ‘Closed’ model of the magnetosphere . . . 5
5 ‘Open’ model of the magnetosphere . . . 6
6 Representation of the near-Earth current systems . . . 7
7 Geomagnetic regions as defined by latitude . . . 8
8 In-situ solar wind data from the June 2015 geomagnetic storm . . . 9
9 Cleaned GIC spectrogram at Montgomery . . . 21
10 Representation of the GIC induction loop . . . 23
11 Frequency response relative to GIC at Memanbetsu, Japan . . . 30
12 Frequency response slopes at Paradise, TVA . . . 30
13 Coherence between GIC and the B-field or its time derivative . . . 31
14 Synthetic B-field and E-field given typical spectral responses and a homogeneous Earth 32
15 Visualisation of the attenuation of the disturbance B-field and corresponding EMF contributions . . . 32
16 Realistic visualisation of EMF components given different E-field frequencies . . . 33
17 Contributions to E-field and EMF as a function of depth . . . 34
18 Equivalent current theory underpinning SECS interpolation . . . 36
19 Divergence-free elementary currents used in SECS . . . 37
20 Visualisation of the sources of uncertainty in the GIC modelling chain . . . 39
21 Map of the HV network in southern Africa . . . 43
22 Map of the local HV and lower voltage network around Memanbetsu in Japan . . . 44
23 Map of the 500 kV HV network around TVA Paradise node in the USA . . . 45
24 Less detailed map of the greater TVA HV network . . . 45
25 Map of the HV network in northeastern Australia . . . 46
26 Data cleaning results using MMB GIC data . . . 47
27 B-field coordinate conversion between XYZ and HDZ . . . 48
28 SSC lag between US and Australia seen at 4 second cadence . . . 49
29 Underestimation of profile peaks when lower cadence data is used . . . 49
30 B-field variation in the TVA network from dense magnetometer measurements . . . 51
31 E-field magnitude variation in the TVA network, as derived from measured surface impedances . . . 52
32 Angular variation of the E-field in the TVA network . . . 52
33 Comparison of adjacent MT sites near Paradise in the TVA network . . . 53
34 Inversion of adjacent MT profiles near Paradise in the TVA network . . . 54
35 Visualisation of variation in the MT responses across the TVA network . . . 54
36 Noise regimes of GIC data . . . 56
37 Representative GIC profile using 98% of the base GIC spectral content . . . 56

38 Pulsations seen in noise-level GIC data at Paradise 57
39 Large GICs from long-period pulsations seen at Paradise 58
40 Pulsation-finding using the power network as an antenna 58
41 Synthetic white and red/pink noise relating to dB/dt and GIC 59
42 Discrepancy seen in representing signals with discrete frequency driving given incorrect spectral slopes 60
43 Correction in implementation of the dB/dt proxy 61
44 Ensemble estimation using a synthetic dataset 66
45 A visualization of effect of a geophysical strike on the E-field 68
46 Spectral weighting/averaging as applied to transfer function estimation 71
47 Summary of the different modelling approaches relevant to the ensemble methodology 72
48 Example of the resulting network parameter ensembles at Weakley, TVA 74
49 Convergence of the ensemble methodology 75
50 Stability of network parameters given different conductivity assumptions (local vs. generalised) and B-fields (local vs. remote) 77
51 Visualisation of the percentile ranges used to probe network parameter responses . 79
52 Network parameter sub-ensembles as defined by GIC magnitude percentile ranges . 79
53 Variation of network parameters with GIC magnitude 80
54 E-field directionality as a function of GIC magnitude 82
55 Network parameter directionality as defined by parameter ensembles 82
56 Network parameter directionality similar to Figure 55, but using a synthetic conductivity profile 83
57 B-field-to-GIC transfer function suffering from a poor signal-to-noise ratio 84
58 Improved B-field-to-GIC transfer function with dB/dt training 84
59 Frequency dependent network parameters as defined by an E-field-to-GIC transfer function 86
60 Uncertainty bounds for GIC modelling using the ensemble methodology 88
61 Network parameter ensembles for the Grassridge substation 90
62 Variation in network parameters at Grassridge due to conductivity assumptions . . 90
63 Variation in network parameters with GIC magnitude at Grassridge 91
64 Uncertainty bounds for GIC modelling at Grassridge 92
65 Low data fidelity network parameter modelling at the Matimba substation 94
66 Extrapolation to a Halloween Storm scenario at Matimba given current network state 95
67 E-field directionality at Murrarie, Australia 96
68 Local network topology around Murrarie and Middle Ridge 97
69 Corresponding network parameter directionality at Murrarie and Middle Ridge . . 97
70 Network parameter directionality at Bowen North, Australia 98
71 Poor signal-to-noise ratio B-field-to-GIC transfer function at Bowen North 99
72 dB/dt trained B-field-to-GIC transfer function at Bowen North 99
73 Network parameter ensembles at Memanbetsu 100
74 E-field-to-GIC transfer function at Memanbetsu 102
75 B-field interpolation result over southern Africa using a planar implementation of SECS 104
76 Map of variometers, magnetometers and magnetotelluric stations across southern Africa 108
77 dB/dt interpolation over southern Africa 108
78 Improvements in interpolation performance using dSECS 109
79 Error distributions of dSECS compared to typical SECS interpolation 110
80 Backus-Gilbert resolution matrix 113
81 Backus-Gilbert covariance matrix 114
82 Merged uncertainty taking into account both model and data limitations 115
83 Map of mid-latitude magnetometers used to compute semi-variance 116

84 Range distribution of binned variogram 116
85 Global mid-latitude variogram as defined for B_x and B_y components 117
86 Variogram parameter variation through a geomagnetic storm 117
87 Resulting simulation of experimental variogram 118
88 Inversion of simulated B-field to define typical current node values given a physical context 119
89 Final current node uncertainty, using model and data uncertainty estimates to scale physical uncertainty 119
90 Uncertainty bounds for B-field interpolation 120
91 Physically correct implementation of elementary current system interpolation at mid-latitudes 121
92 Corrected mid-latitude SECS implementation in the calculation plane 121
93 Equivalent current system between SECS implementations 123

Acronyms and Abbreviations

1D/2D/3D	1-dimensional, 2-dimensional, 3-dimensional
ac	alternating current
ACE	Advanced Composition Explorer satellite
AEST	Australian Eastern Standard Time
B-field	shorthand for magnetic/geomagnetic field
$B_{x,y}$	horizontal geomagnetic field components (geographical north and east)
CIR	co-rotating interaction region
CME	coronal mass ejection
dB/dt	time-derivative of the B-field
dc	direct current
DSCOVR	Deep Space Climate Observatory satellite, successor to ACE
E-field	shorthand for electric/geoelectric field
EMF	electromotive force
FEM	finite element method/modelling
FERC	Federal Energy Regulatory Commission
FFT	fast Fourier transform
GIC(s)	geomagnetically induced current(s)
GMD	geomagnetic disturbance
GSU	generator step-up unit
IFFT	inverse fast Fourier transform
IMF	interplanetary magnetic field
INTERMAGNET	global network of geomagnetic observatories
JST	Japan Standard Time
L1	Lagrangian point between the Sun and Earth
MT	magnetotelluric
NERC	North American Electric Reliability Corporation
RMS	Root mean square
RMSE	Root mean square error, also known as root mean square deviation (RMSD)
SAST	South African Standard Time
SECS	spherical elementary current systems
SI	sudden impulse
SNR	signal-to-noise ratio
SOHO	Solar and Heliospheric Observatory satellite
SSC	storm sudden commencement
SuperMAG	international collaboration of geomagnetic measurements
SVD	singular value decomposition
TVA	Tennessee Valley Authority
TF	transfer function
ULF	ultra low-frequency (roughly 1 mHz – 1 Hz)
USGS	United States Geological Survey
UT/UTC	universal time / universal time constant

Indices

Dst	Disturbance storm time index, measures the intensity of the symmetric ring current as derived from the H component of the B-field at low- and mid-latitude stations
Kp	K-index or planetary K-index, a 3 hour index of geomagnetic activity derived from mid-latitude data
SYM-H	symmetric disturbance of H component of geomagnetic field, a higher resolution version of *Dst*

1 Introduction to GICs

Geomagnetically induced currents (GICs) are naturally occurring electrical currents induced within the conductive Earth due to fluctuations of the geomagnetic field (B-field). When a grounded conducting network such as railway, pipeline or power grid is present, then these GICs may enter the network. Of the different forms of infrastructure that may be affected or disrupted by GICs, modern reliance on electrical power distribution drives the focus of most current GIC research, and this thesis in particular. Within previous studies there has been a skewed emphasis on extreme events. This is understandable since the direct and knock-on effects of GIC damage in power networks can be devastating to society at large[1,2]. Although the occurrence of an extreme 1-in-100 year event, such as the Carrington event of 1859, is low in frequency and extreme in scale, it is more than just a possibility. It is rather just a matter of time[3–5]. With this in mind, there has been a growing awareness in many countries about the potential threat that GICs pose. Research directly relating to the economic impact of GICs on power networks has also gained momentum[6,7].

The scope of possible regional GIC risk to power networks has increased since the original research papers focussing on auroral regions[8,9]. During the famous March 1989 storm, when the Hydro-Québec blackout occurred in Canada[1,10–12], extensive thermal damage was seen at a Salem substation transformer in New Jersey[13]. At mid-latitudes, GIC related damage has been recorded in the US[14], South Africa[15,16] and New Zealand[17]. At low-latitudes, large GICs have been recorded along with abnormal transformer noise in China[18]. Specifically within a power network, there is a distinction between GICs flowing in transmission lines and those flowing through grounded transformers. In terms of risk, the GICs that flow through a transformer are more likely to cause network instability and direct transformer damage, with edge nodes being most susceptible[19]. Line GICs on the other hand are larger in the interior of a network[20]. In this thesis focus is on modelling nodal GICs at a transformer and not network modelling at large. Since high-latitude utilities are aware of the risk posed by GICs and generally have more resources available for monitoring and mitigating GICs (examples being dense magnetometer networks and series capacitors respectively), this work will further focus on the mid- and low-latitude regions.

The effects of GICs on power network infrastructure is an active field of research[21–23] and the exact details of these effects are ignored here. Acknowledging the nature of GIC effects in a power network does however inform modelling requirements. The best known GIC effect is transformer part-cycle saturation, which has further follow-on effects. During core saturation, GICs introduce a quasi-dc offset that pushes the relation between magnetising current and the magnetic flux into a non-linear regime which results in stray flux. This leads to heating and gas evolution, decreased efficiency, reactive power demands and harmonic generation[9,24]. The exact nature of reactive power demands due to GICs requires reactive power to be properly defined[25,26]. Most studies dealing with reactive power assume sinusoidal waveforms, which are not the case in real-world operation or in GIC driving. Recent research has also found the simplistic hysteresis curve typically used to explain part-cycle saturation is misleading and not in fact non-linear[22]. In terms of the network, part-cycle saturation and its associated harmonics nevertheless results in unusual power flows, voltage fluctuations, frequency shifts and protective system malfunctions[1,27–29].

Most modelling aims to identify and address GICs magnitude levels where transformer damage would occur. NERC in this vein has defined a thermal damage limit threshold of 225 A in the neutral to be used as a risk benchmarking tool for utilities[30]. Modelling peak GICs alone is however not enough, especially given that GIC effects themselves are not always fully modelled using realistic conditions. Previous studies suggest that accumulated degradation may drive transformer failures where the initiating GICs in the neutral were not particularly large[16,17]. Saturation can occur with currents lower than 10 A in a ‘resilient’ three-phase three-limb (3P3L) transformer[15], creating localised hotspots and bubbles in the transformer paper/oil that may lead to partial discharge[31]. These conditions may initiate further degradation (or accelerate existing degradation) under normal operation. The extent of unbalance and distortion introduced by low-frequency GIC instead of purely dc GIC has material effects on system response and is the subject of continuing research[23]. More in line with the IEEE standard C57.163-2015 ("Guide for Establishing Power Transformer Capability while under Geomagnetic Disturbances"), modelling needs to recognise moderate GIC levels in addition to peak GICs. To be able to fully describe the system response there is the further requirement not only to model magnitude, but also the GIC profile shape – acknowledging that GICs are not purely dc. In all cases there is a need to include uncertainty in estimates for operational use, similar to what is required by the space weather community for uncertainty and reliability in general physics modelling[32].

1.1 Resolving Complexity

The full GIC problem is a complex system with multiple variables and fields involved. Instead of trying to solve the entire system in a single step, complexity is reduced by coupling simpler sub-systems. The use of proxies fits into this approach, with dB/dt, E-field or even geomagnetic indices used to quantify possible GIC exposure. Conventional coupling recognises different physical processes and addresses them separately, largely in the space physics, geophysics and engineering domains.

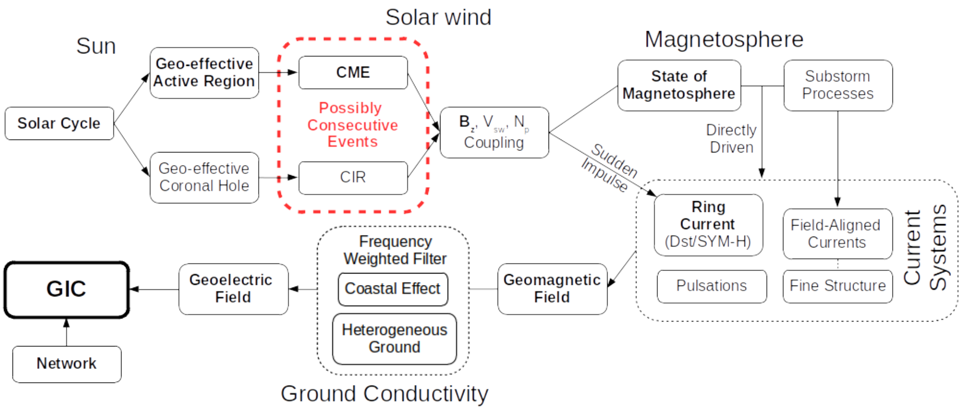

Figure 1: Breaking down GIC modelling into a process chain of coupled systems, we can get a feeling for the different factors to consider when modelling GICs at mid-latitudes. Factors with large influence at mid-latitudes are indicated in bold. Within the main solar wind coupling, B_z refers to the north-south component of the interplanetary magnetic field in geocentric solar magnetospheric coordinates, i.e. aligned to the Earth's magnetic pole axis, V_{sw} refers to the solar wind speed and N_p refers to the solar wind density.

In Figure 1, we have a high-level overview of the typical process flow identified. In the space physics field, research focuses on modelling of the Sun, solar wind, magnetosphere-ionosphere coupling and near-Earth current systems. From satellite observations, propagation models can predict the arrival of solar storms at Earth and the possible nature of their coupling. Simulations of the current systems in turn allow for scenario analysis[34]. Although each sub-system is well defined, there exist higher order factors that occur independently to the first-order drivers. An example of such higher order effects is from geomagnetic pulsations[35]. These B-field disturbances are ground signatures of cavity modes in the magnetosphere that ring when the system is perturbed. Other ionospheric current structures with fine spatial scales due to field-aligned currents and turbulence in the magnetotail have been shown to drive large GICs at high-latitudes[36]. The geophysics community in turn aims to use B-field measurements and information about the Earth's conductivity structure to estimate a driving E-field for GICs[37]. Here significant complexity arises with regards to the true heterogeneity of Earth's geophysical structure and without dense surface impedance measurements, simplifying assumptions need to be made. Finally, the engineering step of the process chain takes the derived E-field as input and scales the integrated result over the network footprint with network characteristics to estimate the end GIC[38]. The engineering calculation makes further simplifying assumptions of a resistive network. In most cases the resistances used are not measured, and the entire network, with different voltage levels, is not modelled.

1.2 Coupled System Process Chain of GIC Driving

1.2.1 Solar and Solar Wind Processes

To describe the process chain of coupled systems to consider in GIC modelling, we start at the root of solar-terrestrial interactions that cause GICs. Most of the driving disturbances seen on solar surface and solar wind are related to the convection zone immediately below the surface of the Sun and the Sun's more complex magnetic field. To a first approximation the Sun has a dipolar main field, but higher order factors are evident – especially at equatorial and mid-latitudes. Due to differential rotation (27 day average rotation period), the rotation frequency is higher at the core than the surface, and higher at the equator than the poles. Taking into account that solar plasma (and most space plasmas) is sparse and that collisions can be neglected, we can assume zero resistivity. For such a perfectly conducting plasma there is no diffusion of the magnetic field through the plasma. Magnetic field lines within the solar plasma are rather frozen-in, with advection possible. This allows motions to distort and twist the field lines. As a result of differential rotation, the higher order toroidal field seen in Figure 2 is produced. Further taking into account the convective cell motions on this toroidal field, the rising and falling of plasma further distorts the field lines creating a poloidal field in the north-south direction with a complicated loop-structure. These loop-structures are ultimately visible as granulation on the surface of the Sun. Granulation of roughly 1,000 km due to granule convection cells is observable and has a characteristic time of 10 minutes[33]. Supergranulation from larger convection cells of roughly 20,000 km across and a characteristic time-scale of days are also seen. More often associated with supergranulation are sunspots, which additionally track the roughly 11 year solar cycle that modulates general solar activity.

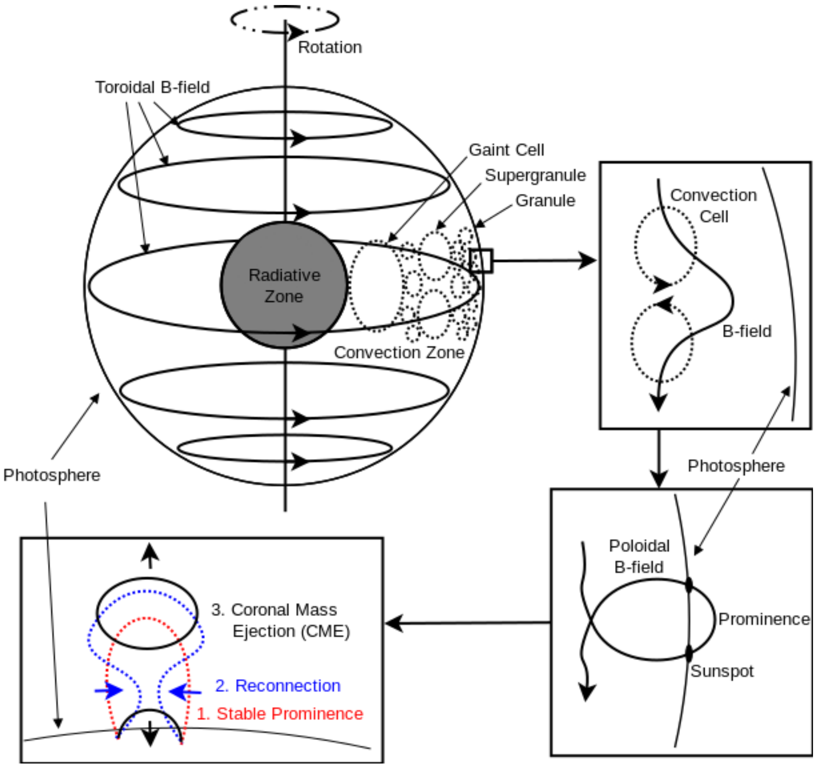

Figure 2: A representation of the solar magnetic field, along with convection cells that ultimately create sunspots, active regions and associated CMEs – the main drivers of intense GICs. Adapted from various figure exhibits in Cravens[33].

Sunspots are darker regions on the Sun that are cooler (3,000 K cooler) than the surrounding regions. The driver of sunspots is illustrated best with a single sunspot pair. When plasma, with its magnetic field and accompanying complicated loop, becomes buoyant and moves upward in the convection zone, it cools adiabatically. As the structure emerges at the surface, it is cooler than the surrounding plasma and observed as a darker region. As seen in Figure 2, the bipolar sunspot pair has two 'spots' where the magnetic field lines of the loop structure penetrate the photosphere. If the cooling is too extreme, buoyancy is lost and the sunspot disappears. The strong magnetic field associated with sunspots extends above the solar surface and results in an active region (which may contain magnetic 'arch' or 'loop' structures along which gas and plasma may travel). In each hemisphere, sunspots are confined to a latitude zone with implications regarding geo-effectiveness, i.e. would result in effects on Earth. These zones are closely related to the solar cycle, varying in number (first increasing to solar maximum and then decreasing to solar minimum) and location (initiated at mid-latitudes around 35° and moving equatorward to roughly 10-15°) during the course of a solar cycle. Sunspots of course do not only occur in pairs, but also in groups. Sunspot groups or active regions are inherently more complex and unstable.

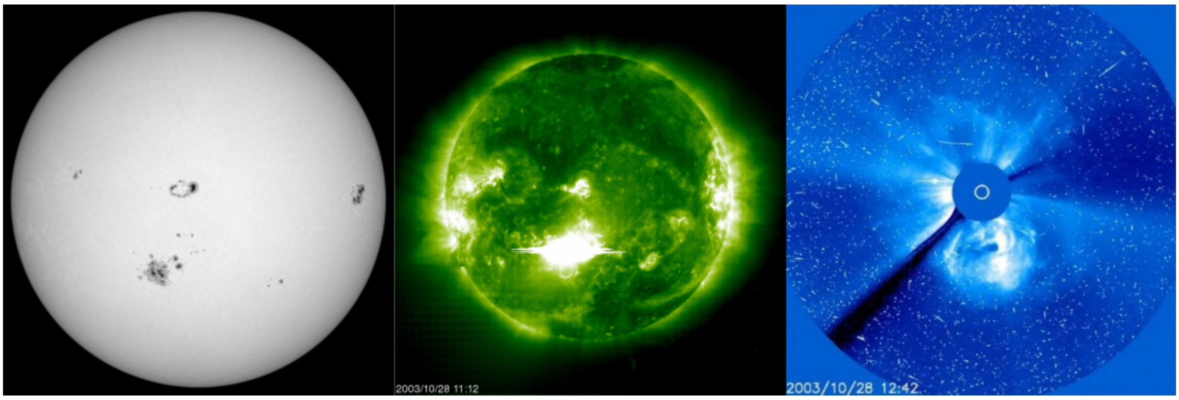

Figure 3: Images from different instruments on the Solar and Heliospheric Observatory (SOHO) satellite of the events on the Sun relating to the Halloween Storm of 2003. A visible light image by the Michelson Doppler Imager (MDI) of the solar disc shows the sunspot group that produced the solar eruption (gray). An ultraviolet image by the Extreme ultraviolet Imaging Telescope (EIT) includes a bright flash from the X17 solar flare (green). In the outer coronagraph from LASCO/C3 (blue), the resulting CME is seen. Images are courtesy of the SOHO/MDI, SOHO/EIT and SOHO/LASCO consortia. SOHO is a project of international cooperation between ESA and NASA.

When the equilibrium maintained by the magnetic cushion fails and the active region structure becomes unstable, reconnection of magnetic field lines can occur. At this point, a huge amount of energy is released across the electromagnetic spectrum and the explosively eruptive prominence is seen as a solar flare, as was the case for the 2003 Halloween Storm in Figure 3. In the case of larger denser active region structures becoming unstable, they are ejected from the surface as coronal mass ejections (CMEs) in a similar way to a typical explosively eruptive prominence. Although related, there is not a very good correlation between CMEs and solar flares. The mass of coronal plasma ejected then accelerates through the interplanetary medium, reaching Earth within a day for high solar wind speed CMEs[39]. Associated with the elevated solar wind is a shock front. The shock and CME plasma drives enhanced solar wind dynamic pressure and possibly an interplanetary magnetic field (IMF) change from the typical northward to southward, which ultimately initiates a geomagnetic storm in the near-Earth environment[40].

Other features related to the solar magnetic field are coronal holes. These regions are very large in comparison to sunspots, up to half a solar radius in extent, and usually seen at the poles but sometimes at lower latitudes. The 'holes' are ultimately open field lines that are the source of high-speed solar wind streams[41]. Since solar rotation creates an Archimedian spiral, the elevated solar wind compresses the ambient solar wind ahead it. The resulting shock has a direct effect on the near-Earth current systems, allowing for extended low-amplitude disturbances, such as CIR-type geomagnetic storms[40].

1.2.2 Magnetospheric Processes

When the solar wind finally reaches the near-Earth environment, the Earth's magnetic field (i.e. the magnetosphere) and the associated current systems are affected. Loosely, there are two main models of the ‘closed’ and ‘open’ magnetosphere. To a first approximation, the ‘closed’ model is related to a northward IMF and the ‘open’ model related to southward IMF. In the ‘closed’ case, shown in Figure 4, the coupling of the IMF is ignored. Charged solar wind particles form a bow shock when they encounter the magnetosphere, forcing the sunward boundary of the magnetosphere inward. The solar wind further reconfigures the entire magnetosphere into a tear drop shape with a trailing tail, dragging field lines continually from Sun to tail. Currents flow on the outer magnetopause, either closing in on themselves toward the sunward side or through the current sheet at the center of the magnetotail. The magnetopause current in effect opposes the dipole field outside the magnetopause, but enhances the dipole field within. In the case of increased solar wind pressure due to shock or CME, the magnetopause current initially intensifies and there is an increase in the B-field by a few tens of nanotesla as measured on the surface of the Earth. The intensification is seen as either sudden impulse (SI) or storm sudden commencement (SSC), depending in the IMF orientation, solar wind speed and dynamic pressure. On the sunward side, the magnetopause current closes in on itself at two neutral points. These are associated with the cusp region, where geomagnetic field lines are split between those that are ‘closed’ in on themselves at the poles and ‘open’ field lines that extend down the magnetotail. Magnetosheath plasma between the magnetopause and bow shock has its most direct access to the magnetosphere though these regions and the precipitating energetic particles are what ultimately result in increased atmospheric conductivity on the dayside auroral oval. On the nightside, the auroral oval is more often linked to the plasma sheet and field aligned currents.

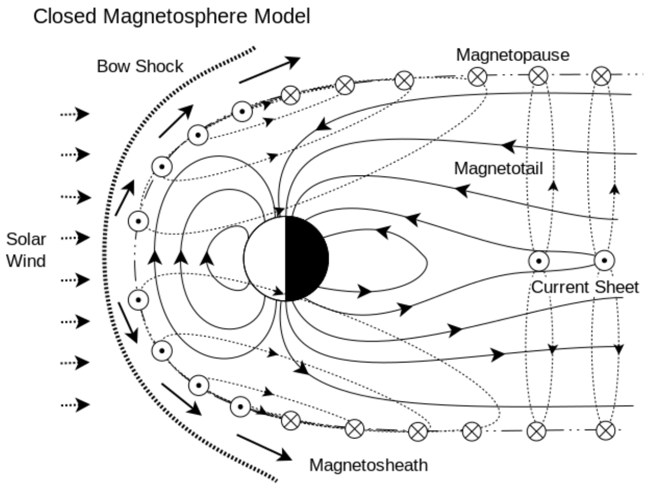

Figure 4: Assuming an incident solar wind without interplanetary magnetic field (IMF) coupling, the ‘closed’ model of the magnetosphere forms a generally accepted representation. Magnetic field lines are indicated by thin solid lines and arrows. Magnetopause currents are indicated by dots and crosses, with the thin dotted lines and small arrows indicating flows. A similar representation is used for the current sheet in the magnetotail. To note, this representation does not take into account any asymmetry between hemispheres.

The ‘closed’ model alone does not however explain the observed dependence on IMF orientation or open field lines in the cusp region. It also needs to assume an effective viscosity to account for momentum transfer to the magnetopause when the solar wind plasma is assumed to be collisionless. An alternative ‘open’ model that takes into account many factors of the original model attempts to

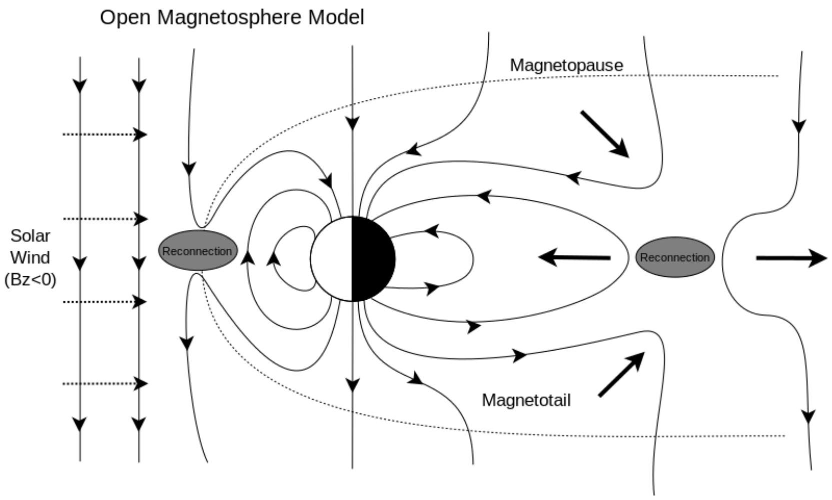

Figure 5: Addressing many shortcomings of the 'closed' magnetosphere model, the 'open' magnetosphere model takes into account IMF orientation and magnetic reconnection as intrinsic parts of the configuration of the magnetosphere. Here magnetic field lines are indicated by solid lines and arrows.

address these issues[33,40]. In the 'open' model, shown in Figure 5, it is assumed that the magnetosphere connects to the IMF via reconnection. The solar wind electric field in this case couples to open field lines and creates a convection electric field across the magnetopause from the dawn to dusk side. The plasma responds with E×B drift, as observed in the magnetopause currents. The extent of the drift and these currents is related to the efficiency of the reconnection, with a southward IMF being most effective as it is anti-aligned to the geomagnetic dipole. Simple reconnection in a diffuse region on the dayside of the Earth occurs in this case. When the IMF is non-southward, the associated reconnection is more complicated. Regardless, the reconnected field lines convect tailward over the polar caps. Magnetic flux accumulates in the tail where circulation forms the intense westward tail sheet current (measurable at low-latitudes during the midnight hours). Reconnection occurs again in this region and magnetic field lines are carried back Earthwards, often manifesting as geomagnetic substorms.

Besides the magnetospheric currents, the ring current in the inner magnetosphere is one of the dominant drivers of B-field fluctuations at mid-latitudes and the basis of the *Dst* (and SYM-H) index that measures global geomagnetic activity and characterises geomagnetic storms. The ring current region contains particles with energies in the order of tens of keV as well as colder plasmaspheric plasma. Generally the colder plasmas are dominated by E×B drift, but the more energetic ring current region also has magnetic gradient and curvature drifts[40]. The resulting drifts produce the westward electrical current around the Earth, i.e. the ring current. A typical current amplitude is about one million amperes, but varies significantly with geomagnetic activity as ions are injected from the tail current sheet during geomagnetic storms.

The ring current is not alone in the inner magnetosphere, but rather a single aspect of more complicated circuit (Figure 6), that includes ionospheric currents, partial ring currents and field-aligned currents linking the magnetosphere and ionosphere. Associated with each current system is a region on Earth that is more susceptible. Specific regions of interest are shown in Figure 7, and within each region there is a tendency for induced currents within Earth to be in a similar east-west direction to the driving current systems. At high-latitudes, the auroral ionospheric currents dominate, with larger perturbations and finer spatial scales compared to the ring current driving of mid-latitudes. Of particular interest are the east-west auroral electrojets. Related to the auroral electrojet system is substorm driving due to reconnection in the magnetotail. When there is enough loading in the tail region and reconnection occurs, the substorm current wedge (Figure 6) snaps back to Earth, carrying with it plasma and injecting charged particles into the electrojet system. This substorm current wedge is made up of an inbound dawnside current and outbound duskside current, with the result that the westward electrojet is increased. The direct impacts at high-latitudes are fluctuations in the B-field. In the low-latitude equatorial regions an equatorial electrojet exists on the dayside[41]. This current system is not related to the auroral electrojets and is much smaller in comparison.

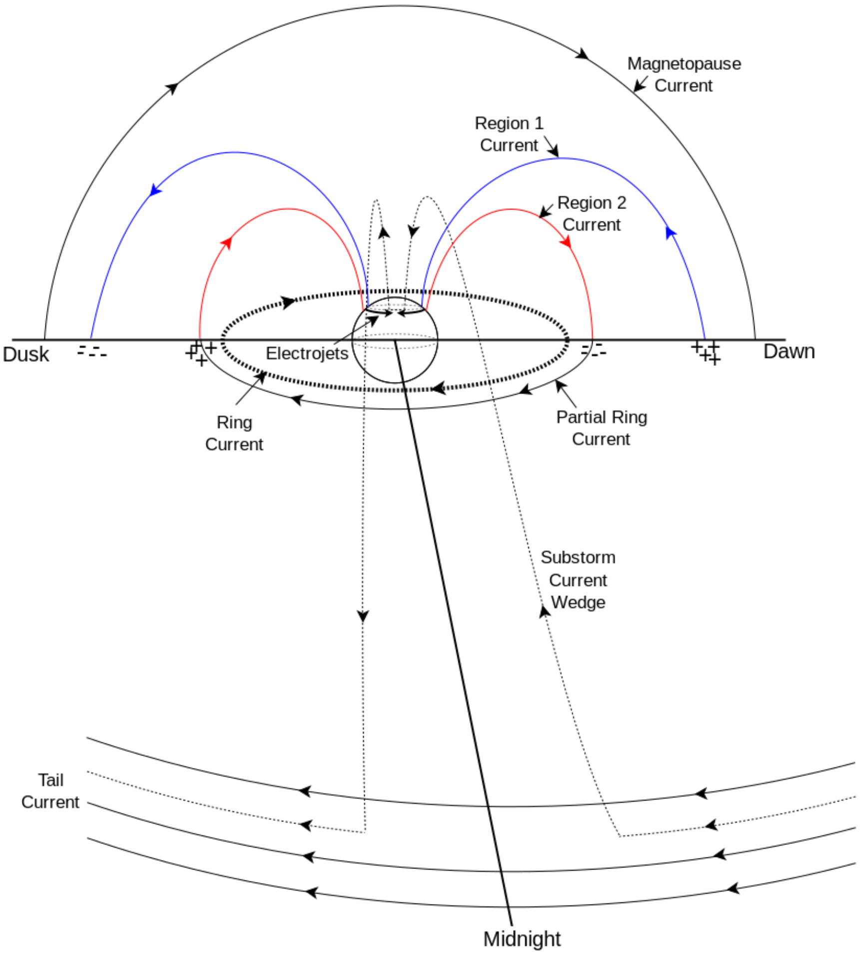

Figure 6: Simplistic representation of the near-Earth current systems and the substorm current wedge that drives substorms (related to reconnection in the magnetotail after magnetospheric loading). Arrows indicate current flow, with the red and blue currents referring to the region 1 and region 2 field-aligned current systems. Also indicated are the midnight, dawn and dusk axes and the charge accumulation (pluses and minuses) that drives the current circuit.

1.2.3 Geomagnetic Storms

In terms of geomagnetic storms that ultimately drive GICs, most display common features, seen in Figure 8[43]. An intense geomagnetic storm is defined as when the *Dst* or SYM-H indices drop to below -100 nT[44]. As mentioned previously, these indices are indicative of ring current intensity and to a lesser extent the magnetopause and partial ring current contributions. Using these indices, a geomagnetic storm can be broken down into phases that are related to different driving regimes[40].

Typically a geomagnetic storm would start with a sudden commencement (SC) or storm sudden commencement (SSC) that occurs near instantaneously across Earth, with the sunward signature slightly preceding other regions. The initial intensification or sudden impulse (SI) is due to the shock wave formed by the arrival of an elevated solar wind at the magnetopause. The SI is often associated with an increase in the northward component of the B-field, called the initial phase, and due to the compression effect of the magnetosphere. This phase can last for a number of hours.

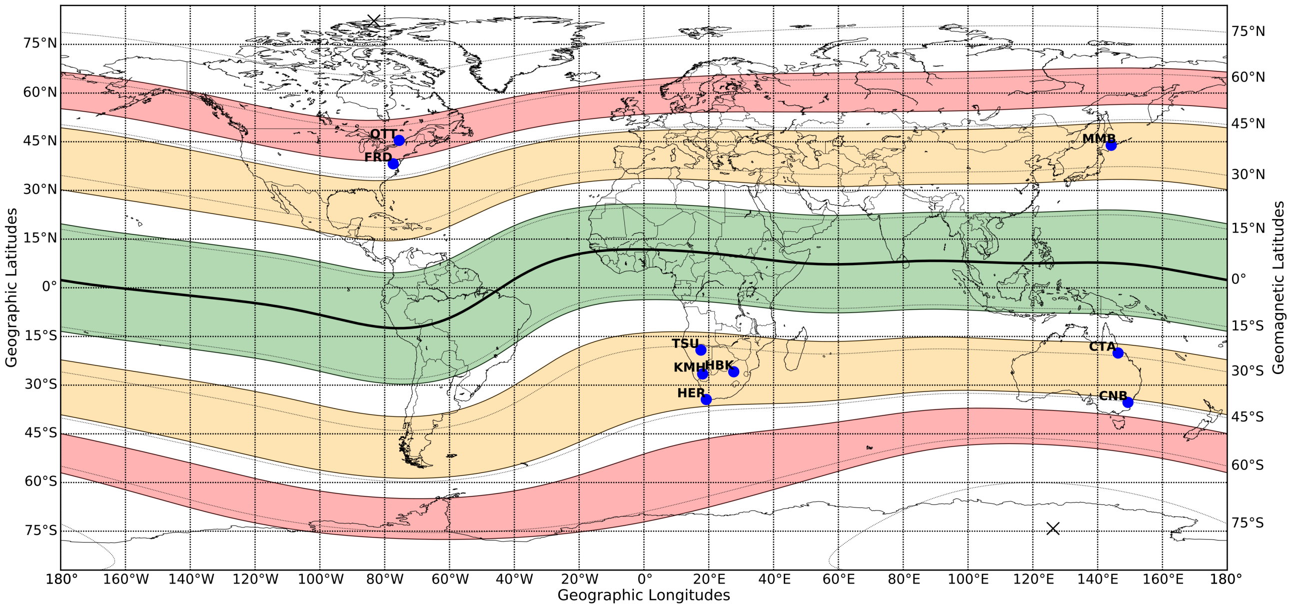

Figure 7: The geomagnetic observatories (blue) used in this work are shown along with geomagnetic poles (crosses) and the low- (green), mid- (orange) and high-latitude (red) geomagnetic regions. Modified apex coordinates and a quasi-dipole approximation are used for geomagnetic coordinates[42].

The next phase is the growth or main phase of the geomagnetic storm, triggered by coupling with the IMF as described by the 'open' magnetosphere model. Often the main phase is the only visible phase of the storm. The principle component of the B-field (aligned with geomagnetic north) decreases and shows large fluctuations for a longer time and with larger magnitudes than the initial phase.

Following on from the main phase is the recovery phase, where the B-field gradually recovers to its original undisturbed level. During the recovery phase there is little to no solar wind driving and the ring current response is dependent on the state of the magnetosphere. This phase lasts much longer than the previous phases put together, sometimes extending several days.

During the recovery phase the near-Earth environment is more sensitive to driving than it would be otherwise. If the Sun is particularly active, then it is possible that multiple CMEs can occur in quick succession, with a second CME impacting Earth during a recovery phase of a previous CME. Coupled with the fact the secondary CMEs have higher speeds due to the solar wind being 'cleared' by the preceding CME[12], the cumulative effects of CME chains are particularly destructive.

1.2.4 Geophysical Processes

Using the assumption of a plane-wave vertically incident disturbance B-field due to the near-Earth current systems, we next have to estimate the geoelectric field (E-field) that is related to the induced electromotive force (EMF) that drives either currents within the Earth or GICs within a power network. In deriving the E-field, a complication exists regarding the conductivity structure of the Earth. Simply put, the conductive Earth acts as a diffusive medium for penetrating disturbance B-fields. In the frequency domain, the E-field and B-field can be related by taking the conductivity of Earth into account. Since the conductivity is not homogeneous, local derivations of the E-field can vary significantly. In this sense, even the measured B-field ground signatures include various geophysical conditions that play a variable role. In certain regions, 40% of the surface B-field can arise from internal induced currents[45–47]. Not only has it been shown that the heterogeneity of the geophysical structures within Earth has a material effect on B-field and E-field estimation, but so too do land-sea interfaces. In both cases, the interface between different conductivity regions creates an accumulation of charge with its own contribution to the E-field.

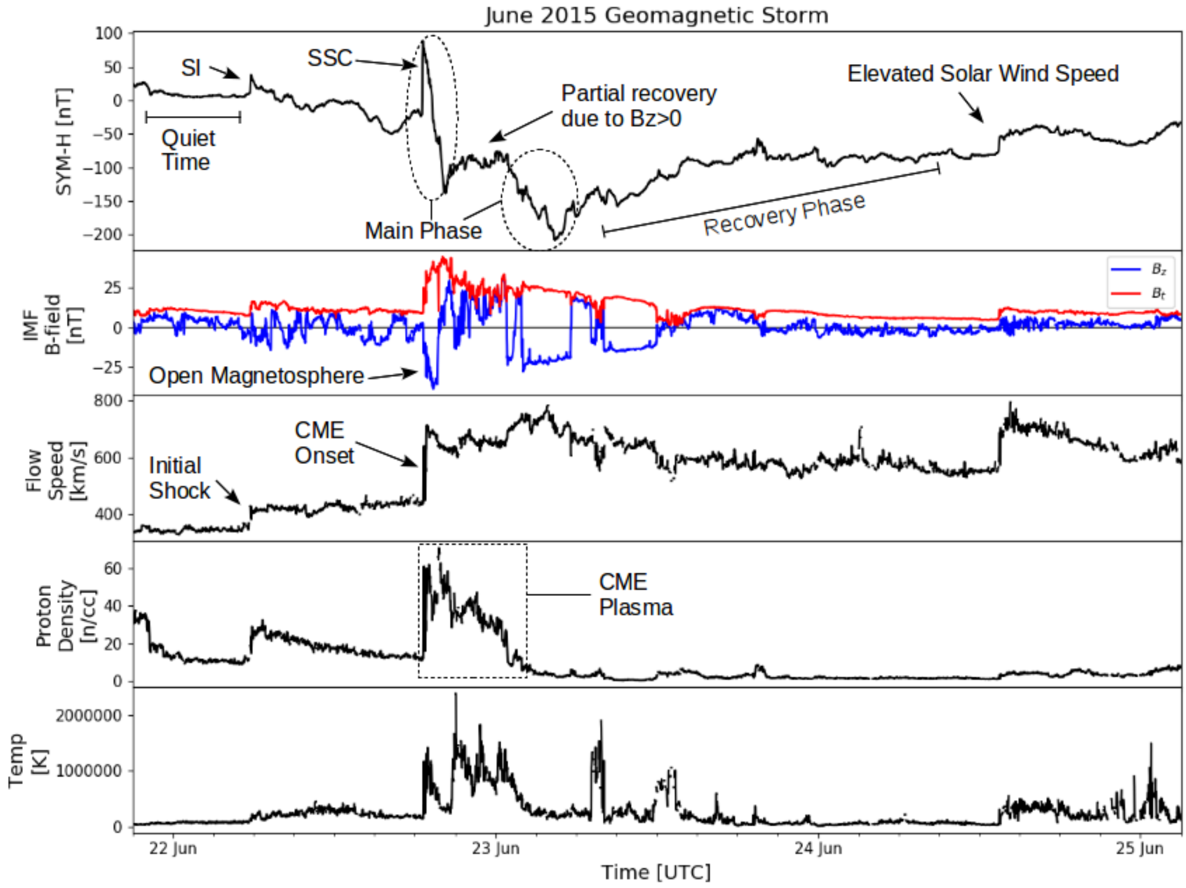

Figure 8: In-situ solar wind data taken from ACE and DISCOVR satellites during the June 2015 geomagnetic storm. The passing of CME plasma is indicated by the increased density and solar wind speed and the onset of the geomagnetic storm is seen southward IMF B-field (B_z component). Other interesting features include the initial shock front preceding the CME creating the sudden impulse (SI) and the slight recovery seen in SYM-H when the IMF B-field turned northward.

Up to this point, all the factors described occur regardless of whether a power network is present. When considering GICs, the network at large provides a favourable path for induced currents to flow and becomes a significant and active link in the coupled process chain. The network weights EMF contributions from the spatially variable E-field according to the network footprint and scales the result given various assumed or measured network resistances. If a large E-field is present but not aligned to the network, then the measured GIC would not reflect the apparently large driving. Common grounding and connections allow GICs to flow between different voltage levels and within a substation between multiple nodes. Inductive components of the network may add additional frequency dependence, which is not assumed in traditional GIC modelling. Transformer responses to GICs are further not linear, especially after saturation, and are not included in traditional modelling. The distortion created in this case can affect additional nodes, driving further unbalance.

1.3 Problems of Coupled System Approach

The chain of coupled systems approach is useful to probe the GIC problem, but some shortcomings need to be addressed for there to be confidence in operational modelling. In the coupled systems, each sub-system uses independent simplifying assumptions with the result that there may be inconsistency in modelling. The engineering step for example assumes the network reacts to quasi-dc GIC in comparison to the power frequency of 50–60 Hz, whereas the geophysical step defines complex GIC profiles which are not quasi-dc. It is further difficult to validate the accuracy of an assumption or sub-system within the coupled GIC problem. Where opportunities for validation in a certain sub-system exist, it is not guaranteed that the result is transferable to the larger GIC problem. In the geophysical sub-system, large undertakings of dense magnetotelluric surveys (e.g. USArray Transportable Array) are being done to estimate the E-field with increasing accuracy. Within the GIC problem, there is the additional factor of the network modulation of the E-field that needs to be defined. Errors all along the process chain are cumulative, and with no way to separate factors with high certainty, there is a significant need for uncertainty estimates when looking towards operational modelling.

The flow of GICs at the very end of the process chain takes into account all sub-systems together, regardless of which factors are modelled. Attempting to sequentially model the various sub-systems is bound to result in error between observation, which is defined by measurement, and model output, which is defined by representative modelling. In operational modelling there is danger in this gap between observation, assumed to be a reflection of reality, and model estimation.

1.4 New Possibilities

With the increased awareness of space weather and GIC risks, there has been a concerted effort to collect data. In the United States, the Federal Energy Regulatory Commission (FERC)[48] has directed power utilities to take GIC measurements and make these available for research purposes. Internationally, other utilities are similarly making transformer and system data available along with high cadence GIC measurements[49,50]. Geophysical research has pushed for large scale dense magnetotelluric surveys[51,52], which compliment the geophysical step of GIC modelling. The long datasets of geomagnetic observatory records have already been useful in extreme value analysis of possible scenarios and general risk assessment but not for operational modelling[53–55]. These B-field measurements are increasingly supplemented with low-cost variometers, which add to the modernisation of existing geomagnetic observatories to take higher 1 second cadence measurements. With the additional availability of data, we have also seen the increase in computing power to be able to process multiple large datasets in real-time. Leveraging all these resources, and the measured B-field and GIC data in particular, it is possible that the real-world dynamics of the GIC problem can be revealed. The rich datasets offer a statistical modelling alternative that can supplement traditional analytical models, while attempting to accurately model the reality as defined by operational measurements.

In approaching the GIC problem from a data-driven perspective, there is the distinct advantage of the resulting modelling being evidence-based, i.e. reducing the gap between measurement and representative modelling. The non-trivial coupling of the full GIC problem, which is so difficult to extract and describe analytically, is implicitly absorbed when operational measurements are used to drive modelling. Relating the data-driven methodology to traditional analytical methods further allows for error assessment within various sub-systems and the propagation of error within the larger GIC problem, i.e. the nature of the gap between modelling and measurement can be probed. Keeping to a data-driven and statistical modelling approach, error and the influence of unmodelled factors can be propagated into the final GIC estimates – a base requirement for models used to aid decision-making. The output of such data-driven models with uncertainty would ultimately be an estimate of the real system state along with confidence of the model estimate. Utilities and regulators alike would in turn be able to use such models in operational applications.

1.5 Hypothesis

Considering the nature of the disadvantages of the conventional coupled process chain, the evolving data availability, and the possible benefits of reaching the identified objective of operational modelling, this work explores an hypothesis that,

> *"Data-driven adaptations of conventional modelling of measured GICs from geomagnetic field disturbances can improve operational modelling application and accuracy."*

1.6 Research Questions

The research questions related to the hypothesis and used to guide research are defined as:

RQ1: *What measured GIC and geomagnetic data are available to utilities for operational modelling?*
Since we are linking geomagnetic data to GIC data, specifically what are the limitations of the data available? How large a dataset is needed to be representative? Does data cadence play a role? Does the data fidelity available inform the modelling methodology to be used? How are data sources calibrated and is there a significant issue of noise or poor data quality? Regarding the B-field driving GICs over the entire network, what type of spatial resolution is needed in B-field modelling for GIC studies? When this resolution is not available through measured data, what approaches are used to define the B-field needed?

RQ2: *Can data-driven methods encode more complicated dynamics and do they improve on conventional modelling accuracy?*
Using the same base assumptions, do data-driven models result in more accurate models? In the case that base assumptions relating measured B-field and GIC are incorrect, do data-driven models remain representative? Typical cases of the latter are when the frequency dependence of the E-field is incorrectly defined or the network modelling assumes incorrect system parameters.

RQ3: *Do conventional models quantify the associated uncertainties in modelling?*
Dealing with operational modelling, are there any probabilistic or error bands associated with GIC models previously developed? Do we have an idea of where there are drivers of uncertainty in the modelling chain and how this uncertainty propagates? Understanding the drivers of error and the robustness of methods given these errors is critical to operational application.

RQ4: *Are there any further characteristics of the modelling chain that can be inferred from the analysis of measured data?*
Besides the modelling of GIC time series, can we say anything about the drivers or network purely by looking at the measured data and empirical modelling? Using different datasets, can we infer the impact of different factors? Do any of these factors or characteristics inform operational applications?

RQ5: *Are there any particular benefits or differences regarding modelling in the time and frequency domains?*
Since modelling can be approached from either perspective, are there any benefits to choosing a single domain? Are there operational considerations regarding either modelling approach? Can uncertainty estimates in the frequency domain be propagated to the time domain?

1.7 Arrangement of Dissertation

Chapter 1	has introduced the GIC problem and formulated the hypothesis of this thesis, with appropriate research questions to guide research.
Chapter 2	will further investigate the current research environment that exists in the published literature, with an emphasis on operational modelling and uncertainty estimation.
Chapter 3	puts together the background theory needed for operational model development.
Chapter 4	outlines the framework to be used in developing operational models and defines the procedure for validation of these models, with emphasis on the data used.
Chapter 5	considers the frequency response of GICs and the use of appropriate GIC proxies before developing the operational ensemble models in both the time and frequency domains.
Chapter 6	specifically looks at results of empirical modelling using the ensemble methodology developed. Analysis of the modelling performance and uncertainty is done along with characterisation of elements in the GIC problem and drivers of uncertainty.
Chapter 7	probes the application of B-field interpolation often used and the associated uncertainty. The previous implementation in southern Africa is shown to be incorrect and is improved on. Explicit uncertainty is derived for the first time, with more general application to other fields possible.
Chapter 8	discusses the results, benefits and possible limitations of various aspects of the modelling methodology presented. Further, the contributions to the field are summarised.
Chapter 9	ties together the previous chapters by answering the research questions and assessing the validity of the hypothesis. Finally, implications of the hypothesis and research relevant to utilities and regulators are addressed.

2 Literature Review

GICs ultimately are a sub-field in a much larger field of solar-terrestrial interactions, making up a huge body of literature. Recently, the topic of space weather and how these interactions affect technological systems has become more relevant and more studied. There is a large body of work dealing with the engineering side of GICs, looking specifically at aspects of their effects on transformers and the power network in general. Although the effects of GIC justify the need for modelling, the effects of GICs are not the topic of this thesis. Rather, the nature of GICs that lead to the effects (i.e. magnitude and profile) inform the output of modelling required. A number of recent textbooks and review papers explore the current state of GIC modelling for general reference[56–58]. Besides operational GIC modelling, further GIC related research has an emphasis on simulations[34,59,60], real-time prediction[61,62] or forecasting capability[5,63] as part of the more general space weather hazard mitigation efforts. A separate field critical to GIC modelling is geophysics and the understanding of general induction in the Earth[37]. This field has seen significant development since the original papers detailing practical estimation of the relation between the B-field and the E-field, for example Cagniard[64] and references therein. Aspects of geophysics relating to GIC modelling are included in this literature review, but for general literature regarding the techniques typically employed two textbooks focussing on the magnetotelluric (MT) method are referred to[65,66]. Lastly, it should be noted that the scope of this thesis is an extension of the author's previous research and any previous research done by the author is not included in this literature review.

2.1 Operational Modelling Perspectives

Before looking at specific GIC modelling, for many utilities what is important is an estimate of the risk associated with GIC driving or the likelihood and extent of GIC activity. The results of such analysis usually fits into a larger risk matrix that is then used for decision-making on whether the cost associated with GIC damage justifies further modelling or mitigation. In the US, all utilities now have to comply with the FERC directive that requires full modelling and monitoring of GICs, with the aim to increase resilience amongst utilities[48]. Directly tied into these risk assessments are extreme value estimates of GIC in a network, which have been the topic of most recent research internationally. In its broadest sense, once extreme values are computed they are compared to a risk level, such as the thermal damage limit threshold of 225 A in the neutral as defined by NERC[30]. Depending on where the estimated risk sits, either further analysis is done with possible mitigation schemes developed or GICs are deemed not to be a risk. The use of GIC risk thresholds is not as definitive, with damage seen at much lower GIC levels in the past[15]. Thermal damage is also only a single aspect of possible damage, with system stability and cumulative degradation seldom being taken into account. An alternative to the NERC reliability standard, specifically defined in GIC terms using benchmark events, is the IEEE transformer standard ["Guide for Establishing Power Transformer Capability while under Geomagnetic Disturbances", C57.163-2015]. This standard takes into account transformer design and state, giving a weighting to moderate driving if a transformer is susceptible. Merging the two standards gives a more realistic estimation of GIC risk.

Since the E-field drives GICs and can be related to current magnitude in amperes through analytical network modelling, most of the extreme value analyses that inform overall risk assessment are restricted to E-field estimates. General extreme value analysis of the E-field using synthetic conductivity profiles and historic B-field measurements has been done for high-latitudes in general[3]. This analysis showed that in extreme cases GIC amplitudes of 2,000 A are likely in the 1-in-100 year scenario. Conditional probabilities were further used to estimate the probable level of the Carrington event. Other studies have focused on the global climatology of the E-field as a function of latitude[67], with similar climatology defined using a GIC index[68] and dB/dt[69]. NERC similarly defines GIC according to latitude, introducing scaling factors to estimate the locally relevant benchmark geomagnetic disturbances originally defined at high-latitudes. The NERC benchmark events however do not fully sample the possible drivers of GICs, limiting the profiles to the March 1989 Québec storm and simple conductivity assumptions. Other extreme value analysis has shown that current system variation at a small scale can cause extreme E-fields at high-latitudes[70] and that extreme dB/dt values are often localised[71]. Using the dB/dt as a GIC proxy, further work has characterised extreme driving and created an operational framework to warn utilities at different latitudes[72]. In terms of operational application extreme value estimates always have the down side of large associated uncertainty bounds given their scarce nature. The best case in terms of a long representative GIC dataset that allows for extreme value extrapolation comes from New Zealand. Here GIC data has been recorded for over 20 years over a significant portion of the network. The GIC data further shows high correlation to dB/dt, which has a longer dataset[49,73]. To increase dataset size further for extreme value analysis, approaches correlating GICs with longer datasets, such as Dst, are often applied[74].

In other cases, proxies have been used effectively to determine baseline susceptibility and risk, as well as being used extensively for simulation purposes[75]. Of the proxies used, the time derivative of the B-field, dB/dt is the most common followed by the disturbance B-field above a baseline, ΔB. Initial analysis of dB/dt as an induction proxy showed that it is sensitive to small scale structures[76]. When taking into account dB/dt direction, the conductivity structure of the region plays a role in the resulting proxy result, as well as the driving sheet current systems in the ionosphere. At high-latitudes it was found the proxy matches the directionality or orientation of the westward electrojet for large scale driving, with additional small scale perturbations[77]. Further analysis has shown that the proxy is also sensitive to seasonal and diurnal variation, coupled to current system driving[78]. At mid-latitudes, similar analysis has been done using dB/dt, with both dB/dt and ΔB being used to establish why the Halloween storm was as effective as it was given it was not as impulsive as less effective storms[79]. Similar analysis was done looking at the sudden impulse driving due to the ring current or substorms, with dB/dt as a proxy for damage at mid and higher latitudes[80]. Other than raw dB/dt, rolling envelopes of 1 to 3 hours have been shown to more accurately quantify GIC activity, with directionality and local proxies being important[81]. Similarly, for regional forecasting of GIC in particular, a rolling window of 30 minutes has been shown to be effective with high correlation[82]. There have however been instances where dB/dt does not describe observed GICs[83], but rather ΔB. These cases are usually explained through the local conductivity structure, i.e. a conductive upper layer in a two layer conductivity approximation[84,85].

A further operational risk proxy has been developed by Marshall et al.[86], first for pipelines and then extended for the Australian power network[87] and more recently applied in the Italian power grid[88]. This GIC proxy does better than B-field based proxies as it takes into account the low-pass filter nature of GICs and calibrates the general GIC proxy to measured instances of damage or disruption in the power network. Using the calibrated proxy, thresholds of varying risk are defined and can give a utility an idea of where its GIC risk sits relative to previous known effects. The use of a proxy that takes into account frequency scaling of the B-field is encouraging as it should provide a better link to GIC driving.

2.2 GIC Modelling

Although recordings of extreme geomagnetic disturbances have been identified in the 1800's[2], the first papers addressing GIC in power networks only appeared in the 1970's [for example 8,9]. These original papers cited previous power system and communication system disturbances noted in the 1940's, but were the first attempt to identify and model GICs and their effects in power systems. The next big step in GIC modelling came in the next decade with rigorous modelling of the induced E-fields and additional measurements of geomagnetically induced currents in Finland[45,89]. In March 1989, the now famous Hydro-Québec blackout occurred[1,10–12]. The blackout, a direct result of a large geomagnetic storm and associated GICs, can be thought of the catalyst to the modern intense research interest in GIC modelling. In subsequent years, a stream of research regarding the effects of GICs on power systems appeared, including harmonic distortion, phase imbalance, protective relay and static var compensator maloperation and general transformer and generator damage[24,90]. Interest from utilities also increased, with a focus on possible mitigation strategies, operating guidelines and monitoring procedures detailed[90]. The very successful EPRI-SUNBURST monitoring programme was started[91], which allowed wide scale GIC monitoring, which up until then had been limited. The SUNBURST monitoring program has provided the basis for many further programs and focuses on measuring the GIC in the transformer neutral. Of recent there has been a move towards differential magnetometer measurements along transmission lines that can estimate line GICs[20,92]. Interest in GIC modelling has also grown from a geophysical perspective. It was noted that GIC in a power network can often include significant information of both the regional geophysical environment and the driving current systems[93]. Viljanen and Pirjola[94] went further, formalising the since widely used approach of splitting GIC modelling into 'geophysical' and 'engineering' steps. In this case the geophysical step deals with the estimation of the E-field, which is then passed on as input to the engineering step that takes into account the network and ultimately estimates the resulting GICs.

2.2.1 Network Modelling

Analytical modelling of GICs modelling within a network has changed little over the last 30 years, seeing only incremental improvements. The base approach employed is the Lehtinen-Pirjola method[38], which assumes a resistive network and known system parameters. The method uses an input E-field and applies Kirchoff's law to calculate the resulting currents at nodes. The E-field is ultimately modelled as voltage sources in the lines and not at the ground points, implying that realistic non-uniform fields can be used[95]. In subsequent work, the analytical network modelling formulation has been validated through significant GIC measurements by Viljanen and Pirjola[94]. In the same study, the nodal formalism of using network parameters was employed, where network parameters are defined for a single node without requiring full network modelling. Along with improved E-field models using more realistic current sources for the high-latitude region and better conductivity modelling using layered-Earth surface impedances, simulated GICs were produced for the entire network. Such GIC simulations have been the basis of many future works where the aim is estimating GIC risk in a network. In terms of incremental improvements on the original Lehtinen-Pirjola method, the method subsequently been shown to be equivalent to the Nodal Admittance Matrix formulation of the GIC problem that has been extensively used as well[96]. Neighbouring networks can be modelled separately, using the connecting line voltage and line resistance as a Thévenin equivalent circuit, with neighbours only affecting the edge node[97]. Other improvements include the representation of autotransformers and two-winding transformers[96], multiple voltage levels[58] and the application of this in transformer-level modelling within a substation for different voltage levels[17]. Recent research has also questioned the resistive assumption of the network[98]. Although no definitive frequency contribution from the network was found, frequency based transfer function modelling was found to achieve more accurate modelling.

Within the analytical framework defined by the Lehtinen-Pirjola method for modelling GICs across a network, there is a further possibility of estimating the directional sensitivity of different nodes given initial full network modelling[99]. Building on the directional sensitivity of the network as defined by network analysis, the preferential directionality of a calculated E-field can be included that effectively modulates the total GIC susceptibility[100]. Similar analytical network-wide susceptibility of nodes has been done in Spain[101], with the output of both relevant to mitigation strategies.

In the time domain there have been a number of empirical alternatives to analytical network parameters that require assumptions of system resistances. Pulkkinen et al.[102] was one of the first to allow estimation of the ratio of nodal network parameters via best fit of expectation values between the E-field and measured GIC. Subsequently this approach has been applied successfully in various contexts[103,104]. Expanding, Wik et al.[105] assume a least squares approach to solving the governing GIC equation and note the ratio of network parameters change with GIC threshold used, linking to the empirical 'tuning' of the network parameters. In South Africa, a separate empirical approach has been developed that uses zero-crossings of the E-field components to constrain either network parameter[106]. Although this approach does provide improvement, there are few zero-crossing available for best fit and the method is biased towards the cardinal directions when either component is zero. An improvement on defining a distribution of network parameter estimates instead of a single value has been applied by Weigel and Cilliers[98] by making use of multiple days of data separately before applying a statistical best fit routine. The result again shows variation in network parameters where they are typically assumed to be constant. A final quasi-empirical approach is shown by Marshall et al.[50] where, after analytical modelling, the model result was scaled by a factor to minimise the RMSE. Although the profile shape and correlation coefficient gave adequate results using analytical network parameters, the scaling factor again acted as an empirical network parameter to 'tune' the result. In essence, this shows that there are possibilities in calibrating a network empirically and driving the model analytically for operational application.

2.2.2 Geophysical Modelling

Since analytical network modelling adequately models GICs given a E-field in cases where system information is available, significant emphasis and resources have gone into ensuring the E-field estimation is as accurate as possible. Expanding on this concept, the need to estimate GICs exactly has often been replaced by a proxy of induction hazard, as defined by the E-field. In either case of induction hazard estimation or GIC modelling, deriving the E-field from B-field observations requires an understanding of the driving current systems as well as the conductivity of the Earth. Even when just considering the disturbance B-field, the inductive component from geomagnetically induced subsurface currents can be as much as 40%[45–47]. Lateral conductivity discontinuities add additional complexity to the E-field response. The coastal effect is such an example and a recurring topic in GIC modelling, with known impact on modelling globally. Simply put, where there is a land-sea interface or other lateral conductivity discontinuity, there is an associated enhancement of the E-field due to charge accumulation at conductivity contrasts. Analytic calculations are possible, but these are very dependent on the specific case used[107].

Stemming from the principles of induction in the Earth, a number of different methods have been developed over the years. The methods range from analytic to purely empirical, but all find their root in the relation of the B-field to E-field in the frequency domain[64]. The implementation of this basic relation varies in complexity, ranging from the homogeneous Earth case to full-physics finite element method modelling[108,109]. Of the various approaches, the most popular is the magnetotelluric (MT) method that relates B-field and E-field through a complex surface impedance[64]. Modelling that takes into account frequency responses can further be done in the time domain through impulse response functions, either formally defined for surface impedance[110] or as a look-back window using homogeneous Earth conductivity and a set look-back period[45,111].

Complementary approaches to the MT method are the complex image method (CIM)[112,113] and thin-sheet modelling[114–116]. The former makes use of a complex subsurface current source at the skin depth defined by the surface impedance (and can take into account a layered-Earth, but not lateral variation of conductivity). The resulting equations allows for a simple and fast analytical relation between internal and external B and E-fields. Thin-sheet modelling was developed prior to the use of the MT method, but intrinsically is based on the same concepts. Initially a thin-sheet was assumed on uniform conductivity[114], which was then extended to layered conductivity[116]. By defining a thin layer or thin-sheet of laterally variable conductivity on top of a 1D profile, the method can encode the coastal effect[117], with the laterally varying thin-sheet including the sea. Within GIC modelling, the thin-sheet approach has been used successfully in various contexts[118–120]. There are however limitations in the frequency range that can be modelled using the thin-sheet approach, due to the depth of the sheet and conductivity[121,122]. Recent work has shown that to characterise the GIC frequency response correctly, higher frequencies than those defined by the thin-sheet approach are needed[123].

Of the various E-field estimation methods, the MT approach provides the most overlap with the geophysics community. The modern implementations of the MT relation have improved significantly from the first-order homogeneous Earth assumptions first used[64]. The first improvement in geophysical modelling came in the form of 1D layered-Earth models. In terms of the surface impedance tensor, the off-diagonal is non-zero and frequency dependent. Local layered-Earth models are sufficiently representative unless there are significant heterogeneities in Earth's conductivity. In the case of well known strikes (interfaces between regions with different conductivity profiles), such as those expected from the coastal effect, simple 2D models can be employed. The surface impedance tensor in the 2D case still has non-zero off-diagonal components, but these are no longer equal and rather describe the orthogonal and parallel components of induction relative to the strike. A rotation of 2D conductivity to take into account the angle of the land-sea interface has been shown to perform as well as full 3D conductivity modelling, which requires all surface impedance tensor components to be independently defined[124].

A further improvement on the layered-Earth and 2D models has been the use of piece-wise modelling of different physiographic zones across a network[119,125–127]. Given more accurate regional modelling of the conductivity structure in turn allows for better E-field magnitude estimation and better risk assessment given analytical modelling. The piece-wise approach however does not provide more accuracy than an empirically tuned simple 1D model. For truly representative geophysical modelling one has to turn to full scale MT survey[51] modelling using various methods[110,128]. The US leads in the use of MT surveys for induction hazard studies, with numerous geoelectric hazard maps that have been produced[129–132]. Australia is also involved in current large scale dense MT studies that would be able to provide similar analysis in the future[133,134]. Using the dense US survey, it is generally recognised that local conductivity is needed as there can be huge variation in responses within a physiographic zone[135]. Nevertheless, corrected simpler models can work[136] and when coupled with validation from measured GIC data, some network averaging or interpolation is seen to improve on solely 3D approaches[137]. Elsewhere, the initial 1D conductivity model used in Finland was validated and it was rather the small scale structure of near-Earth current system driving that was found to be important in modelling[138]. Further analysis of the US data has also shown that induction effects other than the coastal effect are seen to produce significant polarisation of the E-field, specifically for larger geomagnetic disturbances[132]. In either case of current source or conductivity heterogeneity, fine scale deviations are apparent. When the network scale length between nodes is comparable then these effects become relevant and network averaging does not help.

Although measured GIC validation in the state-of-the-art geophysical modelling approach remains limited, full network related voltages calculated using realistic impedances have been estimated[139]. Without GIC measurements for validation, there is up to an order of magnitude difference in voltage estimates when compared to simpler models. Recently, a promising new modelling approach has been developed to bypass integration of the E-field along the network footprint for GIC modelling, but rather build in the 3D surface impedance into line-specific frequency responses that act as transfer functions and are driven by the B-field, only needing the scaling provided by network parameters[140]. Unfortunately, the question of correct network parameters still needs to be addressed for accurate GIC modelling. In this case the impact of the entire network needs to be taken into account, while being non-trivially weighted with unmodelled factors. The result is that given high-fidelity geophysical modelling there remains no ground truth besides measured GIC validation.

2.2.3 Transfer Function Modelling

A different approach to traditional GIC modelling is that of transfer functions that map the B-field directly to GICs. These empirical relations in the frequency domain sidestep the need for conductivity and network assumptions. In the frequency domain and using a conventional approach of an E-field related to GIC through network parameters, incorrect conductivity assumptions may be observed as a phase shift, similar to the phase shift seen between driving B-field and E-field expected due to the conductivity structure[141,142]. Previous applications of transfer functions driven by the B-field have been limited, with examples in the UK[62,122], New Zealand[143] and Japan[98]. For the former, transfer functions were coupled with more extensive hazard estimation in the UK that noted lower voltage networks need to be considered along with better network modelling. In an operational context the 1D modelling was seen as accurate enough in comparison with previous work[144]. The latter example in New Zealand makes use of the transfer functions as a basis for extrapolation to a Carrington-level event. An amplitude correction was further applied to bypass the issue of lower sampling rates not adequately describing peaks. A basis for operational modelling that includes transfer functions is presented by Pulkkinen et al.[145], where different levels of input data can be used. The modelling inputs range from dB/dt to the spectral response, single estimates and empirical modelling. Extending this work, an empirical approach was developed to estimate network parameters from measured B-field and GIC data, which was then used to estimate a surface impedance and invert an effective conductivity profile[102]. This approach is essentially a quasi-transfer function has been applied very successfully in geophysically complex regions[146] and the South African network[104]. Of the shortcomings of transfer function modelling is the fact that all calculations are in the frequency domain and require a set amount of data, with edge effects an issue in real-time estimation. To overcome this, impulse responses can be derived to get the same result in the time domain. This has been done in GIC modelling in a move away from the homogeneous Earth assumption[147] and in real-time E-field estimation[110].

2.3 Input Parameter Sensitivity

Through the development of different modelling applications and approaches in the literature, general GIC characteristics that have become apparent. Continental scale modelling undertaken in Europe, initially using simple layered-Earth conductivity and network assumptions[148,149], has shown that local conductivity and variations of the driving current system relative to network are important for accurate modelling. For such large scale modelling, spherical geometry is needed in contrast to local modelling where a planar approximation suffices. Using both small and large networks, it has been shown that the local environment is very important and an effective network response is required, similar to original papers stating that up to two nodes away are relevant[19]. The point is made that although arbitrary network parameters can be used, the error or uncertainty should ideally be estimated.

In terms of other operational factors, although the general network topology plays a role in GIC modelling, analytically it was found that geophysical conditions have a far greater impact. Using realistic resistive and conductive Earth profiles resulted in E-field differences on the order of 100 times[150]. In this analysis, cumulative exposure showed similar sensitivity. Expanding on the effect of different apparent resistivities, within a surface impedance response there can be definite complex geological effects. That said, the most important factor in GIC modelling is still in the accuracy of B-field estimation[123], with the distance between magnetometer and network critical to this accuracy[151]. Making use of the improved layered-Earth profile and virtual magnetometers by interpolation, the minimum distance for adequate GIC modelling at mid-latitudes has been determined[152]. Relatively accurate GIC modelling can be done at mid-latitudes within a spatial scale of about 600 km in the east-west direction and 300 km in the north-south direction. These scale lengths assume mid-latitude driving without fine scale current structure as is seen at higher latitudes driving large GICs[36,153].

Looking more closely at the network information inputs, recent research includes state-of-the-art transformer level modelling[17], where more than an order of magnitude variation is seen between transformers in same substation due to transformer characteristics and connections. Detailed network information and GIC data available for such transformer-level modelling is not typical for utilities. Given a case where this level of modelling is not possible, but there still exists uneven GIC distributions in a substation, there would be significant unmodelled factors assuming traditional modelling approaches. Further research in the Irish network found that variable grounding resistance and lower voltage networks are important in GIC modelling[154]. The case of lower voltage networks affecting HV modelling results is often seen[96,118]. A possible explicit example of this is seen in the complex part of the Australian network where analytical modelling of the HV is anti-aligned with measured GIC[155].

2.4 Geomagnetic Field Interpolation

In terms of B-field input into GIC modelling, interpolation is commonly used[106,127,156,157]. Of the many interpolation methods, the most used is the physics-based spherical elementary current systems (SECS) interpolation scheme[158,159]. This method assumes an equivalent current system in spherical coordinates at a certain height (above and/or below ground) and then estimates this system by inverting ground magnetometer measurements. To complete the interpolation, the equivalent current system is used to estimate the B-field at some other point on the ground. The method describes the current system in terms of divergence-free nodes, which are representative of high-latitude Hall currents. The application of the method is widespread and not limited to GIC studies[160,161]. A fast planar version of the SECS method has also been derived, with particular application to GIC modelling using simple 1D conductivity profiles[162]. This planar version has found extensive use in South African studies, with successful GIC modelling[152] but the surprising result of significant vortex-like spatial variation in the interpolated disturbance B-field[157]. The distant ring current is the predominant driver for mid-latitude regions and the spatial variation as such should be smoother. The observed vortex-like spatial variation may in fact be an artefact of using divergence-free equivalent current nodes. Ngwira et al.[152] went further to use this implementation to define the typical mid-latitude spatial separation between magnetometer and network node appropriate for GIC modelling mentioned previously. In mid-latitude Spain, the SECS interpolation scheme was not found to be particularly accurate[124], which is further supported by analysis in the UK where a similarly sparse magnetometer array was used[163]. Torta et al.[124] similarly cites the issue with divergence-free equivalent current nodes unable to describe a relatively flat-field. In comparison with other methods at mid-latitudes, Torta et al.[124] found that using a nearest neighbour or a magnetic scalar potential method that does not make use of divergence-free nodes achieved better results. No approaches to estimating the uncertainty involved with interpolation were found in literature.

2.5 Summary

In summary, after an extensive review of GIC literature it was found that although power networks in all regions can experience GICs, the level of GICs is dependent on the local conductivity and network characteristics. Higher latitudes regions are more susceptible to induction risks and smaller scale effects due to fine scale and nearer current sources are apparent. Within the context of induction risks to power networks, some network smoothing allows regional estimates of the B-fields and E-fields to be adequate, but not when there are large heterogeneous conductivity structures (similar in scale to the network size). The state of the art can be seen as full 3D conductivity modelling, coupled with dense magnetometers or interpolated B-field to estimate the E-field along the network footprint and possibly a scaling of the result using accurate network information. With high accuracy network data that includes transformer characteristics, transformer level modelling can be achieved. Unfortunately, there are no cases where all these factors come together. In terms of general susceptibility, traditional GIC modelling using simplifying assumptions or the current state-of-the-art modelling can be used to give an idea of the risk to utility, with global climatological models of GIC related proxies also being used. For extreme value analysis, the results are very much dependent on the dataset length and quality, with the best cases still having large uncertainties. A large gap still lies within the operational modelling of GICs, i.e. being able to estimate the GIC profile that would be seen by a transformer in real-time with uncertainty included for decision-making.

With regards to gaps in operational GIC modelling, the first and foremost is the lack of uncertainty estimates in general GIC modelling or the various steps in the modelling chain. In contrast to MT studies that have defined error estimates in the surface impedance estimates used for GIC modelling, no further error propagation is done. For GIC modelling, the only uncertainty estimates of final GIC profiles have been as confidence intervals[142]. In the interpolation of the B-field, often done and acknowledged as critical to general modelling accuracy, no uncertainty estimates are included. Here we also have a discrepancy where planar SECS interpolation in South Africa reportedly works, but the same interpolation scheme gives poor results in other mid-latitude regions. Although this may be due to a geological effects and different current sources, the SECS methodology as applied in South Africa should be validated.

Part of the lack of uncertainty estimation is that there is a distinct lack of validation of models with measured GIC data. In the past, the lack of validation can largely be attributed to the lack of data availability due to its commercial sensitivity. The lack of validation sets also points to the general emphasis on physics-based modelling instead of empirical modelling, although it is acknowledged that many factors are not modelled or uncertain in these analytical models. In the case of data being available, there is still a distinct emphasis on state-of-the-art modelling and not on modelling that is robust and can be implemented in real-world scenarios with limited or poor quality data. In cases where the state of the art is not viable, GICs could still be modelled using simple models which can be made operational if uncertainty is included.

Although conductivity plays a large part of the complexity in GIC modelling, there are many cases where simple assumptions are adequate. Regardless, a lot of recent work has gone into improving the geophysical step of the modelling process with better estimations of the E-field, leaving many network factors unmodelled. Empirical methods provide a mapping can sidestep both conductivity and network assumptions, but are often avoided due to them not being generalisable. Given that analytical methods can define susceptibility well, for operational modelling it may be worth developing empirical methods for at-risk nodes after an initial susceptibility study has been done.

Besides the lack of empirical modelling, there is also a lack of modelling in the frequency domain. Most modelling restricts the estimated E-field to the time domain, although there are indications of different driving regimes in the frequency domain that make frequency domain modelling more accurate. Part of the frequency domain analysis is probing the resistive network assumption made in GIC modelling, where more work is needed given the limited validation of this assumption empirically. Lastly, there are also indications that the much used dB/dt is not always the best proxy to use, with some cases making use of ΔB instead, either for large scale driving or complex conductivity.

3 Theoretical Background

In this chapter, theoretical concepts that make up the basis of model development are explored. GICs are ultimately the result of geomagnetic induction in the Earth, driven by fluctuations of a disturbance B-field within an induction loop that includes a conducting network. Through Faraday's law of induction, the driving EMF can be estimated by the E-field. The link between GICs and the E-field provides significant overlap with geophysics. Within geophysics, magnetotelluric studies extensively use and/or estimate the E-field, forming the theoretical basis for induction within the Earth. Although complex geophysical modelling of the E-field exists and may improve estimates of E-field magnitude, the majority of variation in the E-field can be represented by much simpler, first-order approximations of dispersion within Earth. In both the first-order and complex E-field estimation, the conductivity of the Earth affects the associated skin depth of the incident electromagnetic wave differently for different frequencies and analysis needs to be done in the frequency domain. In Figure 9, we see the dynamic GIC spectrum that results from driving geomagnetic disturbances with different spectral characteristics that are convolved with the Earth's response. Although not novel, the link between spectral characteristics and EMF driving is further clarified with illustration. Having established a basis for thinking about induction within the Earth, the theoretical background of modelling GICs at a network node is explored. Lastly, in the often seen case of limited B-field data, the popular spherical elementary current systems (SECS) interpolation scheme is described.

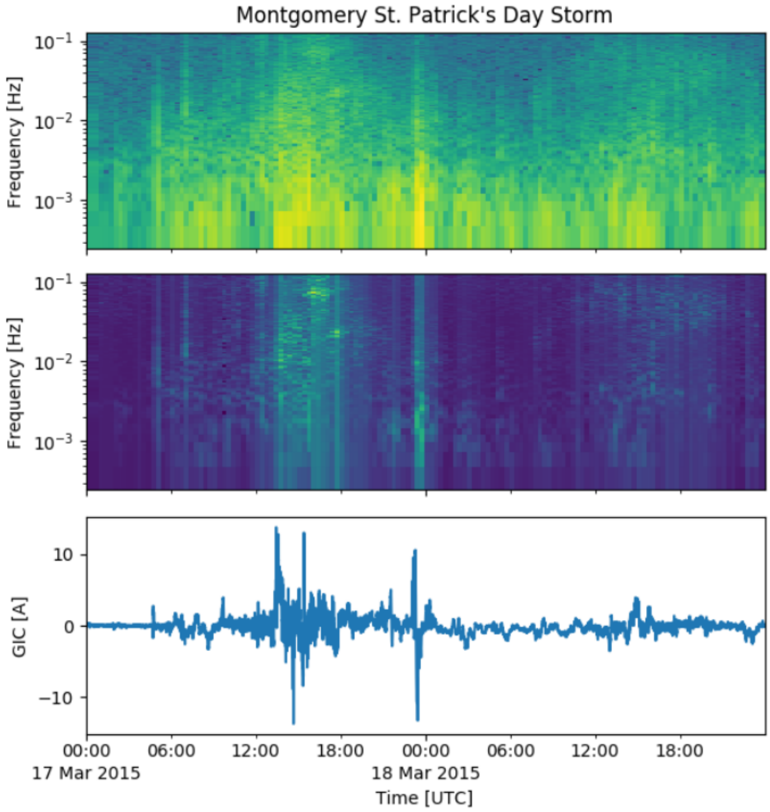

Figure 9: Although GICs are dominated by low frequencies, a spectrogram using the Montgomery (MONT) node in the TVA network (see Figure 24) identifies dynamic frequency contributions during a geomagnetic storm. The upper panel shows the raw GIC spectrogram. To emphasize the dynamic spectrum, the middle panel shows the GIC spectrogram normalised to the baseline low-frequency bias, as estimated during quiet geomagnetic conditions. The baseline is estimated by fitting a linear trend in log-space of the GIC power spectrum. Correcting for the low-pass response associated with GICs results in a clean response of the relative spectral content during a disturbance.

3.1 Induction Driving of GICs

Irrespective of driver, let us assume there is some geomagnetic disturbance that causes fluctuations in the B-field. Given a large grounded conductor at the surface, there is an inductive loop that produces an EMF and ultimately currents through Faraday's law of induction. In the absence of power networks or pipelines, induced currents still flow through the conductive Earth with the effect measurable at the surface as the E-field. Given the very low conductivity of air at roughly 10^{-14} S/m, there is no galvanic connection nor is there any significant attenuation between the Earth and the driving current systems[164], i.e. the currents in the Earth are purely from induction and the associated induction loops do not include the air. In the case of a grounded conductor, a favourable lower resistance path is often created and the E-field can be seen as driving induced currents into the network. An implication of the network providing a favourable path for GICs to flow is that increasing the grounding resistances to be greater than the effective crustal resistance of the Earth will limit currents entering the network. Having large grounding resistances come with their own complications with regards to power system operation and may not always be a valid mitigation strategy.

Before diving into the theoretical basis of electromagnetic induction in the Earth, it is useful to give a simplistic representation of the GIC induction loop and the factors involved. In Figure 10, we have a simple line current source that produces a vertically incident electromagnetic wave, with the B-field fluctuating into the page. Indicated is the penetration of the B-field and the flow of current in the induction loop, defined by a grounded line, perpendicular to the B-field and the rate of change of the B-field.

Starting from Faraday's law in its differential form,

$$\nabla \times \vec{E} = -\frac{\partial \vec{B}}{\partial t}, \tag{1}$$

we have the curl of the E-field related to the change of the B-field. Here there is often a misconception that the curl of $\vec{E}$ from Faraday's law implicitly means that the E-field is not conservative across a network. The issue here is a misinterpretation of the reference frame. Faraday's law in this simplistic case is applied to the vertical cross section of Earth and not the surface or a horizontal cross section. Due to the attenuation of the incident electromagnetic field, both magnetic and electric fields decrease in magnitude with depth and result in a non-zero curl. The implication is that even a spatially uniform B-field at the surface can drive GICs across a network.

More useful for getting a feel for GIC driving is the integral form of Faraday's law as it defines the EMF, i.e.

$$\oint \vec{E} \cdot \vec{dl} = -\frac{d\Phi_B}{dt} = EMF, \tag{2}$$

where Φ_B is the magnetic flux through the closed path as defined by the line integral of the induction loop. Here it must be emphasised that it is not the B-field itself which drives the GIC, but rather the B-field fluctuations. The 'constant' dipole field of the Earth acts as a baseline for the disturbance B-field from the driving current systems. Of course the main field of the Earth does change over time, but these changes are very slow in comparison with the fast geomagnetic disturbance related B-field changes. To a first approximation, the internal B-field changes produce no significant EMF. A magnetometer at the surface of the Earth also measures the B-field contribution from induced currents within Earth, which in effect scales the externally driven B-field[164]. In GIC modelling, we are not concerned about the source of these fields but rather the net fluctuations. Assuming there are such fluctuations, Lenz's law further states that the direction of this induced current would be such that the resulting B-field flux from the induced current opposes the initial B-field flux in the induction loop. In Figure 10, by Lenz's law the direction of the induced current in the ABCD induction loop would be anti-clockwise.

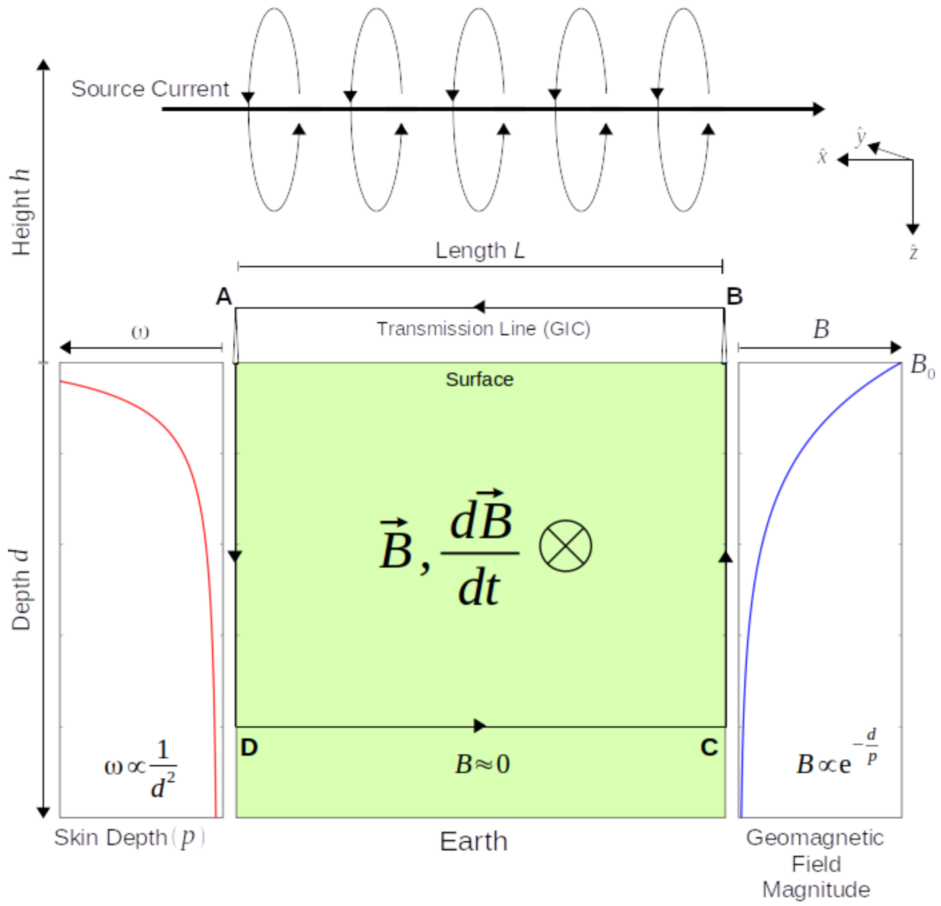

Figure 10: Simplistic representation of the induction loop that ultimately drives GICs. Here an source current at height h drives a changing magnetic field into the page. An EMF is created in the induction loop defined by ABCD. Due to the transmission line being grounded at A and B, a current (defined by the arrows in the induction loop) can enter the network and flow along the transmission line with length L. Indicated on the right is the dissipation of the B-field (and E-field) within Earth, related to the skin depth p, i.e. the depth d at which the magnitude of the surface B-field is decreased by a factor of e. The skin depth itself is frequency dependent as shown on the left, with lower frequencies ω penetrating deeper. All these concepts are explored further in the text.

Since the EMF ultimately drives the GICs, a large part of research is dedicated to estimating the E-field required to calculate the line integral. When defining the induction loop, a common mistake is the assumption that the driving induction loop is formed by the transmission line and its grounding points, with a return path along the surface of the Earth. The line integral of this induction loop is essentially zero and the slowly varying B-field requires a much larger loop to drive the GICs seen[58]. Considering the broader range of B-field variations relevant to GICs and attenuation of driving fields within the Earth, the induction loop becomes even more important. Making use of the entire conductive Earth beneath the transmission line as a possible induction loop is the correct approach and produces a larger EMF compared to to only considering the line and surface of the Earth. Including the entire conductive Earth beneath the transmission line also allows the return current to have negligible resistance as observed.

The induction concepts needed in GIC modelling have the distinct advantage of being part of the more developed field of magnetotelluric (MT) modelling. The MT method relates the B-field and induced E-field, with the view of defining the nature of the Earth's structure in the induction loop. Various sophisticated methods allow for accurate estimates of the conductive substructure, which is very useful for prospecting. For GIC modelling, this level of sophistication in terms of MT inversion is not required. All that is needed is an estimate of the surface E-field, usually defined by a derived or measured surface impedance and the B-field. In this step of E-field estimation, there are a number of assumptions inherent in MT studies and GIC modelling. The first of these assumptions is that the disturbance B-field originating from the near-Earth current systems is harmonic in time. Secondly, it is assumed that the disturbance B-field is a vertically incident plane-wave at Earth's surface. These general assumptions are usually valid locally but there are definite cases where they break down, such as when the lateral extension of the current source is not significantly larger than the penetration depth of the resulting disturbance wave[110,165–167]. To generate a plane-wave over the network, there would either need to be a very long line (or uniform sheet) current relative to the system or a very distant source. In the real-world, these cases are first-order approximations and cannot be used over an entire network. Of the regions mentioned, the mid-latitudes are the closest to the plane-wave approximation with main ring current driving being far enough away relative to power network scale lengths. In contrast, the auroral regions with the dominant auroral electrojet current system can diverge significantly from the plane-wave assumption. The nearer ionospheric electrojet current system is more variable and has finer spatial scales when compared to mid-latitude drivers, making the interactions more complicated[14,79,95,168,169]. Nevertheless, at a local level given dense magnetometer coverage or a dense network, splitting the calculations to smaller scale lengths between individual nodes, the plane-wave assumption can still be valid. A further complication is the variation of the geophysical conductivity of Earth that drives variations in the E-field often being at scale lengths similar to transmission line lengths, further diverging from traditional conservative E-field modelling for GICs.

While acknowledging that the deviations from plane-wave driving and often complicated geophysical structures significantly affect GIC modelling, it is illustrative to derive the general formalism of electromagnetic induction in the Earth using first-order approximations. Specifically, we will assume a vertically incident plane-wave disturbance and homogeneous ground conductivity structure. Modelling using these simplistic assumptions often performs adequately and in itself can be useful for utility decision-making. Besides operational considerations, the first approximation gives a very good idea of the drivers and spectral characteristics of GICs in general. Theoretically, the homogeneous Earth base case can be extended into the more physical and accurate layered-Earth conductivity approximation, where conductivity varies with depth. Globally, there is a tendency for conductivity to increase with depth[170]. There are of course cases where the layered approach itself is complicated such as in Memanbetsu, Japan, where a highly conductive layer sits atop a resistive layer and causes anomalous responses[171]. Further effects may arise separately from the inductive Earth response, such as charge accumulation at conductivity discontinuities. Lastly, for our purposes the Earth is assumed to be an ohmic conductor, with no internal current sources, i.e. electromagnetic waves can only be absorbed or dissipated.

Starting with the vertically incident disturbance electromagnetic plane-waves, we have the magnetic (B) field and electric (E) fields defined by,

$$E = E_0 e^{i\omega t - kz} \qquad \text{and} \qquad B = B_0 e^{i\omega t - kz}, \tag{3}$$

where z is downwards, ω is the angular frequency, k is the wave number ($k = 2\pi/\lambda$) and B_0 and E_0 are the wave amplitudes at their origin. The curvature of the Earth is generally not thought to have significant effects on induction for periods less than a day and hence Cartesian coordinates are used[65].

Let us now consider the differential form of Maxwell's equations and apply them to a vertically incident plane-wave with B-field in the y direction. Firstly, we have,

$$\nabla \times \vec{E} = -\frac{\partial \vec{B}}{\partial t}, \tag{4}$$

$$\nabla \times \vec{H} = \vec{j}_f + \frac{\partial \vec{D}}{\partial t}, \tag{5}$$

$$\nabla \cdot \vec{B} = 0, \tag{6}$$

$$\nabla \cdot \vec{D} = \eta_f, \tag{7}$$

where $\vec{D} = \epsilon\vec{E}$ and $\vec{H} = \mu\vec{B}$ for a linear isotropic medium. Making use of the further assumption that variation of permittivities and permeabilities are negligible when compared to variations of bulk rock conductivities, the free-space values of ϵ_0 and μ_0 are assumed. Since displacement currents are also assumed negligible in MT studies and that no current sources exist within Earth, (5) and (7) can both be simplified. Explicitly, we assume the system is quasi-static,

$$\frac{\partial \vec{D}}{\partial t} = 0, \tag{8}$$

and that there is no accumulation of electric charge, i.e. $\eta_f = 0$. No current sources implies that $\nabla \cdot \vec{j} = 0$. Through Ohm's law, $\vec{j} = \sigma\vec{E}$, we have,

$$\nabla \cdot \vec{j} = \nabla \cdot (\sigma\vec{E}) = 0. \tag{9}$$

Making use of the assumption of an homogeneous half-space, which can also be extended to a layered-Earth case, we have $\nabla\sigma = 0$ and hence,

$$\nabla \cdot (\sigma\vec{E}) = \sigma(\nabla \cdot \vec{E}) + \vec{E}\nabla\sigma = \sigma(\nabla \cdot \vec{E}) = 0, \tag{10}$$

or alternately,

$$\nabla \cdot \vec{E} = 0. \tag{11}$$

These assumptions result in a simplified version of Maxwell's equations that are now defined by,

$$\nabla \times \vec{E} = -\frac{\partial \vec{B}}{\partial t}, \tag{12}$$

$$\nabla \times \vec{B} = \mu_0(\sigma\vec{E}), \tag{13}$$

$$\nabla \cdot \vec{B} = 0, \tag{14}$$

$$\nabla \cdot \vec{E} = 0. \tag{15}$$

In the case of a layered-Earth that also varies laterally in a single direction, the continuity condition of vertical field components previously applied at vertical interfaces with boundary conditions at the surface and at depth, no longer apply. Charge accumulation at the lateral interface creates an additional E-field. As a result the divergence of the E-field parallel to the interface of conductivity variation remains zero but the divergence perpendicular is non-zero[65]. A very good example of this lateral variation or strike is at the coast. Here the lateral interface between land and ocean water, with their different conductivity profiles, creates a 'coast effect' where an enhanced E-field perpendicular to the coast is observed.

Moving on, at the heart of MT research is the concept that a time varying B-field induces an E-field, which in turn induces a secondary B-field. Relating these various fields can give us an idea of the Earth's conductivity structure. Let us take the curl of Faraday's law, which defines the initial induction,

$$\nabla \times \left(\nabla \times \vec{E}\right) = -\frac{\partial}{\partial t}\left(\nabla \times \vec{B}\right), \tag{16}$$

and then substitute Ampere's law, which defines the secondary induction,

$$\nabla \times \left(\nabla \times \vec{E}\right) = \nabla(\nabla \cdot \vec{E}) - \nabla^2 \vec{E} = -\mu_0 \sigma \frac{\partial \vec{E}}{\partial t}. \tag{17}$$

Recalling that $\nabla \cdot \vec{E} = 0$, we can simplify and rearrange to obtain a diffusion equation,

$$\nabla^2 \vec{E} = \mu_0 \sigma \frac{\partial \vec{E}}{\partial t}. \tag{18}$$

Similarly, it can be shown that the B-field $\vec{B}$ results in a diffusion equation. Taking the curl of Ampere's law and then Faraday's law into the result we get,

$$\nabla \times \left(\nabla \times \vec{B}\right) = \nabla\left(\nabla \cdot \vec{B}\right) - \nabla^2 \vec{B} = \mu_0 \sigma \left(\nabla \times \vec{E}\right) = -\mu_0 \sigma \frac{\partial \vec{B}}{\partial t}. \tag{19}$$

Recalling that $\nabla \cdot \vec{B} = 0$, we can simplify and rearrange to obtain a diffusion equation once again,

$$\nabla^2 \vec{B} = \mu_0 \sigma \frac{\partial \vec{B}}{\partial t}. \tag{20}$$

The implication of this is that simple induction in the Earth relies on an external source of energy that diffuses through the Earth and is exponentially dissipated with depth, with the typical measure of penetration being the skin depth. From the diffusion equations, we can derive the appropriate boundary conditions and apply the standard techniques of using an induction loop to calculate the EMF.

The first boundary condition to take into account is that the magnitude of the magnetic and induced electric fields must tend to 0 as z tends to ∞ (very deep and very far away from the line current source). Additionally, it is expected that there is no vertical component of the external B-field (as defined) and that the system is aligned in such a way that the B-field only has a y component in the coordinate system we have defined (which may be redefined arbitrarily). The induced E-field would always be perpendicular to this B-field (i.e. in the xz-plane as in Figure 10). At the surface, an additional boundary condition on the electric and magnetic field can be applied. Here, the B-field would have the defined magnitude B_0 in the y direction as defined by the system. The E-field on the other hand has to satisfy the divergence-free condition assuming no current sources within Earth. This implies that at the surface of Earth and throughout the induction loop, the vertical component of the induced E-field is assumed to be zero as well. Hence, although the induced E-field is in the xz-plane, only the horizontal component in the x direction is non-zero. In summary, the diffusive nature of the fields in the Earth leads to horizontal magnetic and electric fields. Considering Figure 10, the B-field has an initial magnitude B_0 in the y direction at the surface, and falls away to zero at a significant depth. The associated induced E-field has an initial magnitude of E_0 in the orthogonal x direction at the surface, and also falls away to zero at a significant depth.

The nature of diffusion can be more formally defined using the concept of a skin depth. Simply put, the skin depth can be defined as the depth at which the surface B-field is attenuated by a factor of $1/e$. Assuming the skin depth is defined by p, we would have the B-field in the Earth defined by $B = B_0 e^{-\frac{d}{p}}$. To derive this relation for the skin depth, let us assume the case of a homogeneous Earth conductivity. Taking the diffusion equation for the E-field and acknowledging that there are no energy sources within Earth and that the E-field would be dampened with depth, we can assume a solution of the form $E_0 e^{i\omega t - qz}$ and,

$$\nabla^2 E = \frac{\partial^2 E}{\partial z^2} = \left[q^2 E_0 e^{i\omega t - qz} = i\omega\mu_0\sigma E_0 e^{i\omega t - qz} \right] = \mu_0\sigma\frac{\partial \vec{E}}{\partial t}. \tag{21}$$

Equating the coefficients of the middle terms in square brackets, we have,

$$q^2 = i\omega\mu_0\sigma. \tag{22}$$

Commonly the skin depth p is defined as the real part of $1/q$, i.e. $p = \sqrt{2/\omega\mu_0\sigma}$. The skin depth is the penetration depth of the E-field, given a half space conductivity of σ and angular frequency of ω. For MT application, more useful is the complex frequency dependent Schmucker-Weidelt transfer function, defined by $1/q$. This transfer function allows the B-field and E-field to be related and in MT studies allows the conductivity to be estimated. Using the solutions obtained for the diffusion equations, we can substitute into Faraday's law once again, recalling that the fields only vary with depth,

$$\frac{\partial E_x}{\partial z} = \left[-qE_x = -i\omega B_y \right] = -\frac{\partial B_y}{\partial t}, \tag{23}$$

and

$$\frac{\partial E_y}{\partial z} = \left[qE_y = -i\omega B_x \right] = -\frac{\partial B_x}{\partial t}. \tag{24}$$

Equating the fields using the transfer function, we have,

$$\frac{1}{q} = \frac{E_x}{i\omega B_y} = -\frac{E_y}{i\omega B_x}, \tag{25}$$

which in turn relates to the more general surface impedance tensor (Z) relation often used in MT studies, i.e.

$$Z = \frac{i\omega}{q} = \frac{E_x}{B_y} = -\frac{E_y}{B_x}, \tag{26}$$

where Z for the homogeneous Earth case would be a single value of $Z = \sqrt{\frac{i\omega}{\mu_o\sigma}}$. The homogeneous case can easily be extended into a layered-Earth case, assuming the base relation applies within each half space. Ensuring that the field components are continuous at the interfaces allows a continuity relation to be derived known as Wait's recursion formula[65]. Starting at the deepest layer (infinite half space), defined in a similar way to the homogeneous Earth case, we iterate though successive layers. The resulting transfer function is also dependent on frequency and can be represented by an equivalent homogeneous Earth, as is done when computing the apparent resistivity. There are two main conventions for Z, with the ratio of E-field and B-field and units of (mV/km)/nT being favoured in this thesis. The other convention excludes μ_0, i.e. $Z' = \mu_0 Z$, and has resulting units of Ω. For either case, it should be noted that the transfer function between B and E-fields is dependent on frequency, with associated phase and magnitude arguments.

More explicitly for more complex geological cases, the general surface impedance tensor would be defined in components as,

$$\vec{E}_{x,y}(\omega) = Z(\omega)\vec{B}_{x,y}(\omega), \text{ with } Z(\omega) = \left[\begin{array}{cc} Z_{xx}(\omega) & Z_{xy}(\omega) \\ Z_{yx}(\omega) & Z_{yy}(\omega) \end{array} \right]. \tag{27}$$

As already indicated, for the homogeneous Earth case the impedance tensor components would be $Z_{xx} = Z_{yy} = 0$ and $Z_{xy} = -Z_{yx} = Z$[64]. For a 2D Earth model, where there is lateral variation, $Z_{xx} = -Z_{yy}$ and $Z_{xy} \neq -Z_{yx}$. The surface impedance tensor can be rotated such that the diagonal is zero and $Z_{xy} = Z_{\parallel}$ (induction parallel to the geophysical strike) and $Z_{yx} = Z_{\perp}$ (induction perpendicular to the geophysical strike). Such a scenario is typical in coastal regions where there is a definite lateral discontinuity formed by the sea-land interface[58,124]. In 2D cases, the empirical network parameters can encode the rotation and scaling of simple geophysical strikes. Given measured surface impedance, which is the most realistic and fully 3D, each component of the impedance tensor is unique[110]. The current state of the art for such 3D measured surface impedances are large scale MT surveys that use remote referencing for noise reduction and stability of estimation.

With the nature of the fields in the Earth defined, we can apply Faraday's law of induction to the system. Using Figure 10, we can define the EMF,

$$\begin{aligned} EMF &= -\oint \vec{E} \cdot dl \\ &= -\big(E_x(z=0) \cdot dl_{AB} + E_z \cdot dl_{BC} + E_x(z \rightarrow \infty) \cdot dl_{CD} + E_z \cdot dl_{DA}\big) \\ &= -E_x(z=0) \cdot dl_{AB} \\ &= -E_0 L, \end{aligned} \tag{28}$$

where L is the length of the transmission line. This result is due to the conditions derived earlier, i.e. the induced E-field is always horizontal ($E_z = 0$) and at a significant depth the fields are approximately zero (field magnitude decreases exponentially with depth). The resulting relation in this case means the EMF produced by the induction loop ABCD (which is the same as the CD-surface loop) effectively comes from the induced E-field at the surface. After taking into account the circuit resistances, the current produced can be linearly related to the induced E-field at the surface through the EMF (which in effect is the often used governing equation for GICs). This means that if you know the induced E-field at the surface, you can calculate the associated EMF and scale appropriately to get the induced current.

In the case of a realistic non-uniform B-field or heterogeneous conductivity structure, then the system is not quite as representative. A typical example is when the rate of change of the B-field is not in the xy-plane (perhaps as a result of an incidence angle not equal to 90°). In this case the curl of the induced E-field as we have defined it would no longer just be in the xz-plane and the field at the surface no longer conservative. Taking real-world heterogeneous conductivity into account only compounds deviations away from a conservative field. In these cases, any line integral is path dependent. It is not possible to take into account all these different variables analytically. The best we can do is to define the system in such a way as that locally it represents the typical plane-wave defined system we have used up to now. One way to do this is to choose an appropriate induction loop where the B-field is roughly uniform along the length. This length would typically be a lot shorter than the system length. Using such a loop, we would need to derive the induced surface E-field valid for that length of transmission line. To model the GIC in this case, the dot product of the local E-field and transmission line segment needs to be integrated along the transmission line. This in effect can be thought of as modelling discrete voltage sources in the transmission lines.

3.2 Spectral Characteristics

To expand on the implications of frequency domain calculation it is useful to define the spectral characteristics of induction within the Earth and GICs. Let us assume the special case of a homogeneous

Earth, where the induced E-field (a proxy to GIC) can be explicitly related to the B-field,

$$E(\omega) = \sqrt{\frac{i\omega}{\mu_0\sigma}}B(\omega). \tag{29}$$

Here σ is the conductivity in S/m and μ_0 is the permeability of free space i.e. $4\pi \times 10^{-7}$ H/m. The conductivity of the Earth lies in the 1-100 mS/m range. In the frequency domain, the time derivative of a function is analytically defined as $FFT\{X(t)\} = X(\omega)$, then $FFT\{dX(t)/dt\} = i\omega X(\omega)$, and as such we alternatively have,

$$E(\omega) = \frac{1}{\sqrt{\mu_0\sigma i\omega}}Bdot(\omega), \tag{30}$$

where $Bdot(\omega)$ is dB/dt in the frequency domain.

From (29), we see that there is a high-pass filtering effect from the Earth on the B-field when deriving the E-field from the B-field, i.e.

$$E(\omega) \propto \sqrt{\omega}B(\omega). \tag{31}$$

Given $Bdot$ in (30), the same Earth conductivity has a low-pass filtering effect, i.e.

$$E(\omega) \propto \frac{1}{\sqrt{\omega}}Bdot(\omega). \tag{32}$$

The underlying disturbance B-field has been shown to have roughly '$1/f$' (where $\omega = 2\pi f$) characteristics in its power spectrum. Using a power spectrum parametrisation of f^{-m} (where f is frequency), m is often between 1 and 2[172], but can be higher[65]. The dominant periods in the B and E fields range from a couple of hours to tens of seconds, with a so called 'dead-band' between 0.5 and 5 Hz providing little to no driving in comparison[65,173]. Since the power spectrum is defined as the magnitude of frequency components squared, a general relationship proportional to f^x would result in a power spectrum parametrisation related to f^{2x}, i.e. the slope of the power spectrum would be $m = 2x$.

If we assume that the B-field has a power spectrum with slope m, then the corresponding E-field power spectrum slope would be less steep, i.e. less than m. $Bdot$ or dB/dt, proportional to $fB(f)$ in the frequency domain, would have a flatter response still. Explicitly for a homogeneous Earth, if we assume $m_B \approx 2$ for the B-field power spectrum, then $m_E \approx 1$ for the E-field and $m_{Bdot} \approx 0$ for $Bdot$. More generally, the filter characteristics of the Earth define spectral slope responses that follow $m_B > m_E > m_{Bdot} = m_B - 2$, and apply even in particularly conductive or resistive settings[150]. Expanding on the basis of the E-field frequency response, it is assumed that the GIC would share roughly the same spectral characteristics given a resistive network (i.e. assuming no network related frequency response). The measured GIC includes the effect of the network itself, which may introduce relative alignment weighting (or directionality) between components and possible filtering effects. The overall relative characteristics of the filters should however not change.

To illustrate the spectral characteristics described, spectra of all the different components were computed for Memanbetsu (MMB) node in Hokkaido, Japan. Here the Kakioka Magnetic Observatory of the Japan Meteorological Agency has 1 second cadence B-field and E-field measurements. Hokkaido Electric Power has measured GIC at a similar cadence[83]. In Figure 11, the spectral responses for a geomagnetic storm were found to be consistent with the theoretical expectations, i.e. across almost all frequencies the GIC is a low-pass filter for $Bdot$, a high-pass filter for the B-field and its frequency components are similar to the E-field.

A similar result can be seen in Figure 12 where there are measured surface impedances and hence accurate E-field estimates for the Paradise (PAR) node in the North American TVA network. In this case the effective directionality is north-south for the PAR node and a single component of the

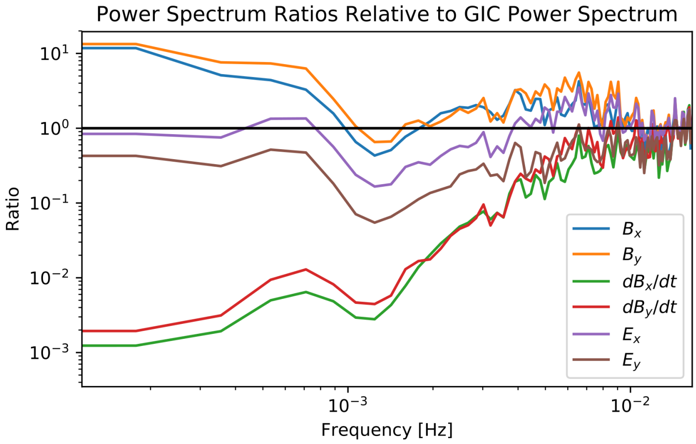

Figure 11: The theoretical relations between the different frequency responses can be seen clearly in data[174]. Here we have the geologically complex MMB region (see Table 1) with high cadence data in all the different datasets. Taking the ratio of each parameter's power spectrum with the GIC power spectrum, we see that over the most frequencies the E-field (purple and brown) are largely linear (flat) with the GIC. The B-field (blue and orange) on the other hand exhibits a low-pass response relative to GIC and dB/dt (red and green) exhibits a high-pass response relative to GIC.

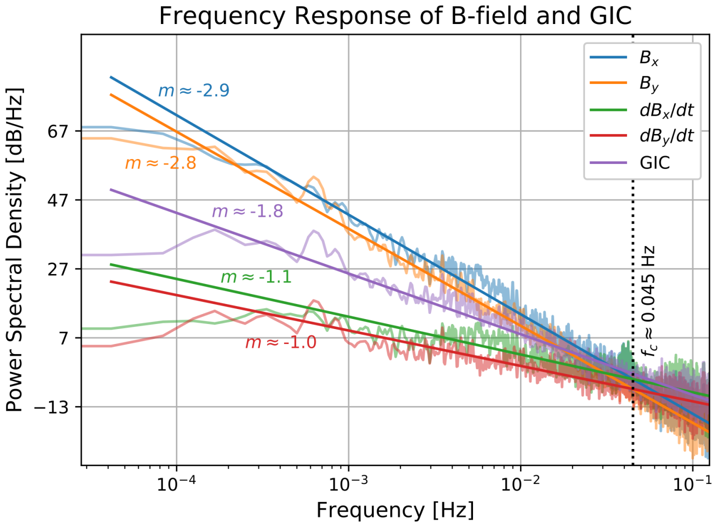

Figure 12: The frequency responses for the PAR node in the TVA network is shown along with the frequency response of accurate B-field measurements. The various measurements are denoted by different colours, with the power spectrum slopes superimposed on the partially transparent power spectrums. Consistent with Figure 11, the responses match the expectation of the power spectrum slopes (quantitatively indicated by m) with the GIC (purple) sitting between the high-pass dB/dt (red and green) and low-pass B-field (blue and orange). Of interest here for frequency domain calculations is the crossover between B-field and dB/dt responses at higher frequencies.

various fields can be used. In the simpler geological context, the responses are much cleaner and better defined. The complex geology at MMB has been the subject of various studies around the validity of dB/dt as a proxy to GIC activity, with the B-field profile showing better agreement[83]. A possible explanation lies in the conductivity, where a poorly-conducting bottom layer that underlies a thin good conductor would reproduce the observed characteristics[85]. Even in such cases, lower frequencies dominate the GIC spectral response.

Of interest in Figure 12 is the trade off between B-field and dB/dt slopes at higher frequencies. In this case the PAR node is rather susceptible with larger GICs than at MMB. In the frequency response, we see that above f_c, the dB/dt frequency response has a larger weighting than the B-field response. Considering that at high frequencies the signal-to-noise ratio (SNR) is usually poor, making use of dB/dt in frequency domain calculations may be beneficial. Taking Figure 13 into account, we see that the coherence between B-field and dB/dt is virtually exact and no information is lost by using dB/dt instead of the B-field.

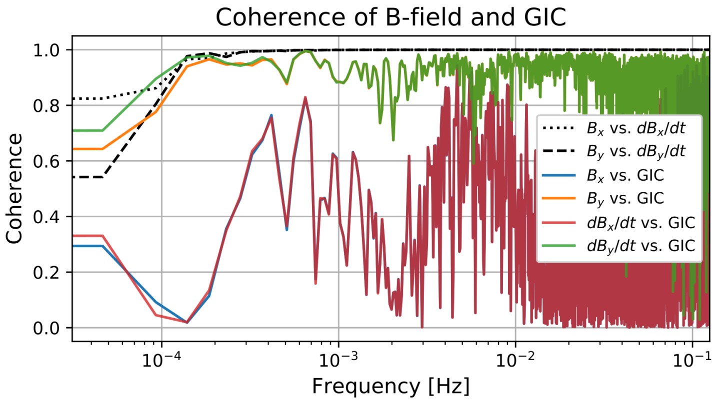

Figure 13: In terms of the coherence between GIC and the B-field, we have higher coherence with the y component at PAR, which is expected due to the north-south network orientation. Between the B-field and dB/dt, coherence is practically perfect, except at low frequencies where the baseline removal of the B-field would introduce some deviations. The coherence between the B-field and GIC or dB/dt and GIC are identical. Using either B-field or dB/dt would be feasible for frequency domain estimation with no information lost, the only difference is the different signal-to-noise ratios at different frequencies, particularly above f_c where dB/dt dominates.

3.3 Linking Spectral Characteristics with EMF Driving

To see the link between B-field, induced E-field and driving EMF in practice, we can make use of a synthetic example, similar to work done by Boteler et al.[175]. Let us assume a number of frequency components made up only of sinusoidal components, with a random phase angle for each between 0 and 45 degrees. The frequency components f will be defined for the B-field as 10 log-spaced frequencies with periods between 3 hours and 1 second, with an amplitude of 100 nT for the lowest frequency. The B-field has a physical spectral response of $1/f$, with the lowest frequency having the highest weighting. In general, the synthetic B-field defined may be more extreme than typical but it will suffice for illustrative purposes. From the B-field, the induced E-field is approximated using an assumed homogeneous Earth with conductivity of 0.01 S/m, with both fields being seen in Figure 14.

Assuming a B-field with an intrinsic spectral response of $1/f$, the corresponding E-field is a high-pass filter of the B-field and would have a spectral response of $1/\sqrt{f}$. dB/dt is a further high-pass filter of the E-field and has a flat spectral response, i.e. equal weighting for all frequencies. Regardless of the initial field used, all electromagnetic fields are diffusive in the Earth, with higher frequencies

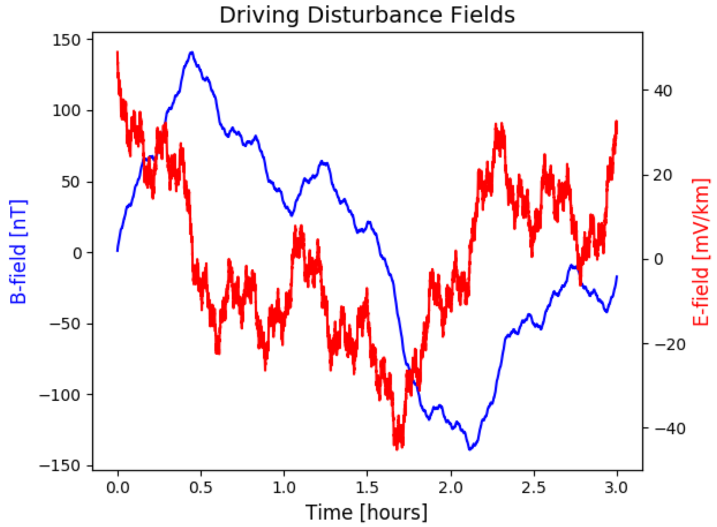

Figure 14: Making use of the typical frequency response of the B- and E-field, a synthetic field can be estimated assuming uniform conductivity of the Earth at 0.01 S/m. The high-pass filter effect of the E-field given B-field is evident, especially in the lowest frequency variations where the E-field clearly leads the B-field by $\pi/4$ in this simple test case.

being attenuated more quickly than lower frequencies which penetrate more deeply, as seen in left of Figure 15. Using the E-field estimates, we can also compute the relative increase in EMF with depth in the right of Figure 15. At a given depth, the EMF is simply the difference between surface E-field and the E-field at that depth, since no vertical E-fields contribute to the line integral.

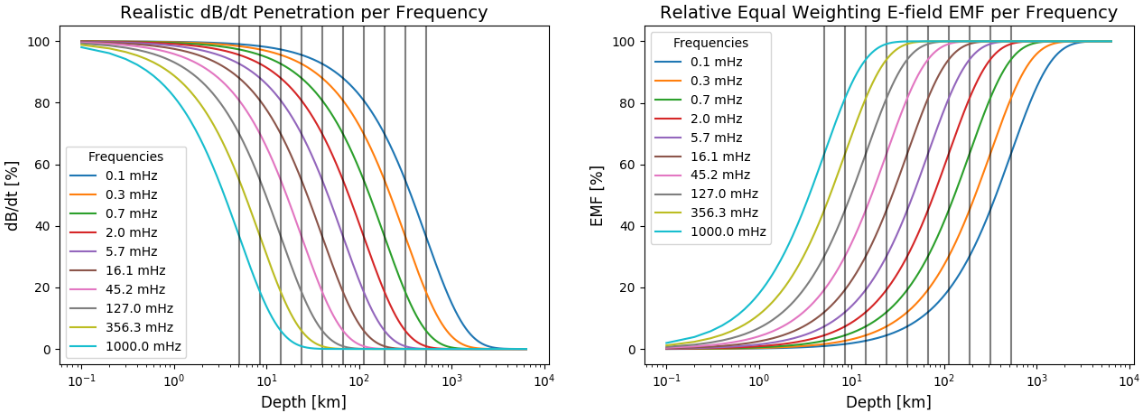

Figure 15: Taking the flat frequency response of dB/dt, we see that the higher frequencies are attenuated more quickly and lower frequencies penetrate more deeply. Assuming equal weighting of the E-field and calculating the proportion of the total possible EMF from the particular frequency, we see that the higher frequencies reach their full EMF at shallower depths.

There are a number of interesting factors that arise from the observation of the fields and EMF driving at different depths. Firstly, we have that the effective induction loop of lower frequencies is much larger and it would be assumed that the larger area should contribute to a larger driving EMF. Without taking into account the nature of the initial B-field, this view is wrong as the variation associated with the rate of change of the B-field also needs to be taken into account. Given lower frequencies, the fact that the rate of change is also lower outweighs the larger induction loop. Formally, let us assume a homogeneous Earth and unit transmission line length. In this case the area of the induction loop is proportional to $1/\sqrt{f} = \sqrt{T}$ as defined by the skin depth and where f is frequency and T is the corresponding period. Assuming equal unit frequency weighting between B-field flux frequency components and taking their contributions per frequency, the EMF in turn would be related to,

$$EMF \propto -\frac{\sqrt{T}}{T} = \frac{1}{\sqrt{T}} = \sqrt{f}. \tag{33}$$

Assuming frequency components in this idealised case can be taken separately, the EMF per frequency is related to $\sqrt{f}$. This would mean that the EMF has an overall high frequency bias, which is not observed in practice.

Of course the B-field does not have a flat power spectrum, but rather follows a $1/f$ type spectral response, where lower frequency variations tend to be larger in magnitude than higher frequencies. So in reality we have to update the relative flux contributions per frequency by $1/f = T$, i.e.

$$EMF \propto -\frac{T\sqrt{T}}{T} = \sqrt{T} = \frac{1}{\sqrt{f}}. \tag{34}$$

Including that lower B-field frequencies have larger contributions, the resulting EMF is related to $1/\sqrt{f}$ (visualised in Figure 16), which is very similar to the skin depth and the E-field relations derived previously. In this case, the often used explanation that lower frequencies penetrate deeper and have larger weighting as a result is wrong. Lower frequencies have larger weighting because the driving B-field has a low-pass characteristic, likely due to external solar wind and/or magnetosphere coupling – not due to the geophysical environment.

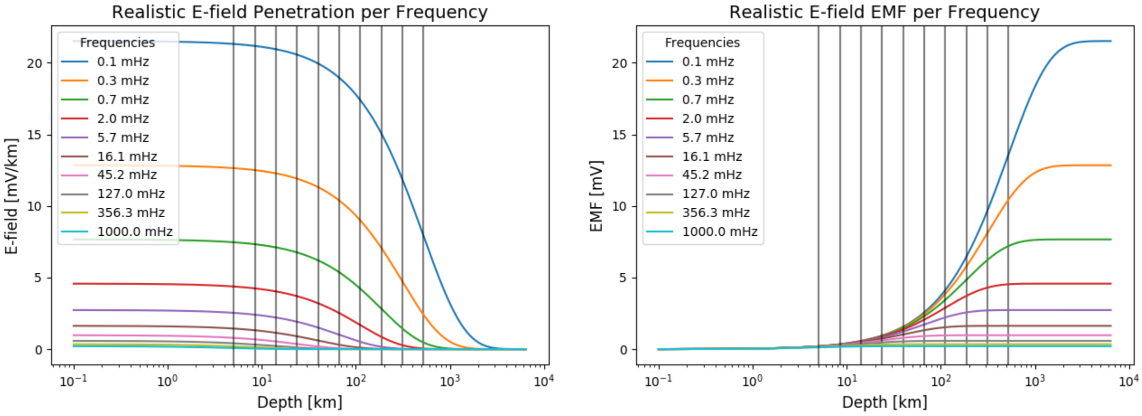

Figure 16: Taking into account the realistic weighting of the different E-field components (i.e. lower frequencies have larger weighting), we see the effects of the E-field penetration is more apparent than for a flat response in Figure 15. Instead of looking at the proportion of possible EMF for frequency at a given depth, we see that the lower frequencies contribute not only most of the total EMF but also at deeper depths.

The visualisation of EMF driving with depth and frequency as is done in Figure 17 is useful, but limited. In the real-world there are many other geophysical considerations to take into account. The conductivity structure is seldom simple, with strikes and anisotropies common. Even in the simplest of cases, the Earth conductivity is not uniform and changes with depth. With the multitude of conditions available, there is the general rule of thumb that particularly resistive regions would produce the largest GICs. This is due to a number of factors. Firstly, more resistive regions allow for deeper penetration for all frequencies, increasing the inductive loop, induced E-field and driving EMF. At the same time, a more resistive ground is likely to provide a more favourable path for GICs to flow through the network. Networks generally tend to have small grounding resistances for control purposes which would not mitigate the entry of GICs in these cases.

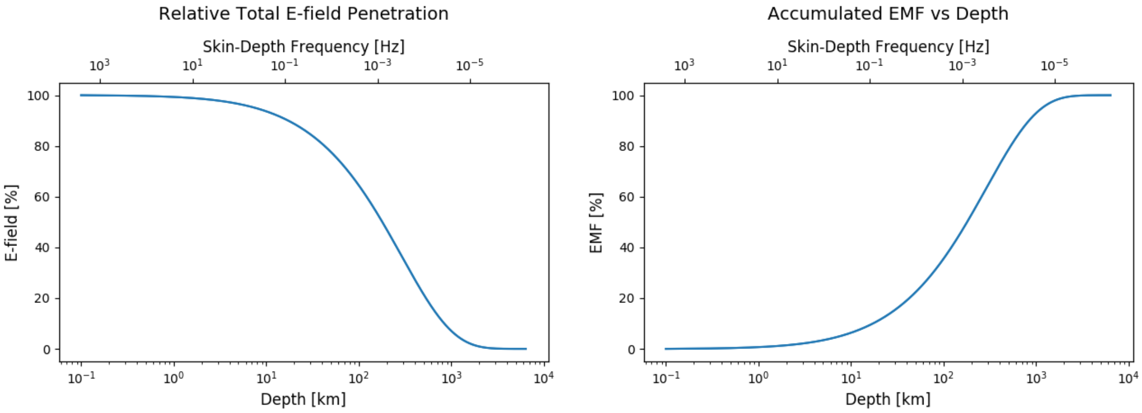

Figure 17: Taking all frequency components, we see that with the attenuation of the E-field with depth, the EMF increases as expected. For this synthetic case, most of the EMF contribution comes at depths over 100 km. Real-world cases with more complex shallow structures may differ, but as we go deeper the Earth is more homogeneous to a first approximation and results are more generalisable.

3.4 Modelling Nodal GICs

Spectral characteristics and induction driving aside, most traditional GIC modelling relies on calculation of the engineering step in the time domain. As an initial step, the E-field can be related to the effective driving EMF by integrating the field along the transmission line footprints. In the specific case of a node, the GIC in the transformer neutral can be estimated by modelling the resulting effective EMF as a voltage source in the line and taking into account all appropriate resistances. Nodal analysis does this for a single node, but an entire network can be modelled in such a way using the Lehtinen-Pirjola or Nodal Admittance Matrix methods. Assuming a uniform E-field or an empirically defined effective E-field, the GIC at a node in the network can be modelled by the nodal GIC equation[94],

$$GIC(t) = aE_x(t) + bE_y(t). \tag{35}$$

The pair of constants, a and b, known as the network parameters, relate the magnitude of the GIC to the northward (E_x) and eastward (E_y) components of the induced E-field[94]. The network parameters take into account the topology and assume a resistive network[93,111]. These network parameters have the units of A/(V/km) and are unique to each node of the power system[94], representing the net effective contributions from the network. Typical resistances considered would include the transformer resistances, line resistances (dependent on line length), grounding resistances and network control resistors. In general modelling, the network characteristics can have a large impact and are not always well modelled or measured with the characteristics themselves also being dynamic. Corrosion of grounding plates or rain soaked soil changes the grounding resistances of a node and are good examples of such complications.

An alternate representation of the network parameters is in cylindrical coordinates where the total aligned network scaling is represented by $\sqrt{a^2 + b^2}$. To take into account the network topology and non-alignment the preferred direction of the E-field to produce large GICs is given by the network defined directionality,

$$\theta = \arctan\left(\frac{a}{b}\right). \tag{36}$$

Any deviation of the E-field away from the preferred angle θ would result in a fraction of the total E-field magnitude contributing to the measured GIC. The ratio of network parameters b/a used in previous work[104] is in effect representative of the same concept but related to an angle from north, whereas a/b as used above is the angle from east. Since the nodal GICs can only flow from the transmission lines, we have a constraint on the direction of E-field coupling to the GIC.

Whatever the convention, the network parameters have to take into account the entire network, which can become complicated. Nevertheless, there are the analytical methods already mentioned for estimating the network parameters[38,94]. In the real-world, the relationship between the E-field and the measured GIC is not one-to-one and the conductivity and other factors are absorbed into the empirically estimated network parameters. Another consideration is the fact that in a real-world system there are often a number of transmission lines connected to a node. In this case, the measured GIC at the node would be a combination of the different line GICs. To get the directionality dependence in such a case, each specific line needs to be taken into account and the result weighted according to line length, conductivity, predominant near-Earth current system driving and other factors influencing the resulting GIC magnitude. It could often be the case that multiple directions are relevant, with a network parameter defined directionality distribution being the net result.

The basis of the resistive approximation as applied in the Lehtinen-Pirjola method is widely used, but there are obvious questions as to the real-world applicability of the approximation. Besides there being inductive components of in the network, the transformer response is non-linear, with a further non-linear hysteresis curve. Coupled to this is a non-sinusoid base waveform with distortion and low-frequency driving instead of purely dc as usually assumed under GIC driving. All these unmodelled factors introduce significant uncertainty in the engineering step of modelling, adding to the uncertainty introduced by error in the geophysical step and B-field estimation. Empirical methods that link GIC measurements to B-field or E-field measurements take this into account as they measure both the theoretical induced current that enters from the Earth and the higher-order effects of the network itself. Other factors that can be modelled using the traditional modelling assumptions, but often are not, are lower voltage networks, line shapes and variable grounding resistances. Empirical models similarly can absorb the effects of these unmodelled factors, creating an effective response per node.

An alternative to the network parameter approach in the time domain is to map the B-field to GICs in the frequency domain, bypassing the estimation of the E-field and network responses. Similar to the surface impedance tensor relating E- and B-fields, the transfer function (TF) approach relates the measured GIC to B_x and B_y components in the frequency domain[98,122,143]. No assumptions of a resistive network or general geophysics are made and the result is a true mapping. In the mapping, although not constrained by assumptions of conductivity or network characteristics, it is expected that general characteristics assumed in traditional GIC will be able to be seen and can be used for interpretation. As alluded to in the previous section regarding spectral characteristics, either the B-field or its time derivative can be used for such frequency domain calculation.

3.5 Modelling the Geomagnetic Field

For most utilities, B-field data comes from a sparse grid of remote magnetometers. At mid-latitudes, the typical separation between magnetometer and network that allows for feasible GIC modelling is around 300 km in the north-south direction, and 600 km in the east-wast direction[152]. In cases where more B-field accuracy is needed or the separation is too great, interpolation is used. The most popular of the various interpolation techniques used is the spherical elementary current systems (SECS) interpolation technique[158,159].

SECS uses the basis of a driving equivalent current system to create a physically inspired interpolation scheme based on Maxwell's equations. Including this prior adds significant robustness when compared to other purely mathematical interpolation schemes (examples include Fourier, spherical cap or spherical harmonic interpolation schemes) that do not consider the the physical context[159]. From Helmholtz's theorem, any current flowing on a surface can be broken into a curl-free part (allowing current flow into and out of the surface) and a divergence-free part (allowing current flow on the surface). In terms of the real-world current systems at play, overhead Hall currents associated with the auroral electrojet system would be linked to the divergence-free part. The curl-free part is more often associated with field-aligned currents and Pedersen currents that connect the region 1

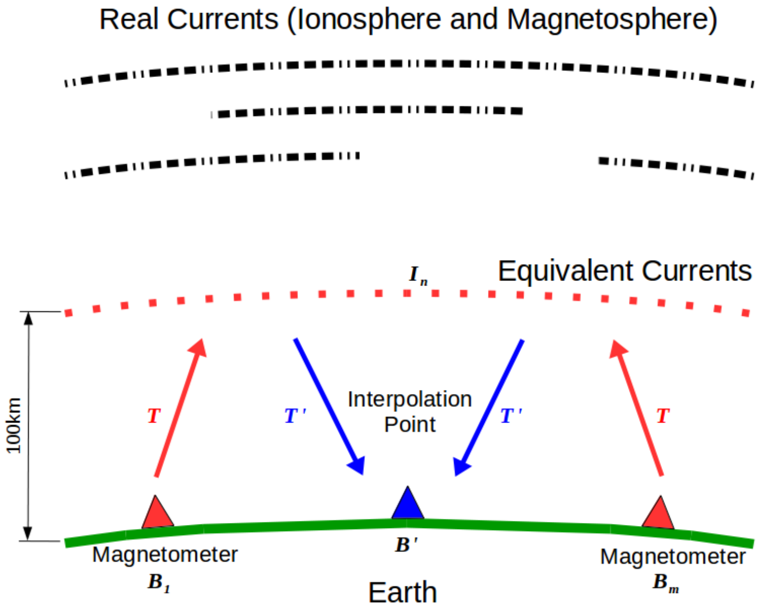

Figure 18: The theory underpinning SECS interpolation is as simple as it is satisfying[176]. An equivalent current system (I_n) is defined in terms of nodes at a defined height and taking into account all the various current system contributions. Measured magnetometers (B_1 and B_m) are used to calibrate this grid through an inversion problem (T). Once the equivalent current system is defined, the B-field at any point on the ground (B') can be calculated through Biot-Savart (T').

and region 2 current systems. Assuming a uniform conductivity of the ionosphere and field-aligned currents that are perpendicular to the ground, ground-based measurements would predominantly measure the overhead divergence-free currents at high-latitudes[177]. SECS aims to approximate a similar real-world current system with an equivalent current system at an arbitrary height, as shown in Figure 18. More than one equivalent current system can be defined, and at more than one height. Some studies have used this approach to attempt the separation of internal and external contributions to the B-field. To do this, the vertical component of the B-field needs to be included in the SECS interpolation scheme[160,161,178]. When considering only the horizontal B-field components, it has been shown that a single external equivalent current system suffices[163]. In the same study, it was shown that SECS interpolation with a single equivalent current system is accurate during geomagnetic storm conditions when a sparse magnetometer grid is used[163].

Of the different implementations, we assume cylindrical coordinates ($r = \sqrt{x^2 + y^2}, \phi, z$)[162], with a current element of amplitude of I at height h as shown in Figure 19. For equivalent current studies at high-latitudes, where Hall currents dominate, h is around 100 km. Implementation of SECS at mid-latitudes assumes that current system representation using only divergence-free current nodes still holds, although the main driving current system is now the magnetospheric ring current. As such, a similar equivalent current height has been used in implementations in southern Africa[152,157], but no physical current system is assumed at this height. Assuming representation through divergence-free current nodes, the equivalent surface current density would be,

$$\vec{J_{df}}(\rho) = \frac{I}{2\pi\rho}\vec{e_\phi}, \tag{37}$$

where ρ is the radial distance from current node.

Assuming a coordinate system where z is downwards and that the distubance B-field shows harmonic time dependence (i.e. $e^{i\omega t}$)[160], a current node would then be related to a measured B-field

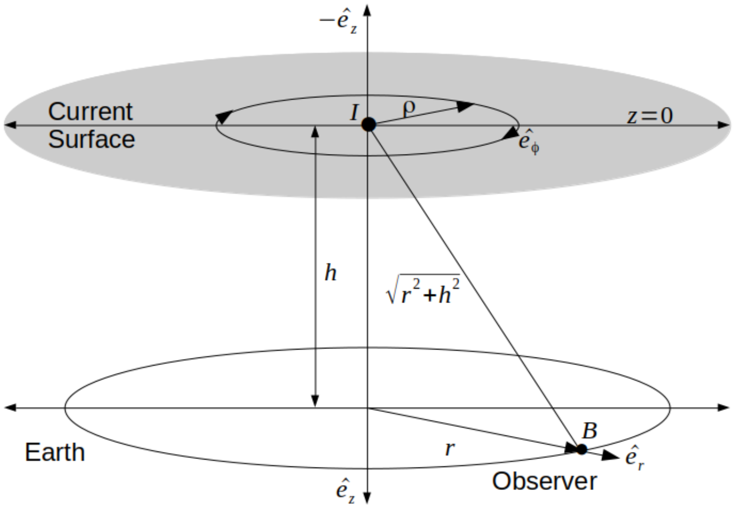

Figure 19: The divergence-free SECS set-up in cylindrical coordinates is shown in more detail. A divergence-free equivalent current node with amplitude I and surface current density defined by $\vec{J}_{df}$ on the current surface at height h will produce a radial horizontal B-field at the observer on the ground. Note that the current system is defined at $z = 0$ and that the positive z-axis points downwards, allowing positive I to relate to a downward field-aligned current that produces a clockwise Hall current in the positive azimuthal direction and a horizontal B-field in the positive radial direction.

on the ground through,

$$\vec{B} = \frac{\mu_0 I}{4\pi r}\left(\left(1 - \frac{h}{\sqrt{r^2+h^2}}\right)\vec{e_r} + \left(\frac{r}{\sqrt{r^2+h^2}}\right)\vec{e_z}\right). \tag{38}$$

For some defined spatial extent, we can the extend this Biot-Savart relation for a single current element, at a single time instance point in time, to a grid of elementary current elements. Taking the grid (say n elements), we group all current elements into a vector I. To constrain the elementary currents, we require B-field measurements. Assuming there are multiple magnetometers (say m stations), we can similarly group the B-field measurements into a vector B. Since interpolation is usually needed for sparse magnetometer grids, $m < n$ and the problem is underdetermined. As the method aims to interpolate the disturbance B-field, which is small in comparison to the main field and otherwise linked to near-Earth current systems, the baseline of Earth's B-field must be subtracted from the measured B-field. Finally, to solve for I, a matrix equation is set up, i.e. $B = T \cdot I$, where T is a transfer function matrix that relates the elementary currents and the measured B-field, encoding the geometry of the problem. Since we are only interested in the horizontal field, only the $\vec{e_r}$ component of the B-field is defined in T. An important property of the transfer function is that it is purely a spatial relationship between the elementary current and the magnetometer station. Following previous implementations in southern Africa, the matrix equation calculation is performed separately for the x (north-south) and y (east-west) components of I and B respectively[157]. More explicitly,

$$\begin{bmatrix} B_{x,y:1} \\ \vdots \\ B_{x,y:m} \end{bmatrix} = \begin{bmatrix} T_{x,y:11} & \cdots & T_{x,y:1n} \\ \vdots & \ddots & \vdots \\ T_{x,y:m1} & \cdots & T_{x,y:mn} \end{bmatrix} \begin{bmatrix} I_1 \\ \vdots \\ I_n \end{bmatrix} \tag{39}$$

where,

$$T_{x,y:ij} = \frac{\mu_0}{4\pi r}\left(1 - \frac{h}{\sqrt{r_{ij}^2 + h^2}}\right). \tag{40}$$

Since T is non-square ($m \neq n$), I is calculated using a quasi-inverse T^{-1}, i.e. $I = T^{-1} \cdot B$. Commonly, this quasi-inverse T^{-1} is obtained through singular value decomposition (SVD). After successfully solving the inversion problem and the vector I is estimated by the measured B-field, I can be used to interpolate the B-field to any other point of of interest, i.e. $B' = T' \cdot I$. This procedure is then repeated for all required time instances.

Some implementations of the method include the standard deviation of error in B-field measurement, but propagate these to the transfer matrix without any further impact on uncertainty estimates besides the estimation of a unit covariance matrix. The SVD inversion in turn can also be tweaked to define at what threshold singular values are excluded in the inversion[160,164]. A larger threshold means more singular values are excluded and that a smoother basis function is defined. Similar to the concept of a subsurface further constraining the inversion, other conditions such as flatness and smoothness can be taken into account. This makes use of the minimisation property of the inversion method and is applied as further rows in both the transfer matrix, B-field vector and current vector. Ultimately the flatness or smoothness condition encodes the idea that neighbouring points should ideally have a minimum first derivative and minimum second derivative according to some weighting. Although no obvious benefit is seen in implementing this for the underdetermined problem in initial testing, the concept of including spatial information in the inversion problem is revisited later in improvements of the B-field interpolation.

4 Framework for Operational Model Development

In this chapter we describe where the proposed data-driven modelling sits within an operational framework and define the procedure for analysis and data sourcing. An overview is first presented in Section 4.1, with uncertainties in conventional modelling identified. Data-driven adaptations of conventional modelling approaches will aim to quantify and/or reduce these uncertainties.

4.1 Framework Overview

From an operational perspective, there are different levels of operational GIC modelling that a utility may be interested in. On one end of the spectrum is coarse modelling of occurrence and probability of GIC damage to the network in the long-term, most commonly estimated through extreme value analysis. This type of operational modelling couples to the cost associated with GIC damage in a risk matrix that then informs high-level decision-making[179,180]. On the other end of the spectrum is real-time modelling of the actual GIC currents in the network where the aim is in informing real-time operations. There are other outputs between the extremes such as transmission line planning, stress testing or sensitivity analysis and asset management with a utility. For many operational applications, proxies are used instead of full modelling of the induced currents. The coarse proxies in general give a very good idea of elevated activity and can flag risk[87,88]. Due to typically good quality and long-term data sets managed by geomagnetic observatories (e.g. INTERMAGNET network; `www.intermagnet.org`), correctly defined geomagnetic proxies can be useful for susceptibility and extreme value analysis. Given the large cost associated with mitigation, proxies are however not a solution for real-time operations. For this, accurate estimates of currents in the network are needed.

Loosely, the GIC modelling chain can be split into three main parts, namely space physics, the geophysical step and the engineering step[94]. In the space physics step of modelling, all the upstream dynamics of the GIC problem are grouped into drivers of perturbations of the ground B-field. For the purposes of this work, emphasis is on modelling from the B-field onwards to the observed nodal GICs. Associated modelling approaches are summarised in Figure 20.

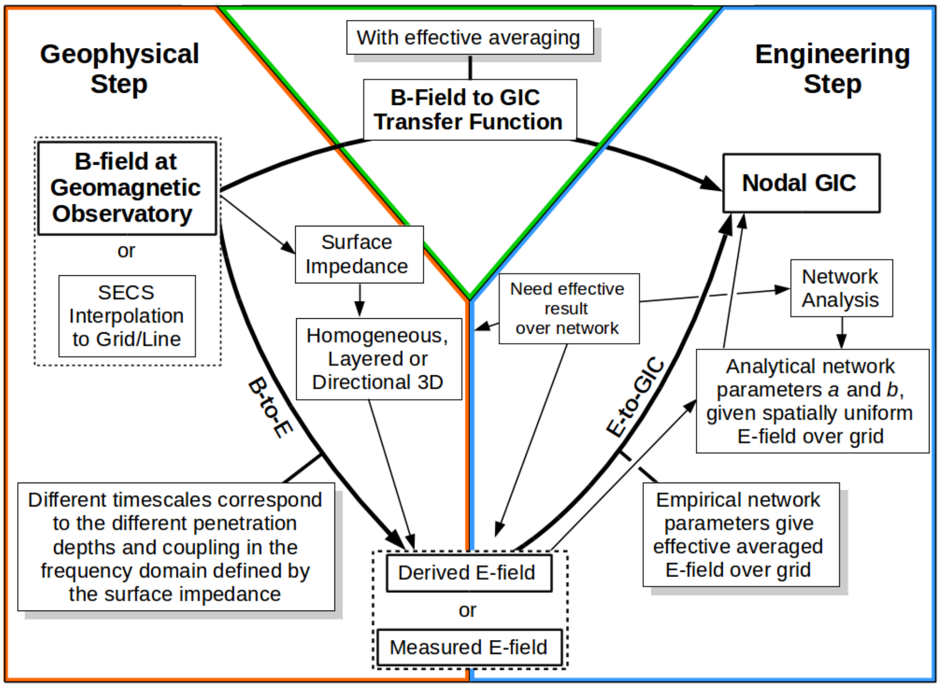

Figure 20: The modelling chain associated with GIC modelling can be broken into different steps, each with an associated uncertainty. The flow chart summaries the specific parts of the modelling chain relevant to this thesis.

In the geophysical step of modelling, there is an optional initial step of B-field interpolation to improve on the estimate of the local B-field for a utility. Following this there is estimation of the E-field in the frequency domain using magnetotelluric based methods, or in the time domain through a look-back window approach or the thin-sheet method. For this, either measured surface impedances or synthetic profiles are used to define the Earth's filtering effect. Once an E-field has been estimated, or in a few cases measured, the engineering step aims to model the network response given EMF driving. The EMF in this case is ultimately an integrated E-field. For most modelling efforts, network information is taken into account to model analytical network parameters that scale an assumed uniform E-field in the principle component directions. There is a complication that accurate network state information is not often available and that the resulting scaling of the integrated E-field needs to consider the entire network. The effective response at a node in this sense is not a simple integration. In the E-field to GIC step, if there is measured GIC data, empirical approaches can however define the effective response. An alternative alluded to is the mapping straight from B-field to GIC. This transfer function (TF) mapping is possible in the frequency domain if there is measured B-field and GIC data. The TF approach inherently includes the effective network and geophysical responses with no further integration or assumptions required.

Looking at the GIC problem from this high-level viewpoint and focussing on the practical modelling aspects, we can also identify a number of challenges. Firstly there is the question of predictability of GICs. For this aspect of modelling, critical to effective mitigation, we need to work backwards from the nodal GIC. Assuming an accurately characterised system, it is possible that the B-field at a geomagnetic observatory can be mapped to resulting GIC. For any prediction capability, we would need to look to the space physics link in the chain. Here we can identify active regions of the Sun that may flare many days in advance [181,182]. When a CME does occur, then propagation models can give a lead time of less than a day for particularly extreme events. These models can give an idea of the rough magnitude but not the exact dynamics [183]. Next, we have satellites at the first Lagrangian point (L1) that can inform further models estimating the large scale near-Earth current systems with measured solar wind data. This data, if real-time, would give a prediction lead time on the order of minutes. The scenario described is the ideal case and can flag the possibility of a geomagnetic storm or not. It cannot however predict the fine scale effects, such as substorms, that have been shown to cause significant GICs [153].

In broad terms there are three major sources of uncertainty and modelling error in the geophysical and engineering steps of the chain. The first main source of uncertainty is in the estimation of the B-field. Generally, magnetometers with high-quality data are sparsely located and interpolation needs to be done to get a B-field estimate within a network. Either in doing this interpolation, or in using a remote magnetometer, error creeps into the modelling chain. The second main source of uncertainty has to do with the estimation of the E-field that drives GICs. Assuming the B-field is accurately estimated, which we have established is a challenge in its own right, there are usually many assumptions made regarding the Earth's conductivity structure that introduce error and uncertainty. Regardless of the assumptions made, Earth's conductivity structure can be very complicated with multiple factors influencing the true E-field. Very few regions have the surveys required to quantify the conductivity structure for accurate modelling. Although the spatial resolution required from an MT survey is still an active area of research, the USArray, with scale distances of 50 km between sites, has found significant variation in the surface impedances and resulting E-fields [139]. Even in the cases where there are such surveys, there is a third source of uncertainty that is seldom addressed, and that is the network itself. For this part of the modelling chain, network analysis is usually done using particularly simplistic assumptions not always aligned to more complicated modelling in the geophysical step. Ultimately, the entire network weights the effective contributions of the E-field or B-field driving non-trivially, introducing error even when previous steps are modelled accurately.

The main aim of this thesis is to develop operational approaches that are able to overcome the identified sources of uncertainty in the geophysical and engineering steps. An additional aim is to probe system characteristics during model development. In order to achieve these aims, data-driven methods will be used, but this brings along its own challenges. The largest of these challenges is the availability of high-fidelity or high-quality data. As briefly mentioned, magnetometers in general are sparse and there are very few regions with extensive geophysical information relevant to GIC modelling. Until recently, the availability of measured GIC data was also rare, making data-driven methods infeasible. Of recent there has been a drive for more magnetometers, MT surveys and GIC data, but there are still many utilities that do not have access to such data. To ensure that the outputs of this thesis are practical for general utilities, there has to be an emphasis on robust modelling that can also estimate uncertainty given limited or low-fidelity data.

Lastly, there is the challenge of what mitigation strategy is best to use. This question is well beyond the scope of this work and very dependent on the particular situation of the utility. Besides hard mitigation such as design changes of transformers or the introduction of series capacitors that effectively block GICs, there are also operational approaches such as line switching[184] or warning systems that inform maintenance scheduling, load reduction and load sharing. Utilities may also decide that the risk faced is acceptable given the cost of hard mitigation and focus on resilience, asset management and the ability to replace transformers or deal with cascading failures. When making such decisions, a utility would have to consider that extreme events do not occur in isolation and occur during normal system operation, where other failures or stresses unrelated to geomagnetic driving can possibly occur simultaneously[185].

4.2 Procedure for Analysis

With the general operational modelling framework defined, the procedure for analysis will follow simple steps of model development and data acquisition, followed by model testing and discussion around the results.

More specifically, model development in the next chapter would entail developing an empirical methodology for GIC modelling in both time and frequency domains. Empirical in this case refers to general data-driven mappings that, although inspired by physical relations, are defined by measured datasets. Analytical methodologies in contrast are unaffected by measured data and are specific in their representation. The operational aspects of uncertainty and robustness need to be addressed by whichever methodology is used. For this work, further validation of the frequency response of GICs and the implications of the frequency response in proxies will be explored in the model development step as these concepts underpin a lot of our understanding.

Concurrent to model development, there is the issue of data availability and acquisition. The different datasets used need to be cleaned and calibrated, with certain implications regarding cadence and coverage. These factors are addressed in the next section of the current chapter.

Once the empirical methodology has been developed, with suitable data available, the methodology is to be tested. In order for accuracy to be tested, the methodology is compared to previous empirical modelling attempts in South Africa. An improvement in the general error metrics would indicate higher accuracy, above what is required for operational application. From an operational perspective, the propagation of uncertainty through the modelling chain (Figure 20) would further need to form an error bound along with modelling estimates. For robustness, the methodology would also be tested in different networks, with different data fidelity levels. This ensures that the methodology developed can generalise to arbitrary networks and produce useful results in varying data conditions. More specifically, the TVA network in the USA will be used with medium- to high-fidelity (defined more precisely later) data modelling, the Powerlink network in Australia will be used with medium-fidelity data and an additional node in the South African network will be included with low-fidelity data, i.e. as a worst case for modelling. In Japan, the MMB node (with its geomagnetic, geoelectric and GIC monitoring) in Hokkaido will be tested given its well known challenging geophysical environment. During the testing step of analysis, different modelling inputs (e.g. B-fields, conductivity profiles and data cadences) will be further stress tested and GIC characteristics defined. GIC characteristics will be probed where there is high-fidelity data available in particular as to ensure the observed features are not artefacts of poor data quality.

Diving deeper into the B-field modelling aspect of operational GIC modelling later in Chapter 7, a similar analysis procedure will be followed. Firstly, available B-field data will be used to validate existing interpolation results by comparing with out-of-sample sites in southern Africa. Next, improvements in the interpolation scheme along with an approach to uncertainty estimation in interpolation will be developed. The new approaches will be tested, again using out-of-sample B-field measurements for validation but in this case from a high-fidelity INTERMAGNET site.

4.3 Data

With the use of empirical methods for GIC modelling, the data used becomes critical to modelling success. For the various analyses in this thesis, data from a number of different networks around the world have been used, with an emphasis on the mid-latitudes. Although there are more GIC data holdings and more extensive analysis has been done by the author, the storms and sites presented in this chapter are those that are relevant to this study.

The most common method of GIC measurement, and the method used for datasets in this work, is through a Hall-effect sensor placed on the transformer neutral. The sensor usually takes the form of a non-intrusive clamp that is placed around the neutral and detects the magnitude of the magnetic field produced by a current in the neutral. This in turn allows the magnitude of the current in the neutral to be calculated. Polarity of the resulting GIC measurements is entirely dependent on the setup, but can be inferred from physical constraints. Given a network predominantly northward of a measurement node, a southward E-field would drive a current through the network that grounds at the measurement node. Network parameters ultimately capture this behaviour, but should be checked for consistency. The data fidelity or quality between the nodes varies, with different cadences, different noise levels and different sensitivities all possible. For empirical modelling to be robust, the model used should be able to use the various types of data. Table 1 summaries the locations and data coverage of the different nodes. Low-fidelity as we will define it is GIC data characterised by low cadence measurements (1 minute or more), data gaps, noise contamination and offsets. High-fidelity data is defined by high cadence measurements (4 seconds or less), low noise levels and no data gaps or offsets to be corrected for. Medium data fidelity lies between the two, usually as a result of large noise levels.

Table 1: GIC data from power networks around the world used in various parts of this thesis. See map in Figure 7 for a visualisation of where these sites lie relative to geomagnetic coordinates.

Region	Year	Geomagnetic Storms	Site	Data Fidelity	Cadence	Geographic Lat.	Geographic Lon.
South Africa	2001,2003	2	GRS	High	2 s	-33.7°	25.6°
	2015	1	MAT	Low	60 s	-23.7°	27.6°
Japan	2006	1	MMB	Med	1 s	43.8°	144.2°
USA	2014-2016	4	PAR	High	2 s	37.3°	-87.0°
	2015-2016	4	WEAK	High	2 s	36.3°	-88.8°
	2014-2016	5	MONT	High	2 s	36.6°	-87.2°
Australia	2015	1	BOW	High	4 s	-20.0°	148.2°
	2015	1	MUR	Med	4 s	-27.5°	153.1°
	2015	1	MDR	High	4 s	-27.6°	151.9°

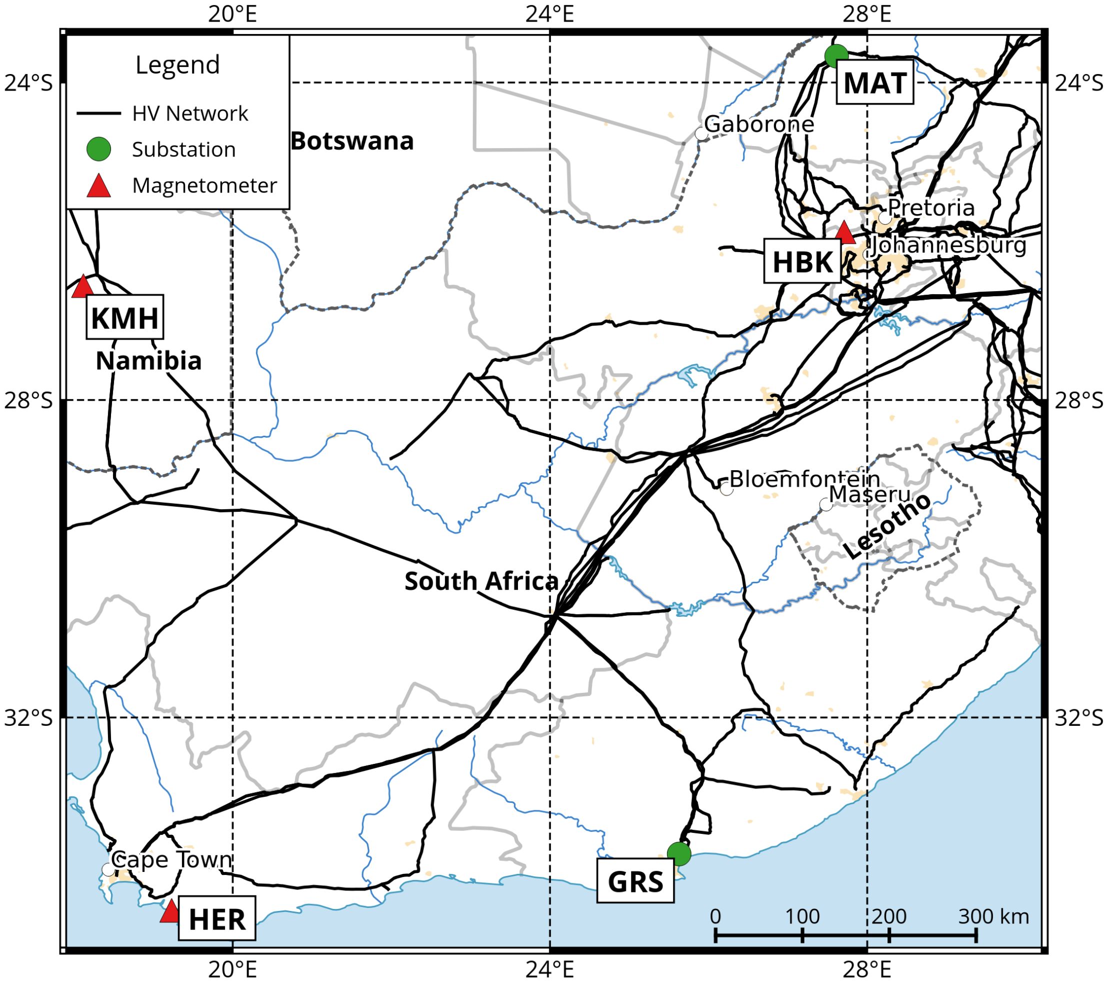

Figure 21: HV network in southern Africa, with the magnetometers and GIC measurement sites shown.

In the South African Eskom network, shown in Figure 21, GIC data from the Grassridge (GRS) and Matimba (MAT) nodes are used. All nodes form part of the 400 kV HV network, with MAT being a GSU type transformer and GRS a 400/132/22 kV three-phase three-limb autotransformer. GRS GIC data is part of the EPRI SUNBURST monitoring programme, with high-fidelity 2 second cadence data. MAT on the other hand is monitored by the utility at 1 minute cadence, with questionable fidelity and a poor SNR of roughly 7. This 1 minute data is an average of 1 second sampling with a resolution of 0.1 A. Given that the expected GIC is in the order of a few ampere for an intense storm, a lot of information might be lost at this coarse resolution.

For GRS, B-field measurements from the Hermanus (HER) INTERMAGNET station are used. At the time of GIC measurements, the only B-field data available were at 1 minute cadence and GIC data had to be downsampled (1 minute averages) to this cadence for modelling purposes. Using the ratio of RMS squared as an proxy, the SNR for GRS during the Halloween storm is roughly 23. MAT makes use of either the close Hartebeesthoek (HBK) or the more distant Keetmanshoop (KMH) observatories. By this stage B-field measurements were at the 1 second cadence, but GIC measurements at MAT are still at 1 minute cadence, again limiting modelling. Additional magnetometer measurements from southern Africa are used in the B-field interpolation analysis in Chapter 7 and are described in more detail there. No additional conductivity information is assumed for modelling in South Africa, although future studies may want to leverage the survey work done by the geophysical community[170].

In Japan, numerous studies have used GIC data from the Memanbetsu (MMB) 187/66 kV substation in Hokkaido, seen in Figure 22. The GIC data in this case is at 1 second cadence, with issues of artificial spikes being apparent in the data. The SNR for this event is around 35. The Japanese Meteorological Agency and Kakioka geomagnetic observatory has been recording both geomagnetic and geoelectric data at MMB at 1 second cadence since 2000[186]. For the time period concerned, the E-field has baseline offsets and noise that can be corrected for using geomagnetic data and computed MT responses[187]. Most GIC studies attribute the main GIC contribution at MMB to the 187 kV HV line from Ashoro power station[83,146].

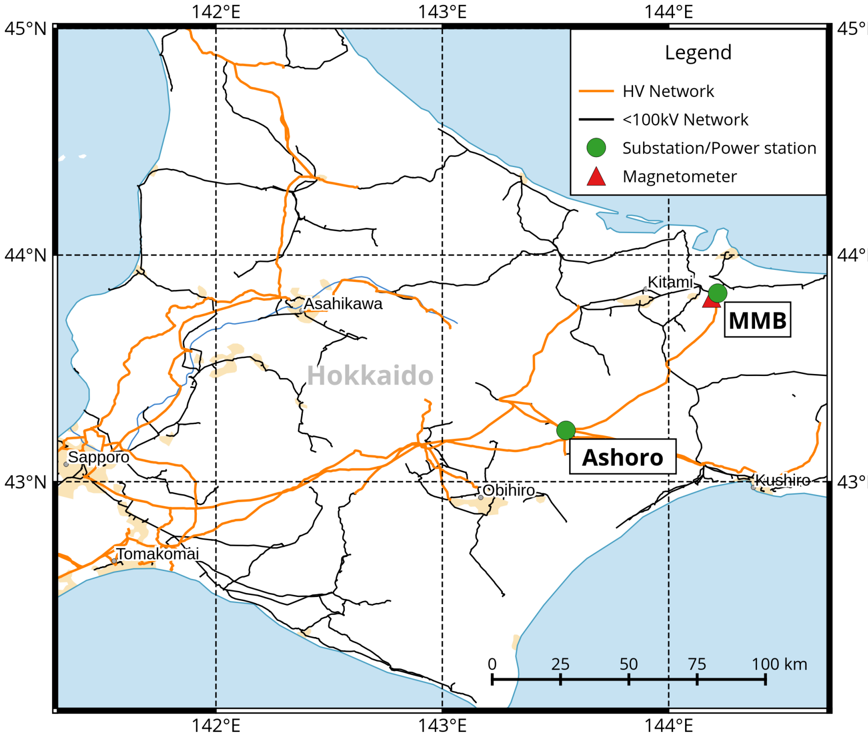

Figure 22: Local HV and lower voltage network around Memanbetsu in Japan, with the Ashoro power station included for context.

Of the various datasets used, the Tennessee Valley Authority (TVA) 500 kV HV network in south-eastern USA provides the most extensive and highest fidelity set of measurements. All GIC measurement is at 2 second cadence and besides a low SNR at certain nodes (less than 2), there seems to be minimal artificial noise. In particular, the Paradise (PAR) GSU node, with a large SNR (around 100), is analysed in depth. This region has significant conductivity information as provided by the USGS EarthScope Transportable Array project (available through the The IRIS Data Management Center (IRISDMC); doi:10.7914/SN/EM). Using a dense MT survey with remote referencing, electromagnetic transfer functions are estimated. For the June 2015 geomagnetic storm there were active MT sites within the network that managed to record the B-field, giving rare multi-instrument measurements of both the B and E-fields within the TVA network, as seen in Figure 23. The implications of this kind of measurement are explored further in Section 4.3.3. In the case of other storms not having the local B-field data, a more distant 1 second cadence B-field is obtained from the Fredricksberg (FRD) geomagnetic observatory.

Besides the PAR node in the TVA network, a number of other nodes have been instrumented with variable temporal coverage. All the nodes with measured data are shown in Figure 24 and have been analysed further by Heyns et al.[188]. Some results shown in this work are for the Montgomery (MONT) and Weakley (WEAK) nodes, identified as the next most susceptible nodes.

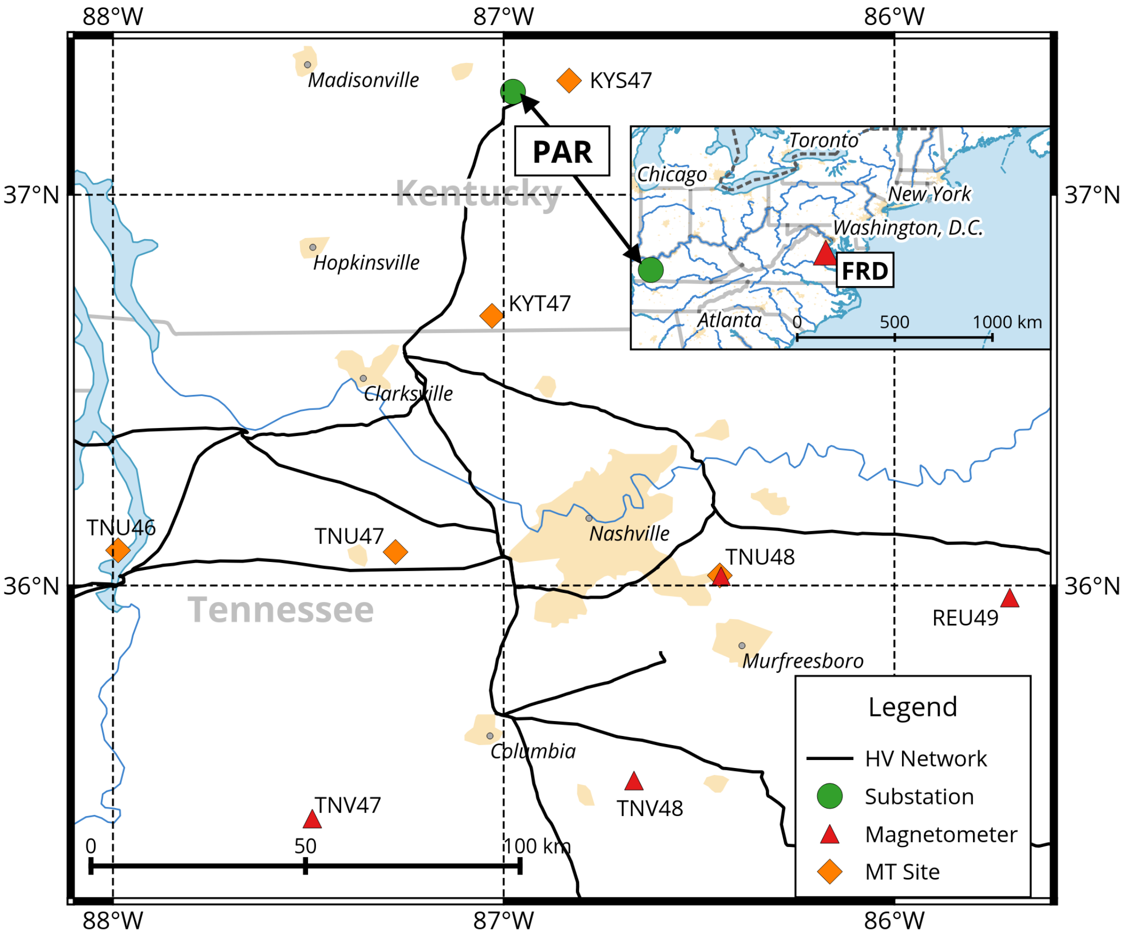

Figure 23: TVA HV network in the USA, with the MT sites and magnetometers shown with the GIC measurement site at PAR for high-fidelity analysis. Lower fidelity modelling uses a synthetic conductivity profile and remote FRD magnetic field measurements.

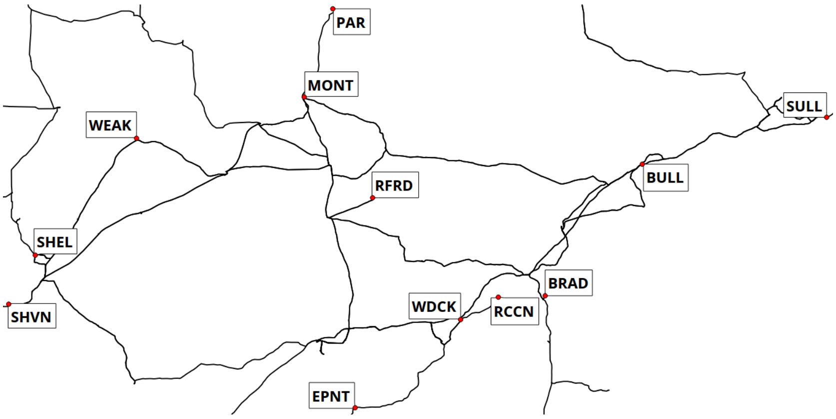

Figure 24: Less detailed map of the greater TVA HV network, as used for a recent susceptibility study of the network[188]. The extent of the network is roughly 750 km east-west and 350km north-south. Of the other sites, MONT and WEAK are used for additional illustrative purposes in this work. For reference PAR shown in more detail in Figure 23.

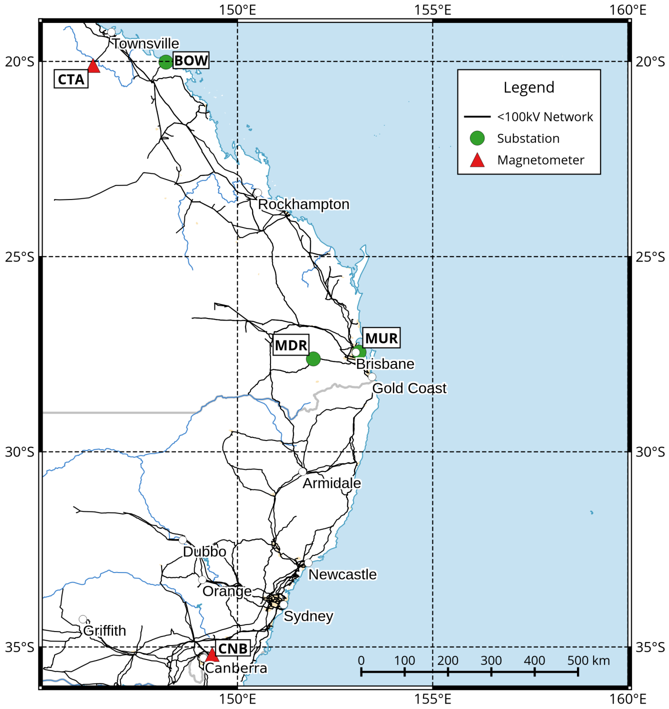

Figure 25: HV network in northeastern Australia, with the measured GIC sites in the Powerlink network indicated. Also shown are the relevant INTERMAGNET magnetometers.

GIC data from the Powerlink network (Figure 25) in Queensland, Australia, has the interesting feature of being dynamically sampled at 4 second cadence. Dynamic sampling in this case refers to the fact that data is only recorded at the maximum 4 second cadence if there is a significant change in the GIC amplitude (above some threshold). Data from the 132/66 kV Bowen North (BOW) node is paired with the INTERMAGNET magnetometer at Charters Towers (CTA), which samples the B-field at 1 second cadence. Further south, the Murrarie (MUR) 275/110 kV and Middle Ridge (MDR) 330/275 kV nodes are related to the average B-field between CTA and Canberra (CNB), which is also sampled at 1 second cadence. All sites have a low SNR's of around 9. MUR is however part of a complex region within the network that may affect modelling. No conductivity information is assumed and a synthetic layered-Earth approach is used.

4.3.1 Data Cleaning and Conversion

As with all data, there is a significant amount of cleaning that has to be done in both the B-field and GIC data. When selecting data for subset modelling or even in general modelling, outliers can influence the results significantly. GIC measurements often are sensitive to temperature, with diurnal variation or drift not directly related to GIC driving apparent over extended periods[189]. Physically, there should not be a constant baseline GIC flow through the network. In this regard any off-sets were removed to insure that the GIC is mean centred about zero during quiet time (periods of little to no geomagnetic driving). Next, a first-order high-pass Butterworth filter of 24 hours was applied. This conservative maximally flat filter preserves variations with periods less than 24 hours and removes the possible non-GIC related diurnal baseline variation.

The removal of any artificial spikes further improves both the modelling accuracy and confidence. The de-spiking procedure is an iterative process, with up to three steps involved. In each step the absolute derivative sum, second absolute derivative sum and standard deviation of the input GIC absolute magnitude are computed in rolling windows. Anything above a chosen threshold of the derivatives show spikes and anything above the second derivative shows sharp peaks, while a large

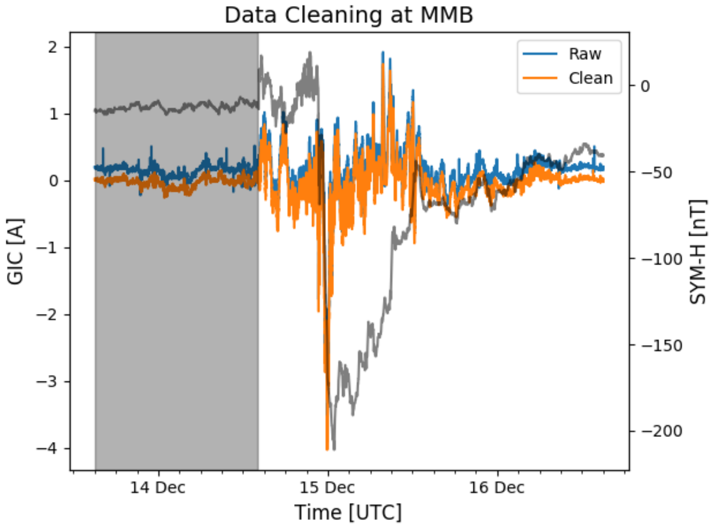

Figure 26: Using the MMB node in Japan, clean versus raw GIC data is shown. The main contributions to cleaning are offset removal, spike removal and diurnal temperature detrending. Quiet time (shaded region), as determined by the SYM-H index (gray), is used to determine any baseline drift.

standard deviation shows that the signal is likely in a disturbed part of the storm where spikes are likely. As a result the quantities are weighed off against each other manually. The rolling windows are defined for each step according to what cleaning is required. In the first step discontinuous spikes are removed and the window length is short, with large thresholds set. Once a spike interval is identified, a period of 2 time instances before and 3 time instances after are masked as noise. All the masked instances are then removed and missing data interpolated using a piece-wise cubic hermite interpolating polynomial, allowing more accurate representation of the derivative than simple linear interpolation. The updated GIC data is then re-evaluated. In second and third steps, missed previous spikes and more systematic noise spikes can be removed, such as in the case of artificial spikes that have a recovery signature. In these steps the thresholds chosen are varied to be more selective towards lower amplitude spikes, but still not removing signals from disturbed times. The end result of such cleaning is seen in Figure 26 for MMB, where there is significant artificial noise.

Further manipulation is needed in the case of using magnetometer or variometer data that is not quoted in geographical coordinates, i.e. XYZ. The discrepancy comes from many magnetic measurements initially being aligned to geomagnetic coordinates, i.e. HDF or HDZ (see Figure 27). In geomagnetic coordinates, the declination D can be represented either in terms of an angle deviation from the main field or a B-field amplitude (in nT) if a three axis magnetometer is used[190]. Most variometers use the latter, whereas magnetic observatories measure the inclination angle and can very accurately define the angular declination. Since the Earth's main field is spatially and temporally variable, the geomagnetic reference frame is not consistent with GIC studies that use extensive network topologies in geographical coordinates.

In order to convert to geographical coordinates, either the exact orientation of the magnetometer needs to be known, or the base declination of the main field needs to be known. The latter is what is typically known at magnetic observatories, and documented with the HDF/HDZ data. When this information is not known, then an estimation of the main field is needed. Having the base declination allows a three axis measurement to be calibrated and conversion between coordinate systems. For our purposes the 2017 Enhanced Magnetic Model (EMM2017) is used (`https://www.ngdc.noaa.gov/geomag/EMM/index.html`) as it includes high resolution crustal geomagnetic field estimates from satellite and ground measurements. Comparison with alternative models, such as CHAOS-4, showed negligible differences and any of these models would suffice for first-order coordinate transformations.

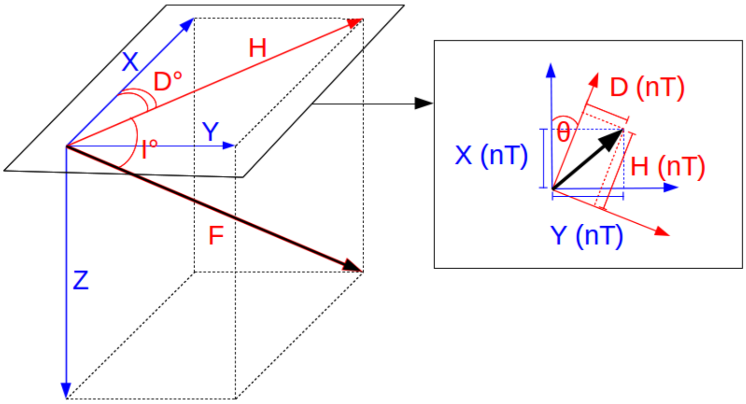

Figure 27: XYZ, HDF or HDZ coordinates used for B-field measurements. Geographic or XYZ coordinates (blue) have X, Y and Z referring to the geographic north, east and downwards, and the sensor is orientated accordingly. In geomagnetic or HDF coordinates, H is total horizontal field component, D is the declination angle from true north (eastward being positive) and F is the total field strength. The inclination angle I, is required to measure the declination accurately. In many variometers, a three-axis magnetometer that is aligned to geomagnetic north at some point in time, with a declination angle θ. The D axis in this case is measured in nT and needs to be converted into an angular argument, taking into account θ as well as updating H. In such cases, Z is usually the third coordinate.

4.3.2 Data Cadence

There are a number of issues around data cadence. Although GICs are thought to be generally quasi-dc and low-frequency phenomena, with most of their power below 8.3 mHz (1 minute cadence), there are dynamics that cannot be seen at lower cadences even if general modelling is accurate. An example seen in Figure 28 using GIC for the same event at a cadence of 4 seconds is the lag in SSC onset across the globe. Here we have the USA GIC, B-field and associated E-field closer to midday, all preceding the same signatures in Australia on the other side of the world. At 1 minute cadence, SSCs seem to happen instantaneously across the globe and no lags are seen between different datasets. In this example the striking correlation between scaled synthetic E-field and GIC is also seen, which confirms the theory presented earlier. The lags between E-field and GIC are not conclusive since the conductivity structure in each case has not been physically modelled.

A further issue with lower sampling rates or averaging in general is that peaks tend to be underestimated[143,174,192]. Simply put, the lower the cadence (or longer the averaging period); the smaller the peaks. A rough example in Figure 29 shows the effect of filtering with a cutoff frequency of 50 mHz (20 second cadence) compared to 2 second cadence raw data. At lower cadences peaks are even further reduced, which raises the question of viability of 1 minute data for peak estimation.

4.3.3 Geoelectric Field Derivation

The geophysical interpretations and extent of what can be modelled exactly by the various flavours of E-field models remains an active field in geophysics[110,128,129,135,187]. For the purposes of the current work, the models used will be limited to layered-Earth and empirical 3D surface impedance tensors from MT surveys where possible. Homogeneous Earth approximations are avoided due to their unrealistic simplicity. That said, the more sophisticated methods still adhere to the general relations defined by an homogeneous Earth which can be used for proxies. Furthermore, this work does not look at impulse response approaches used for E-field estimation, although these are well defined and would ultimately be needed for real-time modelling. Instead, all calculations are done in the

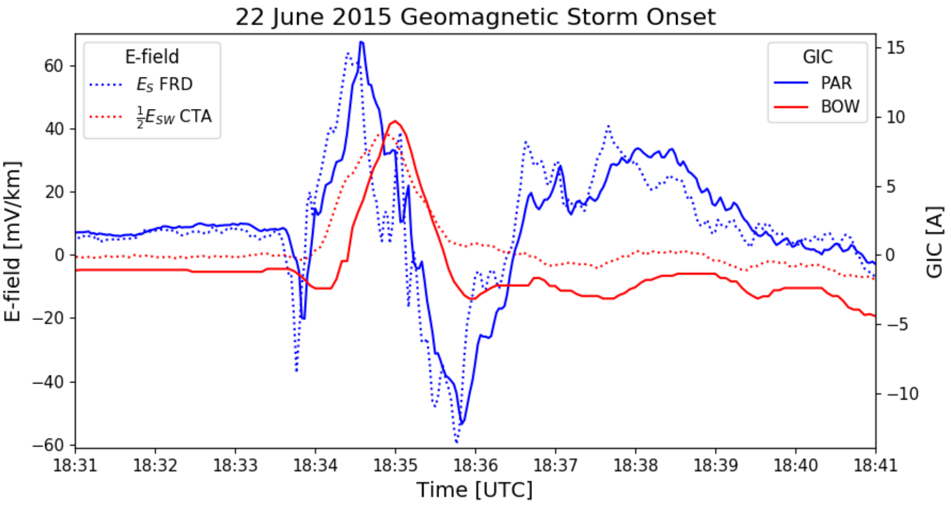

Figure 28: The distinct lag between SSC onsets at different sites can be seen using 4 second cadence[191]. Solid lines indicate measured GIC data in Australia (red) and the US (blue), which is sunward. Dotted lines representing a synthetic E-field for the nearest magnetometer sites using the same conductivity profile. To link the E-field and GIC profiles, the local line direction projection of the E-field is plotted (SW and S respectively). For the Australian data, a scaling factor is included to allow further visual comparison. At 1 minute cadence, SSC onsets are seen as instantaneous across the world.

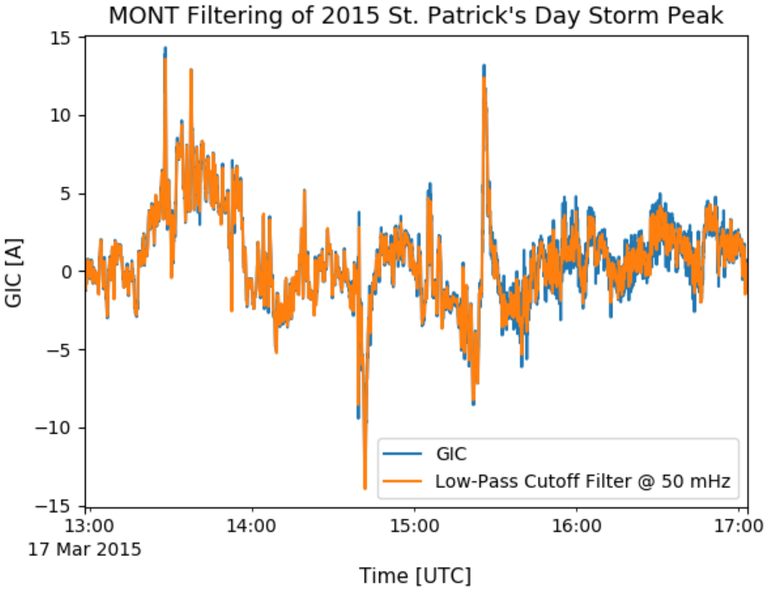

Figure 29: One of the shortcomings of low-pass filtering or using lower cadence data is that peak estimates of the data are underestimated, as seen here for MONT.

frequency domain. For layered-Earth modelling, previously used approaches[5,61] include an extra day of B-field data on either side of the data to be used. The resulting full dataset is then windowed in the time domain using a Parzen window to further reduce any edge effects from the FFT to be applied[5]. Once the windowed B-field is in the frequency domain, it is multiplied by the surface impedance, defined by contributions from the different layers within the Earth or a full 3D tensor, before an IFFT is applied to get the result in the time domain. In the time domain, the central day of data is extracted to ensure minimal contamination from edge effects. An alternative method to deriving the E-field from a surface impedance in a single FFT with padding is making use of rolling windows and multiple FFTs, á la a spectrogram. The method was formulated for use with surface impedance estimates from MT data. In this case, the empirical surface impedance is defined for discrete log-spaced frequencies that need to be interpolated into linear spaced responses. The input B-field is then split into overlapping windows, with interpolated surface impedance then applied and results averaged in overlapping sections.

If the conductivity structure is not known, then an arbitrary physically based profile is often used to derive the surface impedance instead of an overly simplistic homogeneous Earth model. Stress testing can be done using particularly conductive or resistive profiles[150]. In this study, for all cases we demonstrate the use of a generalised synthetic global layered-Earth to obtain physically relevant frequency E-field scaling[193]. As explained in the previous section, the error due to this inaccurate estimate of local E-field is absorbed along with other errors and forms part of the analysis performed. This generalised global synthetic profile has layer thicknesses (from top to bottom) of $d = [40, 210, 160, 260, 230, 1300, 500]$ km and corresponding layer conductivities of $\sigma = [0.0056, 0.0095, 0.0262, 0.0776, 0.526, 1.69, 10]$ S/m. The conductivity of the terminating half-space is 100 S/m.

The TVA network region finds itself in the midst of a large scale MT survey, and in this case full 3D estimation of the E-field is possible and the characteristics of such high-fidelity data can be probed. Furthermore, for the June 2015 geomagnetic storm, the active MT sites allow for multiple B-field and E-field measurements within the network. These dual measurements were used to validate the spectrogram method of B-field to E-field conversion described above. Although only available for a single storm, the local B-field shows variation and an average, more accurate, estimate to be used in modelling efforts and characterisation. The variation between the 4 available sites can be seen in Figure 30, with the maximum standard deviation between stations seldom exceeding 10 nT. The main variation seen is in the B_x component during the SSC, which would be expected from ring current diving and possible timing issues between site peaks at 1 second cadence. B_y variation is seen most strongly during pulsation driving, with movement of the dominant B_y pulsation signatures over the TVA network apparent[194].

Making use of the average B-field over the TVA region, the 6 closest MT surface impedance responses, roughly related to the local power network topology, were used to generate a weighted average E-field, and can be thought of as a full 3D representation of the local E-field. The weighted average effectively encodes the network integration or averaging[137], which in some cases is similar to the combination of empirical fitting and a layered-Earth E-field, where distinct variations in the frequency domain due to inhomogeneities in the geology smaller than the transmission line scale length may be smoothed out. The exact method for averaging the E-field can vary, with Delaunay triangulation or nearest neighbour estimation often used, but with little difference between them given dense MT surveys[139]. The ultimate averaging is done by an empirical transfer function between B-field and GIC, where the entire complex network weighting is taken into account. For this case, a qualitative interpolation is used, with the Clarksville-Paradise line, and hence the central MT site, contributing the most (see Figure 23). Lines more than two nodes away are ignored. The weighted average as defined by relative distance from the center of the Clarksville-Paradise line is,

$$E_{av} = (3E_{KYT47} + 2E_{KYS47} + E_{TNU46} + E_{TNU47} + E_{TNU48})/8. \tag{41}$$

Here, the KYT47 site has the largest weighting due to its location in the central region of the Clarksville-Paradise line directly feeding PAR. KYS47 is weighted a third less due to being on the

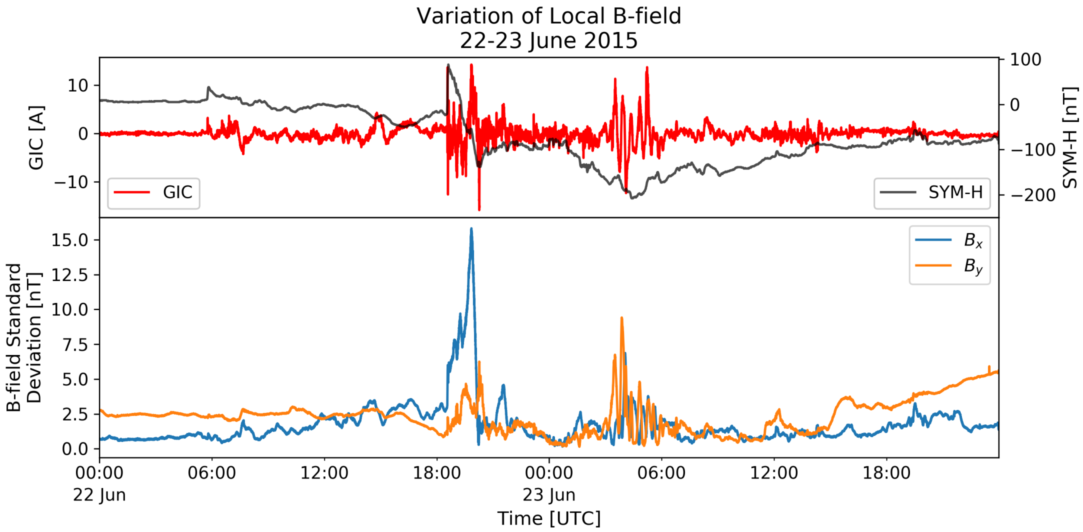

Figure 30: Given the unique case of dense measurements in the TVA network, the B-field variation can be characterised. Plotted in the top panel is measured GIC with the SYM-H index that quantifies disturbed time at mid-latitudes. In the lower panel the standard deviation of the measured B-field components within the TVA network are shown. We see here that even at mid-latitudes the plane-wave assumption of a near uniform B-field over the network is not always relevant, especially during disturbed times. Examples of such deviation from a plane-wave assumption is the variable current system driving pulsations in B_y over the network and the variation in the main phase response. The main phase response variation may include inductive components within the Earth.

end of the line and to the north. The TNU46, TNU47 and TNU48 sites are each contribute a third less due to being two nodes away, but together contribute more than KYS47 as they are south of PAR where the majority of the network lies.

To get the most out of MT survey E-field estimation, an inversion of the surface impedance to determine the 3D ground conductivity structure of area under question needs to be done. From this structure, a high resolution surface impedance can be estimated along the transmission lines and be integrated. The inversion methodology is an open question in geophysics and an area of active research[52,195–197]. Along with the error and uncertainty in inversion, this full-physics approach to GIC modelling assumes an accurate estimation of the B-field and power network information – both of which are not typically available to a utility.

Looking at the E-field estimates of MT sites in the TVA network separately while using the same average B-field, large variation in both E-field magnitude and direction is apparent. This is so even with the region not being particularly complex geologically in previous 3D analysis[55]. Figure 31 gives an idea of this variation, specifically looking at the magnitude range and standard deviation of the individual E-fields, compared to the weighted average E-field magnitude. The range of variation is similar to the actual magnitude of the average E-field itself and the standard deviation is similar to the difference between the average E-field and an E-field derived using the general layered-Earth model described above. In terms of directionality variation seen in Figure 32, there is similar variation both in the range of angle and mean angle deviation – particularly for lower level E-fields. Again, the extent of angular variation is comparable to the difference between average local E-field and generalised E-field.

In the local TVA network around PAR, it is foreseeable that the layered-Earth modelling with independently derived network parameters may provide accurate modelling. A quick litmus test in this case is looking at the frequency response, where the GIC and E-field power spectrum slopes should roughly match for the base GIC theory to hold. In the case of PAR in Figure 12, considering the frequency range from 0.1 mHz to 250 mHz, the E_x and E_y components have slopes of -1.8 and -1.6 respectively, compared to the GIC slope of -1.8. For the general E-field, the E-field slopes are both -1.8, agreeing with the feasibility of the layered-Earth approach at PAR along with empirical network parameters.

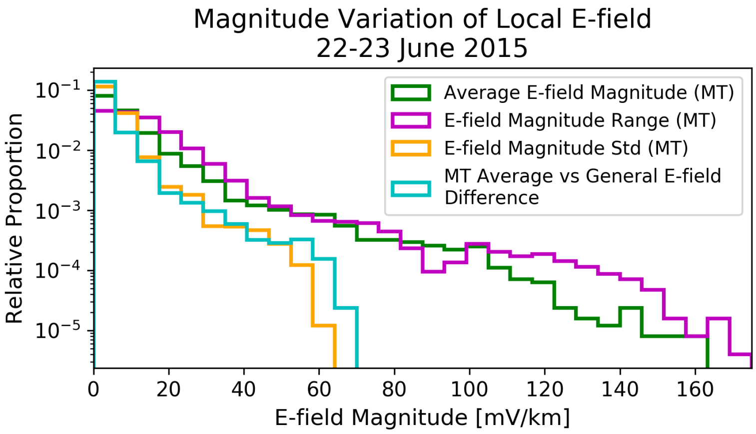

Figure 31: Dense MT measurements in the TVA network allows for the measured E-field variation to be compared. Using the available data for MT sites within the TVA network the average measured E-field magnitude across all sites is shown in green, the standard deviation in orange, and the range between highest and lowest magnitudes in magenta. From this, we see that even though the TVA region has relatively simple geology the associated E-field variation is large. The range of variation over a small area can be as large as the E-field itself and the standard deviation can be of a similar magnitude to the difference between measured E-field and a general layered-Earth modelled E-field (shown in cyan).

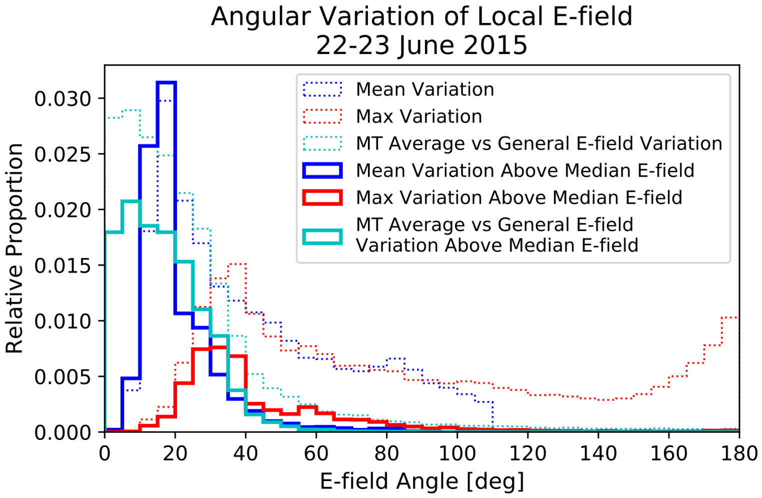

Figure 32: Also relevant to E-field variation is the angular variation, shown here for the TVA region. Again, the variation across all sites is shown as the mean variation in blue, maximum angle range across sites in red, and the variation between the average measured E-field and a general synthetic E-field in cyan. Of interest are the lower E-field magnitudes (dotted profiles) having larger variation than higher magnitudes as defined by using only data above the median E-field magnitude (solid profiles). Both mean and max variation of the E-field are comparable to the difference between measured E-field and general layered-Earth modelled E-field.

Geophysics has a number of tools available for understanding the conductivity structure that defines the measured MT surface impedances. Although not required for GIC modelling and not used in further aspects of this thesis, it is illustrative to see what environment drives the type of variation seen in the TVA network. Firstly, taking the two MT sites closest to PAR (roughly 50 km apart from each other), we see significantly different surface impedance and tipper responses in Figure 33. The tippers in this case are induction arrows made up of the complex ratios of vertical and horizontal B-field components. In the plot they are shown using the Parkinson convention and point towards anomalous currents concentrations as seen at a geophysical strike[65].

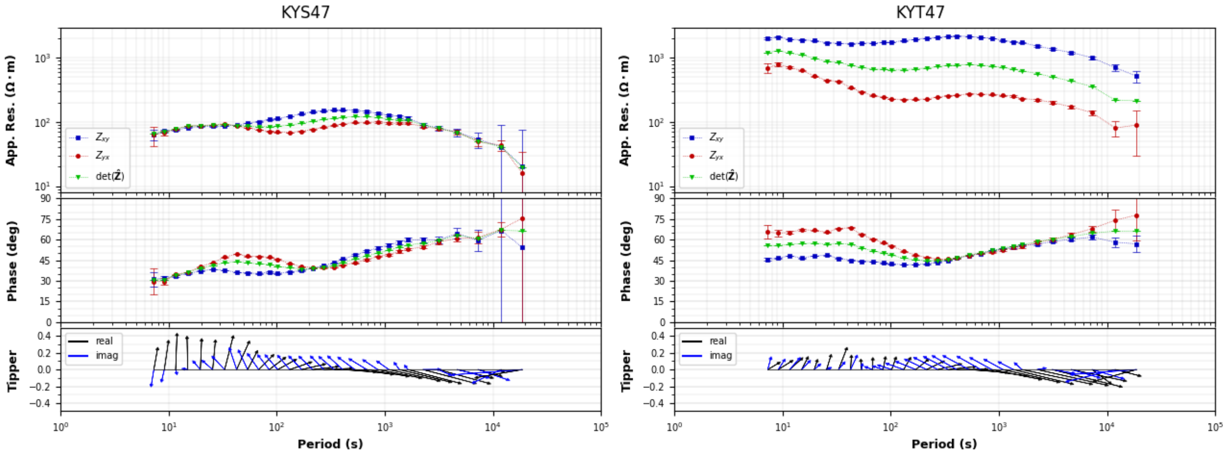

Figure 33: Looking specifically at the relatively simple geological area around PAR, we see that adjacent MT sites less than 50 km apart can have large differences in surface impedance responses. In the upper and middle plots, the apparent resistivity and phase of the main off-diagonal components and determinant of the surface impedance tensor are shown. The lower panel shows the real and imaginary tippers or induction arrows, which are transfer functions that relate the horizontal and vertical B-field components. Using the Parkinson convention in this plot, the tippers point towards a geophysical strike. At deeper depths, the tipper and phase converge, but apparent resistivity remains different. Data for this plot comes from the SPUD EMTF database (`ds.iris.edu/spud/emtf`) and visualisation was done using `mtpy` (`https://github.com/MTgeophysics/mtpy`).

A commonly used visualisation approach is to invert the surface impedance to obtain a representative local Earth. For a simple layered-Earth profile, Occam's 1D inversion is typically used, with the result being seen in Figure 34. Again the two MT sites have very different conductivity profiles below them, with KYT47 being more resistive and more likely to induce larger E-fields. In terms of the wider TVA network, we see similar variation is common.

Using a phase tensor visualisation[198] in Figure 35, we further see that the local structures in the TVA network are not 1D, but generally have 3D contributions to the surface impedance across most frequencies, but particularly the higher frequencies where the crustal contributions are more evident. Without an understanding of the network weighting to this heterogeneous E-field, modelling error may creep in even if geophysical estimation is accurate.

The geophysical E-field derivation can be adapted specifically for GIC modelling – forming the basis for the development of transfer functions. Instead of using MT data, measured GIC data and analytical network parameters can be used to find an effective surface impedance for GIC modelling[102,104]. This impedance acts as a quasi-transfer function between the B-field and GIC, often simplified for a layered-Earth case with Occam's inversion. The quasi-transfer function approach can be very effective, as shown for the geophysically complex Japanese coastal region where simple empirical quasi-transfer function modelling resulted in near perfect GIC modelling[84]. For GRS modelling in South Africa, a similar locally derived GIC effective profile was estimated with 10 layers[104].

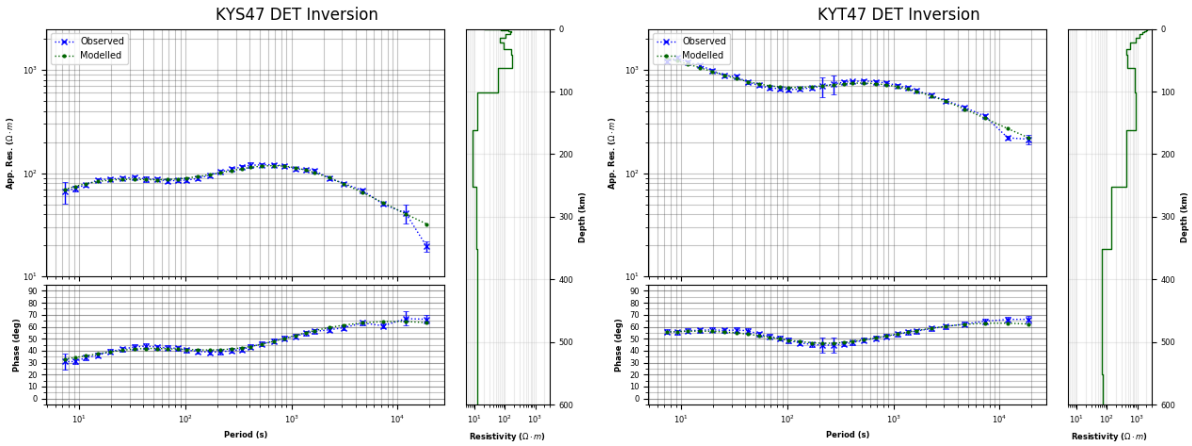

Figure 34: Using Occam's inversion technique for the determinant of the MT responses, an effective 1D layered-Earth can be approximated. The left plots for each site show the apparent resistivity (analogous 1D surface impedance) magnitude and phase of the modelled inversion and measured data. The right plots show the corresponding 1D conductivity structure with depth under each site. Again the adjacent sites have significantly different inversions, with KYT47 having a more resistive environment. Of interest is the close matching of the measured and modelled responses, supporting the result that around PAR a layered-Earth approximation is feasible. Data for this plot comes from the SPUD EMTF database (`ds.iris.edu/spud/emtf`) and visualisation was done using `mtpy` (`https://github.com/MTgeophysics/mtpy`) after using the OCCAM1DCSEM code (`https://marineemlab.ucsd.edu/Projects/Occam/index.html`) to apply Occam's inversion.

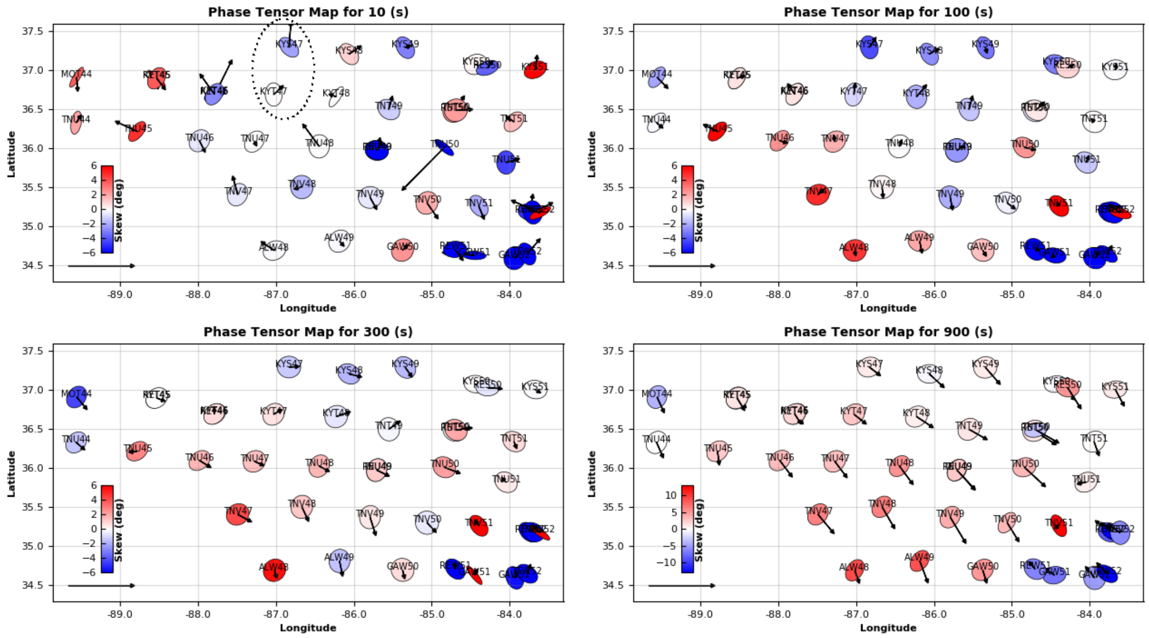

Figure 35: To visualise the geophysical variation across the TVA network, a phase tensor plot can be generated for different frequencies. The dotted region in the 10 second period plot indicates the two MT sites nearest PAR. The skew angle can be thought of as measure of the dimensionality of the responses (anything different from zero being 3D). The eccentricity of the ellipse is a measure of the 2D nature of the response and possible strikes. A purely 1D case will have a unit circle, with zero skew. A further indication of the underlying structure can be seen from induction tipper arrows, which point towards a conductor here. At longer periods, i.e. deeper penetration, the geological structure is more uniform with large scale features evident. Data for this plot comes from the SPUD EMTF database (`ds.iris.edu/spud/emtf`) and visualisation was done using `mtpy` again.

5 Model Development

In this chapter, the previously defined framework along with the measured geomagnetic and GIC data is brought together to develop operational models. Operational in this sense focuses on the estimation of uncertainty in modelling and including the effective driving, which may be made up of non-linear or unmodelled contributions. Before defining the approaches to be used, the frequency response of GICs is explored further. There are a number of operational implications regarding the frequency response of GICs and these feed into further usage in the empirical methodology to be developed.

5.1 Frequency Response of GICs

There are two main points of interest in the frequency response of GICs. The first is the slope of the GIC power spectrum, which defines the filter response of the entire modelling chain taken together. The second main point of interest is where most of the power sits and at what cadence GIC modelling must be done. Both aspects have been analysed in detail by Oyedokun et al.[174]. To estimate the cadence required for GIC modelling, it should be noted that the noise spectrum is used. This allows the spectrum produced to be free of contamination from actual geomagnetic driving. When fitting the power spectrum slope, the knee frequency has to be identified where the GIC noise and instrument noise intersects, as seen in Figure 36. For the second point, a disturbed time is used where there is geomagnetic driving present as would be the case given critical GIC levels.

In order to quantify the characteristic GIC frequency response, GIC measurements from 7 different networks around the world were used for 5 significant geomagnetic disturbances[174]. Across all cases the low-pass effect of the GIC power spectrum was seen, with the spectral slope constrained between $m = -1$ and -2, agreeing with the background theory already presented in Chapter 3. To address the second point of interest, the cumulative energy in the raw GIC power spectrum can be computed. In this case, the $f_{98\%}$ frequency where 98% of the cumulative power spectrum (signal energy) sits below is computed. 98% is chosen arbitrarily to include at information up to a least a 2 sigma level. It was found that across all cases the majority of GIC power sits below 50 mHz, i.e. at periods more than 20 seconds. According to the Nyquist criterion, this means that sampling cadence needs to be at least 10 second or better – agreeing with proposed standards defined by NERC and what most modern GIC recording conforms to. Following up from the previous section regarding data cadence implications, the use of 1 minute data will result in a loss of accuracy.

A caveat already mentioned is that there is some error associated with ignoring higher frequencies. To investigate this error, a low-pass filtered version of GRS GIC data was compared to the unfiltered GIC dataset, sampled at 500 mHz. For the low-pass filter, a cutoff frequency of 50 mHz (roughly $f_{98\%}$ for GRS) was used, with all FFT frequency components above 50 mHz were set to zero before performing an IFFT. The result, shown in Figure 37, is a time-series that seems acceptable, but with peaks around the time of the SSC shifted and underestimated by up to 40%. Mathematically, peaks such as the SSC require higher frequencies to be resolved. Although low-frequency contributions still dominate during the SSC, the omission of higher frequencies affects the peak amplitude estimated. A similar result is seen in under-sampling the B-field, which propagates to the estimation of peak surface E-fields[192]. Even if the physical GIC drivers are not high-frequency in nature, mathematically these high frequencies are often needed to reproduce/resolve peaks or sudden, steep changes.

Of the driving possible in the frequency domain, discrete driving is also possible from geomagnetic pulsations such as those seen in Figure 36. Geomagnetic pulsations are cyclical fluctuations in the geomagnetic field, most often driven by field line resonances or cavity modes within the magnetosphere. For such pulsations there is a characteristic period and duration which varies due to driving mechanism. Common pulsations bands have periods between 1 and 5 minutes, with shorter periods also possible. Long-period pulsations with durations that span hours are more rare, but may be more effective in GIC driving. The longer period pulsations tend to be higher amplitude, and hence have

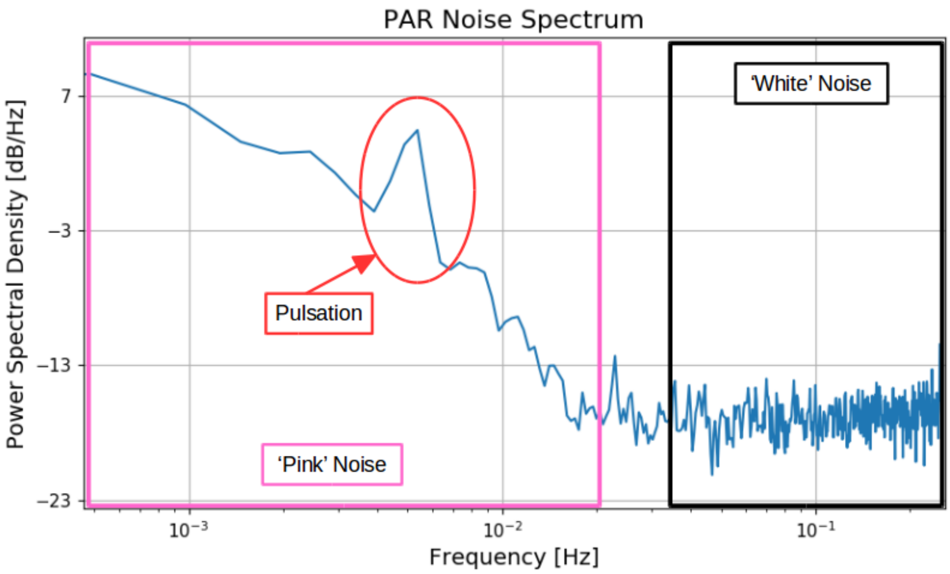

Figure 36: An interesting result from the analysis of the noise spectrum alone is the different regimes of noise. The plot above is produced using PAR data from 22/06/2015 during a 4.5 hour geomagnetically quiet period, with half hour windows and 50% overlap. The 'white' noise is typically associated with instrument noise and the 'red' or 'pink' noise is associated with actual driving noise levels. For most cases there exists a knee where the two regimes meet. Also evident is a pulsation signature in the noise.

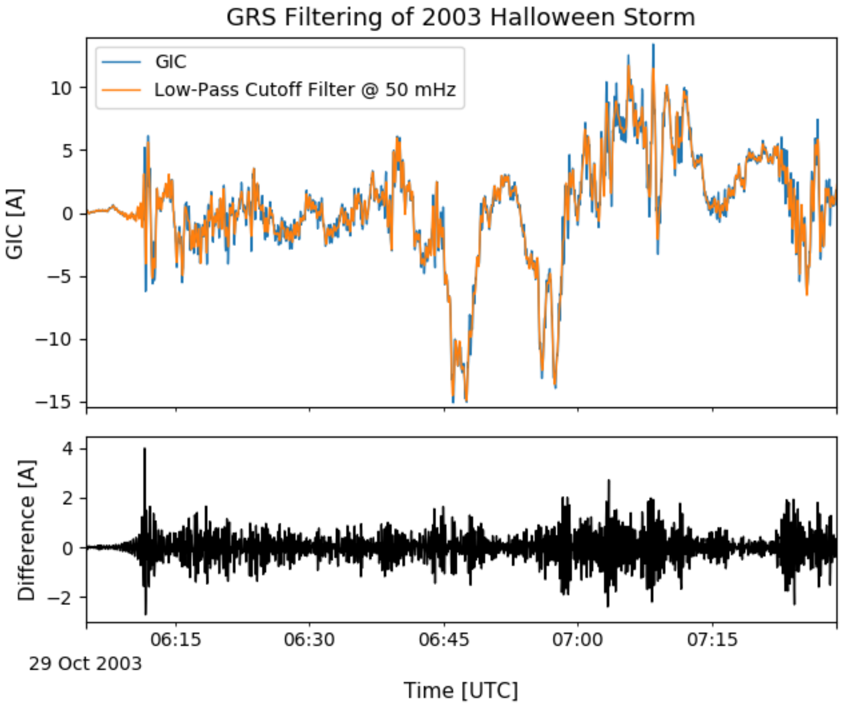

Figure 37: Using the f_{98} critical frequency as a cutoff frequency in a low-pass filter, we can generate representative GIC profile[174]. When applying such a low-pass filter there are significant errors that are introduced where higher frequencies are needed, such as at SSC.

more power to drive GIC. The realisation that pulsation driving is more evident than often thought and needs to be taken into account when modelling GIC response in the power network has been explored further in a recent paper by Heyns et al.[194].

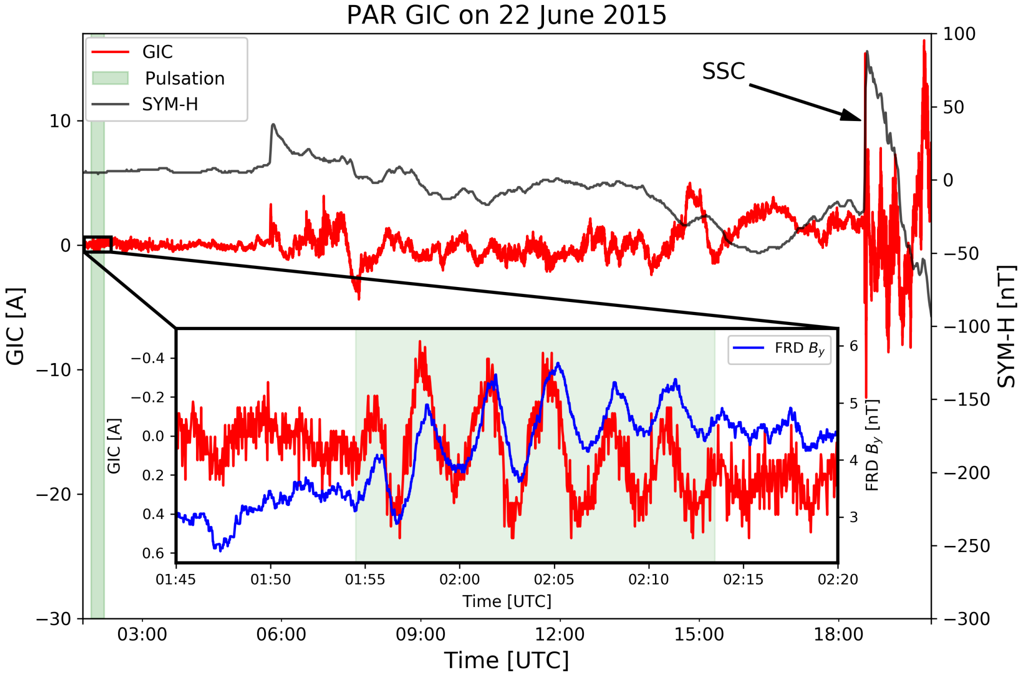

Figure 38: The frequency coupling between GIC and the B-field is seen here for the PAR[194]. Low-amplitude low-frequency pulsations at noise levels are clearly seen. Linking back to skin depth, the roughly 5 mHz pulsations would have a penetration depth of around 70 km ($\sigma = 0.01$ S/m). The high-pass effect of GIC relative to the B-field is also seen with the GIC profile preceding B_y.

Besides the need for accurate representation of discrete frequency driving in GIC modelling, pulsations also show the distinct coupling in the frequency domain that most modelling theory is based on, either in the B-field-to-GIC transfer function mapping, or in the B-field to E-field mapping using the magnetotelluric relation. During the June 2015 geomagnetic storm, the coupling of low-amplitude pulsations to GICs (both B-field and GIC are at noise levels) in the frequency domain is apparent in Figure 38. At these amplitudes, no GIC damage is expected whatsoever. What is nevertheless interesting is the extent of coupling in the frequency domain. In comparison with surrounding higher frequency variations in the time series, the low-amplitude low-frequency signal is lifted out of the high-frequency noise. The power network ultimately shows more sensitivity to low-frequency driving. Longer period pulsations, often associated with larger amplitudes, would in this case possible be effective drivers of sustained and significant GICs. Later during the same June 2015 event, exactly such localised long-period pulsations were seen over the TVA (shown in Figure 39), driving much larger GIC pulsations for an extended period of time. At these amplitudes, the pulsations may become critical to the power network and need to be taken into account. Operationally, there is the complication that the localised nature of these pulsations require denser magnetometer networks for accurate modelling[191].

An interesting implication concerning GIC pulsations is the that the power network can be used as an antenna. Given a susceptible node with an effectively large collecting area to produce large GICs, GIC data can be used concurrently with B-field data to identify pulsation activity with high certainty, particularly those at low-frequencies. A simple algorithm was developed for pulsation signature detection. FFTs of rolling windows of each signal (B-field and GIC) were taken and the spectra normalised such that the baseline linear response tends to a flat response. To determine the frequency dependant baseline 'noise', a log-space linear fit is performed on the power spectrum defined during

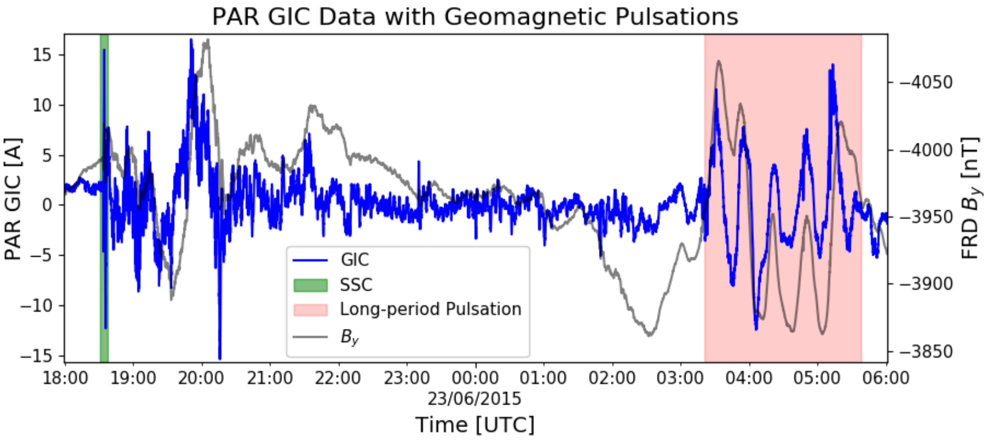

Figure 39: In a more extreme case, pulsations with a period of over 20 minutes were identified in the mid-latitude TVA network[191]. These pulsations are localised, which reduce the separation that can be used between magnetometer and network, and have amplitudes that rival that of the typical peak GIC seen at SSC, making them critical for power system modelling. Looking at penetration, for a homogenous conductivity of 0.01 S/m, these pulsations have a skin depth of around 750 km.

low geomagnetic driving. To ensure that the normalised spectral peaks are significant, significance levels of 5 sigma above the mean power are required across all signals. Lower detection levels can also be used, but should be analysed to ensure pulsation driving is evident. Merging the rolling windows results in a spectrogram version of the pulsation finder. A flagged version of whether or not a pulsation period is present is shown in Figure 40 for the PAR node in the TVA network, where both long-period pulsations and noise pulsations are detected. In an operational context, the pulsation finding algorithm is frequency band agnostic and can be used to assess pulsation specific effects in further studies.

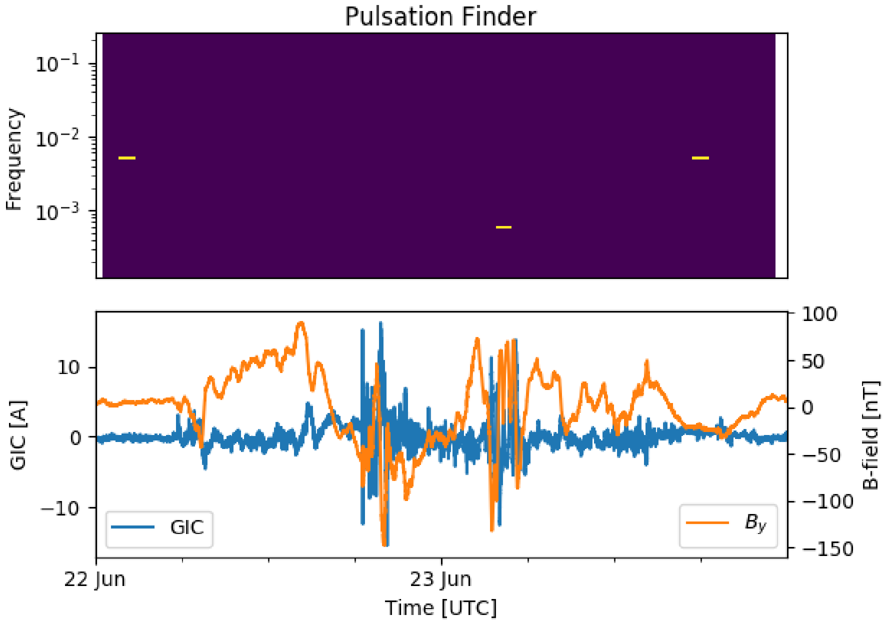

Figure 40: Instead of pulsation analysis constrained to a single time interval, a similar approach can be applied to a spectrogram. Adding the condition that pulsation signatures need to be seen in both B-field and GIC data at greater than the 5 sigma significance level generates an effective pulsation finder that is band agnostic. Applying the approach to the PAR node in the TVA network for the June 2015 storm, both the large scale pulsation signature from Figure 39 and pulsation signature in the noise from Figure 38 are seen, along with an additional pulsation signature in the noise (rightmost).

5.2 Considering the Use of Proxies

The time derivative of the disturbed B-field has long been used as a proxy for GIC activity, largely due to its perceived importance in Faraday's law of induction that drives GICs[77]. Previous studies have found agreement between GIC and dB/dt characteristics[76], with direct relations between the maxima of the two quantities further possible[199]. An improvement on the dB/dt activity proxy is a rolling maximum of either 1 hour or 3 hours[81] or more recently 30 minutes[82]. dB/dt proxies are useful as they do particularly well in resolving the storm or substorm commencement periods, usually associated with large GIC values and high-frequency components due to their impulsive nature.

dB/dt as measured at Earth's surface alone does not drive the E-field or associated GICs. The effective driver is instead due to the Earth's modulation of the disturbance dB/dt within the Earth in the frequency domain, with the conductive Earth acting as a low-pass filter for this variation[58].

Revisiting the earlier theory presented in Section 3.2, the B-field has a power spectrum (proportional to magnitude squared) that follows a f^{-m} relation with frequency, parametrised by the spectral slope m. In the frequency domain, dB/dt or $Bdot$ introduces a high-pass filter of f in relation to the B-field, i.e. $Bdot(f) = 2\pi i f B(f)$, with a slope $m - 2 \geq 0$. The E-field and matching GIC spectra slopes sit between the B-field and dB/dt slopes i.e. $0 \leq m - 2 < m_* < m$, where m_* is the E-field or GIC spectral slope. Relative to the E-field and GIC spectra, the B-field spectrum has a low-pass response and dB/dt a high-pass response. Due to the relative responses, a B-field proxy of GICs would be biased towards low frequencies and a dB/dt proxy of GICs would be biased towards high frequencies. Since dB/dt is usually determined through time domain B-field differencing, noise at the sampling rate of the B-field can effectively drown out signals from low-frequency driving. The largest contribution to high-frequency noise at the sampling rate would be instrument white noise, being more prominent in less sensitive instruments.

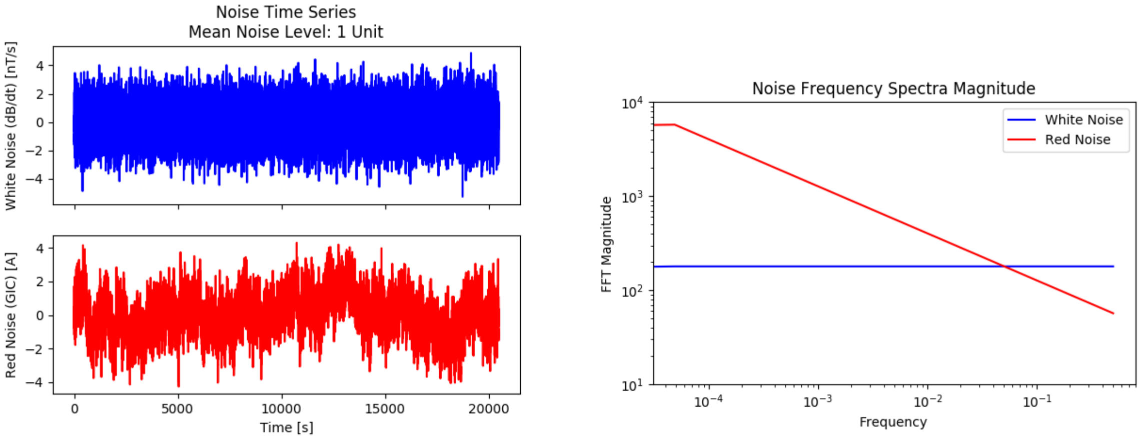

Figure 41: Synthetic white and red/pink noise relating to dB/dt and GIC respectively, both in the time domain and frequency domain.

Illustrative of these relations is the homogeneous Earth case, where $E(f) \propto \sqrt{f}B(f)$[64]. Assuming a B-field with frequency response parametrisation of $m = 2$, the E-field would have a parametrisation of $m = 1$ and dB/dt would have a flat frequency response with $m = 0$. The baseline power spectra are represented in Figure 41. The relative scaling of frequencies is important and often overlooked. At a baseline level with no driving, the responses of the E-field or GIC, B-field and dB/dt are very different. When driving does occur, it sits atop the different baseline noise spectra. To visualise this scenario, let the sampling frequency be the modern 1 Hz standard[200], and there be pulsations with a period of 100 seconds, as seen in Figure 42. For the flat dB/dt spectral response, the ratio of frequency spectral content between the pulsation frequency and Nyquist frequency is 1. For the GIC spectrum, the same ratio would be 50, i.e. for that same pulsation signal the dB/dt signal would need

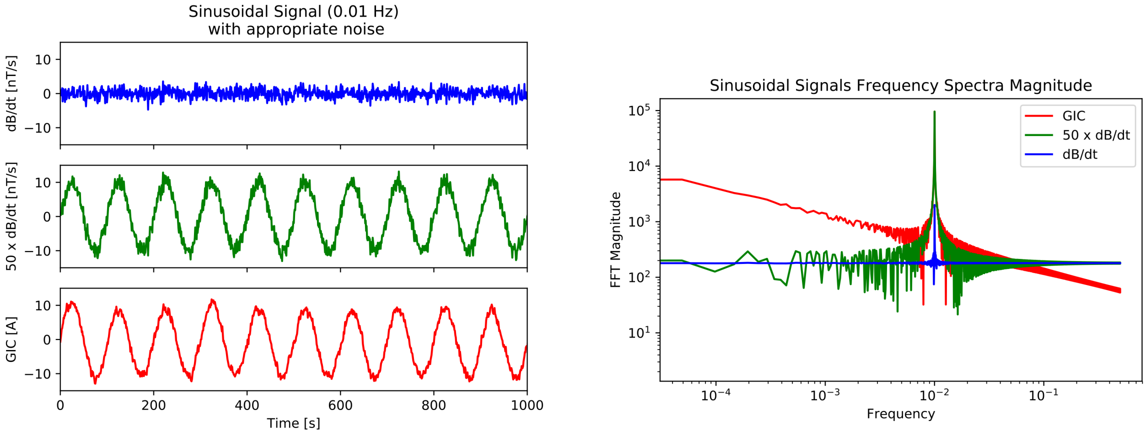

Figure 42: For a sinusoidal GIC signal at 0.01 Hz with amplitude similar to the noise level at that frequency (but sitting atop the noise), we have the red plots in the time and frequency domains. Assuming dB/dt with a similar condition results in the blue plots. The degree of amplification needed for the dB/dt signal at the single frequency to reproduce the required time domain profile needs to take into account the spectral response of the two different quantities.

to be 50 times stronger to be an accurate proxy for the GIC signal in the time domain. Given longer period pulsations, such as the long-period pulsations seen at PAR, the effect would be even larger. In the case of noise at the sampling frequency low-frequency pulsation signals could be drowned out. Impulses such as peaks or spikes on the other hand require broadband driving to be reproduced and are adequately described by dB/dt. In legacy 1 minute cadence B-field data, the sampling rate is closer to the frequency of common pulsations with periods on the order of a few minutes, the result being that dB/dt was more representative than seen using modern 1 second cadence data. Of course too low a cadence will miss the pulsation activity entirely. Ideally, a pulsation effective proxy would need to be as band agnostic as the pulsation finder algorithm. Such a proxy would have to encode the relative weightings of the sampling rate's Nyquist frequency with the narrow-band pulsation's frequency. The proxy would further need to satisfy this condition across all frequencies as there are multiple pulsation bands possible.

The manifestation of frequency response bias has been seen in measured data previously, a good example being at MMB where the 1 second cadence B-field is more closely correlated to GIC than dB/dt[83]. For this case, the complex conductivity structure can explain the observed correlation to a large degree[83–85]. In the more extreme case of long-period pulsations, the sampling bias is more obvious with high correlation between GIC, dB/dt and the B-field during different parts of the storm. During a low-frequency pulsation event, the B-field is representative of the GIC profile and shows similar structure in period and phase. In contrast, during the SSC of the same storm, with a significant higher frequency content, dB/dt is representative of the GIC profile (as seen in the middle panel of Figure 43 for the PAR node in the TVA network)[194]. The B-field intrinsically has lower frequency components than dB/dt, especially at 1 second sampling cadence. It is no surprise then that during a pulsation interval with a roughly 20 minute period, 1 second cadence dB/dt cannot reproduce the variation required as effectively as the B-field can. For the impulse during the SSC on the other hand, a higher cadence can better resolve the peak and dB/dt with its higher frequency content does better.

To define a proxy that adequately describes low-frequency driving while using modern 1 second cadence B-field data, a frequency weighted proxy akin to E-field for a homogeneous Earth will be much more effective[86,87]. In the frequency domain, the two components (directional projections) of the GIC proxy would be,

$$GIC_{x,y}(f) \quad \propto \quad \pm\frac{1}{\sqrt{f}}Bdot_{y,x}(f), \tag{42}$$

where $Bdot$ refers to dB/dt, and orthogonality between driving and induced components is explicitly defined.

In calculating the proxy, either the B-field or dB/dt can be used, the only difference being the factor $2\pi if$ that relates the two quantities in the frequency domain. Of the two, dB/dt does benefit from being centred about zero and no baseline subtraction is needed when applying the FFT. After applying the frequency weighting in frequency domain, taking the IFFT of each component results in a time domain proxy. In Figure 43, the GIC_x proxy related to the FRD B_y component is shown for the north-south effective node at PAR (GIC axis inverted due to network parameter polarity). In all subfigures, the 5 sigma level as defined during quiet time is indicated with horizontal dashed lines. Any proxy used should aim to characterise signals clearly when above this level. In contrast to dB/dt as a proxy, $GIC_{x,y}$ effectively takes into account the low-pass effect needed to reproduce measured GIC across all frequencies, adhering to where GIC power sits independent of sampling rate. Although $GIC_{x,y}$ looks very similar to the derivation of the E-field for a homogeneous Earth it should be stressed that $GIC_{x,y}$ is not accurately scaled to realistic value in ampere. Standardising the proxy with no further scaling means the proxy is comparable for different events and stations. A normalised version of this approach defined by Marshall et al.[87] has been calibrated to instances of known GIC effects and has been used to estimate levels of GIC risk in multiple networks around the world[87,88,201].

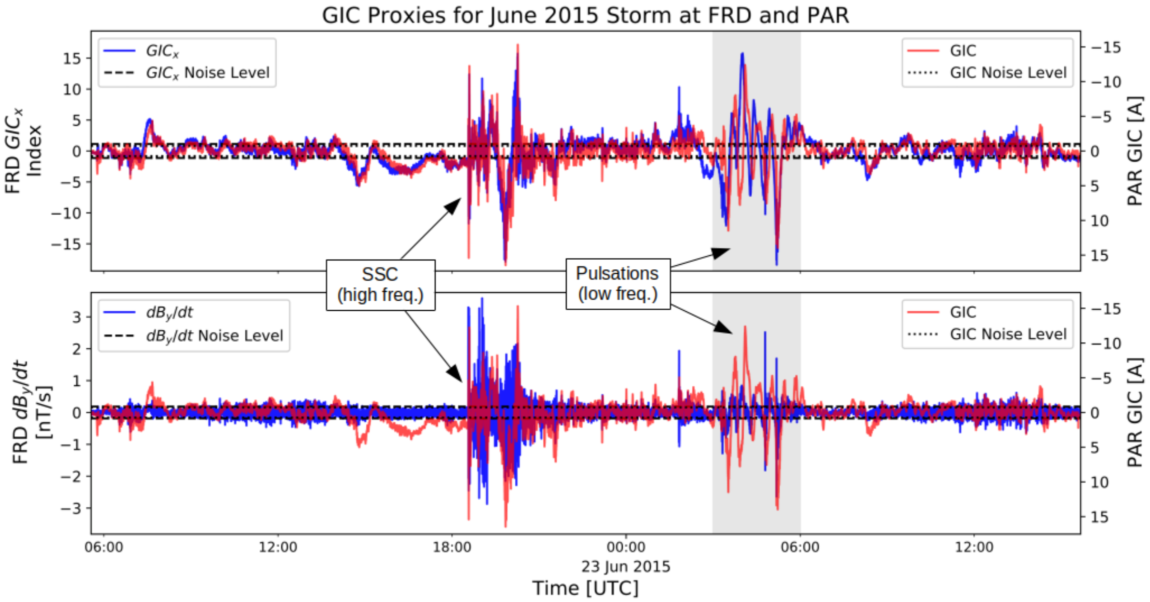

Figure 43: Taking into account the correct frequency weighting in a proxy allows for accurate representation of both low- and high-frequency driving. Using only dB/dt, as is the case in bottom panel, does not accurately capture GIC activity at low frequencies although it does replicate the higher frequency driving periods such as SSC[194].

5.3 Ensemble Methodology in the Time and Frequency Domains

As described in previous sections, modern modelling of GICs has become increasingly sophisticated and detailed, particularly in the geophysical step. The state of the art in this case is full 3D representation of the Earth's conductivity for E-field estimation. Such modelling requires extensive pre-existing magnetotelluric (MT) surveys. Although full 3D modelling is the ideal, many utilities around the world do not have access to such levels of geophysical data. Then there is the engineering step to consider. Modelling approaches of this step have seen little change since some of the initial research into modelling GICs in power networks. Although transformer-level modelling is possible with adequate network information[17], almost all network modelling assumes a purely resistive network[38,96], leaving aspects of the engineering step either unmodelled or uncertain. Examples of this is a lack of inductive or quasi-ac responses, and variable grounding resistances due to groundwater or rainfall. All these aspects lead to uncertainty that is not modelled given analytical network analysis.

An alternative to physics-based models coupled with analytical network modelling is the use of empirical approaches, and is what is this section aims to develop. The nature of empirical or measured data means that complicated or unmodelled dynamics are implicitly included along with uncertainty and often modelled more accurately. A shortcoming often brought up with these methods is that they are only valid for the measurement sites used, and while the system is in a similar state to when the measurements were made. For network-wide analysis, using solely empirical methods would be an issue. On the other hand empirical methods can calibrate and augment more general analytical methods and provide for important validation of our understanding of the GIC phenomenon. Uncertainty calibration is particularly important given the lack of uncertainty estimation in analytical methods when dealing with real-world scenarios. The empirical approaches developed aim further to address operational considerations of utilities with no access to high-fidelity geophysical and network data. In such cases empirical methods applied with low-cost GIC monitoring may offer an attractive solution.

Using empirical approaches, we do not need to derive new or more complex governing equations. Rather we can leverage the simplistic baseline GIC models already developed (proven to be effective approximations) to represent more complicated dynamics. In order to make full use of the empirical relations, we assume that the many observations are measured states of the system, and an ensemble or distribution is formed by the empirical relation. We will refer to this approach in this work as ensemble estimation of some underlying parameter or component. The spread of the resulting ensemble or distribution of the empirical relation is directly related to the uncertainty in the underlying relation, being driven by factors first shown in Figure 20.

In Figure 20, following from the B-field as measured on the ground, we have the split in traditional modelling into the geophysical and engineering steps. In the geophysical step, 3D modelling of Earth's conductivity is needed to represent inhomogeneities such as the coastal effect. This 3D modelling in itself is empirical, being derived from MT responses using measured local B and E-fields at a site. Not including the effects of inhomogeneities causes larger errors than wrong power network information or inaccurate transmission line mapping using traditional physics-based models[123]. The only larger source of error is from an inaccurate B-field. To bypass this issue, interpolation of the B-field based on Biot-Savart inversion from a sparse set of magnetometers using something like the SECS method is usually done[158,159]. Such interpolation and/or denser magnetometer coverage is particularly important in higher latitude regions where the driving current systems are more variable.

Assuming the B-field and E-field have been adequately defined, the engineering step then relates the E-field to the resulting GIC via an analytical model of the network through some derived network parameters. For the model development in this thesis we will consider GICs at a node only and not throughout the network. GICs at a node would need to take into account the entire network nevertheless, i.e. to accurately define the engineering step there needs to be an integrated geophysical response along the network footprint, modulated by network characteristics. The integrated response is itself non-trivial and a form of averaging[137]. Most research assumes a uniform conservative B- and E-field which is simplistic to say the least, even given the assumption that some level of averaging is done by the network. Applying analytical network parameters to this assumption leads to a very rough first-order approximation. The simplistic assumption can however be tuned very effectively through empirical training with even non-3D conductivity profiles[84,102,151]. These 'tuned' empirical network parameters make up the basis of the first empirical approach of using network parameter ensembles.

Instead of requiring assumptions of the underlying conductivity structure of Earth, an empirical relation between the B-field and measured GIC can be derived. This second empirical approach is often referred to as transfer function (TF) analysis in previous work[98,122,143]. Similar limitations as before apply, with the transfer functions (TFs) being only defined for the magnetometer-node pair and a similar system configuration (no line switching). To explicitly split the engineering and geophysical aspects is challenging given a TF approach as both effects are absorbed into a single relation. Using a single measured E-field to extract the network dependence may be misleading, particularly in a geologically complex environment. Probably the most promising physics-based method similar to transfer function analysis is a hybrid approach[140]. Instead of estimating the E-field, multiple geophysical MT responses are integrated along the various lines into averaged frequency domain responses. This means that the B-field can be used to drive the GICs via traditional analytical network modelling, similar to empirical transfer function analysis. The hybrid approach assumes the engineering step is properly defined and modelled, so splitting network and geophysical aspects remains difficult. Uncertainty arising from errors and unmodelled network factors still needs to be taken into account.

5.3.1 Ensemble Estimation of Network Parameters

Focussing on the first approach of network parameters, the GIC at a network node can be modelled by the governing GIC equation previously defined by (35),

$$GIC(t) = aE_x(t) + bE_y(t).$$

Revisiting theory presented earlier, the network parameters can be thought of as scaling factors that penalise non-alignment of the E-field vector with the effective network. The preferred direction for the E-field to produce large GICs can be found through the network parameters. Assuming the E-field is projected onto an effective network scaling vector, we have the total effective network scaling $\sqrt{a^2 + b^2}$ (relating to resistances) and the effective network direction $\theta = \arctan(\frac{a}{b})$ (relating to the network topology, and in this case takes east as 0°)[58,101]. This means that all else being equal, the largest GIC will be induced when the geoelectric field aligns with θ. Any deviation from θ would result in a fraction of the total E-field magnitude contributing to the measured GIC. A similar representation of the directionality is the ratio of network parameters $c = b/a$, used in previous work[102,104,105]. Although we expect the preferred direction of the E-field to reflect the direction of the transmission lines immediately around the substation, the entire network has influence and complex grounding may result in non-trivial responses. In the case that some geophysical strike is present that alters the typical direction of the induced E-field for a given B-field disturbance, then this discrepancy changes the total effective scaling. When the network parameters are empirically derived, the mapping between GIC and E-field will be consistent but rather pick-out a directional sensitivity not quite aligned with the physical network and scale the magnitude accordingly. If the strike direction varies with depth, the mapping is no longer static and can have multiple directional components, each with their own scaling and frequency dependent. More common analysis is done through analytical full network modelling, with the general directionality sensitivity of the network derived[58,81,99,101].

Estimation of the network parameters can be done analytically, using a model of the power system, or empirically, using only data. From simultaneous GIC and $E_{x,y}$ data, an estimate of the network parameters can be derived[102,105,106,145]. It is assumed that these network parameters are constant for the duration of a geomagnetic event, only changing with major alterations of power network infrastructure or operations[149]. Although in theory network parameters can be estimated to a high precision, it does require extensive knowledge of the network along with the exact state of the network. This has been done even to a transformer level[17], but such a level of knowledge is rare. Along with the non-linear nature of the network response, the result is that analytical network parameters are often inaccurate and need further tweaking to replicate measured GICs. Empirical network parameters on the other hand do much better and can absorb more complex effects – albeit without the explicit nature of those effects made evident. In contrast to the assumption of unchanging parameters, it has been observed that different empirical values of a and b may be derived for a variety of different conditions including the specific GIC magnitude threshold used[105,106] and conductivity/network modelling[106]. This suggests that a number of errors from different drivers in the modelling chain are absorbed into these parameters, with different regimes apparent. As a result, the variation in the network parameters should be taken into account when modelling GICs. A shortcoming when using empirical methods is that normally a significant amount of data is needed, which is often not available.

In this work, we will borrow notation from Wik et al.[105], where α and β represent the empirically derived individual network parameters. For ease of reading, the notation will default to a and b when both empirical and traditional network parameters are referred to. Furthermore, we will define the collective ensemble of empirically derived parameter estimates to be $\boldsymbol{\alpha}$ and $\boldsymbol{\beta}$ respectively. Each individual estimate in the ensemble is not defined as the true state of the system, but simply a possible state as calculated by solving simultaneous equations. On the other hand, taking all the ensemble estimates together would reveal the most probable state. Although α and β give improved modelling, $\boldsymbol{\alpha}$ and $\boldsymbol{\beta}$ allow for further analysis, characterisation and error propagation. These concepts can be extended further and applied in a completely empirical method, using a transfer function (TF) from measured B-field data to GIC estimation, sidestepping any need for conductivity assumptions.

Previous empirical estimation of the network parameters has generally included a fit of sorts that results in a single estimate. One approach is to use a least squares routine and fit (35) to the data[102,105]. An alternate approach is to select near-zero crossings of the E-field for a single E-field component and solve (35). This would generate a number of single parameter estimates at these specific time instances. A linear fit is then used to find the best parameter while excluding outliers[106]. If a single parameter is known, the empirical ratio of network parameters can be used to find the other parameter in the parameter pair[104]. These methods are good predictors for the network parameters but do not give an indication of the variation in the parameters or allow for further analysis, which can be achieved using ensemble estimation.

In order to create an ensemble of the network parameters, the linear nature of (35) is exploited. This governing equation assumes that the GIC measurements and the derived $E_{x,y}$ values are perfect. A further assumption is that network doesn't change appreciably over the time series considered. This is not entirely accurate, since errors in the measured GIC and the derived E-field are present. Assuming a and b are constant, a more accurate relationship would be,

$$GIC(t) + GIC(t)_{err} = a\big(E_x(t) + E_x(t)_{err}\big) + b\big(E_y(t) + E_y(t)_{err}\big), \tag{43}$$

where X_{err} indicates the error made in the measurement or estimation of a relevant parameter X. This form of (35) shows explicitly that, due to the errors in $E_{x,y}$, a and b are not independent of induced E-field, and as can be seen later therefore not independent of GIC magnitude. Nevertheless, assuming a relationship between GIC and the E-field of the form of (35) allows for the estimation of network parameters. In order to acknowledge the presence of inaccuracy in measurements, the notation of the governing equation is changed to,

$$\Gamma(t) \approx \alpha E_x(t) + \beta E_y(t), \tag{44}$$

with $\Gamma(t) \equiv GIC(t) + GIC(t)_{err}$ (or the GIC as measured), $\alpha \equiv a(1 + E_x(t)_{err}/E_x)$ and $\beta \equiv b(1 + E_y(t)_{err}/E_y)$. α and β are the network parameter estimates in the updated equation, being empirically derived from measured data. These estimates include the associated error from the E-field, GIC measurements, as well as the traditional definition of the network parameters.

Taking this updated version of the GIC equation, let us think of the network parameters as free variables (not constants) and the E_x and E_y components to be coefficients of these variables. This is exactly the opposite of the common interpretation. The assumption that the network parameters (a and b) are constant over a certain time period (say $t_1, ..., t_n$) allows us to solve for α and β simultaneously given two time instances (say t_i and t_j, where $i \neq j$ and $i, j \in 1, ..., n$). Using any more than two comparable time instances would result in an overdetermined system.

$$\begin{array}{rrcl}
t_1: & \Gamma(t_1) & = & \alpha_1 E_x(t_1) + \beta_1 E_y(t_1) \\
 & & \cdots & \\
t_i: & \Gamma(t_i) & = & \alpha_i E_x(t_i) + \beta_i E_y(t_i) \\
 & & \cdots & \\
t_j: & \Gamma(t_j) & = & \alpha_j E_x(t_j) + \beta_j E_y(t_j) \\
 & & \cdots & \\
t_n: & \Gamma(t_n) & = & \alpha_n E_x(t_n) + \beta_n E_y(t_n)
\end{array}$$

Repeated calculation of α and β for a number of (i, j) pairs creates an ensemble of network parameters $\boldsymbol{\alpha}$ and $\boldsymbol{\beta}$. The result would no longer be a single estimate of the parameters, but a collection of different parameter pairs that satisfy the system for different pairs of time instances. In using simultaneous equations to solve for the network parameters, we implicitly assume that the network parameters are constant across the pair of time instances. Saying that the estimation method allows for variation in network parameters may seem a contradiction in this case, but it must be emphasised that the assumption of constant parameters is only needed for each individual pair. Sampling all possible combinations would in turn sample the network parameter space possible given the governing GIC equation. The resulting statistical network parameter distribution can in turn give an idea of the validity of the governing GIC equation. If the network parameters are indeed roughly constant, then there should be a peaked distribution with some spread given deviations from the assumption. If the governing equation does not hold and the network parameters as defined are not constant, then we would expect a resulting distribution close to a uniform random distribution with no peak evident.

To illustrate the method, we will derive network parameter responses using a synthetic dataset. To generate a realistic dataset, 4,500 GIC data points or time instances are sampled from a normal distribution with a scale of 10 A. Assuming 2 second cadence data, this would equate to 2.5 hours or assuming 1 minute cadence data this would be roughly 3 days worth of data. Similarly, we generate a realistic random E-field in a single component, e.g. E_y, sampling from a normal distribution with a scale of 50 mV/km. Specifying constant network parameters $a = 100$ and $b = 50$, we then can derive the corresponding E_x component, i.e. $E_x = (GIC - bE_y)/a$. The datasets as is are defined perfectly, but to introduce some real-world dynamics additional Gaussian noise is added to each. Specifically, the GIC dataset includes noise with a standard deviation of 1 A, and the E-field components include noise with a standard deviation of 5 mV/km. Of course the assumption random independent samples and only Gaussian or measurement noise is simplistic, but it does give an idea of the ensemble methodology given variation. The resulting network parameter ensembles are shown in Figure 44.

Normalising the ensembles in Figure 44 creates a probability density function, with the peak being the most probable estimate of the network parameters as related to the traditional interpretation of network parameters. Interestingly, the ensembles are heavy tailed and the inherently robust median is the best measure of central tendency – and the appropriate estimate to satisfy the traditional modelling formulation. In other network parameter fits[84,98,103], the distribution of network parameters is not assumed to be heavy tailed and the mean is often used. For the synthetic test case presented, these mean-based models would be particularly well suited as the only variation is based on a normal distribution. The mean is however susceptible to outliers and would not be a robust estimate for any non-normal, non-stationary or heavy-tailed distributions as is likely in real-world scenarios. As

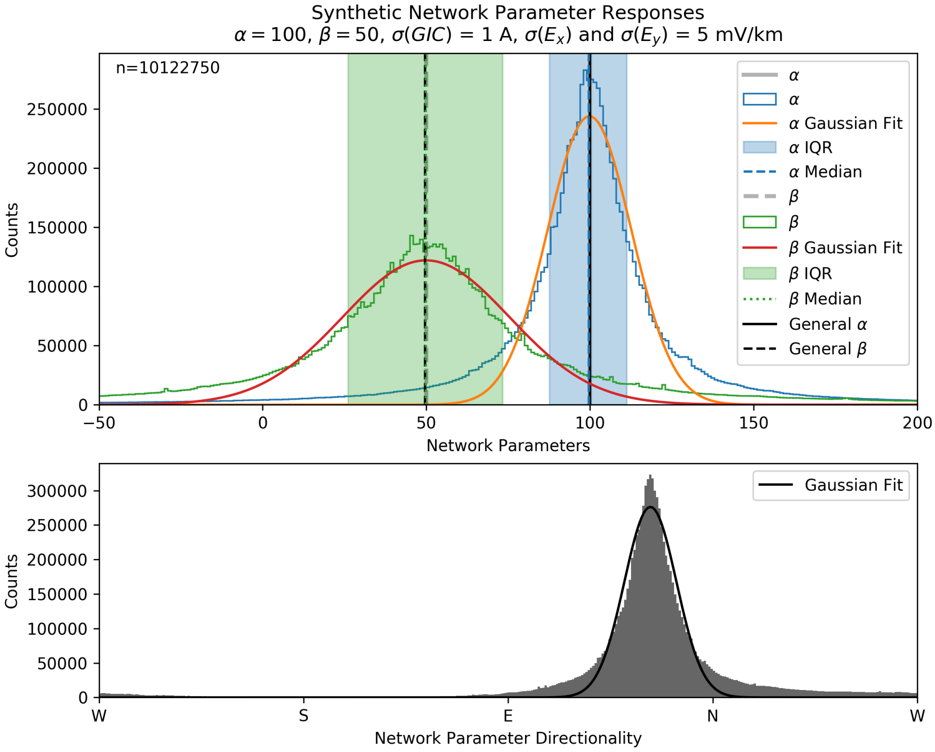

Figure 44: Using a perfect synthetic dataset with Gaussian noise and constant network parameters, the performance of the ensemble methodology can be tested. The source of the Gaussian noise is an illustrative proxy for errors in B-field, E-field and/or GIC measurement or estimation. In the top panel, the network parameter ensembles are shown as histograms with their median and interquartile ranges. For comparison, the constant network parameters are shown as grey lines and the least-squares mean estimation[103] of the network parameters are shown as black lines. The lower panel defines the network parameter directionality, i.e. $\arctan(\alpha/\beta)$. For all profiles a Gaussian fit is included for comparison.

verified by the synthetic example, the median and ensemble methodology correctly reproduces the mean estimate.

The real benefit from the ensemble methodology is that the resulting ensemble includes uncertainty, such as from the associated error from the E-field derivation and measurement. The uncertainty in the estimated network parameter is linked to the spread in the ensemble. To estimate the spread while requiring a robust measure, the inter-quartile range is used. In comparison to the least-squares of mean approach employed under the assumption of normally distributed variation and constant network parameters, the ensemble methodology can produce uncertainty estimation much more efficiently. Typical empirical network parameter estimation using a least-squares approach results in a single estimate with no handle on uncertainty[103]. The only other approach employed is through boot-strapping multiple subsets of data and computing the expected network parameters for each[98]. Practically, this requires long datasets (up to a month long) and produces a limited set of estimates ($n = 30$), whereas the ensemble methodology can achieve the same with only hours of data. Besides long GIC datasets being scarce and biased to quiet geomagnetic conditions, an additional consideration is that over long periods there is no guarantee that the network is unchanged and that the various processes are stationary. The breakdown of these assumptions would result in non-Gaussian variation and stability of the least-squares approach cannot be ensured.

To expand on the limited data needed for the ensemble method, if we assume n points that are all relevant and comparable, then the ensemble obtained would have $n(n-1)/2 \approx n^2/2$ (for large n) pairs of network parameters. Initially, we assume ‘comparable’ to only relate in terms of network stability, but there may be other considerations such as variations in driving E-field changing with storm phase and intensity. To the author’s knowledge there were no network changes during the periods covered in this work. In the case of multiple storms being available, ensemble estimation is done separately for each event and merged for the final ensemble.

Diving into some aspects of the ensemble spread, network parameters (not assumed to be constant in ensemble estimation) can be thought of as simple scaling factors given an input E-field. The most common error in terms of E-field derivations is that of magnitude, especially in geologically simple cases where 1D layered-Earth approximations can apply. Given empirical estimates of the network parameters this error in magnitude can easily be absorbed. For comparisons between two ensembles from E-fields derived from different conductivity profiles, the magnitudes need to be normalised. In the case of a simple 2D structure, such as a strike or coastal effect, the E-field may have further error in terms of direction. As the empirical network parameters do not explicitly take into account network topology and are estimated independently, they are still able to absorb error in an input E-field that does not take into account the 2D structure. Cases where this is very obvious is when the resulting directionality in the total ensemble is different from the local network topology.

To visualize the absorption of geophysical aspects or errors in empirical network parameters, let us assume a 1D E-field compared to a real-world 2D E-field where there is some defined strike (arbitrarily aligned with respect to the network). When rotating an input unit B-field, the 1D E-field vector would plot out a circle. In comparison, the 2D E-field with geophysical strike and the same B-field would plot out an ellipse, semi-major axis perpendicular to the strike[65] (see Figure 45). As was seen in Figure 35, real-world conductivities may have even more complicated E-field responses. In the case of a geophysical strike being present, the projection of the larger magnitude true 2D E-field onto a line may drive larger GICs than an E-field aligned with the transmission line. Empirical training of the network parameters using a 1D E-field assumption picks up this discrepancy and links the largest GICs with the real-world 2D defined semi-major axis direction. Without empirical training and only looking at the line directions and 1D Earth model, a network parameter directionality aligned with the local line direction would have been the result instead. Besides directionality, the network parameters need to absorb the additional magnitude scaling (larger in semi-major axis, smaller in semi-minor axis) from geophysical aspects away from a 1D assumption and the spread of the network parameter ensembles would widen.

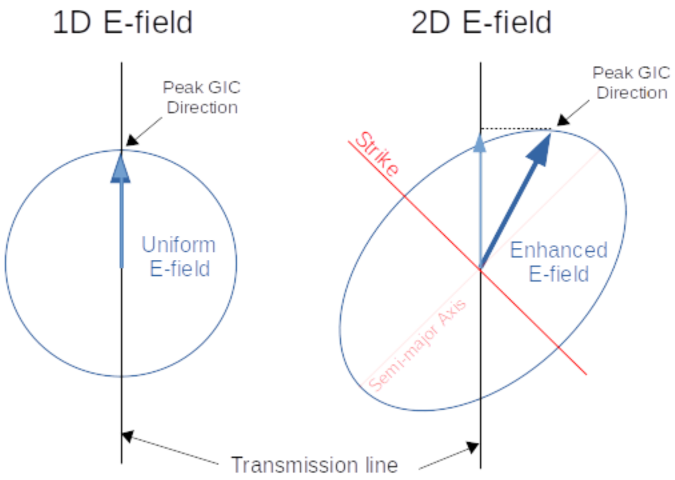

Figure 45: In the presence of geophysical strike, the 2D conductivity interface creates an enhanced E-field. Rotating a driving uniform B-field creates an elliptical E-field response in the case of a 2D conductivity profile, compared to a uniform circular E-field in case of a 1D conductivity profile. When a transmission line is present, the projected E-field not only has a different magnitude but there will be a different E-field direction associated with the maximum GICs. Empirical network parameters would encode this direction and not just represent the network topology.

Since the empirical network parameters can dynamically scale the E-field according to measured GIC, they may vary through the phases of a storm where the E-field and GIC magnitude vary as well. The variation of network parameters given different driving regimes is similar to different conductivity profile assumptions producing different E-fields, which require separate network parameter scaling. During quiet periods where both the E-field and GIC are dominated by instrument noise the derived empirical network parameters are expected to mimic the noise and have low amplitudes and centred around zero. As the storm period increases in intensity, then so must the network parameters in order to match the scaling. A further consideration is that during different phases of a geomagnetic storm, different frequency components may dominate. An example is seen at SSC, where broadband driving typically includes the largest GIC, compared to main or recovery phases, where discrete frequency pulsation intervals drive intermediate GIC magnitudes. Dynamically allowing for the network parameters to be estimated using these different intervals may result in different scaling. The driving frequencies in the respective intervals are associated with frequencies in the E-field derivation, which may be wrong and are corrected for through the dynamic network parameters. This is true for both magnitude and directionality as a strike may be depth, and hence frequency, dependent. Breaking the ensembles into sub-ensembles may reveal this higher resolution quasi-frequency scaling possibly associated with geophysical conditions.

In addition, any time lags between the measured GIC and estimated E-field would need to be corrected for in order to minimize spread when assuming a resistive network. This issue is seen in the higher cadence data (< 1 minute), where delays in the datasets are seen either due to measurement error, conductivity assumptions or possible network effects. Assuming the delays have been corrected for and that network parameters are still constant, the traditional GIC nodal (35) can be updated to a difference (or delta) version,

$$\begin{aligned} GIC(t_n) - GIC(t_{n-1}) &= a\big(E_x(t_n) - E_x(t_{n-1})\big) + b\big(E_y(t_n) - E_y(t_{n-1})\big) \\ \text{or } \Delta GIC &= a\Delta E_x + b\Delta E_y. \end{aligned} \tag{45}$$

The delta version of the GIC equation can be trained in a similar way, with the network parameters having the same magnitude in theory. In the case of any timing delays between datasets, the delta approach would not be consistent with the ensemble estimation approach already presented. If there is confidence that no delays exist, such as is likely with 1 minute cadence data where timing delays of the order of seconds are averaged out, then the delta approach can augment modelling. Since more than enough estimates are created through ensemble application of (35), the delta version is not used further in this work. In higher cadence data, the delta assumption breaks down when the time lag cannot be perfectly corrected for and measured datasets are not concurrent. In the ensemble approach, these shortcomings are seen as additional spread in the ensembles and do not effect the end result. A last consideration in terms of datasets linked to cadence is that resampling to another cadence influences the network parameters, with smoothing from downsampling reducing the peak values of the GIC and E-field. If the E-field and GIC spectral responses do not match, empirically estimated network parameters for the down-sampled datasets may differ when compared to the full dataset.

5.3.2 Ensemble Estimation of Transfer Functions

Instead of requiring an estimate of the E-field, it is possible to directly relate the B-field to GIC via an empirical transfer function (TF). In this approach, the ground conductivity assumption used to derive the E-field is bypassed – reducing a possible source of error. Further, the derived TF is the net effective transform of the Earth over the entire network area and includes any power network response. In the past, the B-field-to-GIC TF approach has been followed more from a traditional MT background and there have been no attempts to decompose the network filtering[143]. Although TF results have shown good correspondence with known geophysical features, there are cases where such interpretations failed[122] – likely due to the inclusion of the network reducing the sensitivity in a GIC based TF. An example is that a north-south network would no be able to resolve the east-west TF component or the analogous east-west E-field. To account for the network effects, we update (35) with $c = \beta/\alpha$. The matrix form of this equation becomes,

$$\begin{aligned}\Gamma(t) &= \alpha E_x(t) + \alpha c E_y(t)\\ &= \begin{bmatrix} \alpha & \alpha c \end{bmatrix} \begin{bmatrix} E_x(t) \\ E_y(t) \end{bmatrix}. \end{aligned} \tag{46}$$

Moving over to the frequency domain, measured B-field data can be related directly to measured GIC data. The assumed conductivity related impedance tensor, and the uncertainty that goes with it, is absorbed with the network parameter scaling into frequency dependent components of the TF,

$$\begin{aligned}\Gamma(\omega) &= \begin{bmatrix} \alpha & \alpha c \end{bmatrix} \begin{bmatrix} E_x(\omega) \\ E_y(\omega) \end{bmatrix}\\ &= \begin{bmatrix} \alpha & \alpha c \end{bmatrix} \begin{bmatrix} Z_{xx}(\omega) & Z_{xy}(\omega) \\ Z_{yx}(\omega) & Z_{yy}(\omega) \end{bmatrix} \begin{bmatrix} B_x(\omega) \\ B_y(\omega) \end{bmatrix}\\ \\ &= \begin{bmatrix} \alpha\big(Z_{xx}(\omega) + cZ_{yx}(\omega)\big) \\ \alpha\big(Z_{xy}(\omega) + cZ_{yy}(\omega)\big) \end{bmatrix}^T \begin{bmatrix} B_x(\omega) \\ B_y(\omega) \end{bmatrix}\\ &= \begin{bmatrix} T_x(\omega) & T_y(\omega) \end{bmatrix} \begin{bmatrix} B_x(\omega) \\ B_y(\omega) \end{bmatrix} \qquad (47)\\ &= \mathbf{TF}_{B_x}(\omega) + \mathbf{TF}_{B_y}(\omega). \qquad (48)\end{aligned}$$

In the formalism above, $T_{x,y}(\omega)$ in (47) are the components of the B-field-to-GIC TF. $\mathbf{TF}_{B_x,B_y}(\omega)$ in (48) are not TF components, but rather the result of multiplying $T_{x,y}(\omega)$ with their associated B-field components. Recent work by Kelbert and Lucas[140] has similarly defined TFs based on traditional MT surface impedances for each node in a network that can then be driven using B-field measurements to derive the nodal E-field. This alternative to computing a general E-field that then has to be integrated is an improvement in the computational efficiency of GIC modelling. The approach here effectively does the same integration of the conductivity structure over the network through empirical modelling, but includes the network response. To aid in identifying effective contributions of the surface impedance tensor Z in the TF, the geometric scaling c is split from the network parameters. The final TF absorbs all network scaling introduced by α (which cannot be separated) and can be directionally limited given certain effective network topologies (when c or $c^{-1} \approx 0$). In such cases, the c can severely affect the SNR of the less dominant component.

In a resistive network, α is assumed to be constant. Recent work has probed this assumption, suggesting rather that a frequency dependent α may perform better in modelling[98]. The TF estimation as defined above can be extended to independently estimate such frequency dependent network parameters. To do so, an E-field input is required instead of a B-field, and the TF_x and TF_y components would relate to $\alpha(\omega)$ and $\beta(\omega)$. Due to the similarity in estimation, the frequency dependent network parameters are referred to as E-field-to-GIC TFs when used in this work.

Propagating frequency domain uncertainty into the time domain reconstruction is not trivial. The frequency specific uncertainty bounds can occur in any combination, constructively or destructively. To obtain an uncertainty estimate in the time domain, the time domain ensemble method previously used for the network parameters is reintroduced. Allowing similar parameter ensembles to be estimated for analogous time domain TF components (instead of the E-field components), time domain scaling and uncertainty bounds can be generated. To do this, we take the IFFT of the TF result $\mathbf{TF}_{B_x,B_y}(\omega)$ in (48) to obtain time domain TF components (denoted by TF*),

$$\Gamma(t) = g\mathbf{TF}^*_{B_x}(t) + h\mathbf{TF}^*_{B_y}(t). \tag{49}$$

The g and h parameters from (49) generate an uncertainty spread and improve modelling by tuning TF* or the analogous ‘network effective E-field’ in the time domain. In comparison with network parameters that include network scaling, the g and h parameters ensembles are expected to be centred roughly around 1 (all network scaling is already encoded in the TF). Any significant deviation from unity scaling suggests the TF does not adequately map the B-field to GIC, such as when the separation between magnetometer and substation is too great. In contrast to the traditional network parameter approach presented that requires additional integration of the E-field, the TFs are fully 3D and conductivity is not expected to drive scaling issues, besides in the case of a low SNR. When further scaling is needed, the TF parameter ensembles can further improve modelling. The spread of these g and h parameter ensembles further allow for accurate uncertainty estimation in the time domain, and not the frequency domain where the TF and TF uncertainty are defined.

Practically, input datasets were mean-subtracted for the current work. TFs were estimated using rectangular windows of at least 6 hours, which were then padded. To be representative, a 6 hour window is about the limit where low-frequency (up to 0.1 mHz) geomagnetic disturbance signals are still captured and longer windows should ideally be used. Windows were defined by a shift to create multiple datasets and apply the ensemble methodology. Various initial testing suggested that the procedure is relatively insensitive to exact parameters regarding window length or window function as the same procedure applied to input datasets should result in similar mapping. A rectangular window was used to provide simple normalisation and accurate visualisation of the TF components. Once the raw TF has been estimated, there is further processing done in terms of spectral averaging, seen in Figure 46. In the vein of MT analysis, it is ideal that there be at least 4 samples per frequency for estimation purposes, i.e. $f_{max} = f_n/2$, where f_n is the Nyquist frequency. Furthermore, from an MT perspective it is assumed that TFs vary smoothly with frequency and that neighbouring frequencies predict similar results[65]. A direct result of this is that spectral averaging or weighted stacking can be done to clean the resulting spectrum, with a rule of thumb that at least 6-10 frequencies be used per decade on a logarithmic scale, or in this case using a factor of 1.1 between evaluation frequencies. The factor of 1.1 scaling is better for modelling and stable but is a higher resolution than that often used for MT studies. The use of evaluation frequencies equally spaced on a logarithmic scale means that relative error related to penetration depth is similar. On a linear scale, the relative error between different evaluation frequencies will relate to different penetration depths. For visualisation purposes in Figure 46, spectral averaging is done using a Parzen window as defined by Simpson and Bahr[65]. Similar to a higher resolution being required to represent TF variation in the components, it was also found that spectral averaging worsened modelling performance due to additional smoothing between frequencies introduced by the Parzen window. Instead for modelling purposes components were estimated through log-binning according to the 1.1 factor and estimating the median value per bin.

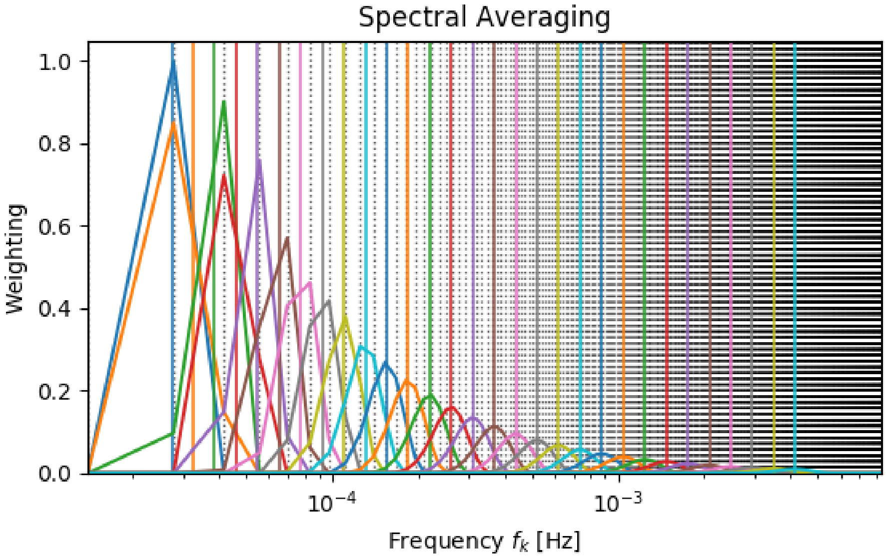

Figure 46: The spectral weighting/averaging is shown here as applied for TF estimation at a node with 1 minute cadence data. Dotted lines refer to the output frequencies from the FFT to be applied on the window, coloured lines indicate the evaluation frequencies and the coloured profiles indicate the Parzen window weighting of each FFT frequency associated with the corresponding evaluation frequency having the same colour.

Before any binning, all TF component ensembles are estimated from solving sets of linear equations arising from (47), explicitly defined by,

$$\Gamma = T_x Bx - \tilde{T_x}\tilde{B_x} + T_y B_y - \tilde{T_y}\tilde{B_y} \tag{50}$$

for the real parts, and

$$\tilde{\Gamma} = T_x \tilde{Bx} + \tilde{T_x} B_x + T_y \tilde{B_y} + \tilde{T_y} B_y \tag{51}$$

for the imaginary parts. Here $\tilde{X}$ refers to the imaginary part of the input variable X. For an input dataset, the two sets of relations in the real and imaginary domains allow for additional simultaneous equations to constrain the 4 unknown TF components. Each TF component estimate is weighted according to the spectral averaging procedure before being binned into the TF ensembles. Similar to the network parameter ensembles, and to ensure robust estimation of TF components, the central tendency is estimated by the spectrally weighted median and spread by the spectrally weighted interquartile range. In the case of the magnitude and phase shown later in Figures 57-59,71-72 and 74 later, both magnitude and phase are calculated for each estimate and weighted appropriately before being binned. The magnitude once again relies on the weighted median and inter-quartile range, whereas the phase makes use of circular mean and circular dispersion estimates[202].

When the TF has to be used for GIC modelling, the result has to be convolved with an input B-field in the frequency domain and the inverse FFT taken. To do this, the data has to be linearly spaced in the frequency domain. Interestingly, the best responses in modelling using the B-field came through higher resolution TFs and not interpolation of the spectrally averaged response. To increase efficiency with the larger number of frequencies to be processed, the raw TF was not spectrally averaged using a Parzen window but rather split into logarithmic bins with a factor of 1.1 between consecutive frequencies. The median for each bin was estimated as before. In testing, having a higher resolution of around 24 estimates per decade improves on the modelling and suggests that there is variation at higher resolution that is important for GIC modelling given network integration over the network footprint, possibly overlooked in local MT response estimation.

An alternative to estimating the TF by using the B-field is to use its time derivative, which is analytically defined in the FFT. Assuming $FFT\{B(t)\} = B(f)$, then $FFT\{dB(t)/dt\} = 2\pi i f B(f)$. The simple mapping allows the dB/dt to be used instead of the B-field as the input data for estimating the TF already described, or alternatively a new TF that solely maps dB/dt to GIC. A technicality in implementation is that the frequency argument for link between discrete dB/dt and B needs to be scaled by the sampling frequency, i.e. $FFT\{dB(t)/dt\} = 2\pi i(f/f_s)B(f)$. For consistency and comparison with other implementations, this work keeps the definition of the TF being defined from B-field to GIC. The use of dB/dt has some inherent advantages. Probably the most obvious and simplest is that there is no need for mean subtraction or baseline removal, which can be complex given the B-field. The resulting dB/dt input links well to GIC data, which also has a mean of zero. dB/dt is also better defined at higher frequencies, with a better SNR evident in comparison to the B-field. The coherence between the B-field and dB/dt is virtually exact, with slight differences at the very low frequencies, possibly due to baseline removal in the B-field being rudimentary. This means that no information is lost given the use of dB/dt.

A further general benefit of using a TF is the estimation of time lags, often not seen in autocorrelation analysis in the time domain. Simply put, if there is a constant slope in log space of the phase response of the TF, the most likely cause is a constant shift or lag in the time domain. If there is any inductive time constant or lag in data acquisition systems, it should be absorbed in this lag. After estimating the lag, t_{lag}, in the phase response through a linear fit of the slope for frequencies higher than 1.5 mHz, the input dataset can be shifted in the frequency domain through,

$$X_{shift}(f) = e^{(2\pi i f t_{lag})}X(f). \tag{52}$$

5.4 Summary

In summary, this chapter first validated the theoretical background regarding frequency response of GICs and then used the theoretical basis and operational modelling framework previously presented to develop a novel empirical ensemble methodology. The resulting ensemble methodology is defined in both the time and frequency domains and can be driven by limited data. In the time domain, traditionally defined network parameters were leveraged to create network parameter ensembles that can include uncertainty. In the frequency domain, MT inspired transfer functions were derived in a similar way, with uncertainty being estimated in the time domain subsequently analogous to ensemble estimation of the network parameter ensembles.

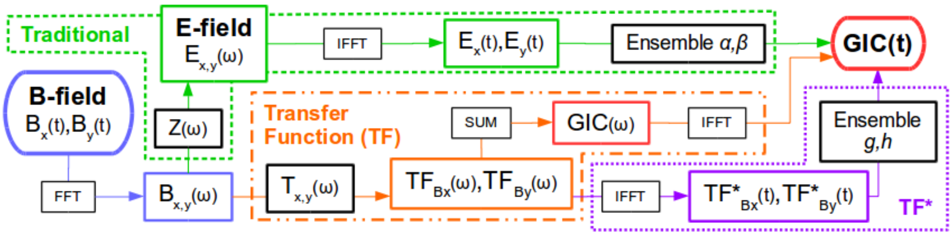

Figure 47: Summary of the different modelling approaches relevant to the ensemble methodology, ultimately linking a measured B-field to measured GIC[191].

Using Figure 47 to recap the modelling approaches, let us initially start with some measured or interpolated B-field. From here, the frequency domain representation of B-field is computed via

Fourier transform. In the frequency domain, the modelling approach splits into either estimating an E-field or a direct transfer function to map the B-field to measured GIC. In the first case, we follow traditional GIC modelling, with a surface impedance being used to derive the E-field. Continuing with this path, the E-field is then mapped back to the time domain and the result linked to measured GIC through network parameters. Here a novel approach of empirically derived network parameter ensembles is employed to include accurate mapping and uncertainty. Backtracking to the second option of the TF approach, either the TF components relating to the different B-field components are used to compute a resulting GIC estimate in the frequency domain alone (which can then be mapped back to the time domain), or the TF components can be individually mapped back to the time domain. When the latter option is applied, the resulting time domain TF* components can once again be mapped to measured GIC via parameter ensembles. These analogous ensembles would not provide any additional network information, but the spread can quantify the error in the approach, which is need for operational modelling.

In the frequency response analysis it was found that at least 98% of the GIC signal's energy is below 50 mHz, as defined using baseline of 2 second cadence and 3 hour windowing for the 100% level. In comparison, the often used 1 minute cadence data (16 mHz) includes between 90% and 95% of the GIC energy. Limiting the bandwidth of the GIC to below 50 mHz introduces an underestimation of the peak GIC, with varying degrees of underestimation given different conditions. In terms of the GIC power spectrum, the relative frequency weighting in the GIC power spectrum is between $1/\sqrt{f}$ and $1/f$, which agrees with the underlying theory.

Of the possible GIC driving sources in the frequency domain, pulsations were identified as coupling particularly well in the frequency domain. Taking the power spectrum slope into account, this coupling is proportional to the period, making low-frequency pulsations significant. Peak dB/dt is not the ultimate proxy for GIC-related damage. Efficient coupling during lower frequency pulsation intervals can occur while dB/dt, as defined by the higher sampling frequency, is moderate. Given larger disparities between modern high sampling rates and possible low-frequency driving, a high sampling rate alone is not satisfactorily representative of pulsation activity in multiple bands. Instead, a frequency weighted proxy that captures the low-pass filter effect of the Earth's conductivity on dB/dt needs to be employed.

6 GIC Modelling Results

In this chapter, the proposed empirical methodology is tested across four different power networks with varying degrees of data fidelity. In addition to the performance of the modelling itself, various characteristics concerning GICs are highlighted in the analysis. Some of these aspects include using different conductivity profiles, different magnetic field measurements, the directionality of the network and general variation in responses.

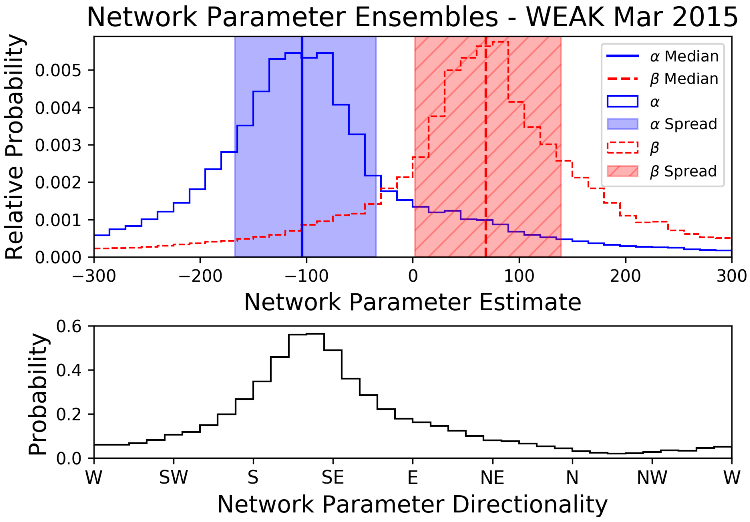

Figure 48: An example of the resulting network parameter ensembles, in this case for the WEAK node in the TVA network[188]. Here the upper panel shows the network parameter ensembles, with median (vertical lines) and inter-quartile range (shaded spread), and the lower panel shows the network parameter directionality as defined by the ratio of network parameters.

To give an idea of the ensemble methodology, taking a synthetic layered-Earth conductivity profile and using remote B-field measurements, operational network parameter ensembles can be seen in the upper panel of Figure 48[188]. The final or most probable estimates that are consistent with traditional nodal modelling are defined by the medians, shown in Figure 48 by vertical lines (α indicated by a solid blue line and β indicated by a dashed red line). Deviations from these assumptions of constant network parameters are quantified by the ensemble spreads. Estimation of TF components similarly use ensemble estimation, with each ensemble defined per frequency.

In the case of comparisons with other conductivity profiles, there would likely be a different E-field response with the network parameters scaling appropriately. To allow the network parameters ensembles of different conductivity profiles to be comparable, the corresponding E-fields should be normalised through a scaling factor, ensuring that the E-field profile shape is not changed, only the magnitudes.

To illustrate normalisation of E-fields for comparison, let us assume two conductivity profiles with associated E-fields, denoted by $E^{\dagger}$ and E^{*}. Let us further assume that the only difference between the two conductivity profiles is a factor of 2, which reproduces itself as a scaling factor of 2 in the E-field magnitudes. Network parameters trained with the different datasets would similarly display a factor 2 difference, with the smaller E-field requiring larger network parameters and visa versa. The apparent spreads are affected in the same way. For analysis of uncertainty drivers, we want to compare ensemble shapes and not be influenced by scaling constants that can be absorbed by the network parameters. To normalise the E-field magnitudes, we estimate the RMS of each component for the different E-field, i.e. $RMS(E_x)$ and $RMS(E_y)$, and take the average, i.e. $E_{RMS} = \left(RMS(E_x) + RMS(E_y)\right)/2$. The result is the average RMS levels for each E-field, $E^{\dagger}_{RMS}$ and E^{*}_{RMS}. Choosing a target E-field, say $E^{\dagger}$, we apply a scaling factor λ to the alternate E-field, $E^{*}_{new} = \lambda E^{*}$, such that $E^{\dagger}_{RMS} = \lambda E^{*}_{RMS}$. In our simple analogy, λ would extract the factor 2 difference and the ensemble spreads can be related, with network parameter magnitudes comparable.

After E-field normalisation there may still be differences in network parameter magnitudes, which requires a further level of normalisation when comparing ensemble spreads. The metric to be used in this case is the ratio of individual network parameter spread (defined by the inter-quartile range or IQR) to absolute network parameter scaling, which takes into account both network parameters,

$$\frac{IQR_{\alpha,\beta}}{\sqrt{\alpha^2+\beta^2}}. \tag{53}$$

Here $IQR_{\alpha,\beta}$ refers to the separate α and β inter-quartile ranges as the metric is calculated for each parameter separately. Qualitatively, the spread ratio (53) would be able to distinguish that a large spread relative to small absolute network parameter scaling ($\sqrt{\alpha^2+\beta^2}$) corresponds to more uncertainty in network parameters than the same spread given large absolute network parameter scaling.

Due to the nature of the ensemble method, large sets of network parameter estimates can be computed with relatively limited input dataset sizes. Although using full datasets increases accuracy in the final parameter estimates, there is an operational downside of excessive computational resources needed, specifically in terms of the memory to store the large ensembles. The method converges relatively quickly, with adequate convergence seen at around $n \approx 4{,}500$ for 2 second data which relates to roughly 10^7 estimates, as shown in analysis by Heyns et al.[194] and seen in Figure 49. To determine the convergence of the method, GIC data from GRS and PAR was used with remote magnetometer measurements at HER and FRD, convolved with a synthetic conductivity profile[193] to produce E-field estimates. The ensemble method was then applied using GIC data of different lengths, randomly sampled. For each resulting ensemble size, 25 model runs produced an average network parameter estimate with some standard deviation, denoted by the error bars. A best-fit of all the runs is further shown, which matches the bulk estimate using all available data (total ensemble sizes of 5 million estimates for GRS and 2.1 billion estimates for PAR). 1 minute data is smoother and converges more quickly with only $n \approx 450$ time instances or roughly 10^5 estimates needed. Both these datasets are of the order of hours and not days in length.

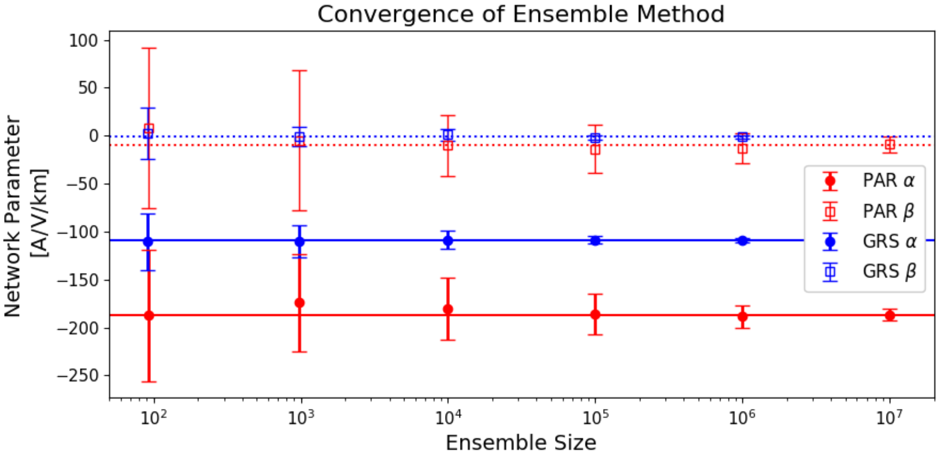

Figure 49: In the case of larger datasets, it is not feasible to use the entire dataset available for training purposes. The ensemble methodology converges suitably quickly for sub-sets to be used instead[191]. Here only the α parameter is shown since it dominates the local north-south PAR and GRS networks.

Looking at the rest of this chapter, for the geomagnetic storm of June 2015 there was a fortunate coincidence that MT sites part of the EarthScope project managed to take B-field recordings in the TVA network where there were concurrent GIC measurements. It is rare to have concurrent B-field, multiple MT sites and measured E-field. Although no previous modelling has been done in the TVA network for comparison, this ideal case is used in Section 6.1 to probe the characteristics of GIC modelling and sensitivity to input parameters using the models developed. More extensive modelling of the TVA network has been done by Heyns et al.[188], leveraging all available GIC data and estimating susceptibility of the various nodes shown in Figure 24. More common is for utilities to have access only to synthetic layered-Earth models such as presented for GRS in Section 6.2. Here extensive empirical modelling has been attempted in the past and comparisons with the current models are possible. Staying in the Eskom network, in Section 6.3 we look at a pathological case of poor data at the MAT node and what would be possible operationally using the methods developed.

For measured E-field, generally there are only single measurements sites. An example of such measurements are those run by Kakioka Magnetic Observatory, Japan Meteorological Agency, with the Memanbetsu (MMB) site having contributed to a large body of GIC research[53,83,84,98,103]. For completeness, an analysis of the MMB node is done using the methods developed here. In addition, nodes from the Powerlink network in Australia are used to look at specific GIC characteristics given previous modelling in the Australian network where there have been some interesting results. Both these cases are covered in Section 6.4.

6.1 An Ideal Case

Recently, large scale MT surveys have resulted in high resolution E-field estimation in the USA[51,55,129–132] and Australia[134]. Although these surveys allow for dense surface impedance estimates, they rely on a remote or interpolated B-field to derive an E-field. Having dense co-located estimates of the B-field and MT responses along with GIC measurements is the highest fidelity data a utility can hope for. For the TVA case, the measured E-field data further confirmed the EarthScope MT responses and gives confidence in the E-field estimates at MT site locations. Aside from the operational aspects, this high-fidelity data also allows various aspects of the ensemble methodology to be stress tested, such as using different conductivity profiles and B-field measurements.

With the measured MT responses and local B-field, variability of the estimates within the geophysical step is still not lost. As described in Section 4.3, there is measured variation in the local B-field and E-field. The deviations away from this single average estimate, although small and possible due to measurement error, would ultimately be absorbed in modelling and need to be described. In the ensemble methodology, the ensemble spreads quantify the uncertainty.

Most utilities do not have access to dense MT surveys with surface impedance estimates. Instead some sort of conductivity profile has to be assumed. In this particular case, we can test the stability of the ensemble network parameters given different conductivity profiles and compare the result with the MT derived E-field, which we can assume is the most accurate available. After normalising the E-field magnitudes to ensure profiles are comparable, we would expect to see a decrease in spread for the more accurate E-field estimation. Similar to the more accurate conductivity profile reducing spread, a more accurate B-field estimate should have a similar result. Again for the TVA network, we can use the measured local B-field as the most accurate estimate and compare with more remote B-field measurements that have shown stability and operationally useful results[191]. Further work has used the remote B-field data and synthetic conductivity profile to analyse the response of TVA network nodes over different events, with the modelling results consistent for similar driving and network conditions[188].

6.1.1 Network Parameters in Different Contexts

In Figure 50 and Table 2, we have the resulting normalised α ensembles for the dominant north-south PAR node in the TVA network using a variety of different datasets with varying fidelity. The highest fidelity, which is rare for utilities, is the E-field estimated given local B-field and MT surface impedance responses. Next best is the intermediate fidelity of either local TVA B-field but a synthetic layered-Earth conductivity profile or a local MT surface impedance with remote FRD B-field measurement, roughly 1,100 km away. Lastly, and up to now probably the most common for most utilities, is the low-fidelity combination of a remote B-field along with synthetic layered-Earth conductivity profile. There are a few interesting and surprising points to note from this figure. First is the general stability of the network parameter estimate, particularly the invariance to B-field given a conductivity profile. As seen in Table 2, the spread is however significantly affected, with the more local B-field being more accurate for both conductivity profiles. The increased spread when using remote B-field is expected as local perturbations, such as pulsations[194], are not concurrent across the region which is the case with typical large scale mid-latitude driving.

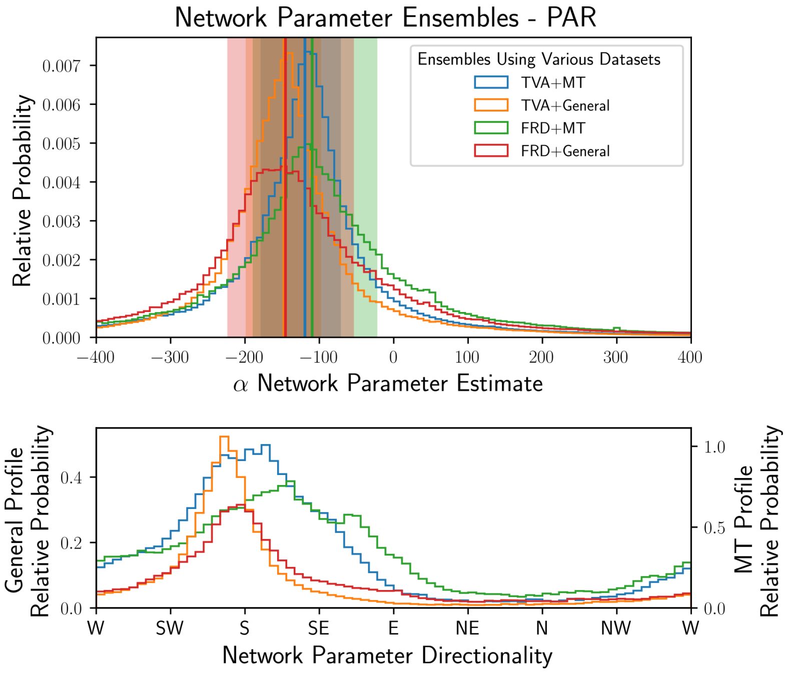

Figure 50: The stability of network parameters is seen here for dominant α parameter at PAR given different conductivity assumptions (local vs. generalised) and B-fields (local vs. remote) for a representative parameter ensemble. The measures of spread are characteristic of the uncertainty associated with modelling. Surprising is the better constrained generalised conductivity profile in both network parameter ensemble (upper panel) and corresponding directionality ensemble (lower panel). Quantitative values are shown in Table 2.

Table 2: Network parameter spreads associated with different B-fields (local vs. remote) and conductivity profiles (MT vs. synthetic layered-Earth) at PAR, as defined by the inter-quartile range (IQR). Also indicated is the spread ratio, i.e. the IQR divided by absolute network scaling ($\sqrt{\alpha^2+\beta^2}$). The lower the spread ratio, the more accurate the network parameter estimate.

	Network Parameter	B-field Type	Conductivity Type	IQR	Spread Ratio
$\boldsymbol{\alpha}$	-119	Local TVA	MT	106	0.89
	-148	Local TVA	Synthetic LE	99	0.65
	-110	Remote FRD	MT	165	1.47
	-147	Remote FRD	Synthetic LE	168	1.14
$\boldsymbol{\beta}$	-1	Local TVA	MT	164	1.38
	-35	Local TVA	Synthetic LE	93	0.61
	23	Remote FRD	MT	240	2.14
	-14	Remote FRD	Synthetic LE	168	1.14

Between conductivity profiles with the same B-field estimate, it is interesting to note that the network parameter profiles are similar besides a magnitude shift, with less spread in the synthetic profile. The directionality response is also cleaner for the simpler layered-Earth model with a different dominant direction. A possible explanation of this is that the full 3D surface impedance introduces more variability than the integrated or effective response which the network 'sees', and that the smoothed response requires a different network parameter directionality to represent any 2D strikes.

A full 3D surface impedance is needed to accurately reproduce the E-field in complex geological cases. Where the extent of geological complexity is however a strike, then a general conductivity profile can absorb the directionality projection when coupled to empirical network parameters. Network parameters in the ensemble estimation are free variables and although topology can be used to interpret them, they are not defined by the topology alone and choose the most optimal mapping between measured GIC and the input E-field. Using the synthetic E-field, the mapping between E-field and GIC is cleaner and performs more accurately in modelling, with directionality different from the MT derived E-field which is assumed to be more accurate. Additional noise in the MT derived E-field is possible, with higher frequencies better defined and local distortions possible. These distortions may prove irrelevant to the GIC problem where the E-field is integrated and the local variation often averaged out or compensated for elsewhere. Integration of the E-field is not trivial, as is how currents split within a node given uneven GIC distributions. Using the litmus test of the slope of the frequency response (see Section 4.3.3), the general synthetic E-field slope more closely matches the GIC frequency response slope, which aids in the improved performance. Ultimately an inversion of the surface impedance data to generate a 3D conductivity model, which in turn can be used to derive high resolution E-field data along the network footprint, would be the best. The inversion process in itself is a challenge with large associated uncertainty. Then comes the need to effective network integration of the E-field, which may also be misleading, as is shown in the TVA network where a 2 node away or 150 km scale is not representative. It may be that the specific TVA network is fortunate in this case, but more empirical validation of high resolution physics-based models is required.

6.1.2 Variation of Network Parameters

Given that empirical network parameters ultimately act as scaling knobs to the input E-field, different regimes of GIC strength associated with different levels of E-field driving may show different network parameter responses. A similar argument can be made for making sure that the data used and responses are relevant and trained on periods with significant geomagnetic disturbances. In previous work, thresholds have been used to define the criteria for noise levels[106]. After using some criteria to select significant GIC data, corresponding E-field data are selected. In the zero-crossing and least squares fit methods of parameter estimation, it is important to select the relevant E-field to prevent divergent results. In the case of ensemble estimation, we are solving a matrix of simultaneous equations. There are times where the matrix itself would be singular and can be avoided if the data set is masked correctly. Since ensemble estimation uses all possible pairs of comparable and relevant time instances to calculate parameter pairs, a large ensemble of parameters is produced. This means we can afford to ignore the few cases of a singular matrix without implementing any selection at all, i.e. we are able to obtain full network parameter representation at all GIC levels. Sampling bias arising from using thresholds around zero and significant single E-field components is further avoided (this would in effect create a directional bias along the cardinal directions).

Making use of all GIC levels and applying the ensemble methodology to subsets further allows the weighting and change of network parameter scaling with driving magnitudes to be probed. It is foreseeable that at different levels of GIC driving, different factors may become apparent or dominate. To define magnitude-related GIC characteristics in the ensemble methodology, the total training dataset is broken up into percentile range subsets defined by GIC magnitude (indicated for PAR in

Figure 51) that form sub-ensembles. Methods previously employed are not able to perform such dynamic probing, only being able to estimate an average response.

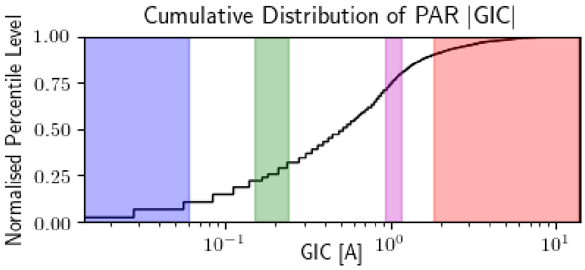

Figure 51: A visualisation of the GIC percentile ranges used to probe different driving level responses. Indicated in this cumulative distibution of the GIC magnitude at PAR are the 0-10 (blue), 20-30 (green),70-80 (magenta) and 90-100 (red) percentile ranges. Using different percentile ranges for analysis allow different GIC regimes to be probed.

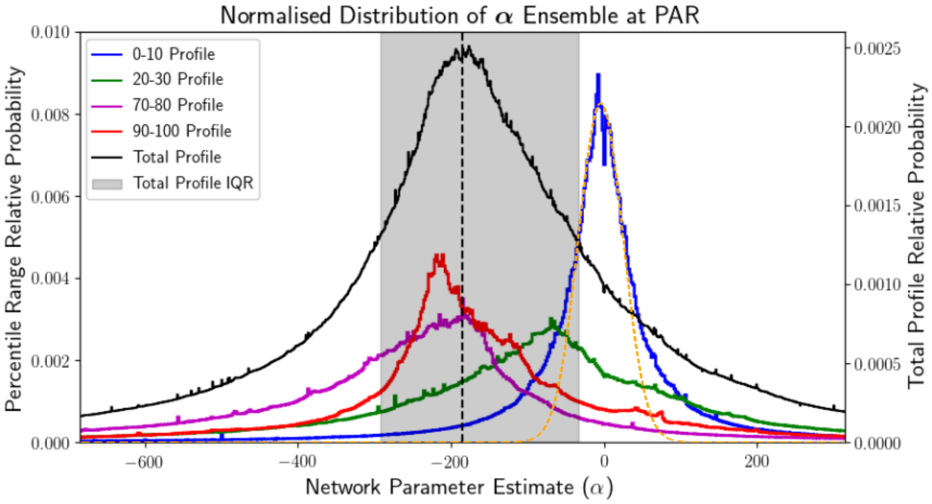

Figure 52: Splitting the α ensemble for PAR (black) into different GIC magnitude regimes produces different responses. A synthetic conductivity profile and remote B-field measurements at FRD are used. A zero-centred Gaussian distribution is fitted (orange) to the lowest percentile range (blue).

Previous studies have noted the change of estimated empirical network parameters given different regimes[105,106] and in Figures 52 and 53 we see this explicitly for the ensemble estimated network parameters. Figure 52 makes use of a synthetic conductivity profile and remote B-field data from FRD and Figure 53 makes use of local B-field data and a local MT derived E-field. In Figure 53 and its complementary Table 3, local B-field and MT defined E-field are used to eliminate variation of network parameters due to poor correlation or geophysical conditions.

The variation seen in empirical network parameters given GIC magnitude can be driven by other processes, such as different frequency components. Comparing back to the synthetic example of ensemble estimation presented in the previous chapter, the noise associated with network parameters at the lowest percentile level is related to a zero-centred Gaussian but with heavy-tails due to the ensemble estimation methodology. At this low level of GIC, it is likely that the variation seen is associated with instrument noise. As the network parameters move out of the noise levels, they become more apparent and have to scale to higher GICs. The stronger parts of a geomagnetic storm have different frequency components that may not be effectively modelled. The network parameters pick up this slack and, for representative parts of the storm, scale better. An example is that low magnitude GICs are dominated by high-frequency components, or inversely high-frequency components of the GIC carry the least power and are small in magnitude due to the low-pass nature of the GIC frequency response. These low GIC levels sit at the noise level, have near-zero network parameters and some associated spread. Midrange GIC levels have increased network parameters, but also increased spread, which most likely can be attributed to varied E-field across the network and low SNR. Given the largest magnitude GICs associated with broadband driving and long-period pulsations in the TVA network, the local B-field and MT derived E-field ensemble is well defined with the narrowest spread. In the remote B-field and synthetic conductivity profile ensemble, the highest percentile range subset shares the characteristic larger network parameters, but with a complex spread. Contributions from a timing offset between measured B-field disturbances and GICs may be to blame. More illustrative of the spread behaviour is seen in the spread ratio in Table 3, where it is clear that with increasing GIC magnitude the ratio decreases and confidence in network parameter estimates increase. To avoid misleading results from low-level GIC (noise), it would be best to disregard GIC levels below the median GIC level (roughly 0.5 A for PAR).

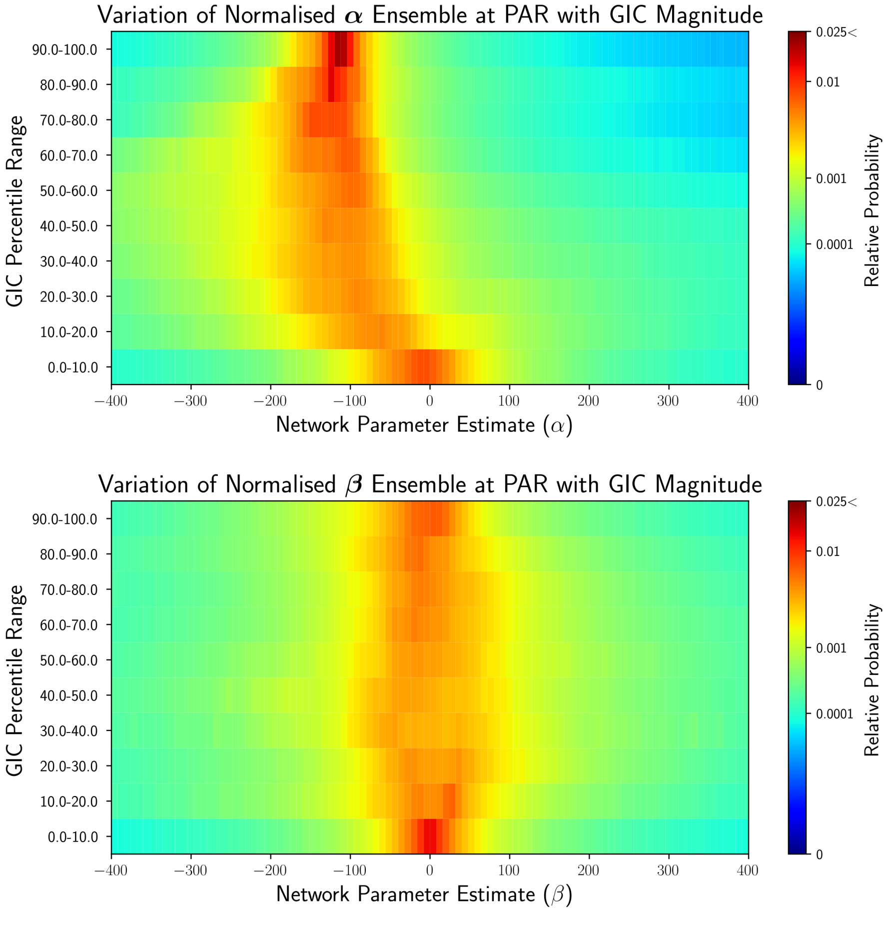

Figure 53: The full variation of both α and β network parameters with GIC magnitude using a local MT defined conductivity profile with local B-field measurements is shown. Clearly seen in this visualisation is the north-south orientation of the network, i.e. the α parameter is more responsive. Both network parameters start at noise-level based zero-centred Gaussians. While the α parameter becomes more apparent, β adds less and less to the total network scaling, remaining zero-centred. Using quantitative estimates of the ensemble spreads in Table 3, we see that the spread ratio for both parameters decreases with GIC magnitude – again with the α linked to network directionality being more responsive.

Table 3: Complementing Figure 53, the variation in network parameters is shown here with ensemble spreads and spread ratios for local B-field and an MT derived E-field at PAR.

	α			β		
Percentile Range	Network Parameter	IQR	Spread Ratio	Network Parameter	IQR	Spread Ratio
0.0-10.0	-14	91	6.5	0	58	4.1
10.0-20.0	-70	156	2.2	1	128	1.8
20.0-30.0	-99	154	1.6	6	155	1.6
30.0-40.0	-119	167	1.4	-5	177	1.5
40.0-50.0	-126	170	1.3	-11	190	1.5
50.0-60.0	-130	148	1.1	-2	186	1.4
60.0-70.0	-134	106	0.8	-2	159	1.2
70.0-80.0	-134	71	0.5	0	146	1.1
80.0-90.0	-124	60	0.5	-13	138	1.1
90.0-100.0	-115	32	0.3	-10	106	0.9

6.1.3 Directionality of Network Parameters

Similar to the variation of the actual network parameter estimates, the effective directionality ensemble can also be probed given different GIC levels. The network parameter defined directionality needs to be taken into account with the E-field directionality in terms of operational considerations. Certain E-field directions are more prevalent or have a larger magnitude due to geophysical conditions and near-Earth current system driving. The network sits on top of these aspects and allows certain E-field components to drive currents when aligned to the power lines. In Figure 54, taking the percentile binned E-field direction alone shows the local transmission line direction given a realistic E-field at the highest percentile. The percentile range just above noise shows roughly the orthogonal contributions to GIC and intermediate levels show a mix of large off-line driving and weak aligned driving. In the E-field representation the largest contribution to large GICs would come from E-field along the line. There is significant weighting off these lines though, with the projection of strong E-fields still contributing to large GICs such as the westerly maximum E-field not seen clearly in Figure 54, or the more clear south-easterly contribution.

The network parameter version of directionality in Figure 55 is the averaged response that takes into account all the projected contributions due to the pairwise calculations, including the off-line contributions. The result is that the network parameter directionality ensemble may appear to deviate from the local lines, but this is the weighted effective response and not the most common response. Given a simple synthetic E-field this difference may be greater due to geophysical strikes not being taken into account. For the same reason the network parameter directionality response may be cleaner. Looking specifically at the network parameter directionality in Figure 55 and 56, it is evident that larger GICs are better defined in terms of their effective network directionality. As mentioned, this directionality does not match the line direction exactly but is rather a weighted average of both line topology and E-field driving. Interesting to note is the poorly defined polarity at lower GIC levels. This is likely the result of instrument noise at the lowest levels or low-amplitude variable currents in the transformer windings, which becomes less apparent as the GIC signal becomes stronger.

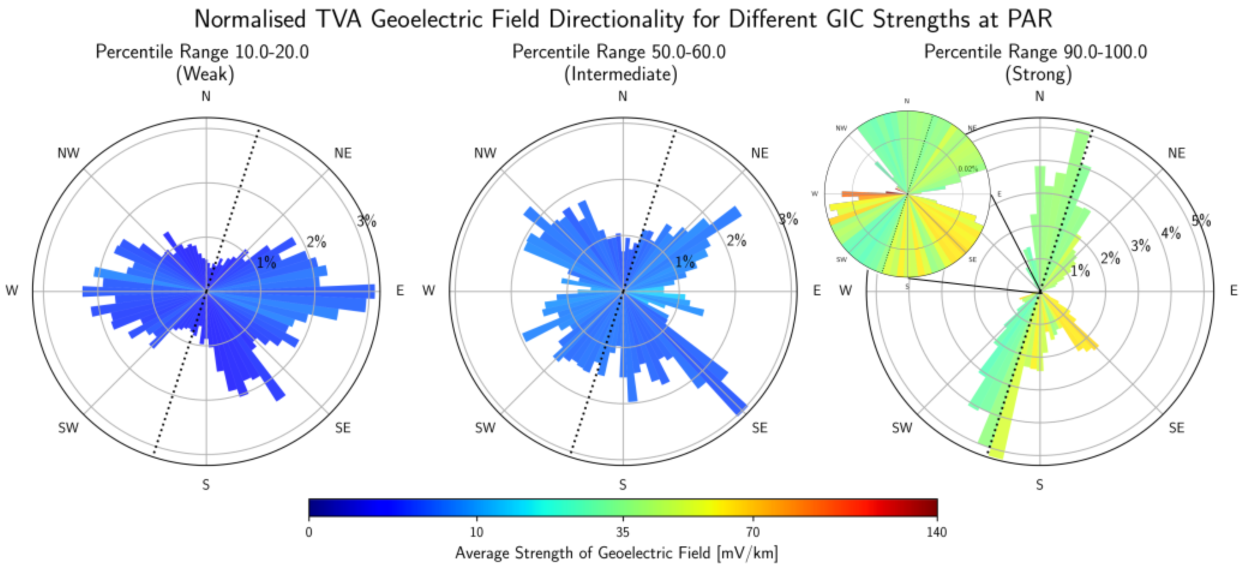

Figure 54: The E-field orientation as related to different GIC magnitudes allows for an independent interpretation of network parameter variation and directionality. The resulting E-field occurrence percentages are normalized according to the total E-field sampled to eliminate sampling biases. The colour bar represents the average E-field strength in a given bin. In the strong GIC range, there are significant E-field contributions of the order of 140 mV/km in the east-west direction associated with the SSC period of the storm. The E-field direction is consistently along the local power line direction (dotted line) in the strong GIC range, although contributions away from this direction result in discrepancies away from local line direction in a network parameter defined directionality.

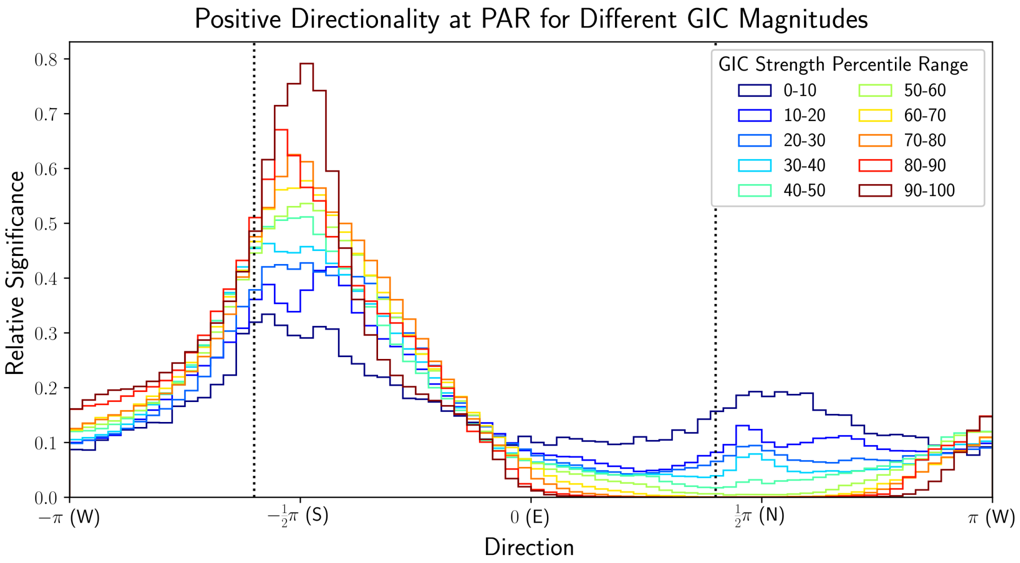

Figure 55: Directionality ensemble for PAR using the local MT derived E-field. Linking to the similar plot for general E-field in Figure 54, the higher GIC magnitudes are better defined. The resulting predominant directionality is not associated with the local line direction (dotted line) but rather the effective response of the measured GIC vs E-field.

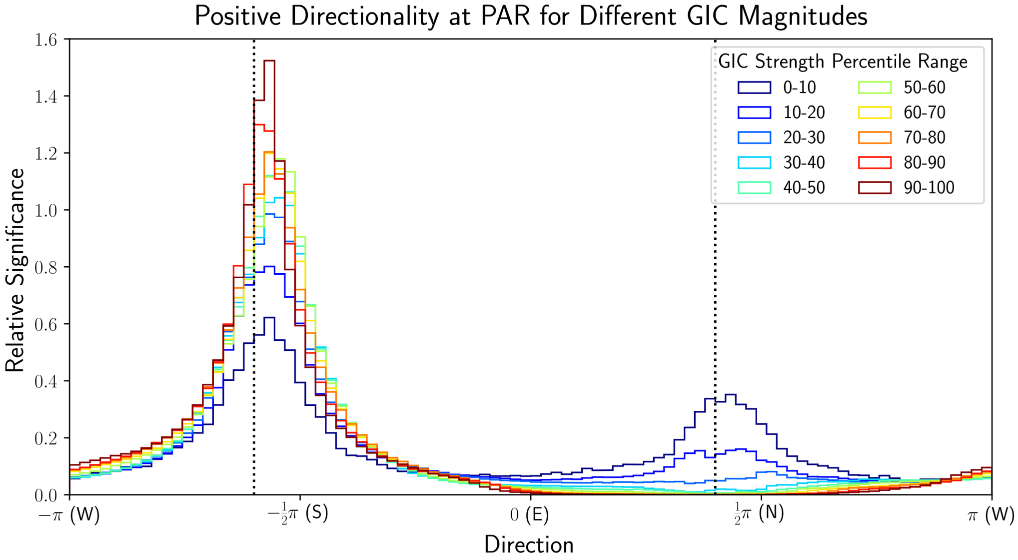

Figure 56: Using the synthetic conductivity profile instead of an MT defined surface impedance, we see that the resulting network parameter directionality is significantly cleaner and more aligned to the local network. This tendency is suggestive of the 3D MT approach adding additional localised complexity in the E-field estimation that the network does not 'see', i.e. integrates over given the region is predominantly 2D.

A further interesting characteristic in the directionality response of the PAR node is that using the simpler synthetic conductivity profile introduces a much cleaner network parameter defined directionality. Again reiterating the points made about a better effective frequency response and less noise, although this conductivity profile is not as physically defined as the MT profile, when allowing the network parameters to tweak it, it becomes operationally more viable.

6.1.4 Frequency Domain Transfer Functions

Moving into the frequency domain and away from traditional network parameters, the B-field-to-GIC transfer function (TF) was estimated at PAR. The TF estimation initially displayed significant issues with SNR given the usual B-field to GIC mapping. Similar to what is seen given indeterminate polarity at low GIC levels in the network parameter directionality, the TF suffers from a multimodal phase response due to noise levels at high frequencies[98], as seen in Figure 57. Cleaning the responses in previous work has resulted in usable GIC modelling for PAR[191], but not at the accuracy that is expected when the ground conductivity assumptions are sidestepped. This previous modelling using the TF also made use of remote B-field data that contributed to poor modelling accuracy due to pulsation driving not being concurrent at both FRD magnetometer and TVA node[194]. These issues regarding TF estimation can however be avoided by using dB/dt instead of the B-field for training. As mentioned in Chapter 3, dB/dt and the B-field can be explicitly related in the frequency domain, with dB/dt effectively being a high-pass filter to the B-field. This improves the SNR in estimating the TF and the phase is now well defined, similar to that seen by McKay[122] (clean PAR TF is shown in Figure 58).

Although the clean TF was estimated using the dB/dt, the mapping from B-field to GIC is shown in Figure 58. Consistent with expectation, the GIC mapping is seen to be an effective high-pass filter of the input B-field[174]. The use of dB/dt allows a higher SNR above f_c (see Figure 12), which in turn cleans up the TF response above 1 mHz previously affected due to spectral averaging. Lower frequencies are however largely unaffected. Compared to typical MT approaches where less than 10 estimates per decade are common[65], the TF response in this case was estimated at a much higher resolution. Nothing is lost in additional resolution, but accuracy in modelling was improved remark-

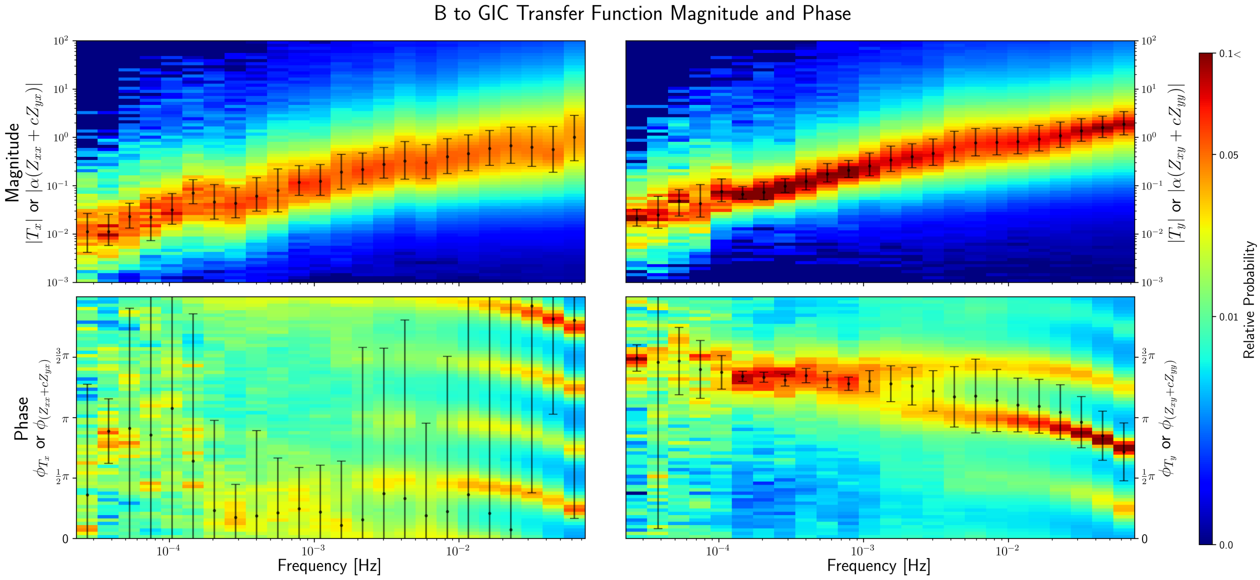

Figure 57: Using high-fidelity B-field and GIC data at the PAR, a transfer function (TF) can be estimated. The left plots are related to the T_x component, linked to B_x (and an east-west E-field or network), and the plots on the right are related to the T_y component linked to B_y (and a north-south E-field and network). The upper plots show the TF component magnitudes and the lower plots the TF phase response. As expected for the north-south network at PAR, T_y is better defined. From the multiple traces (multi-modal) in the phase response, it is evident that the TF suffers from a poor signal-to-noise ratio and poorly defined responses at higher frequencies. For context the temporal lags are not removed.

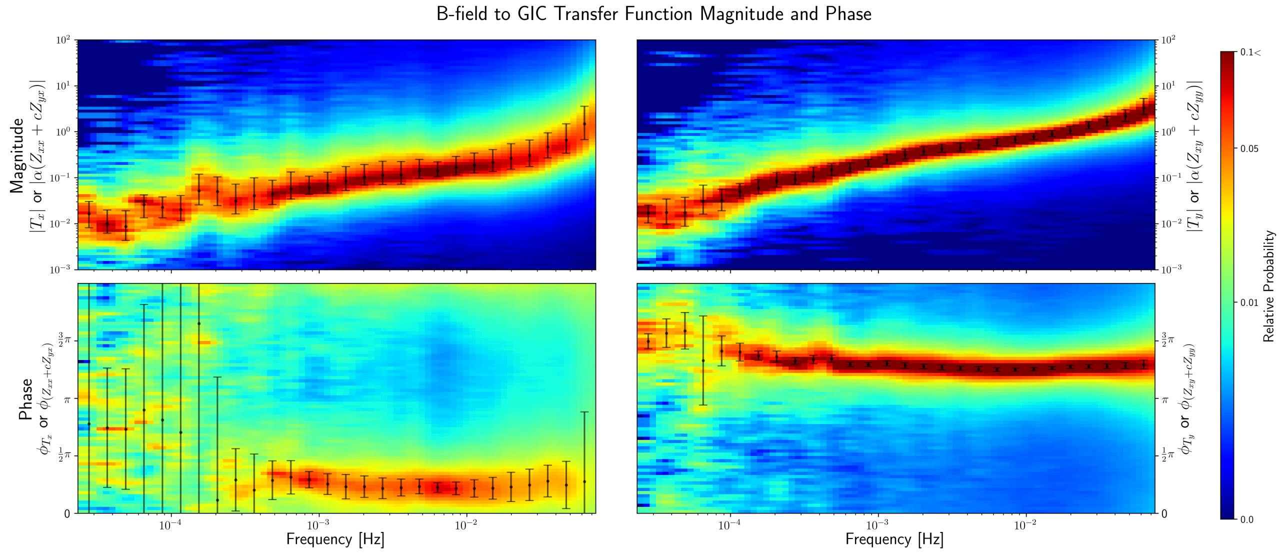

Figure 58: B-field-to-GIC TF as derived for PAR using the local dB/dt and corrected for a roughly 4 second delay in the time domain. The TF implicitly absorbs the surface impedance relation and network parameters, assuming they units [A/(mV/km)] in this case. $T_{x,y}$ hence have units of [A/nT] or [A/(mV/km)][(mV/km)/nT]. This TF has been estimated using 11 datasets created from 18 hour windows padded to 20 hours and shifting of 3 hours across the entire dataset.

ably. Having too low a resolution in log space smooths the response of components with the result not much better than using linear binning. The responses of the two components are consistent with the effective topology and previous ensemble estimation. Due to the north-south network, the T_y component that scales B_y (and an analogous homogeneous-Earth E_x) dominates. The T_x component on the other hand has a poor SNR. This effect is particularly seen in the phase response, but also in the magnitude response with a larger spread. Higher frequencies in both components are better defined in these responses due to the training by dB/dt, not suffering from a multimodal phase response and generally with smaller error bars at high frequencies relative to a B-field driven TF. In future work, a hybrid estimation by B-field and dB/dt may provide the best estimation across all frequencies, with an optimal SNR throughout.

Not explicitly shown here is the estimation of lags between the GIC and B-field data as estimated by the slope of the phase. After estimating this slope and correcting for the lag by shifting data in the time domain, the phase response is flattened and physically interpretable (constrained to a single quadrant). Magnitude is unaffected by shifting in the time domain. The nature of the lag itself is not definitive, with measurement differences or a low-pass filter generating it possible. Lags attributed to measurement have been identified before by McKay[122]. As a test, multiple nodes in the TVA[188] and Australian Powerlink networks have been analysed, along with the examples covered in this work. A range of different lags were estimated, with no coherent pattern suggesting a characteristic of the transformer. Also interesting to note is that no lags are seen in 1 minute data (tested through resampling across the available datasets). For the PAR node, where a local surface impedance is available and E-field estimated, it was found that the E-field-to-GIC TF has a similar lag length to the B-field-to-GIC TF. Furthermore, the magnitude response of the E-field-to-GIC TF is constant across frequencies, suggesting a resistive network with no expected lags there. This suggests that the lag is not due to geophysical conditions but rather a lag between the measured B-field and GIC. The implications of a lag in general is two-fold. Firstly, taking this lag into account when modelling is done in the time domain would improve results. Secondly, if there is a lag present and instances of E-field and GIC are not concurrent, then delta network parameter estimation using (45) would break down. Using the higher cadence TVA data where the lags cannot be estimated perfectly, network parameters defined by (45) have been found not to be consistent, as expected.

Exploring the E-field-to-GIC TF more, this TF can be seen as the frequency version of the network parameters. Previous research has analysed the frequency dependence of these parameters, probing the resistive assumption of the network in GIC modelling[98]. A resistive network would result in flat network parameter responses in both magnitude and phase. The current set-up at PAR with local B-field and multiple surface impedance responses that give an estimate of the effective E-field, offers a unique extension to previous analysis which could only use a single site and could not rule out further geophysical influences. In Figure 59 above, we see that the resulting PAR node frequency dependent network parameters are not statistically different from the flat responses expected for a resistive network. In this case the $\alpha(\omega)$ is better defined (as expected) from a north-south network and consistent with ensemble estimation. The magnitude also reflects the magnitude of the ensemble estimate. The $\beta(\omega)$ parameter, similar to T_x, is drowned by noise and not well defined.

6.1.5 Modelling Results

For modelling purposes, this analysis makes use of a number of different versions of the ensemble methods described. For each dataset, modelling is first done using the network parameters estimated using the entire dataset, which includes noise. Secondly, modelling is done using estimates from training done only on GIC instances larger than the median GIC level. This in turn ensures only significant GIC instances are used, and noise or low levels are excluded. Compared to total ensemble training that is representative of all GIC levels, performance for above median GIC training would be better for higher GIC levels but worse for lower GIC levels. The relative error metric (defined below) that only looks at significant GIC instances as such does better. Thirdly, there is dynamic estimation using sub-ensembles trained using the percentile ranges of GIC magnitude, similar to

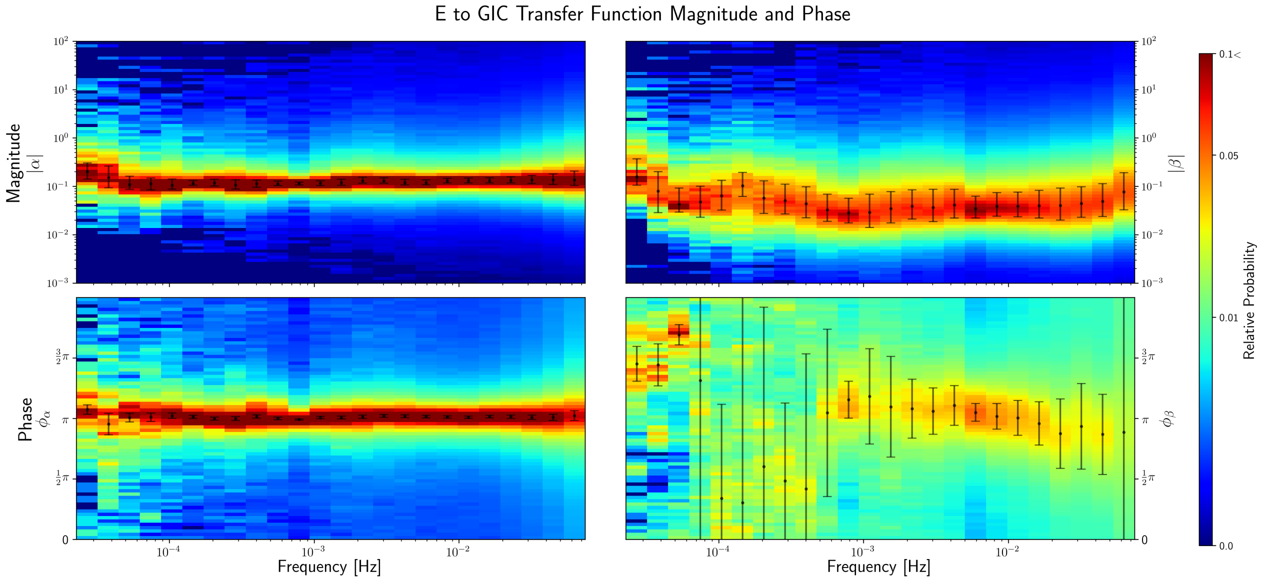

Figure 59: Using the local MT derived E-field, a similar TF approach can be applied between the E-field and GIC to estimate frequency dependent network parameters α (left) and β (right). The TF magnitudes in can be seen as the frequency dependent network parameters, with units of [A/(mV/km)]. Multiplying by 10^3 will result in the same units as the typical definition of network parameters, i.e. [A/(V/km)]. Using the same datasets and considering the well defined α parameter, we see agreement between the TF approach $\alpha \approx 10^{-1}$ A/(mV/km) and ensemble estimation $\alpha \approx 10^2$ A/(V/km).

that seen in Figure 53. Here, the dynamic network parameters should adapt to the different regimes of GIC driving and perform the best[203].

For TF modelling results, a similar set of sub-models are used. Firstly, there is the raw TF. Secondly, there is the ensemble adapted TF, where the TF components are convolved with the B-field components and the g and h ensembles estimated that allow for uncertainty quantification. Lastly, a dynamic version of the g and h ensembles similar to the dynamic network parameter ensembles is used to further improve on modelling. If the TF is well defined, the dynamic g and h parameters should provide little further benefit besides estimation of uncertainty.

The results of validation set modelling are shown in Table 4. The error metrics used are the root mean square error (RMSE), correlation coefficient (ρ) and relative error (RE). The RMSE is a measure of the absolute magnitude error in ampere, whereas the correlation coefficient is a measure of the similarity between profile shapes, irrespective of amplitude. It is expected the empirical network parameters provide optimal scaling so that the RMSE associated with a correlation coefficient cannot be improved on. In previous studies using analytical network parameters, it is assumed that a scaling factor can be included to improve magnitude error given a set correlation[50]. The relative error (RE) in turn weights the absolute magnitude error, being defined as the GIC modelling error relative to measured GIC for GIC instances over 1 A. The median of the result is defined as the RE and quoted as a percentage[106].

For all cases, the validation sets were kept out-of-sample for training. The network parameters are estimated either as a full ensemble or as sub-ensembles, where training is done using GIC instances larger than the median GIC level or fully dynamic estimation using percentile ranges. Due to the high cadence data for PAR, the size of the ensembles can become very large very quickly, with a greater demand on computation time and resources. Instead, using the convergence of the method shown by previous work[191], limited data and multiple runs are used instead[188]. Two separate validation sets are used (both 25% of total dataset length), with training for each excluding its corresponding

Table 4: Modelling results for the PAR node in the TVA network, without E-field normalisation. The second random validation set in this case refers to a random subset of 25% of data kept out-of-sample.

	Validation Sets							
Data/Method	**22 June 12:00-23:59**				**Random**			
	α	β	RMSE [A] (ρ)	RE%	α	β	RMSE [A] (ρ)	RE%
Local MT Earth and Local B-field								
Ensemble Parameters	-117	0	0.53 (0.98)	21	-117	-9	0.40 (0.97)	16
Ensemble Parameters (>median GIC)	-121	-4	0.52 (0.98)	21	-124	-5	0.42 (0.97)	17
Ensemble Parameters (dynamic)	–	–	0.56 (0.98)	24	–	–	0.40 (0.97)	16
Local MT Earth and FRD B-field								
Ensemble Parameters	-93	21	1.07 (0.89)	42	-97	13	1.31 (0.71)	35
Ensemble Parameters (>median GIC)	-110	44	1.07 (0.89)	37	-114	35	1.41 (0.72)	32
Ensemble Parameters (dynamic)	–	–	1.36 (0.84)	45	–	–	1.36 (0.74)	32
General Layered-Earth[193] and Local B-field								
Ensemble Parameters	-216	-48	0.45 (0.98)	13	-215	-51	0.38 (0.98)	14
Ensemble Parameters (>median GIC)	-230	-52	0.41 (0.98)	14	-226	-54	0.37 (0.98)	13
Ensemble Parameters (dynamic)	–	–	0.43 (0.98)	15	–	–	0.36 (0.98)	16
General Layered-Earth[193] and FRD B-field								
Ensemble Parameters	-180	-21	1.02 (0.90)	29	-191	-23	1.21 (0.74)	28
Ensemble Parameters (>median GIC)	-205	-20	0.97 (0.90)	22	-216	-20	1.28 (0.75)	25
Ensemble Parameters (dynamic)	–	–	1.53 (0.80)	32	–	–	1.21 (0.78)	25
Local B-field TF								
Transfer Function	–	–	1.04 (0.91)	38	–	–	–	–
Transfer Function Ensemble	–	–	0.97 (0.91)	31	–	–	–	–
Transfer Function Ensemble (dynamic)	–	–	0.97 (0.91)	33	–	–	–	–

validation set. The first validation set keeps a single 12 hour period relating to the geomagnetic storm onset and main phase out-of-sample. The second validation set aims to use more representative data that includes commencement and main phases of the geomagnetic storm. As such, randomly selected data points are kept out-of-sample. Although the TF approaches are the most physically accurate, they require continuous data and cannot be tested on the second randomly sampled validation set. A further shortcoming with the TF approaches is that when using remote B-field measurements then local perturbations can cause the method to perform very poorly[191]. In the time domain ensemble estimation, the distant data can still be used and is inherently more robust. Figure 60 makes use of the parameter or TF estimates, along with the associated spreads to include the uncertainty in modelling. To do this for the TF, the ensemble modification to the TF components needs to be included. The results in Table 4 further show that the use of local B-field and network parameter estimates are the most accurate. The general layered-Earth estimation of the E-field further shows better modelling performance, as previously suggested by the ensemble spreads. Both the layered-Earth and MT derived E-field approaches do better than the TF estimation. The TF in this case is based on limited data (1.5 days) not representative (excludes the SSC and main phase driving), with the implication that training on longer and more representative data that samples all storm phases will be able to improve on modelling further. Dynamic parameter estimation in both the network parameter ensembles or TFs add little to no benefit, suggesting the various geophysical assumptions are adequately defined for the local PAR node.

Although the response of the TF has been shown to be better with dB/dt training, especially at higher frequencies, there are further considerations with regards to modelling. Due to the B-field having a better defined low-frequency SNR and the GIC signal having a higher spectral content in the lower frequencies, general modelling does marginally better using B-field training (which is quoted in Table 4). There is more to this story though, as the B-field training does not adequately capture the high-frequency variation associated with SSC peak as can be seen in Figure 60. The SSC makes up a small part of the validation set and the error is not too evident. Making use of a weighted RMSE metric, the dB/dt trained TF does better. A hybrid between the two approaches may provide the most accurate final estimate. Taking a simple average between B-field and dB/dt TF results gives a RMSE of 0.93 and ρ of 0.95, which is more accurate than either approach alone and emphasising

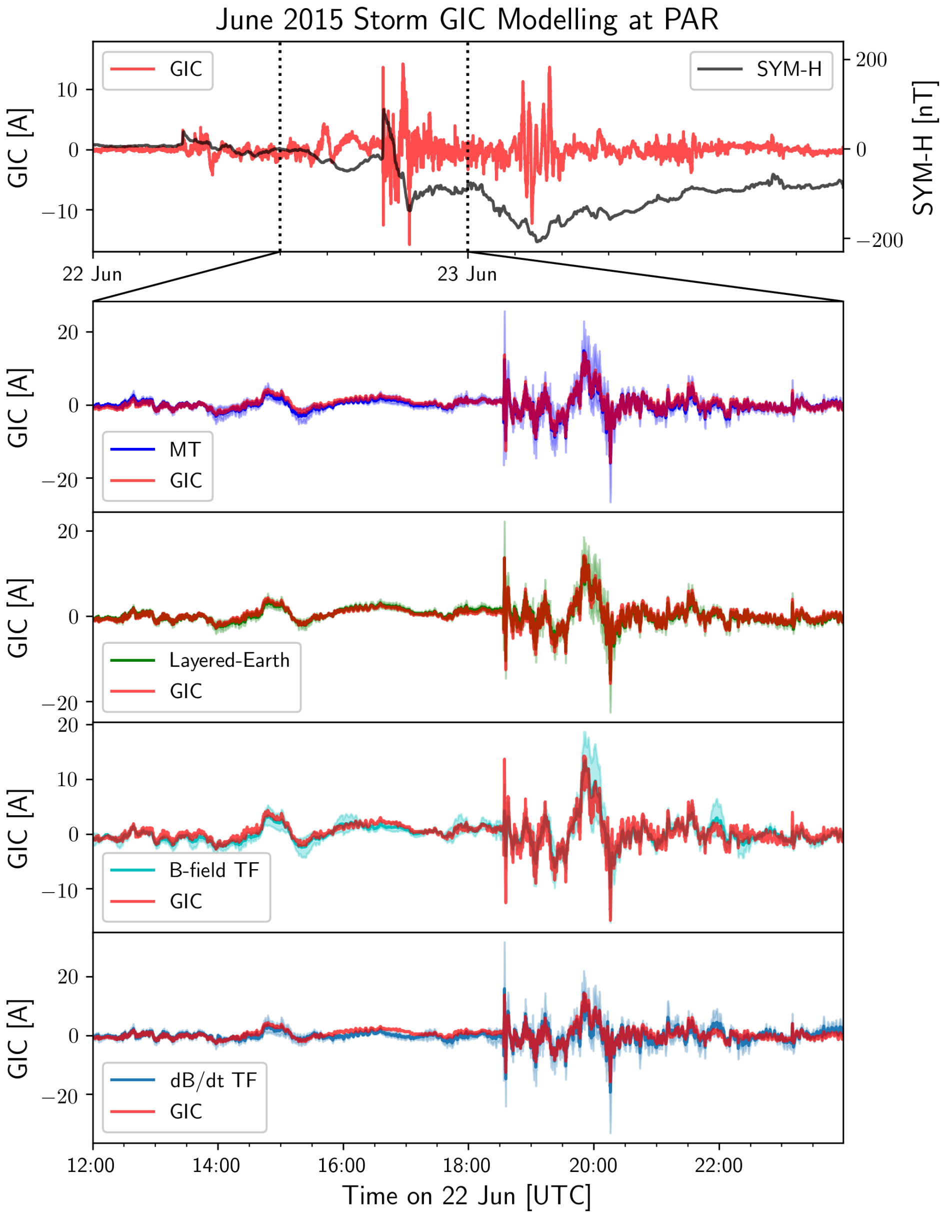

Figure 60: Given the spreads derived through the ensemble methodology, uncertainty estimates in the form of prediction bands can be derived for both network parameter (above median GIC level here) and TF approaches. These bands are ideal for operational modelling, as seen for the PAR validation set between the dotted lines here. Of interest is the low-frequency and high-frequency bias of the B-field and dB/dt trained TFs in the lower two panels respectively.

the need for both high and low-frequency characterisation. Due to limited training set size using a sliding 6 hour window and the training set not including SSC or other significant spike signatures, further improvement can be expected using more representative training.

6.2 A Typical Case & Comparison with Previous Modelling

After the Halloween Storm of 2003, the largest geomagnetic storm of solar cycle 23, significant transformer damage was seen in the South African power network[15]. Although not the largest in terms of minimum *Dst* or SYM-H, the geomagnetic storm was the result of multiple CMEs with the result more complex than typical single CME storms[29,79]. A power network does not differentiate between events and sees the entire period spanning a number of days as continuous driving, which possibly introduces more stress and damage than a single event.

Due to the Halloween storm causing damage in the South African network, the GIC data measured at the GRS node has been been extensively used for modelling purposes[104,106,157]. The GIC data provided by the Sunburst project at GRS is high-fidelity 2 second cadence data. B-field data of that time is 1 minute cadence data from a distant magnetometer at HER, roughly 600 km away. Although there is a move to 1 second cadence B-field measurements, there still are a lot of utilities that only have access to 1 minute data. At the 1 minute cadence, the spectral content of GIC and B-field data is largely representative and can be used for operational decision-making. Higher sampling rates do however introduce more GIC dynamics and larger peak values, and should be used where possible. The GRS case with high-fidelity 1 minute cadence GIC and B-field data, B-field measurements from a remote magnetometer and no conductivity information, is seen as a typical case for a utility. The extent of previous modelling at GRS[104,106,157,204] also allows for comparison and analysis between empirical methods.

At GRS, the previous modelling approaches have included a homogeneous Earth assumption[157,204] and a local layered-Earth conductivity profile[104]. In the case of the 'local' layered-Earth, the profile is not as much a geophysical profile but a layered-Earth approximation of a TF between the B-field and GIC, based on the approach of Pulkkinen et al.[102]. In this quasi-transfer function approach, network parameters are estimated through an analytical network model. The conductivity profile is then obtained by inverting the surface impedance derived from GIC and B-field measurements, taking into account the network parameter scaling and assuming a layered-Earth. The exact values of the network parameters used for the estimation are irrelevant since the GIC related local conductivity profile absorbs any incorrect scaling, with the result that the network parameters and conductivity profile form a pair at a node and cannot be used in a more general sense. Geophysical aspects can nevertheless be seen in such a layered-Earth approach, but the geophysical context taken in a local sense may be misleading as network averaging is already taken into account[102,104]. An MT survey on the other hand includes significantly more variation due to geology and computing a network effective E-field at a node is not trivial. Making use of the local GRS layered-Earth profile and further allowing empirical network parameters to be derived and used in modelling is similar to the concept of the g and h parameters used to further tweak a TF approach.

Further modelling using the local layered-Earth conductivity profile[104], has been attempted with the addition of computing the E-field through a finite element method (FEM) approach[106]. In the FEM study, network parameters were empirically derived for improved estimation using a zero-crossing method, i.e. when either E_x or E_y is near zero then the other term of (35) is used to estimate a single network parameter. The zero-crossing method produces only a few estimates of network parameters and there has been an issue of contamination of the validation set, as the same dataset used to derive network parameters and conductivity profile is used in validation. The mixing of training with validation allows for further tweaking and artificially better fits. Regardless, the FEM approach aims to be physically informed and may provide more accurate results.

The resulting network parameter ensembles of the local layered-Earth conductivity profile and HER

B-field can be seen in the upper panel of Figure 61. The final or most probable estimates are defined by the medians and shown using solid lines. Previous empirical network parameter estimates using the same conductivity profile and B-field data are shown by dashed or dotted lines.

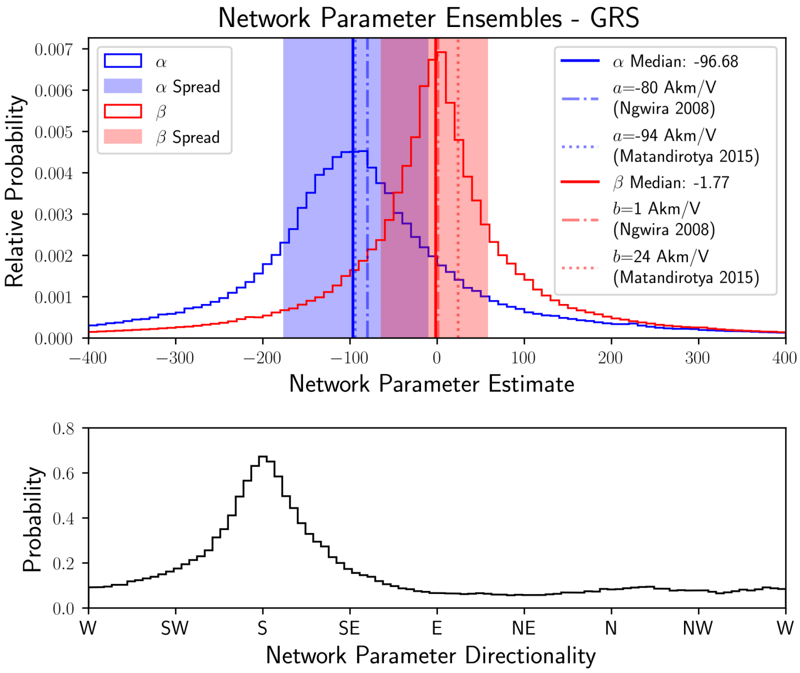

Figure 61: An example of the network parameter ensembles as seen for the GRS substation using the entire available measured dataset. Previous empirical network parameter estimates are indicted by the dashed lines. The lower figure is representative of the directionality ensemble, which aligns closely with the roughly north-south local line directions and reflects the peaks of network parameter ensembles in the upper panel.

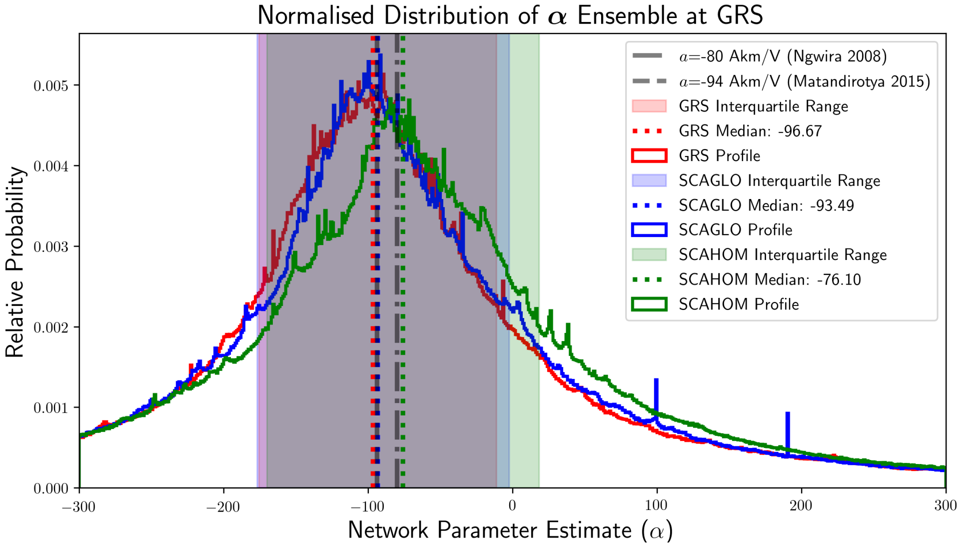

Figure 62: For comparison with PAR (Figure 50), we see similar stability of the ensemble method using different conductivity profiles and remote HER B-field data. Median estimates of α for this similarly north-south network are given with estimates used in previous studies.

For consistency and comparison of the effect of different conductivity profiles seen at PAR in Figure 50, responses for GRS are shown in in Figure 62. Here the different conductivity profiles are defined by previous modelling at GRS, with a homogeneous Earth used[205] (SCAHOM Profile), along with the locally derived layered-Earth profile[104,106] (GRS Profile) and the general synthetic profile employed as a standard in this work[193] (SCAGLO Profile).

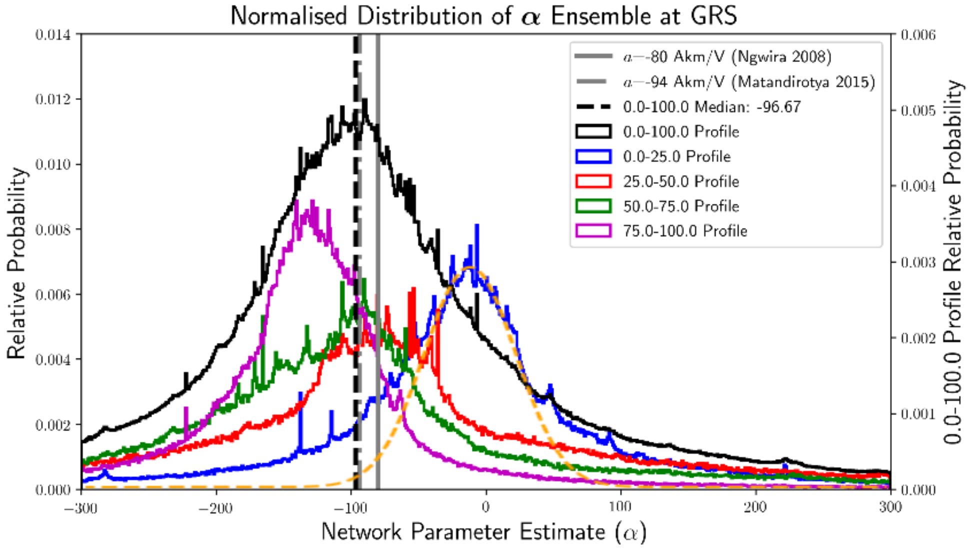

Figure 63: Total ensemble at GRS (HER B-field and GRS layered-Earth profile) is shown, with GIC magnitude percentile range sub-ensembles showing the increase of the α network parameter with magnitude. For the lowest percentile range (blue), a Gaussian distribution is fitted (orange) which matches the observed heavy-tailed result of the ensemble method given measurement noise. Compare with PAR, Figure 52.

Using the local layered-Earth profile profile, the observed variation in network parameter response given different GIC regimes seen at PAR in Figure 52 is also seen for GRS in Figure 63. Due to the lower SNR for GRS relative to PAR, the 0-25 percentile level affects the full ensemble median – which does not accurately represent the 75-100 percentile level. Practically this means only estimates above the median level should be used for modelling, something previous modelling did not do[104,106]. Besides movement away from instrument noise, the variation at GRS may include geophysical aspects. Although it is assumed that the empirical network parameters adequately represent the coastal effect at GRS (roughly 10 km from the coast), there would be different magnitude scaling of network parameters to correct for the resulting GIC given different E-field directions. Similar to PAR, GIC magnitude is linked to the projection of the E-field direction onto the local network and it is likely that there exists a GIC magnitude dependence on the network parameter scaling due to absorption of unmodelled geophysical aspects. For larger E-fields and associated GICs, the difference between a simple E-field and the inductive contribution from geophysically complex E-field is greater[46,132]. In such cases, the network parameters and their spreads also would need scale the difference.

In the lower panel of Figure 61, the directionality ensemble for GRS is shown. Assuming a local layered-Earth conductivity and B-field from HER, the network parameters show an effective north-south response. In this particular case the local network lies to the north and matches the directionality response (see Figure 21).

The directionality response has a direct effect on the SNR in the TF approach using GIC data, with the T_x poorly defined[191]. Using the 1 minute cadence GRS data to estimate the TF, there was no need to use the dB/dt version of the method as the mapping between B-field and GIC is well defined. Although the TF has been estimated and presented in preliminary work[191], the results of modelling using this approach are included in Table 5 for comparison. In both the network parameter ensembles and TF approaches, error and uncertainty are encoded in the spreads. These spreads can be further related to uncertainty bounds which are shown explicitly in Figure 64.

Table 5: Modelling results for GRS substation compared to previous work, keeping the entire 29th of October as an out-of-sample data set for validation. *RMSE* and correlation coefficient (not used in previous work) are calculated for the different storm phases and the entire validation set. The relative error is shown either for half a day (HD) as done by Ngwira et al.[104] or the full day (FD) as done by Matandirotya et al.[106]. Three versions of network parameter ensemble estimation are shown, i.e. using the entire training set, training instances above median GIC or dynamic percentile range training. Frequency domain TF ensemble estimation results that absorb network parameters and E-field in a single step are also shown. Best performing metrics are highlighted in **bold**.

Data/Method	*a*	*b*	RMSE [A] (ρ) 00:00-11:59 (HD)	06:00-11:59	19:00-23:59	00:00-23:59 (FD)	RE% HD/FD
Uniform Earth[205]							
Network Parameters[205]	-80	15	3.49	–	–	–	82/–
Ensemble Parameters	-29	1	1.17 (0.70)	1.63 (0.71)	1.12 (0.90)	1.07 (0.75)	60/52
Ensemble Parameters (>median GIC)	-43	5	1.81 (0.76)	1.95 (0.77)	1.0 (0.91)	1.36 (0.79)	47/42
Ensemble Parameters (dynamic)	–	–	1.16 (0.77)	1.61 (0.78)	0.92 (0.92)	1.02 (0.81)	43/42
Local Layered-Earth[104]							
Network Parameters[104]	-80	1	1.56	–	–	–	48/–
Network Parameters (FEM)[106]	-80	1	–	**0.96** (0.81)	1.07 (0.86)	1.35	–/51
Network Parameters (FEM)[106]	-94	24	–	1.38 (0.82)	1.11 (0.89)	0.98	–/41
Ensemble Parameters	-96	-3	0.84 (0.86)	1.16 (0.88)	0.76 (0.96)	0.79 (0.87)	42/37
Ensemble Parameters (>median GIC)	-128	3	1.49 **(0.90)**	1.61 **(0.90)**	0.55 (0.97)	1.06 **(0.91)**	47/29
Ensemble Parameters (dynamic)	–	–	1.00 (0.89)	1.40 **(0.90)**	0.51 (0.97)	0.82 (0.90)	49/30
General Layered-Earth[193]							
Ensemble Parameters	-109	-1	1.07 (0.78)	1.49 (0.79)	0.83 (0.94)	0.93 (0.82)	46/38
Ensemble Parameters (>median GIC)	-142	11	1.68 (0.83)	1.81 (0.84)	0.70 (0.95)	1.18 (0.87)	44/33
Ensemble Parameters (dynamic)	–	–	1.12 (0.82)	1.56 (0.83)	0.67 (0.95)	0.92 (0.86)	43/33
HER B-field							
Transfer Function	–	–	0.94 (0.85)	1.18 (0.87)	0.67 (0.97)	0.81 (0.86)	38/30
Transfer Function Ensemble	–	–	0.88 (0.85)	1.16 (0.86)	0.72 **(0.98)**	0.78 (0.87)	43/34
Transfer Function Ensemble (dynamic)	–	–	**0.83** (0.89)	1.12 **(0.90)**	**0.49 (0.98)**	**0.69** (0.90)	**36/25**

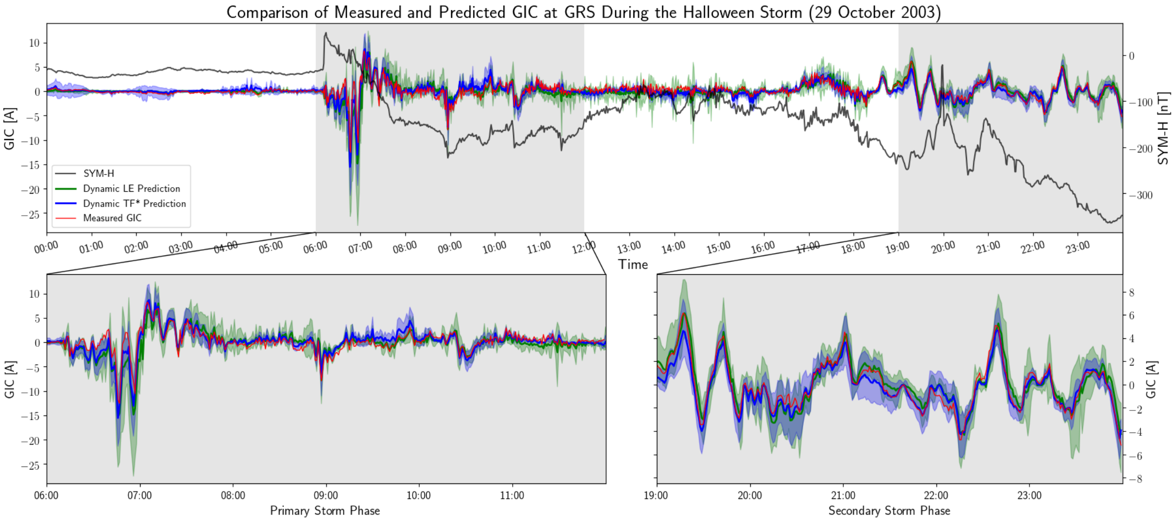

Figure 64: Taking into account modelling uncertainty, we can define error bands for the network parameter and TF approaches at GRS during the 2003 Halloween Storm[191]. Here the general layered-Earth conductivity profile (LE) and ensemble adapted transfer function (TF*) models are shown for periods of interest within the Halloween storm. Also shown is the SYM-H index in the upper panel.

From the defined error metrics we see an improvement in GIC modelling in almost every aspect when compared to previous work, particularly the TF approach. This improvement is seen even though the modelling was done on an independent validation set that was not used in the parameter estimation, which may have had influence in previous work by Matandirotya et al.[106]. In that previous work, the empirically estimated parameters did better than the analytically estimated parameters given the whole day, but not during the significantly disturbed times because those network parameters 'tuned in' to the whole day's measured data. Given that they were trained on the whole day, they are not independent when considering the validation set and in turn perform better given the whole day. Combining this with the second half of the day also being used to determine the conductivity profile initially[104], there is further 'tuning' of the empirical conductivity profile to match observations. The combination results in a more than a 10% improvement in the relative error throughout the day in previous work. Allowing that there may be influence from the second half of the day due to feedback from the conductivity profile estimation, the ensemble method nevertheless does significantly better with a further improvement of 10% using above median or dynamic estimation of network parameters and the same conductivity profile. Comparison with the general layered-Earth dataset, where no prior local information is included, also shows improvement throughout the day in terms of relative error and operationally feasible modelling.

From the results of modelling it is seen that intense GIC driving can be modelled accurately using limited data. The true performance of the models presented may be even better though as training for the most active part of the Halloween Storm was done on less active periods. Not having a representative training is a distinct disadvantage given any data-driven method. For a more accurate performance metric, a random training (75%) and validation set (25%) (of the same size as the other benchmarking set already presented) is applied for the general layered-Earth profile using the ensemble method. Using training set GICs above the median level, ensemble estimates of $\alpha = -138$ and $\beta = 8$ were derived. Across this 'full day' of data we have a RMSE of 0.73 A, correlation coefficient of 0.86 and relative error of 30%, all comparable the results presented for same dataset size and method in Table 5. Unfortunately, due to the requirement of continuous data, a similar representative randomly sampled training set cannot be tested for the TF approach.

6.3 A Pathological Case

Even when a utility only has access to only poor GIC data, it is nevertheless possible to produce useful GIC estimates. GIC data from Matimba (MAT), at 1 minute cadence and with 1 decimal place accuracy, has not been cleaned for artificial spikes or baseline shifts and is about the limit of what is useful. The MAT node in the South African network has shown susceptibility to GICs in the past, with transformer degradation initiated by the Halloween Storm[15].

For this case, the St. Patrick's Day Storm of 2015 has been used for analysis. This storm is a typical example of a geomagnetic driving expected from a geomagnetic storm arising from a CME, with a minimum SYM-H of -234 nT[206]. Besides the poor temporal resolution, the GIC data has a relatively poor sensitivity of 0.1 A. We further test the robustness of the ensemble methodology by using distant KMH B-field data, comparing it with modelling using the nearer HBK data. No prior information of the Earth's conductivity is used for E-field derivation. Ensemble network parameter estimation is done using no selection criteria, i.e. noise levels are included. Operationally, including all available data with a poor SNR is important as it may have been a long time since there was a previous significant disturbance for training purposes. The inclusion of low-amplitude data in itself is also a test of the usefulness of poor data and robustness of the methodology.

Given the two days of data, 25% randomly selected instances were kept out-of-sample for validation purposes. In an operational context, this relates to 18 hours of data used for training, but it is possible to use less as convergence of the ensemble method using 1 minute cadence is roughly on the order of 8 hours. In the pathological case presented here, with missing and uncleaned data, the TF approach cannot accurately be applied, but the network parameter ensemble approach can – this has direct implications for operational use.

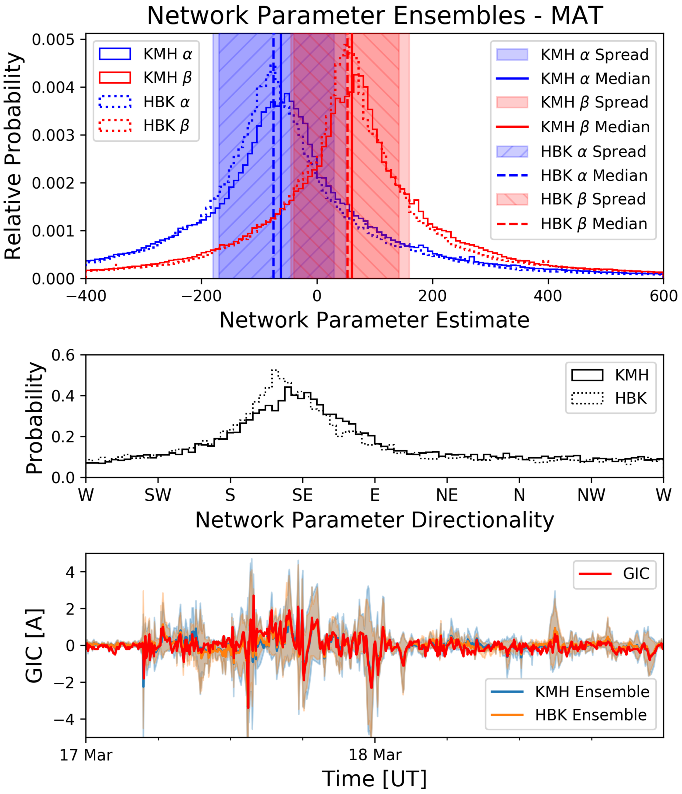

Figure 65: Using raw, uncleaned data for the MAT node in the Eskom network we can nevertheless produce stable network parameter ensembles and prediction bands. In the upper panel, the network parameter ensembles are shown for the nearby HBK B-field and the more remote KMH B-field. In both cases the synthetic general conductivity profile is used to estimate the E-field. The middle panel show the corresponding directionality ensembles, with the lower panel making use of the network parameter estimates and ensemble spreads to generate usable GIC modelling given low-fidelity data.

In the top and middle panels of Figure 65, we have the network parameter ensembles for MAT using two different B-field measurements for the nearby HBK magnetometer (280 km S) and more distant KMH magnetometer (1,120 km WSW). The distance to KMH is extreme and generally thought too be too far for GIC estimation, even at mid-latitudes[152]. In both cases, the E-field is estimated from the synthetic general conductivity profile without being normalised for comparison. For many utilities there simply is no access to conductivity information or nearby magnetometers, which adds to operational suitability of this case.

As expected, the closer HBK B-field measurement has less spread than the KMH B-field. Interestingly the network parameters are relatively stable without normalisation. The estimates of $a = -63$ or -75, and $b = 60$ or 53 for KMH and HBK respectively diverge from previous empirical network parameter estimates of $a = -84.25$ and $b = 44.86$[5] and previous analytical network parameter estimation of $a = 122$ and $b = -23$ done in 2002[204]. The directionality ensemble is also stable and picks up the dominantly south-easterly network seen in Figure 21 (series capacitor to the north). In the lower panel of Figure 65, an operational prediction of the validation set is shown which includes the uncertainty band. For the KMH case, the validation set has an RMSE of 0.25 A and correlation coefficient of 0.83. The RE measure was 26.7% and 81.3% of instances were within the prediction band. Using the nearby HBK B-field, accuracy was improved with the RMSE now 0.23 A and correlation coefficient 0.86. The RE measure was reduced to 20.0% but then 80.7% of instances were within the prediction band. Although marginal improvement is seen, the method adequately tracks uncertainty in the prediction band and even the more distant magnetometer can be used for operational modelling.

Linking to the Halloween Storm where there was damage at MAT, the modelling bounds can used to extrapolate the exposure of the 2015 network. Making use of 2015 GIC levels above median GIC level for training, the relative Halloween Storm exposure including error bounds did not exceed 20 A (Figure 66), assuming there was no large change in the effective network and these two periods are comparable. In this case the network has become more complex since 2003, with the expectation that more GIC could possibly be dissipated in the current network. Comparisons with the larger analytical network parameters of that time seem to support this conclusion. It is however unlikely that the network change reduced to such an extent that they were above the FERC threshold for transformer damage of 75 A per phase[30] when damage occurred, even if the measured peak GIC is underestimated due to 1 minute cadence data.

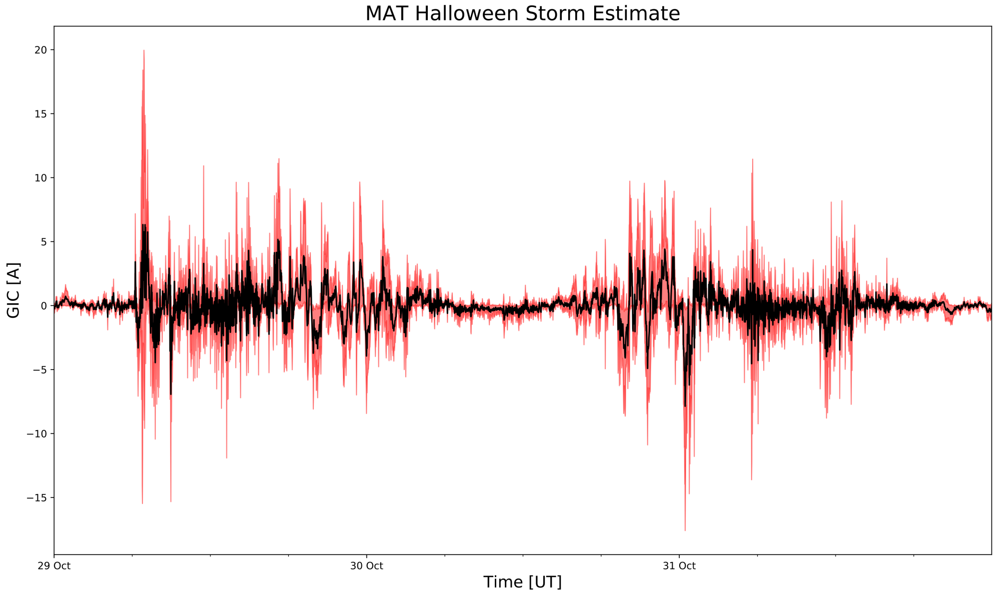

Figure 66: Extrapolating the trained ensembles for MAT using 2015 data, the level of a Halloween Storm type disturbance affecting the 2015 grid can be estimated. Here the extrapolated GIC profile is shown in black, with uncertainty bounds in red.

6.4 A Few Further Cases

Other than operational considerations of modelling using different data fidelities, the ensemble methodology proposed allows for further characterisation of GIC. In Heyns et al.[191], the ensemble methodology has been applied to the BOW node in the Powerlink network in Australia. Section 6.4.1 explores these results and applies the methodology to additional nodes within the Powerlink network. In in similar vein, Section 6.4.2 analyses the results of the ensemble methodology in the geophysically complex case of Memanbetsu (MMB) substation in Hokkaido, Japan.

6.4.1 Applications Down Under

In the testing of the ensemble methodology, BOW, MDR and MUR were all used and found to be consistent with results already shown, although the extent of data is limited and full validation of the TF approach cannot be done with an out-of-sample dataset. For these nodes there further has not been comparable definitive modelling which can be compared to, with only a correlation coefficient quoted[50,155] and regression done post-modelling to define the scale factor (basically fulfilling the role of a network parameter).

A result within previous analytical modelling using a uniform or simple layered-Earth conductivity model is that the modelled GIC at MUR is opposite in polarity when compared to GIC measurements[50,155]. Polarity used by both the GIC monitoring equipment and modelling assumptions in this case is defined by the Australian Energy Market Operator (AEMO) convention (GICs into the ground are positive). When more complicated 3D E-fields have been assumed, then both MUR and MDR have displayed incorrect polarity in modelling[155].

MUR is located in a more complex part of the network that includes lower voltages and coastal effects[134], although it has been shown the east coast of Australia has a reduced coastal effect than would otherwise be expected[155]. Probing this particular node further, we see in Figure 67 a clear directional bias of the E-field towards ENE for large GIC values and N/S for noise levels. Although MUR is coastal, with a ENE coastal effect possible, the network topology is also more complex. Looking at the topology in more detail in Figure 68, we see that the higher voltage 275 kV line at MUR is predominantly north-south, possibly explaining the noise level GIC E-field orientation. Including the lower voltage 110 kV lines, MUR ends up having more east-west contributions possible (the bulk of the network is in a WSW direction relative to MUR), especially if enhanced by general east-west driving from the ring current and coastal effect. In the data-driven mapping of E-field to GIC through network parameters, there is a selection bias towards large or dominating E-field directions. We cannot explicitly split the different contributions, either from geophysical or network related perspective. Using the network parameter directionality ensemble, seen in Figure 69, we generate the net result – which in this case is an easterly effective network direction that would produce positive GICs. Since the bulk of the network is to the west, we expect GICs produced by an easterly E-field to ground at MUR. Assuming the AEMO convention, the resulting GICs would be measured as positive, and no anti-correlation is seen (as has been in conventional modelling). MDR on the other hand shows a cleaner network parameter response and a clear eastward dominance from the 330 kV line in its network parameter directionality (Figure 69).

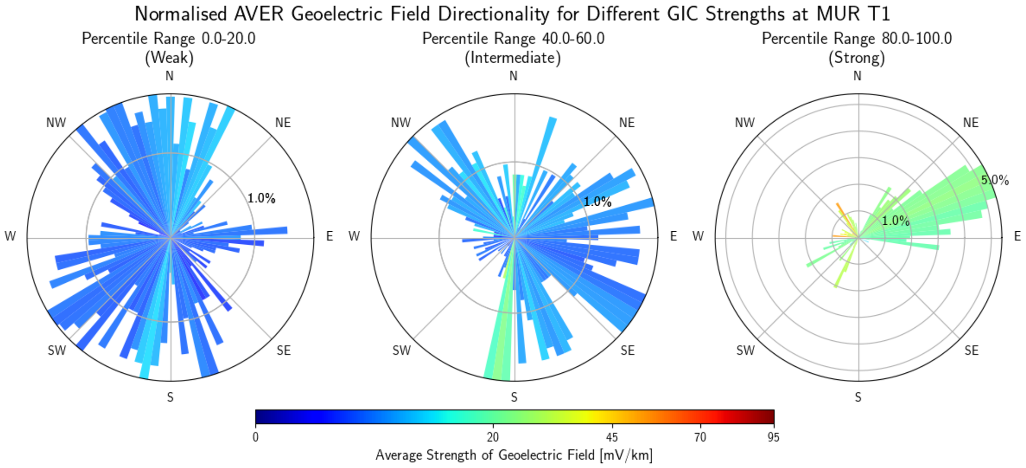

Figure 67: Using a layered-Earth derived E-field, the directionality and strength associated with different GIC magnitudes can be represented. In this case the more complex MUR node in the Powerlink network is shown.

In the case of BOW, the network is less complex and the polarity using different conductivity profiles is consistent[155]. In Figure 70, we see the BOW directionality response for the same storm as MUR and MDR, but with a much cleaner response closely aligned to the 132 kV line that ends at BOW (indicated by a dotted line in the figure, and seen explicitly in the network map in Figure 25). BOW, also being coastal is expected to show a coastal effect, roughly in the same direction as the line itself. What is of interest though is the possible contribution from the larger inland 275 kV line, orthogonal to the BOW line. Evident at higher GIC levels, which is made possible by the ensemble methodology and would not otherwise be seen, is an elevated contribution from the roughly NW

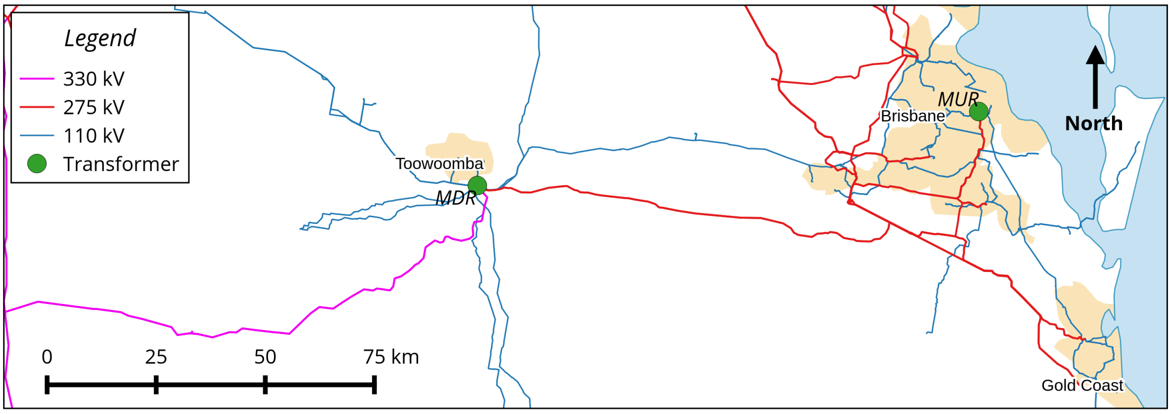

Figure 68: The 330 kV, 275 kV and 110 kV network topologies around the 275/110 kV transformer at MUR and 330/275 kV transformer at MDR.

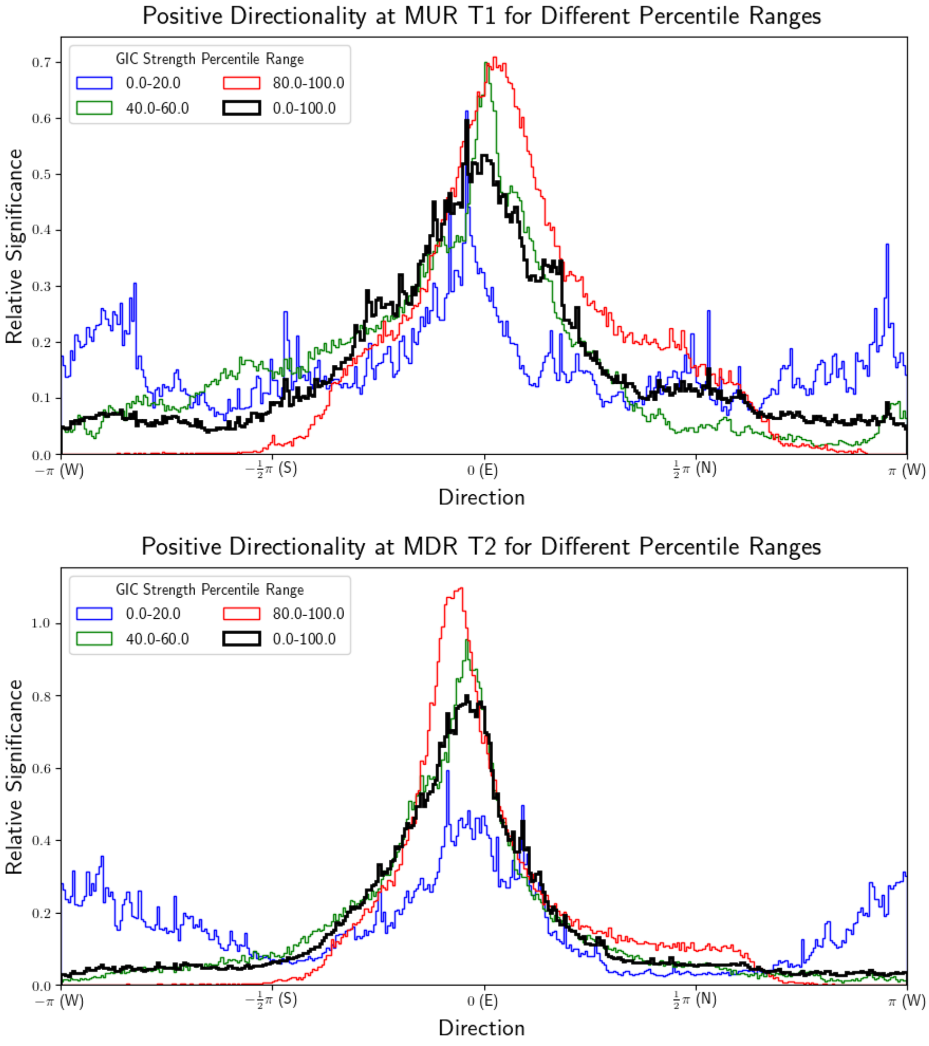

Figure 69: Taking the network parameter defined directionality ensemble and splitting according to GIC magnitude, we also see more complicated contributions in the network parameter defined directionality at MUR and the dominant eastward 330 kV line contribution at MDR.

direction aligning to this more distant but longer higher voltage line. It is possible that contributions from the 275 kV line find their way into the BOW line and ultimately BOW, especially in the case of large driving. In such case, a northerly (NW) direction would be more effective as the majority of the network that acts as an antenna lies to the south of BOW. A southerly (SE) E-field would not be as effective, with only the 132 kV line being applicable.

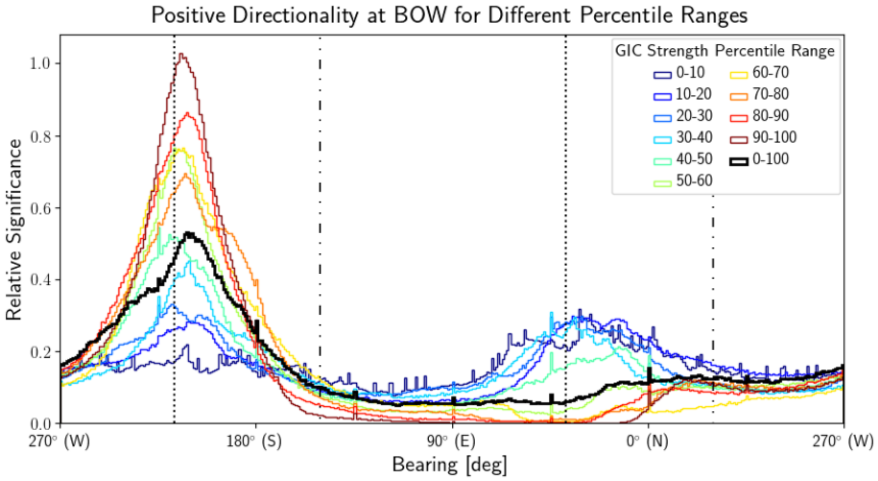

Figure 70: The network parameter directionality is shown for the simpler BOW node, where local line direction is roughly perpendicular to the coastline and denoted by the dotted line. Of interest here is the possible influence of GIC contributions from a line one node away (dash-dot line, and the northerly contribution in particular). With large northerly driving, GIC flow may enter the SW-NE 132 kV line from the larger inland 275 kV SE-NW line. Southerly driving will not have the same effect as the 275 kV contributions will continue through to the rest of the network and only the SW-NE 132 kV line will contribute.

Although there is not enough data to test the TF approach in terms of modelling accuracy on an out-of-sample dataset, the TF response can be computed and analysed. The Powerlink data in this case provides a good validation of high-fidelity data at a 4 second cadence where the SNR of higher frequencies can be tested. An additional test of the method is that the Powerlink data is sampled dynamically, with the highest cadence during disturbed times being 4 seconds. When variation does not exceed a certain threshold, then no data is recorded – the result being a dynamic resolution, with some geomagnetically quiet periods only recording at cadences on the order of minutes.

In Figure 71 we see that similar to the higher cadence data in the TVA network, the use of the B-field in deriving the TF results in a poor multimodal phase response. Training with dB/dt instead, we arrive at a well defined response in Figure 72. Physically, this TF is consistent with what is expected at BOW and the main SW/NE directionality due to network and coast that requires both TF components to contribute. Further, assuming no complex 3D conductivity structures, we expect that the phase responses are directly out of phase with one another (which is what is seen in Figure 72). Both magnitude and phase conditions are satisfied for the TF at BOW. A final remark is the time lag evident at higher frequencies as a curve in the phase. As in the TVA cases, this time lag can be corrected for but does not show any definitive link to geophysical or network related effects.

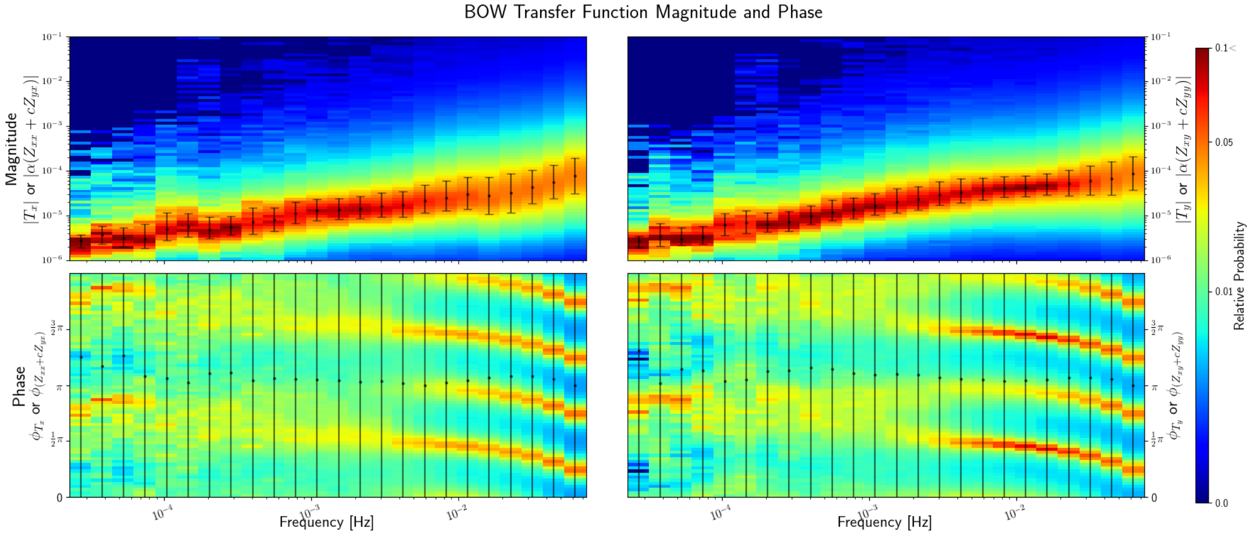

Figure 71: In the BOW case, with limited data and dynamic higher resolution sampling, the ensemble methodology can still derive a TF. In the case the signal-to-noise ratio of the training B-field data results in multi-modal and poorly defined responses in the phase response. For context the temporal lags are not removed.

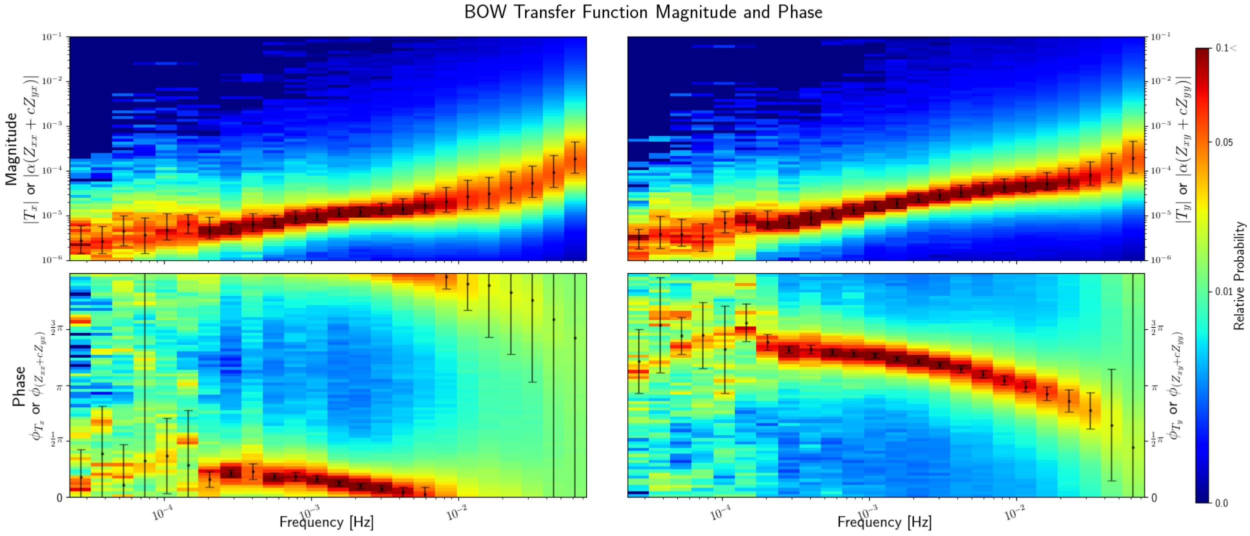

Figure 72: Using dB/dt instead of the B-field improves the signal-to-noise ratio remarkably for BOW and the phase is now well defined and in line with the network parameters previously estimated. For context the temporal lags are not removed.

6.4.2 A Complex Geological Case

The Memanbetsu (MMB) GIC dataset has seen a lot of previous GIC analysis[83,84,98,103,207] and the Kakioka Geomagnetic Observatory has been taking both 1 second cadence B and E-field measurements close to the substation since 2000. Using the long span of geophysical measurements, an accurate MT surface impedance tensor at MMB has been computed, with inductive distortions noted[110,187].

For our purposes of testing the robustness of the ensemble methodology and its use in GIC characterisation, GIC data from the 14-16 December 2006 (JST) geomagnetic storm[83,84,103] is used to first derive network parameter ensembles. The geomagnetic storm in question is comparatively larger than other GIC events analysed at MMB in terms of both GIC and B-field disturbance[83,103]. Measured E-field data at MMB for the period shows large baseline offsets[187]. Instead of correcting for these, an E-field derived using the measured surface impedance tensor is used. Comparing the measured and derived E-field, the general profile shapes are identical[187] but with the derived E-field having correct baseline subtraction and no contamination from artificial noise. In line with previous analysis and as suggested by Fujii et al.[187], the high-frequency data was resampled to 1 minute cadence for higher confidence in the E-field response. The resulting ensembles using only GIC instances above the median to suppress effects from noise are shown in Figure 73 and have network parameter estimates of $\alpha = 133.7$ and $\beta = -270.2$. This result diverges from previous analysis by Watari[103] both in terms of magnitude and directionality.

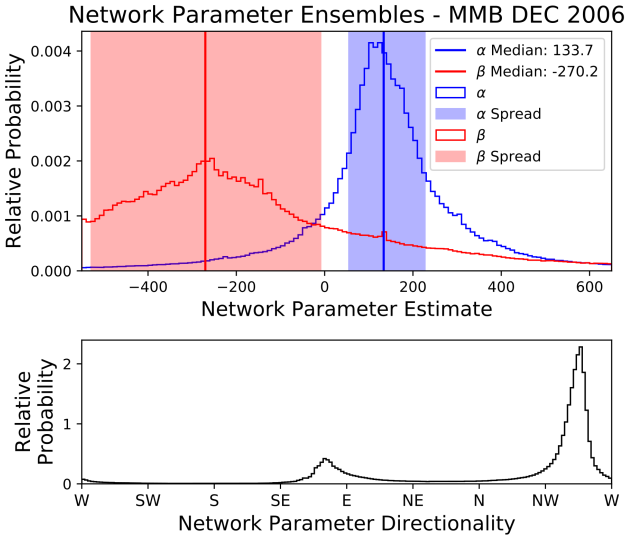

Figure 73: In the geologically complex MMB region, using a single E-field estimate gives an interesting directional response that is more aligned to the lower voltage network than the main line to Ashoro power station.

Before comparing to previous network parameter estimates, it pays to look at the assumption of a single site E-field being used. In previous empirical analysis, this particular storm has been modelled very accurately as a validation set of a quasi-TF approach[84]. This quasi-TF approach is the same as used in deriving a local 1D layered-Earth conductivity at GRS, but here for a much more complex geophysical structure given a conductive upper layer. Due to the quasi-TF approach being trained on a different storm to the validation set, but still being generalisable and accurate suggests that there were no obvious network changes. Deriving the conductivity profile for GIC measurements means that the effective averaged response of the network is absorbed. More common at MMB has been the use of the single site E-field measurement available. Without taking into account the E-field response over the network, modelling performance breaks down completely. Watari[103] used this single site E-field estimate with best-fit empirical network parameters that assume Gaussian error and modelling was out by a factor of 2. When trying to reproduce the result using the same data, rederived empirical network parameters using the same relations were found to be larger ($a = 38.1$ and $b = -7.4$ initially versus $a = 108.6$ and $b = -223.7$ when rederived). Interestingly, the rederived relations result in similar magnitude and directionality responses to the ensemble result. It is not clear where this discrepancy within previous analysis lies. Independently, Weigel and Cilliers[98] used a single site E-field and alternate empirical network parameters that were larger, but still with significant error in modelling. Instead of a single estimate, multiple network parameters estimates were computed and it is apparent that the b parameter had significant spread. The ensemble result similarly shows large spread in the β parameter compared to the better defined α parameter, which may also be associated with the more dominant E_x[187].

Where the ensemble result diverges from all previous studies is in the effective network directionality using single site E-field measurement. Most studies, including empirical estimation, consider the NE high voltage 187 kV line from Ashoro power station to MMB to be the main contributor to GICs at MMB[84,103]. Recent research has suggested a diversion to the NW, orthogonal to the main HV line[98]. The ensemble network parameters in this case suggest a similar WNW directionality, but with the caveat that the β component has huge spread compared to the better defined α parameter. As mentioned before, the empirical network parameters will absorb not only the network topology but also the geophysical aspects. At MMB, besides distortion noted[187] there would be a large coastal effect along with a possible large conducting region eastward[103]. The bathymetry is in agreement with deep water eastward and the coastal effect perpendicular to the main axis of the island chain[207].

Tied in with the geophysical considerations is the possible inclusion of lower voltage network connections in the neutral measurements. In other networks, the inclusion of the connected network has shown to have significant effects[101,154]. In the case of MMB, the connected lower voltage 66 kV network runs in a roughly westerly direction possibly aligning with contributions from geophysical conditions. Similar to MUR in Australia, care should be taken when interpreting the neutral GIC measurement when compared to line GIC in general. The GIC measured in the neutral is the difference of the currents in the windings and polarity of the current in the different voltage bus nodes is important[155]. When analysing directionality, the network as a whole should be taken into account – in this case not excluding the possible contribution from the 66 kV line. When there is uneven distribution of GIC in the bus nodes within a substation where there may additionally be common grounding, the result may be more complex. Although more complicated topologies with multiple lines often dissipate GIC, these regions would also require more accurate network parameter estimates.

For the geomagnetic storm in question, which although the largest of recorded GIC events, peak GIC driving was only a few ampere. With such low susceptibility, the GIC SNR is low during moderate storms and contributions from other voltage levels may generally not be seen. When a more intense geomagnetic storm occurs, the disturbance field at mid-latitudes is driven by the east-west ring current and induction effects from the coastline at MMB would contribute to an elevated east-west E-field, i.e. there is dominant E-field direction that may create a selection bias in data-driven mapping between E-field and GIC. Alignment in such a case favours the lower voltage lines, which may contribute similar GICs to the less aligned 187 kV line – resulting in the increased β parameter spread and effective WNW directionality seen.

As part of recent research into the base assumption of a resistive network for GIC modelling, Weigel and Cilliers[98] made use of the single E-field measurement at MMB to derive the frequency dependence of the network parameters. The result was an estimated low-pass response of the network. At PAR, with a higher voltage network and larger transformers but possibly simpler geology, it was found that the resistive assumption is adequate. A similar test can be done in the case of MMB to validate previous research.

Using a similar ensemble estimation of the TF components between E-field and GIC, a much flatter

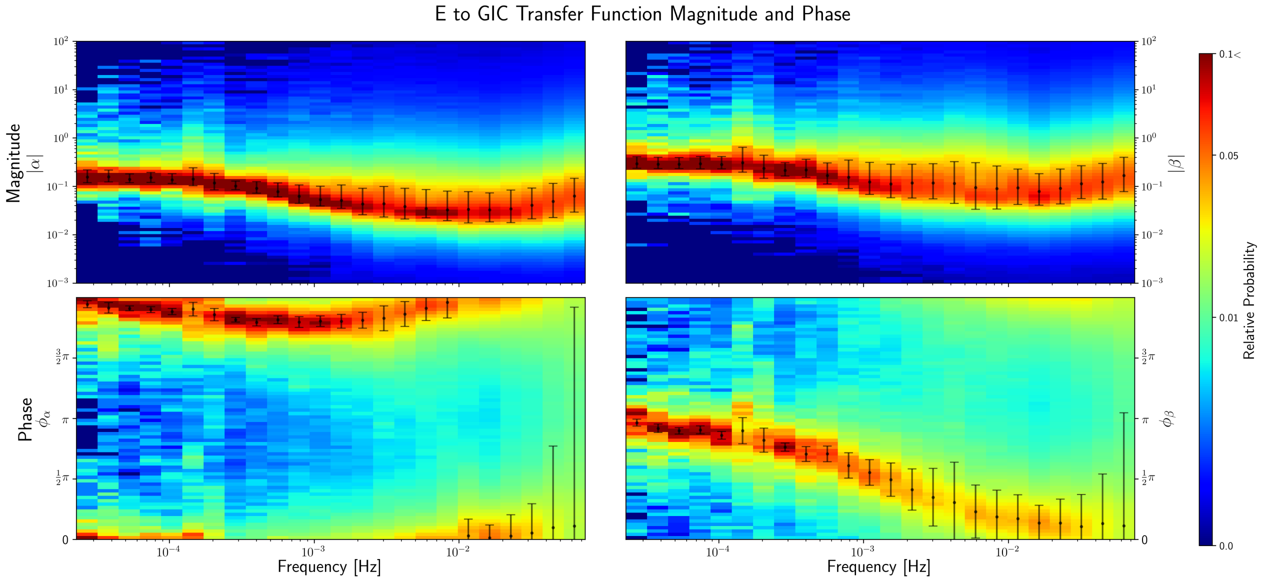

Figure 74: Looking further at MMB, a single E-field estimate may not suffice for GIC modelling. Here the required additional frequency contributions are absorbed into the network parameters, with the result no longer being a flat, constant response.

E-field-to-GIC TF magnitude and phase response was found, the result being near resistive and not low-pass. This result is more in line with the fact that the slopes of the frequency response of the E-field and GIC are similar[174]. Figure 74 shows the magnitude and phase for a time shift corrected response using 4 second cadence data. At lower frequencies the response is well defined, with magnitude flat and phase of network parameters correct. At higher frequencies this breaks down to some extent, with magnitude still well defined but not phase. Specifically, the network parameters are not orthogonal, which explains the difficulty in modelling GIC response using only this single site. Higher frequencies are associated with shallower geophysical structures, which may further indicate the existence of the shallow conducting layer seen in previous work. Of the two parameters, the $\alpha(\omega)$ TF is better defined, relating to the α network parameter being better defined. Both versions of the α parameter in turn relate to the north-south contribution of the network, which most likely is driven by the HV line from Ashoro power station. The variation in the E-field-to-GIC TF components is significantly smaller than that reported by Weigel and Cilliers[98]. Such variation is more likely due to variable E-field over the network footprint, including the lower voltage connection, than a network response which would have also been seen at PAR previously shown. Also to note is that the estimation of the TF by Weigel and Cilliers[98] included multiple days, where this estimation was achieved with a couple of days and a single storm. In the case of a non-stationary system or multiple storms there could indeed be more variation.

Single site E-field measurements can be misleading, but network effects cannot wholly be ruled out. At a high temporal resolution there is often a lag apparent in driving E-field and GIC, especially seen during distinct events such as SSCs. Separating the different drivers of this lag is not trivial and the best validation of this response would be in laboratory tests and simulations of transformers under real induced current conditions.

6.5 Summary

In this chapter, the proposed data-driven approaches using ensemble estimation have been rigorously tested in six installations in four different regions of the world. Despite significant differences in cadence and quality of GIC data, distance from a geomagnetic observatory and high SNR, the ensemble approach consistently identifies the direction and magnitude of network parameters (from one data extreme at PAR in the TVA network to the other extreme at MAT in South Africa). The robust methodology developed means useful GIC modelling is possible, even in cases with low data fidelity.

Comparing the ensemble methodology with previous empirical modelling at GRS in South Africa, the ensemble methodology has been shown to perform better. In comparing modelling using different levels of data fidelity at PAR in the USA, closer B-field measurements gives better results (narrower distribution), but a more complex ground conductivity does not necessarily do the same. Following up from previous work by Heyns[208], the variation in ensemble network parameters due to different driving regimes is confirmed using high-fidelity data at PAR.

Further validation at MUR, MDR and BOW in Australia and MMB in Japan demonstrate the confounding of simple approaches by coastal effects and associated higher or lower voltage lines in the vicinity. At MMB, with its complex geological structure, it has been shown that single E-field measurements are not representative of E-field driving in a network. Using this single value of measured E-field the resistive approximation shown to be invalid recently by Weigel and Cilliers[98] was confirmed, although not to as extreme an extent. In contrast, a similar analysis at PAR results in flat phase response in the E-field to GIC mapping, suggesting the resistive approximation is adequate when the effective E-field is correctly defined.

Looking at the frequency domain modelling in specific, it was shown that the use of dB/dt training for the B-field-to-GIC TF creates stable and accurate responses given spectral scaling that includes higher frequencies. In typical training using the B-field alone, the poor SNR results in poorly defined TFs given higher cadence data (less than 1 minute) with physically incorrect with multimodal phase responses. Including g and h ensemble parameters[191], analogous to the time domain network parameters, allows operational modelling in both cases with uncertainty estimation for the first time.

The ensemble estimation methodology has shown to absorb geophysical aspects of GIC modelling in generating an effective directionality response not necessarily aligned with the local network. With minimal data, a utility can have a accurate real-time picture of the network and susceptible nodes.

7 Improved Interpolation of the Geomagnetic Field

In the previous chapter, it has been important to develop robust empirical approaches that directly map B-field measurements to GICs. In this sense the ensemble estimation methodology (with ensemble spreads that include B-field error) allow remote magnetometers to be used effectively in GIC studies. Coupled with ring-current driving of a near plane-wave at mid-latitudes, interpolation is not always needed to obtain useful GIC estimates from empirical modelling where scaling is absorbed[106]. That said, the analysis of the ensemble methodology has shown that improved B-field representation improves the estimation of network parameters, transfer functions and ultimately GICs. It is therefore useful to improve the B-field interpolation approach and allow for better B-field modelling in sparsely instrumented regions/networks. To note, the general applicability of this chapter allows it to stand alone from the GIC modelling focus of previous chapters.

The sparse coverage of high-fidelity magnetometers is largely due to the cost of equipment and maintenance associated with operating a geomagnetic observatory. It is more feasible for a utility to use variometers, with some idea of the uncertainty involved. Variometers in this case refers to lower cost magnetometers that are not observatory grade (often not temperature controlled, which may affect measurements). These variometers do not accurately measure the absolute B-field, but rather the B-field variations (per timestep). Improvements to B-field interpolation in Section 7.1 focus on the inclusion of variometers, with general uncertainty in interpolation addressed in Section 7.2.

As a basis for interpolation, the planar version of the SECS interpolation scheme as described in Section 3.5 has been used in southern Africa for a number of different studies[106,152,157]. At higher latitudes with closer and more variable current systems, a planar approximation over similar length scales may not be appropriate. As the mid-latitude driving current system is largely the ring current, which is situated a few R_E from Earth, the planar approximation over a couple of thousand kms holds. A typical result of the interpolation scheme is seen in Figure 75, where the B-field is interpolated. Interestingly enough, other mid-latitude regions have not found as much success with the use of SECS interpolation when the main driving current system is the ring current and not Hall-type divergence-free current nodes as seen at high-latitudes[124,163].

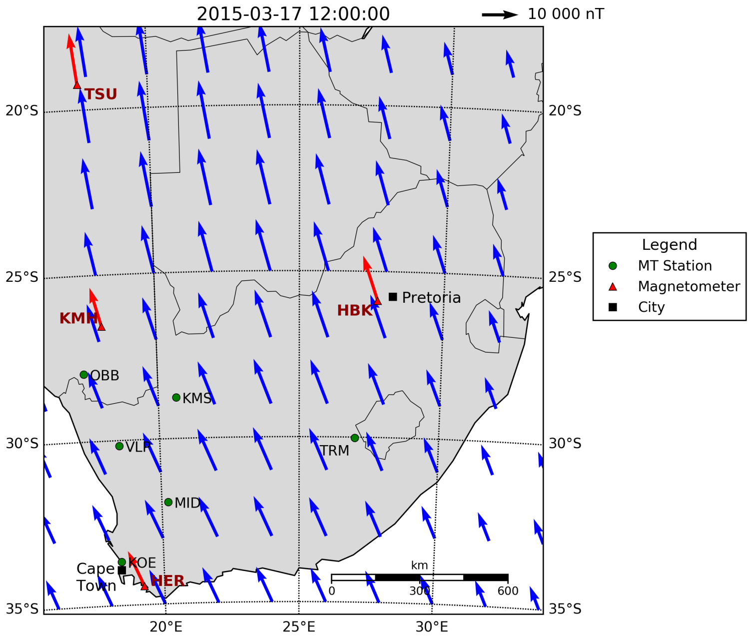

Figure 75: The resulting interpolation using a planar implementation of SECS in southern Africa is shown here for an interpolation grid, with the MT sites used for validation also indicated[176]. Red arrows indicate the measured B-field used to drive the interpolation (blue arrows). INTERMAGNET observatories are indicated by red triangles and MT variometers are indicated by green circles.

Table 6: Data coverage of variometers in southern Africa for SECS validation. All the sites in this case come from magnetotelluric measurements.

MT Station		Date Range Start	End
Hermanus	(HER)	5 Apr 2012	15 Aug 2012
		8 Jan 2015	27 Jan 2015
Hartebeesthoek	(HBK)	1 Nov 2013	7 Jan 2015
Kakamas	(KMS)	1 Sep 2013	19 Oct 2015
Middelpos	(MID)	6 Jul 2012	7 Nov 2012
Obib	(OBB)	30 Aug 2013	11 Dec 2014
		17 Sep 2015	11 Dec 2015
Vaalputs	(VLP)	22 May 2012	9 Nov 2012
		25 May 2014	14 Feb 2015

Table 7: Comparison of results from SECS interpolation or INTERMAGNET sites as compared to the MT site measurements of the B-field.

MT Station	Comparison Type	RMSE [nT]	Correlation Coefficient
HER	INTERMAGNET	16	0.82
HBK	INTERMAGNET	16	0.68
KMS	SECS	4	0.99
MID	SECS	4	0.99
OBB	SECS	8	0.93
VLP	SECS	17	0.76

To test the validity of the interpolation scheme previously used, the accuracy of the SECS interpolation scheme can be measured against a number of variometers available in southern Africa. Table 6 below shows various periods of measured B-field at magnetotelluric (MT) sites that then can be used to validate interpolation accuracy. Of the MT sites used, HER and HBK are co-located with INTERMAGNET stations and the general accuracy of MT variometer measurements can be compared to observatory-grade magnetometer measurements. As described in Section 4.3, an estimated baseline main field is estimated to allow for correct rotation of the HDZ measurements to XYZ for comparison. For interpolation, a current node grid spanning an area larger than the interpolation region is used, with distances between current nodes roughly 100 km. The height of the equivalent current system is taken as 100 km. B-field data from HER, HBK, KMH and TSU INTERMAGNET sites are used to drive the interpolation.

From the resulting comparisons in Table 7, the difference in B-field measurements at co-located INTERMAGNET observatory magnetometers and field variometers is larger than the difference between SECS interpolation and similar variometers at remote sites. The comparison suggests planar SECS interpolation scheme seems to do just as well as having a variometer available – in effect validating previous use of the SECS method for GIC applications in southern Africa. This does however raise the question of why exactly does planar SECS do so well in southern Africa, and not at other mid-latitudes where implemented[124]? This question leads to a further improvement in B-field interpolation, namely mid-latitude representative basis functions, which is addressed in Section 7.3.

7.1 dSECS: Including dB/dt Interpolation

Although there is a sparse grid of high-fidelity INTERMAGNET geomagnetic observatories at Hermanus (HER), Hartebeesthoek (HBK), Tsumeb (TSU) and Keetmanshoop (KMH) in southern Africa, many other regions globally have even fewer stations available. Variometers are much more common worldwide. In southern Africa, two comparable LEMI-250 fluxgate magnetometers used for pulsation studies (adequate frequency range) at Sutherland (SUT) and Waterberg (WAT) can be used as variometers along with LEMI-417M magnetotelluric sites at Kakamas (KMS), Trompsberg (TRM), Obib (OBB), Vaalputs (VLP), Middelpos (MID) and Koeberg (KOE). Including the additional information from the denser variometers array can improve the B-field interpolation.

Variometers are not absolute, but they can measure the change in the B-field very accurately, i.e. $dB/dt = B(t_i) - B(t_{i-1})$. Since the SECS interpolation scheme is entirely linear in time, reusing at the formalism from Section 3.5 we can see that dB/dt can be interpolated in the same way as B using the same mapping (as previously noted, the transfer matrix T spatially relating the current nodes I and B-field measurements B is constant). The only difference in this case is that current nodes used for interpolation (I) becomes the current node variation (dI/dt),

$$\begin{aligned} B(t_i) - B(t_{i-1}) &= T \cdot I(t_i) - T \cdot I(t_{i-1}) \\ &= T \cdot (I(t_i) - I(t_{i-1})) \\ dB/dt &= T \cdot dI/dt. \end{aligned} \tag{54}$$

Here a point of notation should be stressed. dB/dt as used for the dSECS interpolation scheme refers not to the baseline subtracted B-field as usually defined in SECS interpolation (i.e. $B(t_{0,\dots,n}) = B(t_{0,\dots,n}) - B(t_0)$), but rather the time difference dB/dt defined for each time instance.

Magnetometers can of course act as variometers, with the implication that there will be more variometers available than absolute magnetometers. Given a larger number of variometer measurements, the confidence in dB/dt interpolation would be higher than that for B. dB/dt is also what is typically used for geoelectric studies and is interchangeable with the B-field in the frequency domain. Using the greater interpolation accuracy of dB/dt, we can improve the interpolation of B that likely has a higher fidelity baseline (such as would be the case in interpolation using only INTERMAGNET stations). In order to do this, we consider the two time series of B and dB/dt. Let us assume B is of length $N + 1$ and hence dB/dt is of length N. Given a set of perturbations ϵ, the two resulting time series can be equated,

$$\begin{aligned} dB_1/dt &= (B_2 + \epsilon_2) - (B_1 + \epsilon_1) \\ &\cdots \\ dB_N/dt &= (B_{N+1} + \epsilon_{N+1}) - (B_N + \epsilon_N). \end{aligned} \tag{55}$$

This can then be rewritten in a matrix equation of the form $A\vec{x} = \vec{b}$,

$$\begin{array}{cc} & \xrightarrow{\quad N+1 \quad} \\ N\Bigg\downarrow & \begin{bmatrix} -1 & 1 & 0 & \cdots & 0 \\ 0 & -1 & 1 & \cdots & 0 \\ \vdots & \ddots & \ddots & \ddots & \vdots \\ 0 & \cdots & 0 & -1 & 1 \end{bmatrix} \end{array} \begin{bmatrix} \epsilon_1 \\ \epsilon_2 \\ \vdots \\ \epsilon_{N+1} \end{bmatrix} = \begin{bmatrix} dB_1/dt + B_1 - B_2 \\ dB_2/dt + B_2 - B_3 \\ \vdots \\ dB_N/dt + B_N - B_{N+1} \end{bmatrix}. \tag{56}$$

Although the sparse matrix A is non-square, it has a very well behaved and analytical quasi-inverse that does not need to be estimated through SVD.

$$A^{-1} = \begin{bmatrix} -1 & 1 & 0 & 0 & \cdots & 0 \\ 0 & -1 & 1 & 0 & \cdots & 0 \\ 0 & 0 & -1 & 1 & \cdots & 0 \\ \vdots & \vdots & \ddots & \ddots & \ddots & \vdots \\ 0 & 0 & \cdots & 0 & -1 & 1 \end{bmatrix}^{-1} \tag{57}$$

$$= \overset{\xrightarrow{\qquad\qquad N \qquad\qquad}}{\begin{bmatrix} -\frac{N}{N+1} & -\frac{N-1}{N+1} & -\frac{N-2}{N+1} & \cdots & -\frac{1}{N+1} \\ \frac{1}{N+1} & -\frac{N-1}{N+1} & -\frac{N-2}{N+1} & \cdots & -\frac{1}{N+1} \\ \frac{1}{N+1} & \frac{2}{N+1} & -\frac{N-2}{N+1} & \cdots & -\frac{1}{N+1} \\ \vdots & \vdots & \ddots & \ddots & \vdots \\ \frac{1}{N+1} & \frac{2}{N+1} & \cdots & -\frac{2}{N+1} & -\frac{1}{N+1} \\ \frac{1}{N+1} & \frac{2}{N+1} & \cdots & \frac{N-1}{N+1} & -\frac{1}{N+1} \\ \frac{1}{N+1} & \frac{2}{N+1} & \cdots & \frac{N-1}{N+1} & \frac{N}{N+1} \end{bmatrix}} \Bigg\downarrow \scriptstyle N+1 \tag{58}$$

$$AA^{-1} = \mathbb{1}(N \times N) \tag{59}$$

$$A^{-1}A = \overset{\xrightarrow{\qquad\qquad N+1 \qquad\qquad}}{\begin{bmatrix} \frac{N}{N+1} & -\frac{1}{N+1} & -\frac{1}{N+1} & \cdots & -\frac{1}{N+1} \\ -\frac{1}{N+1} & \frac{N}{N+1} & -\frac{1}{N+1} & \cdots & -\frac{1}{N+1} \\ -\frac{1}{N+1} & -\frac{1}{N+1} & \frac{N}{N+1} & \cdots & -\frac{1}{N+1} \\ \vdots & \vdots & \ddots & \ddots & \vdots \\ -\frac{1}{N+1} & -\frac{1}{N+1} & \cdots & \frac{N}{N+1} & -\frac{1}{N+1} \\ -\frac{1}{N+1} & -\frac{1}{N+1} & \cdots & -\frac{1}{N+1} & -\frac{1}{N+1} \\ -\frac{1}{N+1} & -\frac{1}{N+1} & \cdots & -\frac{1}{N+1} & \frac{N}{N+1} \end{bmatrix}} \Bigg\downarrow \scriptstyle N+1 \tag{60}$$

$$\approx \mathbb{1}(N + 1 \times N + 1) \text{ for } N \gg 1 \tag{61}$$

Since all the components in $\vec{b}$ are known, this quasi-inverse approach is again used to solve for the perturbations $\vec{x}$. Each original interpolated B_i time instance is updated by its corresponding perturbation ϵ_i, with the resulting base B-field interpolation now constrained by the more accurate interpolated dB/dt.

Similar to previous validation of the traditional SECS interpolation, an elementary current grid spanning 34.5-18.5°S and 6.5-28.0°E was used, which is roughly 1,200 km in the east-west direction and 1,700 km in the north-south direction. This grid had dimensions 13 x 18 in these respective directions, relating to a grid spacing of roughly 100 km in both directions. In preprocessing the data, a baseline B-field estimate using EMM2017 (`https://www.ngdc.noaa.gov/geomag/EMM/index.html`) was again subtracted to allow the dSECS method to focus on the external contributions. The EMM2017 model aims to estimate the the main field, including crustal contributions, and any deviations would be able to be reproduced by the interpolation scheme. In this case, the driving ground measurements come from the HER, HBK and TSU INTERMAGNET sites for a general SECS interpolation and these are supplemented with pulsation magnetometers at Waterberg (WAT) and Sutherland (SUT), and the MT station at Kakamas (KMS) for dSECS interpolation, as shown in Figure 76.

To ensure accurate validation in comparison to typical SECS implementation, the KMH INTERMAGNET station is used for validation across 4 different geomagnetic storms in 2015 where data for all sites was available. There were some data gaps as a result of instrument availability, but the resulting validation set included quiet time, sudden storm commencements, main phases and recovery phases. Figure 77 shows the resulting dSECS interpolation of dB/dt and Figure 78 shows the resulting time series for the B-field components separately during the June 2015 storm. For this specific storm, using a 24 hour period of disturbed time from 06:00 UT on 22 June 2015, the skill score defined by $P = 1 - \frac{RMSE}{\sigma}$ (where σ is the standard deviation of the measured quantity[101,124]) the dSECS implementation was 0.93 (0.83) as compared to 0.84 (0.73) for SECS in terms of the B_x (B_y) component. Besides the general accuracy of modelling (a P value of 1 reflects zero residuals and indicates perfect modelling), there is an overall improvement of 10% given dSECS implementation.

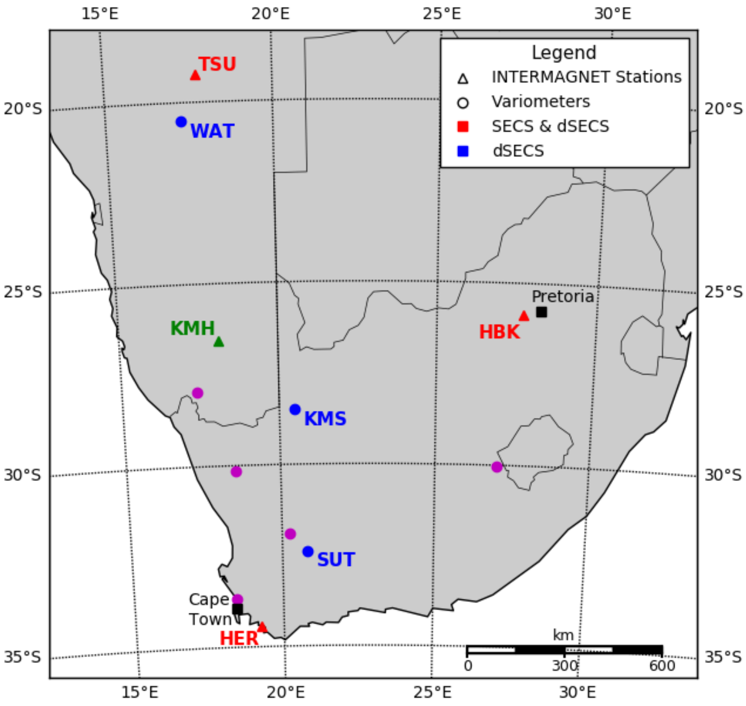

Figure 76: Making the most of the B-field measurements in southern Africa, variometers, magnetometers and MT stations can be used for B-field interpolation[176]. The KMH INTERMAGNET station (green triangle) is used for validation in this work, with the other INTERMAGNET stations (red triangles) used for SECS interpolation and variometers (blue circles) used for dSECS interpolation. Other possible MT variometers with no data coverage for this period are indicated by purple dots.

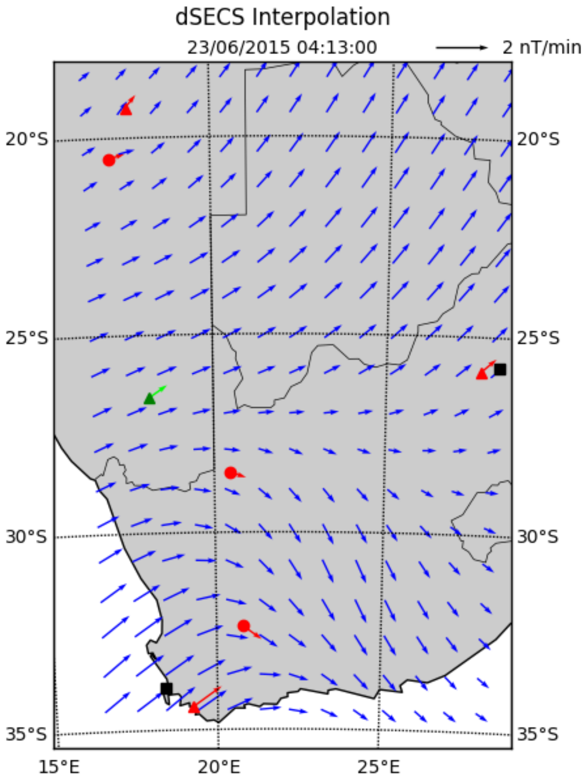

Figure 77: Making use of the dSECS methodology, a typical dB/dt interpolation is shown (blue)[176]. Here the red arrows are measured dB/dt at either the magnetometer (triangles) or variometer (circles) sites used to drive the interpolation, and KMH observatory (green) acts as a validation node.

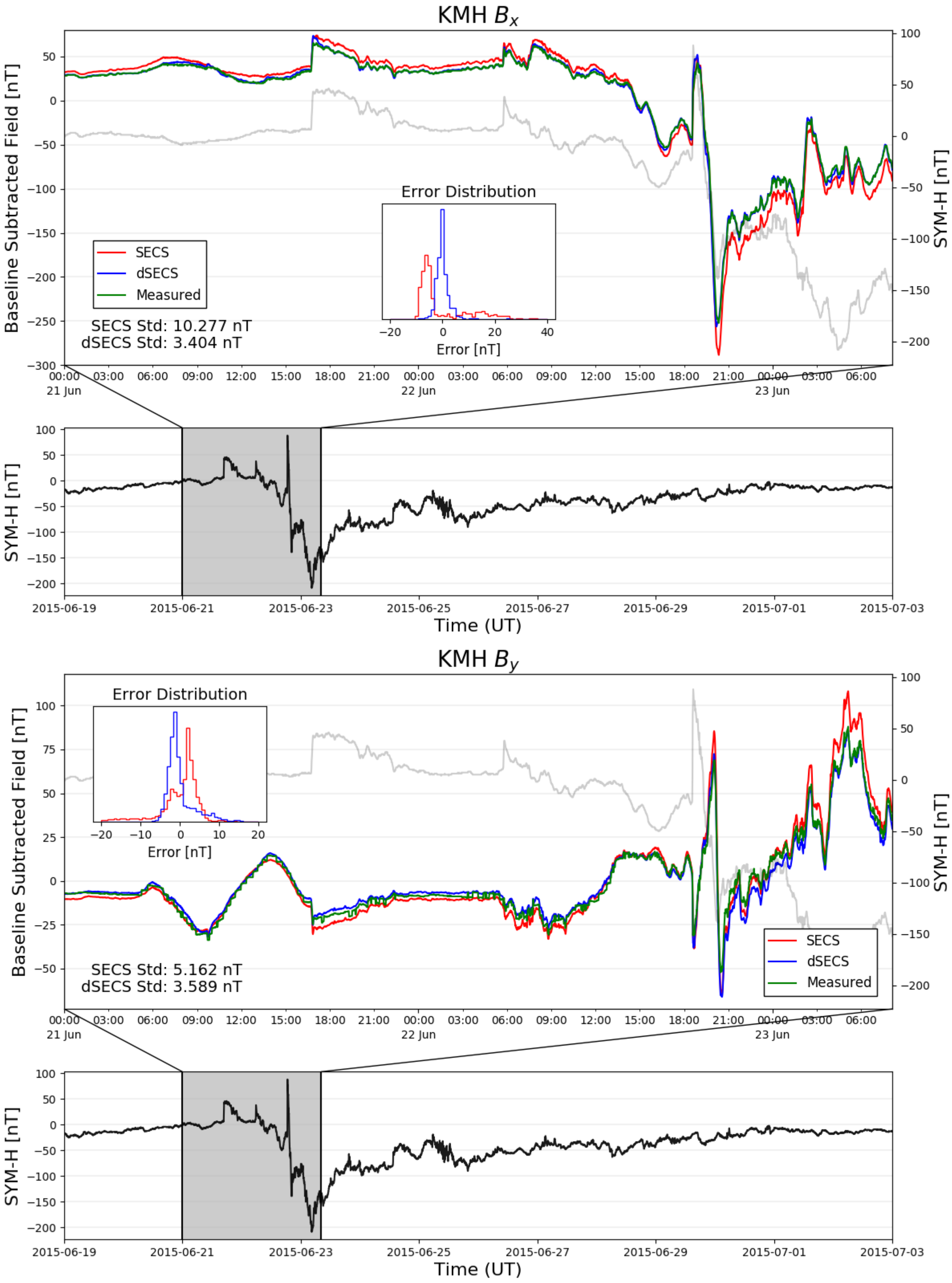

Figure 78: Optimising the use of the available assets improves the interpolation performance significantly as can be seen here for the KMH validation node in both B-field components[176]. Particularly evident is the off-set between the dSECS and SECS models, the dSECS model more closely matching observation. Also shown is the SYM-H index in grey, which gives an idea of performance of the interpolation relative to disturbed time.

More explicitly, the error distributions across all storms are shown in Figure 79. Across these total error distributions it is evident that including the variometers improves B-field interpolation. In all B-field components, the standard deviation is reduced for the dSECS method (between 38-52% improvement). The dSECS error distributions also tend more towards Gaussian error distributions in comparison to the typical SECS method. A more Gaussian profile is suggestive of less systematic error and more random or sampling error. An example of such sampling error would be a known decimal point rounding issue within KMH dataset used. Of the B-field components, the B_y component benefits most from the inclusion of a denser variometer array. At mid-latitudes, the B_y component is more typically associated with induction effects, which in turn tend to be more localised. The addition of more local variometers is likely what drives this improvement. The B_x component in comparison is most affected during storm times, possibly linking to the slightly less Gaussian error distribution. Taking both components into account, the total horizontal field error shows a roughly Gaussian error distribution which is improved by the inclusion of variometers (and more measurements).

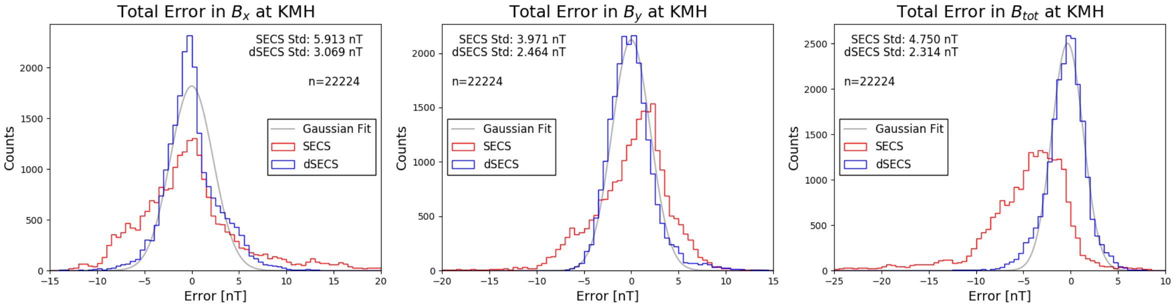

Figure 79: Over an extended period, making use of the dSECS method results in error spreads near to normal and significantly narrower than the SECS method alone[176].

7.2 Uncertainty in Interpolation

In order to obtain an uncertainty estimate in the interpolation scheme, there is a need for two distinctly separate uncertainty estimates. The first of these lies in the model used and the limitations of what is possible in terms of representation. A simple example is that within the same interpolation implementation, edge nodes are less accurately interpolated when compared to central nodes where more neighbouring data points can help constrain the end interpolation. In SECS interpolation implementations up to now there have been no estimates of the uncertainty due to the model alone. The second source of uncertainty lies in the geophysical variation being modelled. Again there are certain limitations with what is possible given scale lengths of variations and density of ground B-field measurements, i.e. does interpolation miss fine scale structure that has an extent less than the spacing between ground magnetometers?

As a broad framework for the development of uncertainty modelling of an interpolation scheme, we will assume that the main current driver at mid-latitudes is the ring current. In terms of the equivalent current system needed, the expectation is that the current sheet is relatively uniform with little to no fine scale structure. Using this as the base assumption, it is proposed that there exists some variation in the equivalent system due to fine scale current structure and induction in the Earth. There would also be edge effect artefacts given a finite interpolation grid. Making assumptions or using a synthetic dataset that can provide a baseline truth, i.e. all current nodes are independently defined with an equal number of ground nodes and we no longer deal with an underdetermined problem. Using this baseline case, we would be able to estimate the typical variation for each grid node and this can be used as the assumed uncertainty for current nodes in general, loosely termed here as physical uncertainty. When implementing interpolation over sparse ground nodes, not all current nodes are equally well determined, i.e. there are different levels of uncertainty associated with nodes relative to the inversion model. Using the initial model uncertainty, as determined by the inversion model, we can scale the general node specific physical uncertainty of the baseline. Inverting the result, we end with model specific and physically inspired uncertainty of the interpolation method at any point.

To estimate modelling uncertainty, we need to start by revisiting the computational step of the interpolation scheme. At its heart SECS interpolation is a standard inverse problem, defined by $B = T \cdot I$, where T is a matrix that encodes the physical spatial relation between current and ground nodes, as defined by the Biot-Savart law (38). Furthermore, we can say that the inverse problem defined by (39) is underdetermined, with no unique solution possible. Using a more general formalism from inverse theory, this inverse problem has the form of $Gm = d$, where G (or T) is the data kernel, m (or I) contains the model parameters and d (or B) is the measured data.

In reality, measured d results in estimated m_{est} and not necessarily the true model parameters. This estimate of model parameters is found by picking parameters that get as close to the measured data as possible, i.e. the objective is to minimise $|Gm_{est} - d| = |d_{est} - d|$. The exact measure of length or minimisation is variable, with the least squares approach being the most common. When dealing with an underdetermined problem, such as is the case with the SECS model, the form of the least squares solution changes to a minimum length solution.

Assuming we have some generalised inverse G^{-g}, where $^{-g}$ refers to the generalised inverse of matrix G, there are two useful concepts that add insight into the inverse problem. Firstly, we have resolution matrices with subsets of model (R) and data (N) resolution matrices[209]. Simply put, these matrices relate the true and estimated quantities (model parameters and data) of the inversion problem. The data resolution matrix, defined as $N = GG^{-g}$ ($= \mathbb{1}$ for an underdetermined problem) is a measure of how well the modelled data matches the measured data. Explicitly, the data resolution matrix satisfies $d_{est} = Nd_{meas}$. Conversely, the model resolution matrix, defined as $R = G^{-g}G$ ($\neq \mathbb{1}$ for an underdetermined problem) is how well resolved/independent the model parameters are. Explicitly, the data resolution matrix satisfies $m_{est} = Rm_{meas}$. If this matrix is not an identity matrix, then the parameters are a weighted average of the true model parameters. The model resolution matrix in turn allows us to see the contributions for each element in the model. Of the two resolution matrices, the model resolution matrix will be most useful in determining uncertainty in the interpolation problem. The second useful concept from inverse theory is that of the covariance matrix (unit), defined as $G^{-g}G^{-gT}$ for an underdetermined problem. These matrices are more often used in analysis and characterise the amplification of error due to the data through the inversion, which can be thought of as a subset of model uncertainty defined by the data or measurement. An important point to note here is that all the matrices mentioned are computed solely from the data kernel or mapping. Hence all inversion model analysis can be done independently of data and set-up optimised.

A last consideration before defining the interpolation uncertainty framework is the choice of inversion method. There are a number of different inverses that can be used, each with pros and cons, some purely data-driven and some including a priori information. Besides the SVD approach usually used with SECS interpolation, there is the minimum length approach ($G^T(GG^T)^{-1}$), with its damped ($G^T(GG^T)^{-1} + \epsilon^2 I$) and weighted ($W_m G^T(GW_m G^T)^{-1}$) versions[209]. In these cases, either an ϵ is is chosen that defines how well the model needs to fit measured data, similar to the SVD approach, or specific model elements are given different weightings through W_m. A combination of both approaches can be seen in the weighted damped minimum length approach ($(G^T W_e G + \epsilon^2 W_m)^{-1} G^T W_e$ or $W_m^{-1} G^T (GW_m^{-1} G^T + \epsilon^2 W_e^{-1})^{-1}$), where both model element weighting W_m, data (error) weighting W_e and model fit ϵ parameters can constrain the inversion[209]. In diagnostic tests of the various different inversion models, there was negligible to no difference in performance given the SECS interpolation problem.

Accuracy is however not the only consideration for an inversion model to be useful. Another approach looked at was the Backus-Gilbert inverse[209,210]. The Backus-Gilbert approach is similar in nature and performance to all the other inverses mentioned, but has the distinct advantage of taking into account the natural ordering of the inverse problem given that (spatially) neighbouring nodes should be more related. To do this, the Backus-Gilbert matrix aims to find a generalised inverse to minimise the spread of the resolution matrix and makes use of a weighting function (2D in this case) to relate adjacent nodes. Explicitly, the previous inverses define the spread of the resolution matrix as a Direchlet spread, whereas the Backus-Gilbert approach includes a weighting function that relates the localisation of model parameters m (total of M model parameters),

$$\text{spread}(R) = \sum_{i=0}^{M} \sum_{j=0}^{M} w(i,j) R_{i,j}^2. \tag{62}$$

To include a 2D spatial relation between model parameters, $w(i,j) = (x_i - x_j)^2 + (y_i - y_j)^2$ is used (x_i, y_i being the index location of parameter m_i on the grid). A small resolution spread is when only the diagonal has large elements, i.e. it is close to the identity matrix. Practically this would mean that individual model parameters are well resolved and independent[209]. When the resolution matrix is not an identity matrix, then the diagonal elements are a measure of how well the specific model parameters are resolved. As an example, a resolution of 1 means perfectly resolved and a resolution 0.8 means 20% of the node's estimation is influenced by other adjacent nodes. The off-diagonal components define how this 20% influence is spread across the other model parameters.

The Backus-Gilbert inverse gives a physical interpretation of the resolution matrix only when properly defined. Properly defined in this case means there are no negative contributions to the spread of the resolution matrix and various contributions can be seen as correct weightings. Minimising this Backus-Gilbert resolution spread is analogous to minimum length solution discussed above. The Backus-Gilbert formalism can be extended further, analogous to the damped minimum length solution as well. To do this, we define a parameter α and include the covariance matrix, allowing the full Backus-Gilbert generalised inverse to minimise $\alpha\text{spread}(R) + (1-\alpha)\text{size}(cov_u m)$. Here the unit covariance matrix $cov_u m$ characterises the degree of error amplification of due to data variance that occurs in the mapping. As such it needs to be normalised. Assuming all the data is uncorrelated and with equal variance σ^2, then $cov_u m = \sigma^{-2} G^{-g} cov(d) G^{-gT}$, where $cov(d)$ is the data variance. In the case of correlated data or variable data variances, a unit data covariance matrix $cov_u d$ can be defined that satisfies $cov_u m = G^{-g} cov_u d G^{-gT}$. The unit covariance size is then defined as the sum of its diagonal elements,

$$\text{size}(cov_u m) = \sum_{i=0}^{M} [cov_u m]_{ii}. \tag{63}$$

A small covariance size indicates that data errors corresponds only to small model parameter errors.

Following the derivation by Menke[209], in component form this generalised inverse is,

$$G_{k,l}^{-g} = \frac{\sum_{i=1}^{N} [S_{ij}]_k^{-1} \left(\sum_{k=1}^{M} G_{ik} \right)}{\sum_{i=1}^{N} \sum_{j=1}^{N} \left(\sum_{k=1}^{M} G_{ik} \right) [S_{ij}]_k^{-1} \left(\sum_{k=1}^{M} G_{jk} \right)} \tag{64}$$

where,

$$[S_{ij}]_k = \alpha \left(\sum_{l=1}^{M} w(l,k) G_{il} G_{jl} \right) + (1-\alpha) [cov_u d]_{ij}. \tag{65}$$

There is a trade-off in choosing α[209]. Besides requiring the resolution matrix to be positively definite to be able to interpret the contributions to model parameters, we also want to maximise the resolution of the model, i.e. ideally every current element should be well defined. This in effect is done by minimising the spread of the resolution matrix. At the same time, we need to minimise the model variance, i.e. cancel out the effect of noise in the data. In the case of a severely underdetermined problem such as the case with sparse B-field interpolation, α would be biased towards 1, i.e.

with few magnetometers available the covariance matrix would have less impact when compared to the resolution matrix with many poorly defined current nodes and large spread. As such α is chosen to minimise the resolution spread while maintaining a positively definite resolution matrix that can be physically interpreted.

Returning to the idea of uncertainty estimation for SECS interpolation, let us use a practical example of the southern African INTERMAGNET network already described. Similar to implementations in the previous section, we will use an elementary current grid at 100 km altitude and current node spacing of roughly 100 km. KMH will be kept out-of-sample for validation, while HER, HBK and TSU will be used as the ground nodes driving the interpolation. Furthermore, the 24 hour disturbed period from 06:00 UT on 22 June 2015 will be used for modelling. This period includes the SSC and main phase of a severe geomagnetic storm, of the level that is critical for operational GIC modelling.

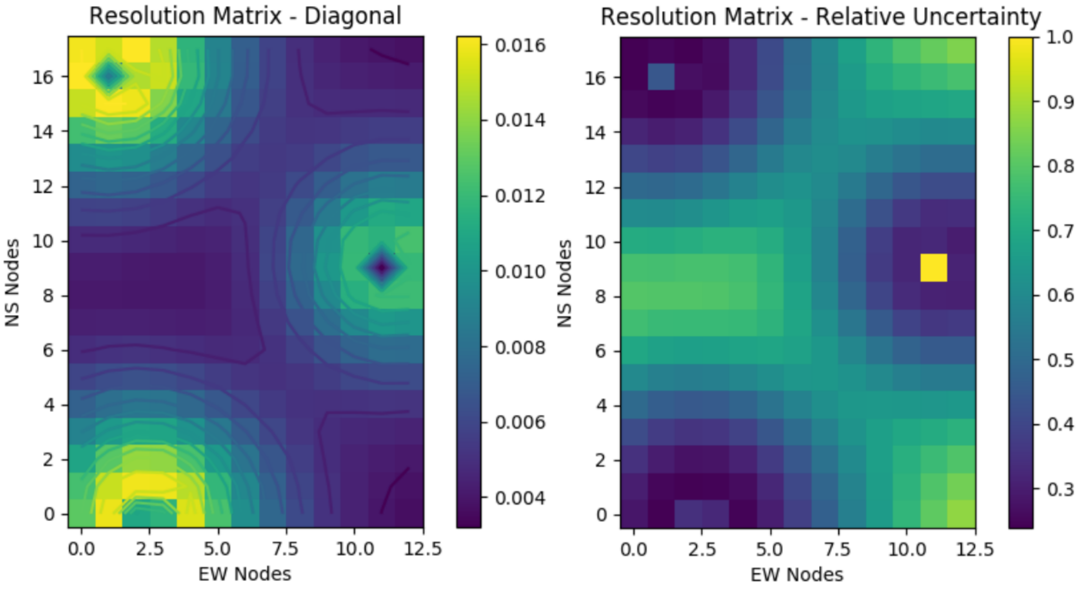

Figure 80: Part of the benefit of using the Backus-Gilbert inverse is that spatial information can implicitly be included in the inversion problem. Here we see the resolution matrix relating to current node estimation on the left. Current nodes (model parameters) near magnetometers are better resolved. The relative uncertainty (on the right) of the current nodes can be estimated by the normalised inverse of the resolution matrix elements. In creating the relative uncertainty of model parameters, the lowest resolution current node is assumed to be 100% uncertain. From here the relative uncertainty of all other nodes is computed, as defined by the inverse of their resolution. As expected, estimation of current nodes far away from magnetometers are most uncertain in the inversion.

Addressing the first question of model uncertainty, or what is the uncertainty of SECS interpolation given the capability and capacity of the model alone, we look solely at the Biot-Savart transfer matrix T. Using the Backus-Gilbert resolution matrix defined for T, the independence of model parameters (or in this case, the current nodes) is computed. In terms of uncertainty, the independence of nodes can be thought of as a level of certainty, i.e. nodes that are well defined have lower associated model uncertainties. When current nodes have low uncertainty, then interpolation to nearby ground nodes should similarly be more accurate than interpolation to those further away. Conversely, if the current node has large uncertainty, then interpolation to nearby ground nodes suffers, but interpolation to ground nodes further away is less affected. Normalising the magnitude of the resolution appropriately, we can get the relative uncertainty across nodes, as seen in Figure 80. It is important for the methodology in this case to identify the nodes with greatest relative uncertainty.

Moving to the next question of including the uncertainty in actual measurements and how these

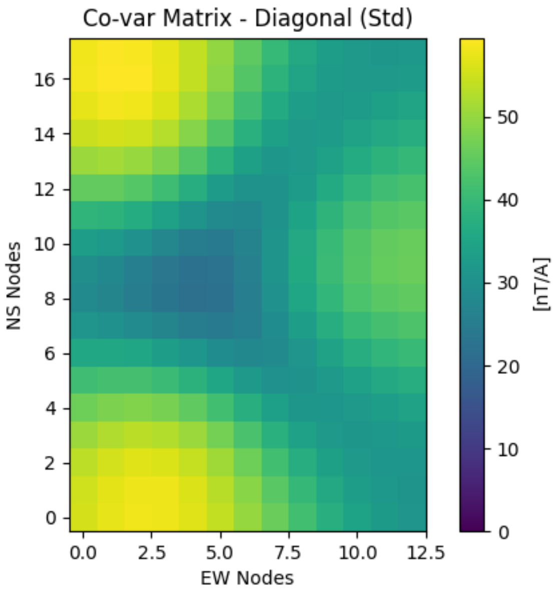

Figure 81: The covariance matrix is a measure of the propagation of error, given that a ground node has some sort of error. As expected the current nodes with highest weighting closest to ground nodes are also the most susceptible to measurement error. Given high-fidelity magnetometer measurements, this error is likely to be constrained to instrument noise.

uncertainties or error propagate into the interpolation scheme, we turn to the covariance matrix. As seen in Figure 81, the unit covariance matrix takes into account the effect of noise or poor ground node data on the current nodes. The square root of the diagonal plotted in this case can be thought of as the current nodes standard deviation given a unit standard deviation in ground measurements. In the case of measurements not scaled by their standard deviation as done in many cases, the result can be scaled by multiplying by a feasible standard deviation of the measurements. For this particular case, we assume that a noise level of 1 nT is acceptable for illustrative purposes and no further normalisation is done.

Putting together the two pieces of uncertainty associated directly with the inversion method, we have the relative merged uncertainty scaling seen in Figure 82. The result, as defined in this work, is the product of the normalised square-rooted covariance matrix and normalised resolution matrix. In essence the resulting relative uncertainty identifies what proportion of a node's estimation is uncertain relative to the most certain node available. We make the assumption that the worst case estimation of a node is entirely wrong and an entirely synthetic estimation of that node from a typical case would work best. Given this assumption, the normalisation feeds into the amplitude of associated error bar. In the merged uncertainty plot, the area between ground nodes shows an extended contour of similar uncertainty, likely due to similarly weighted contributions from the different ground-based measurements. This is the region driven by low covariance size, i.e. the multiple contributions minimize the effect of inaccuracy due to any singular site.

The next step in the estimation of uncertainty has to do with defining the physical variation expected. This ties in with the estimation of the synthetic typical case which is needed to define the most uncertain current nodes. Ultimately, we want to define a high resolution representation of the natural variation associated with current sources and inductive effects. Assuming we set up an inversion problem with an equal number of ground nodes to current nodes, i.e. $m = n$, the current nodes (model parameters) would be uniquely defined. As there are no actual measurements possible to do this worldwide, a synthetic B-field needs to be used. The approach to defining such a synthetic field is to make use of what measurements are available and extract the typical spatial correlation that may exist. The typical variation in turn would define the structure of the synthetic disturbance

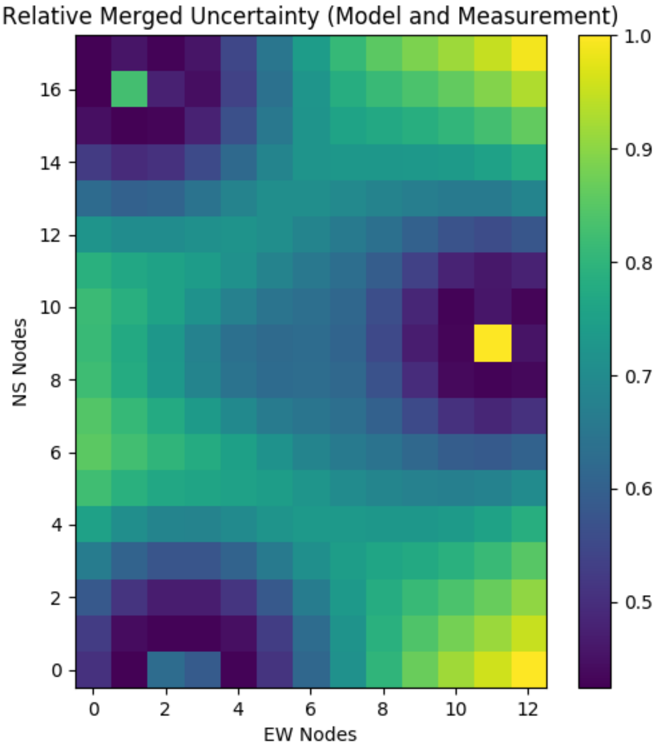

Figure 82: Taking into account the uncertainty in the currents nodes due to the model inversion and measurement error, we can derive a relative merged uncertainty that can be used to scale the physical uncertainty. For the Biot-Savart mapping employed, the current directly above a magnetometer site is poorly defined due to being constrained by a small associated B-field when $r << h = 100$ km.

B-field. The two-point correlation function, defined by all possible pairs, is called a variogram[211]. Explicitly, the semi-variance ($\sigma^2/2$) between each pair is plotted as a function of distance between points and the resulting variogram cloud binned. A variogram alone is a measure of spatial dependence of quantities, with typical scale lengths defined by the range where a quantity becomes spatially independent. The level of semi-variance when the quantity is spatially independent is called the sill and base level of semi-variance, often due to instrument noise, is called the nugget. Knowing the range, nugget and sill defined from an experimental variogram, a synthetic variogram can be simulated given a variogram model. Using an experimental variogram, we can create multiple synthetic datasets. Inverting all the datasets then show the variation in specific current grid nodes.

In our specific case, the interpolation area of interest is in the mid-latitude region. Making no assumptions of geophysical induction effects and focussing on the current drivers, we can make use of all possible mid-latitude B-field measurements for the period of interest. The extent of these measurements is shown in Figure 83.

It is assumed that all stations in the two bands are comparable within each hemispheric band and the absolute great circle distance between the sites is used. In more sophisticated approaches a 2D variogram can be developed that takes into account the latitudinal and longitudinal distances separately. Using the stations defined, we have a range distribution as defined by Figure 84, limited to 4,000 km, which is reasonable for what would be driven by the same magnetospheric current.

To further increase the size of the variogram cloud, 3-hour periods inspired by the Kp index were used to compute separate variograms over the duration of the storm. The variogram cloud was then binned and mean semi-variance taken, each B-field component being separately defined. In this process outliers were moved using a semi-variance threshold of 7,500 nT^2. This threshold for outliers relates to variation over 120 nT, which would be unlikely – that is the sort of variation

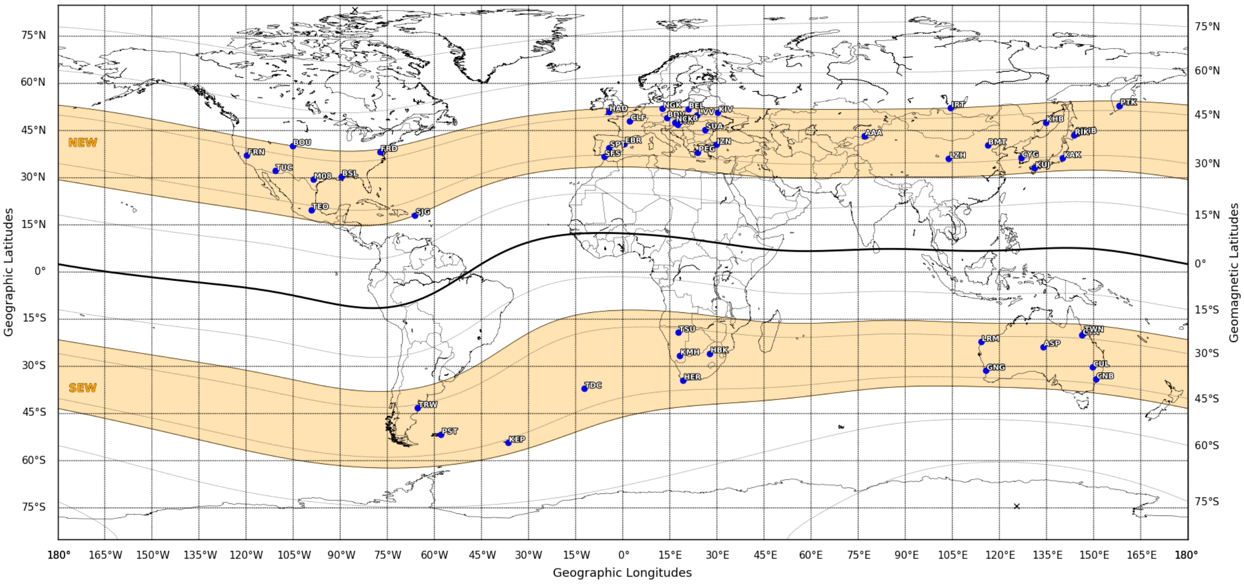

Figure 83: In order to simulate the typical spatial variation in the B-field at mid-latitudes, measured data for all possible mid-latitude stations are used for the given time frame. The two hemisphere bands are chosen conservatively to not be affected by either auroral or equatorial current systems and are analysed separately in computing the two-point semi-variances.

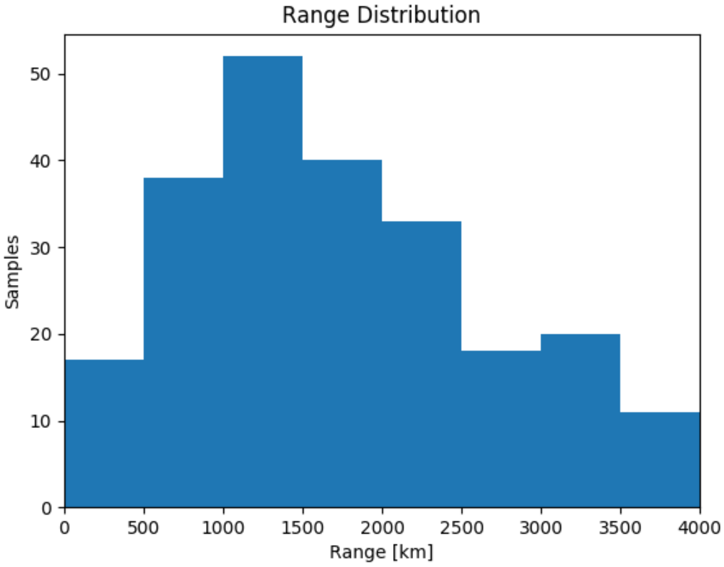

Figure 84: For the variogram, taking pairwise combinations of all the stations we have a range distribution that exceeds 10 samples for each 500 km bin and allows for semi-variance to be computed.

seen during geomagnetic storms. The uncertainty in variogram estimates was further defined by the inter-quartile range of binned values. Taking into account the uncertainty estimates defined, the variogram was fitted using a Gaussian variogram model in Figure 85. As can be seen in Figure 86, the variogram characteristics change throughout the course of a storm. Some interesting features to note are the larger scale structures, possibly linked to current system driving, that become apparent in the B_x during more disturbed periods, i.e. onset and main phase of the geomagnetic storm. The B_y component is more associated with inductive effects so this effect is not as apparent. Also seen is the general trend of more variance across components during elevated geomagnetic driving, as previously validated in this work by dense measured data in the TVA network.

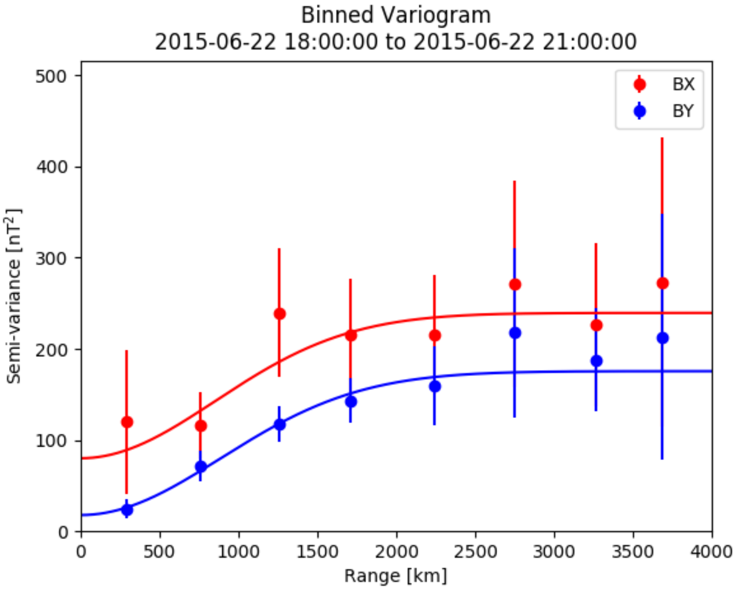

Figure 85: The variogram for the selected 3 hour period is well defined for both B_x and B_y components. As expected the variance in the larger and more directly driven B_x component is larger than the typically inductive variation associated with the B_y component. The nugget of both components is less than 10 nT and range around 1,500 km.

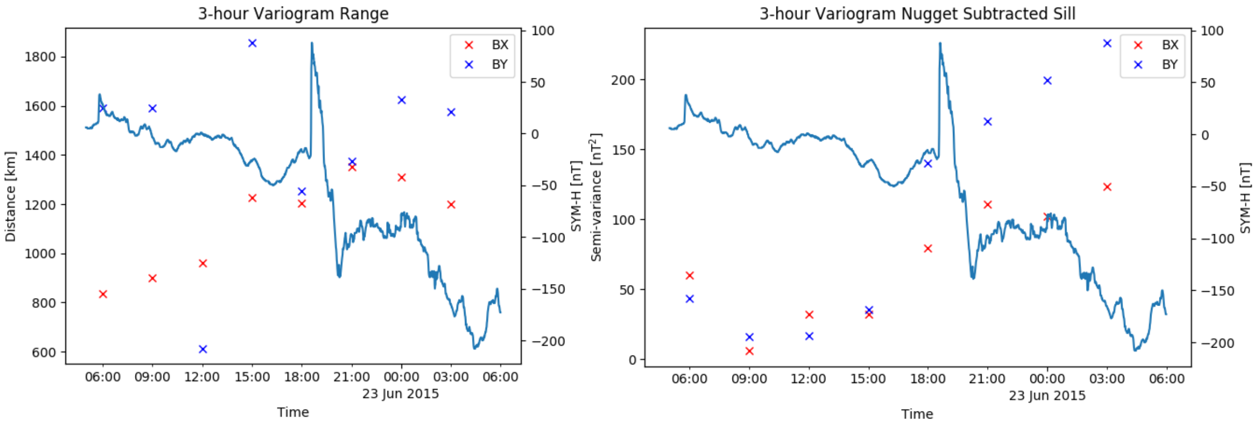

Figure 86: Taking into account the entire storm, we see that there is a definite increase in nugget subtracted sill at the onset and main phase of the storm, linking with previous analysis with higher measured B-field variance during disturbed times. Quiet time sill is very small and possibly close to random, but modelling is usually desired for disturbed time so this issue is avoided. The range is relatively well constrained for the B_x component, with an increase during storm time as well. The B_y range is poorly defined in quiet time, but is more constrained in storm time, suggesting more coherent structures are identified.

Once the variogram has been defined, a B-field can be simulated to replicate the variogram properties, i.e. same two-point correlation would exist. An example of the B_x component for the variogram shown in Figure 85 is shown in Figure 87. Since the simulation is much larger in extent when compared to the interpolation area (red block in bottom left), multiple sections of the single simulation can be used to give separate samples. Making use of multiple simulations, a synthetic dataset of more than 50,000 possible B-field distributions over the interpolation area is generated, given similar characteristic driving conditions as during the period of interest. Including reflection invariance, this dataset size increases to 200,000. Inverting each of these well-defined synthetic datasets (resolution matrix equal to identity matrix and no assumed data error), an associated set of possible current system configurations can be computed. Taking all the equivalent current system possibilities into account, the variation in the current node magnitudes for the different components can be computed. Explicitly, this is defined through the standard deviation of each current node and is shown in Figure 88. Here it should be stressed that the procedure up to now is purely defined as an inverse problem and is applicable to any inversion based interpolation method, as long as mapping is consistent. Any variation of SECS interpolation could similarly be used.

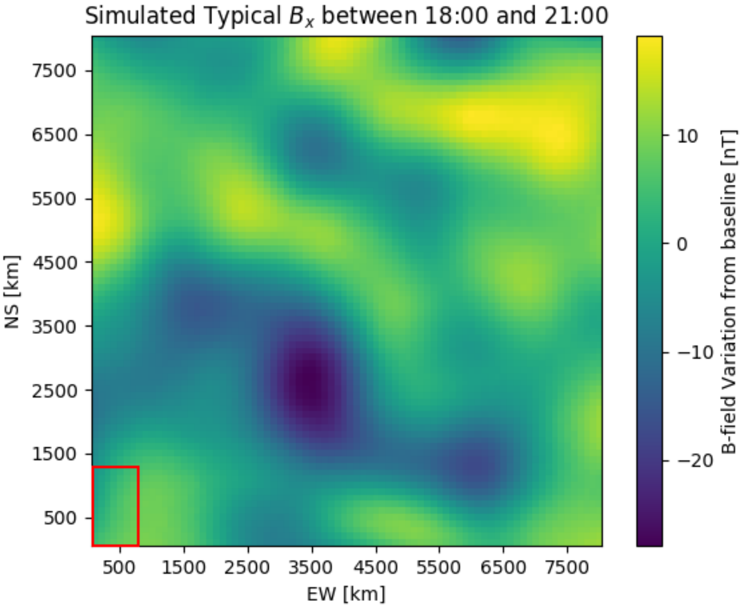

Figure 87: Making use of the variogram, a simulated B-field can be created that replicates the variation seen. Panning a box the size of the interpolation grid across the simulation allows the inversion model to be calibrated across multiple possibilities.

After the variation in current amplitude is estimated, for the approach developed here, we use the merged relative uncertainty (defined by the model uncertainty earlier) to scale the physical uncertainty result. In the case of nodes with unit relative model uncertainty (i.e. no useful information is obtained from the inversion), the full physical variation would apply for the current node uncertainty estimate and give a bound for the possible equivalent current variation. Iterating through all nodes, we finally arrive at the total equivalent current uncertainty as shown in Figure 89. These uncertainties are applied to the original underdetermined current system as upper and lower bounds, implicitly including model, data and physical uncertainty as would be assumed in a similar case. Using the same interpolation mapping while including the current system bounds allows for dynamic uncertainty estimates anywhere in the interpolation region. Figure 90 specifically shows the error bands for interpolation to KMH. Additional application of the methodology developed is in using the spatial uncertainty grid to identify where magnetometer deployment would minimise uncertainty.

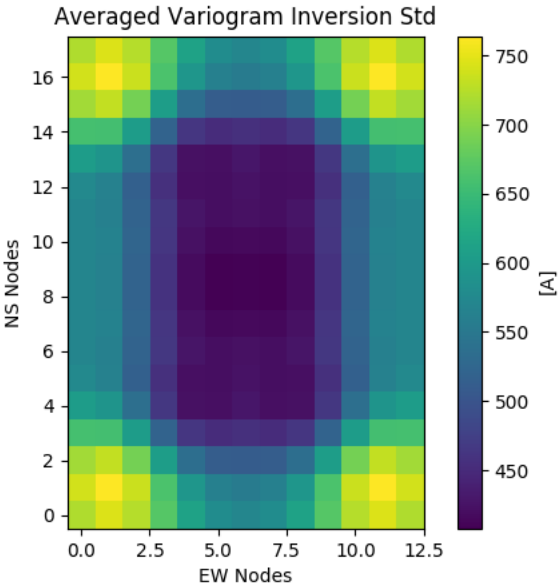

Figure 88: Taking multiple simulations, each with many sub-boxes, the averaged current response that could create the B-field can be calculated. This average is the typical value of the individual current nodes and hence their likely value that may not be estimated by the original inversion.

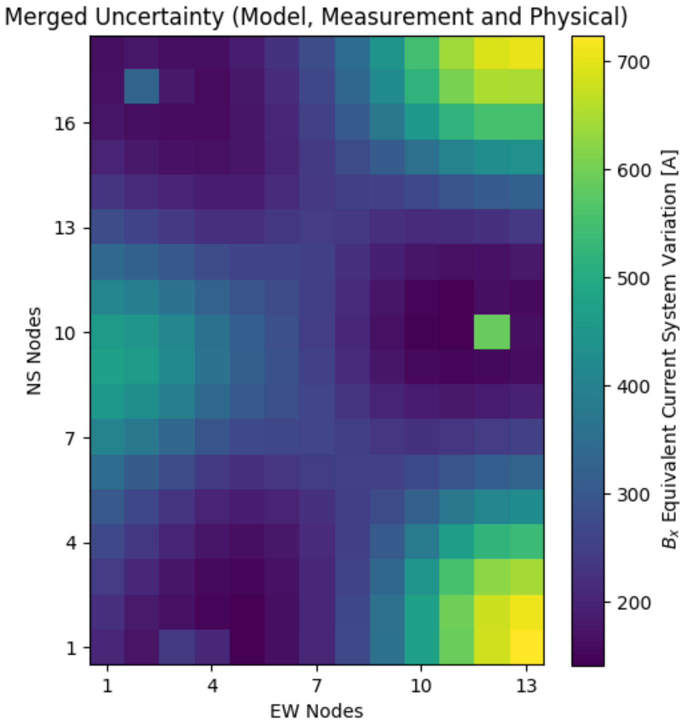

Figure 89: Finally merging the relative uncertainty with the physical current average, we can define the probable uncertainty of the current nodes. Note the poorly defined current nodes (large uncertainty) above magnetometer sites ($r < h = 100$ km), due to the choice of Biot-Savart mapping.

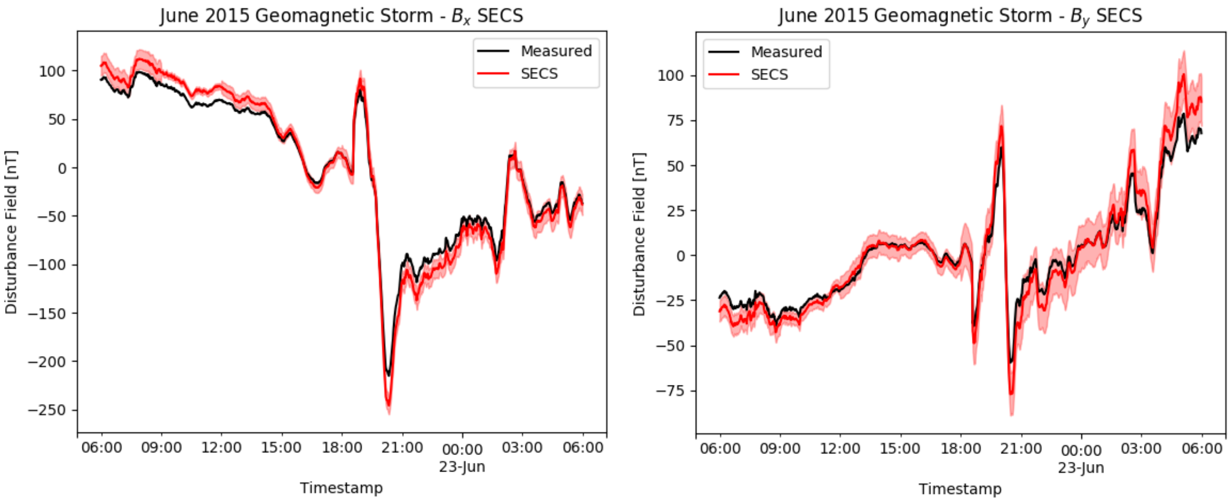

Figure 90: Applying the SECS interpolation with current nodes perturbed by the uncertainty estimates gives physical uncertainty estimates that are defined dynamically throughout the storm. Interesting in B_x is the variation of the error bounds during different phases of the storm. During quiet time between 09:00 and 12:00 on 22 June, the error bound and SECS interpolation both do not capture the measured B-field. Performance during disturbed time is much better, suggesting that the (ring) current system driving is accurately captured.

7.3 Correction of SECS Implementation in southern Africa

After validating that the previous implementation of SECS in southern Africa[106,152,157] is accurate enough for GIC modelling and developing novel improvements to the method, the discrepancy with other SECS implementations in mid-latitude regions was explored further. Initially a subsurface current was included in modelling for completeness and the equivalent current magnitudes were analysed. In doing so it was confirmed that the discrepancy with other SECS implementations is that the southern African implementation was in fact incorrect. Simply put, the problem was not set up correctly as divergence-free current nodes that form current sheets defined by an assumed current density, but rather independent elements in the X and Y directions. When the current nodes were used correctly, defining X and Y as the respective projections of the radial component of the single current node, the interpolation scheme broke down. This would be expected as the sparse grid of magnetometers would need to attempt to model a relatively flat field using current nodes that create significant curl. As a result the equivalent current system would need to largely cancel out contributions of curl from adjacent nodes and the result would be an unstable set-up that may work at some nodes, but not across the entire interpolation grid.

Looking further at the implementation of the current nodes for X and Y components, the previous approach by Bernhardi et al.[157] is not physical. The result is an artificial smoothing of the interpolation across a large area, even though the interpolation scheme defines a divergence-free equivalent current height at 100 km at mid-latitudes where no such current system would exist. The smoothing introduced by $(1 - \frac{h}{\sqrt{r^2+h^2}})$ is compounded by allowing the two components of the B-field to be defined separately. This allows the divergence-free constraint to be broken and a linear B-field and current system to be represented, when Hall-like currents should be the basis.

For consistency and physical relevance, a corrected version of the interpolation scheme can be developed using either line elements or entire line currents. Physically, we expect this to be the case for the ring current driving seen at mid-latitudes. Using the same basis, this correction takes the form of a Biot-Savart mapping between current node and B-field. Making use of the set-up shown in Figures 91 and 92 we have,

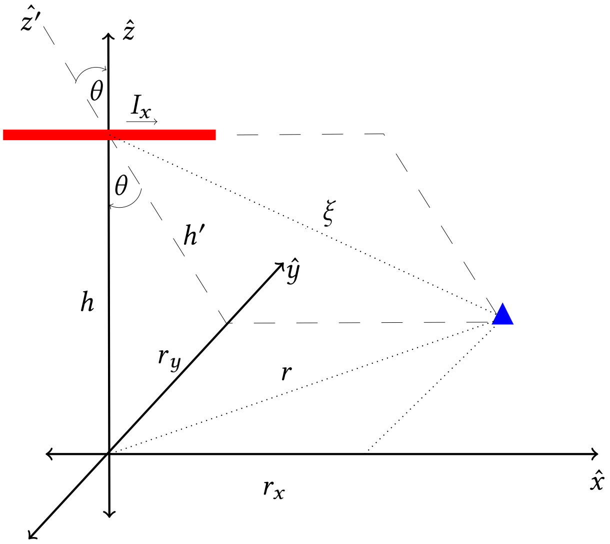

Figure 91: Setting up a physically correct line element implementation of the elementary current system interpolation, we assume a line current element I at height h, a distance ξ away from an ground node. Assuming the current is in the $\hat{x}$ direction, the associated B-field would be in the $\hat{y}$ and/or $\hat{z}$ directions. Changing the reference frame, we define the calculation plane (θ away from the xz-plane) that includes both line current element and ground node (dotted lines). In this secondary reference frame, the current would be at height h' instead and the B-field solely orthogonal to the calculation plane. Although the set-up of the line element implementation is shown for a line current in the $\hat{x}$ direction, a similar orthogonal set-up can be assumed for the $\hat{y}$ direction with associated B-field in the $\hat{x}$ and/or $\hat{z}$ directions.

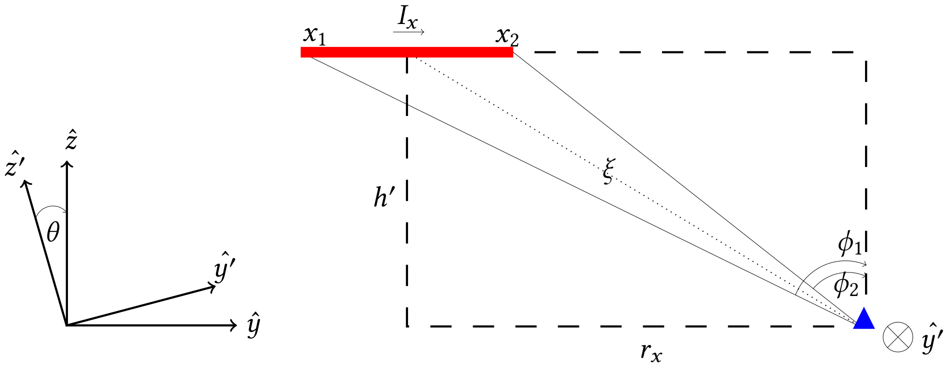

Figure 92: In the calculation plane defined by Figure 91, we can calculate the orthogonal B-field at the ground node defined by the ϕ angles that determine the extent of the current element. Projecting the result back to the $\hat{y}$ direction using $cos(\theta)$ arrives at the resulting ground node horizontal B-field.

$$B_{x,y} = \mp \frac{\mu_0 I_{y,x}}{4\pi h'} cos(\theta)|sin(\phi_1) - sin(\phi_2)| \tag{66}$$

$$= \mp \frac{\mu_0 I_{y,x}}{4\pi h'} \frac{h}{h'}|sin(\phi_1) - sin(\phi_2)| \tag{67}$$

$$= \mp \frac{\mu_0 I_{y,x}}{4\pi} \frac{h}{r_{y,x}^2 + h^2}|sin(\phi_1) - sin(\phi_2)|, \tag{68}$$

where the ϕ's are defined by the angle between ground node and line element end points in the calculation plane, defined by θ away from the vertical-plane. In the geometry of the problem, we explicitly have that the $B_{x,y}$ components are mapped to the orthogonal $I_{y,x}$ components, with the orthogonal component displacement $r_{y,x}$ being used. Note the change of sign for the I_y current driving $-B_x$. In the calculation plane we calculate an orthogonal B-field to the line current, which needs to be projected back to the horizontal plane defined by Earth's surface through a $cos(\theta)$ factor. This projection can be defined more simply in terms of the height (h) and horizontal distance (r) between current and ground nodes in (68). Here it should also be stressed that the calculation for the X and Y components are done separately. The derivation of the Biot-Savart equation takes into account the relation between line element and ground node in the plane formed by the line element and node, with the result then rotated to the typical frame of reference and measurement. As in previous modelling, the distances between current nodes are roughly 100 km and for this case it is assumed that current elements are connected, i.e. the current element lengths either side of node are half the distance to the adjacent node.

Instead of assuming discrete line elements, an infinite line current approach can be used in a similar way with projection from a calculation plane. Assuming the line current is infinite in extent compared to the interpolation distances, we have the simple Biot-Savart form,

$$B_{x,y} = \mp \frac{\mu_0 I_{y,x}}{2\pi} \frac{h}{r_{y,x}^2 + h^2}. \tag{69}$$

In the previous implementation of SECS in southern Africa, with separate calculation of components, the Biot-Savart mapping tends to approximate a line current source when $r >> h$, i.e. $B_{x,y} = \frac{\mu_0 I}{4\pi} \frac{1}{r_{x,y}}$. However, when $r < h$, the divergence-free current system (disc) provides contributions that cancel each other out, and the result is damped by $(1 - \frac{h}{\sqrt{r^2+h^2}})$. In the previous section this was seen as the source of poorly defined current nodes (large uncertainty) above magnetic field measurements. The previous implementation further aims to describe ionospheric currents and fixes $h = 100$ km. In the line element adaptation presented, h dominates instead of r. When $r >> h$, the B-field drops off as $1/r^2$, which requires a magnetometer grid with scale length of at most h for comparable interpolation. Luckily for mid-latitudes, the dominant driving current system is the magnetospheric ring current and $r << h$ for interpolation lengths over southern Africa.

When applying the line current versions of the interpolation scheme, an ionospheric equivalent current system defined at a height of 100 km results in B-field contributions drop off significantly. Only scale lengths of roughly 100 kms can be correlated – not the 1,000 odd kms needed over southern Africa. However, keeping in-line with the mid-latitude physical drivers being largely magnetospheric currents, setting the height of the current system at roughly 5,000 km in turn produces an accurate smooth current system over the region along with accurate B-field interpolation in the central validation site at KMH. To look at the responses of modelling, we see that the performance during the June 2015 storm as defined by P defined earlier is 0.86 (0.76) using incorrectly implemented SECS, 0.98 (0.87) for the line element version and 0.96 (0.87) for the full line current version for the B_x (B_y) component, i.e. there is 10% improvement just due to correct definition of the Biot-Savart mapping.

Besides the overall improvement of modelling using more physically defined versions, also of interest is the difference in performance between B_x and B_y, with B_x more directly driven by the ring current and performing significantly better. A further explanation of why this error has not been uncovered before is that the equivalent current systems created by initial wrong implementation of SECS and the correct line element version are very similar as seen in Figure 93. This is fortuitous from the perspective of previous modelling, but future implementations should aim to avoid the previous mistake and keep to the physically correct line element approach at mid-latitudes.

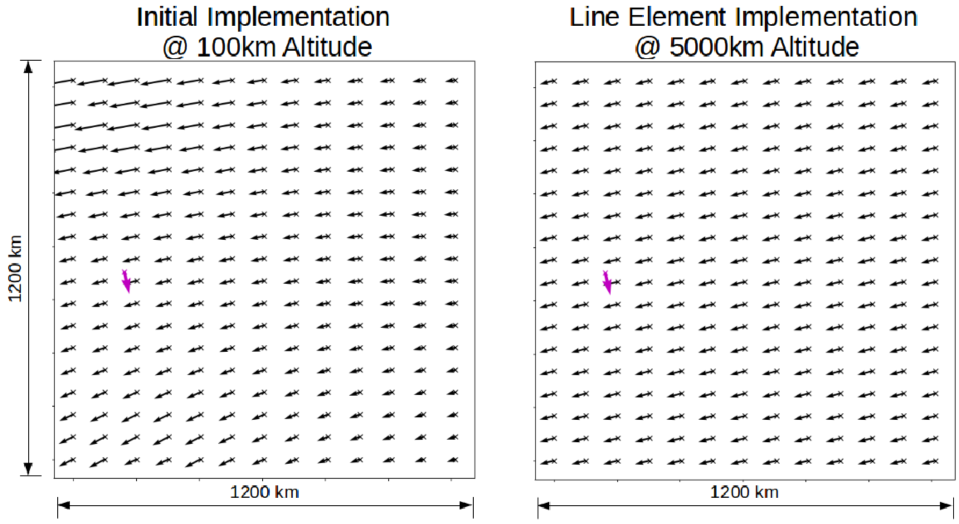

Figure 93: Comparing the equivalent current systems defined by previous incorrect implementations of the SECS interpolation scheme and a physically correct line current implementation, both using HER, HBK and TSU as ground magnetometers, the similarity is striking. The additional spatial variation introduced by the divergence-free assumption of initial incorrect implementations may create non-physical ground B-fields with significant curl[157]. Here the purple arrows indicate the measured validation B-field at KMH and the black arrows indicate the equivalent current system.

7.4 Summary

In this chapter, the often used approach of B-field interpolation via the SECS interpolation scheme is probed further. Firstly, the SECS scheme as implemented previously in southern Africa was validated using measurements for MT sites, although it has been found that SECS does not always perform well at mid-latitudes elsewhere in the world. Realising the possible use of variometers to supplement high-fidelity geomagnetic observatories, a novel method of dB/dt interpolation was defined. The resulting dB/dt field can further be used to improve the baseline B-field interpolation as defined by traditional SECS, or be used for operational modelling as is. The development of dSECS provides a direct way for low-cost magnetometers to be deployed by utilities and improve GIC modelling accuracy. Focussing on the inversion problem separately, a framework using a Backus-Gilbert inverse allows the degree of certainty/uncertainty in model parameters to be estimated. This inverse has similar performance to the SVD approach usually implemented, but additionally takes into account the spatial relation between current nodes and has a positively defined resolution matrix, allowing the resolution matrix to be physically relevant. Typical spatial correlation using measured geomagnetic variation at mid-latitudes can be found and used to simulate synthetic data (over 200,000 per instance here). Inverting this data can then be used to estimate the variation in model parameters and total uncertainty, which in turn is scaled by the model uncertainty as defined by resolution and covariance matrices. The estimated total uncertainty is dynamic and based on real measurements during different parts of a geomagnetic storm. Besides defining a measure of uncertainty in generalised inversion schemes, the total uncertainty map can be used to make an informed choice for future planning of magnetometer/variometer deployment. A final output of the chapter is a correction of the implementation of the SECS interpolation scheme in southern Africa. This correction stems from defining line current basis elements instead of divergence-free current nodes, as would be physically relevant at mid-latitudes. Using line current basis functions improves modelling accuracy, and the previously developed methods of dSECS and uncertainty estimation still apply.

8 Discussion

With recent advances in geophysical modelling, there has been a push to use dense MT surveys for accurate E-field estimation[139,140]. Although this is indeed a large improvement on some of the simpler assumptions made in traditional GIC modelling, there are still a number of factors that contribute to uncertainty in modelling results. If there are no existing MT surveys, then considering the additional cost and efforts, while not guaranteeing increased certainty in estimates, makes this high-fidelity approach difficult for many utilities to implement. An alternative in the form of data-driven modelling approaches is presented instead. These methods assume the simple governing equations, but allow the uncertainties to be absorbed in the model and ultimately encode much more complex dynamics. Specifically, an ensemble estimation methodology is used for both network parameter and TF estimation. These models can be driven with limited data (a couple of days for the TF estimation and a number of hours for network parameter estimation) and are more accurate than previous empirical approaches applied.

Data-Driven Advantages

Probably the biggest advantage of the data-driven GIC modelling approaches presented is that the effective mapping between input and output variables is possible. Given enough instances to derive the mapping, the result is probabilistic and generalisable[188]. In the case of the interconnected power network and GIC modelling, interactions and uncertainties are complex, with errors made at a single node affecting other nodes as well. Physics-based modelling aims to model all these links in the modelling chain separately, but the observed GIC takes all the factors into account together and the different drivers cannot be fully separated. An example is in the variability of both measured B- and E-fields apparent at mid-latitudes, which emphasises the need for more magnetometers and network effective or empirically adapted E-field responses – not single site E-field estimates. In the engineering step, assumptions are not always accurate, nor are they static. Grounding resistances that form a large part of the network modelling are such an example, being dependent on the moisture content of the soil and state of the grounding plate[154]. To make sure the network modelling itself is accurate, accurate measurements of the resistances and the state of the entire system need to be made in near-real time. These efforts would in turn need to assume a resistive network model that is adequately described by dc currents. There is ongoing research into the validity of the resistive network assumption[98] and what the implications of more realistic low-frequency modelling may be[23]. Taking the uncertainties into account, the use of empirical approaches has the distinct advantage of taking the simple analytical basis and estimating the divergence from these base assumptions. The result is that unmodelled aspects can be adequately described. In an ideal operational case, empirical approaches can be used to model at-risk nodes in real-time and augment general models. The level of expenditure would be significantly less than instrumentation needed for state-of-the-art geophysical surveys. At the very least, measured data from a range of conditions should be used for validation of analytical methods.

B-field Modelling

At this point, given the reliance on accurate B-field data, there is also a need for B-field modelling and specifically, interpolation. SECS has been shown to be a good interpolation scheme but may be misleading. At mid-latitudes, artificial smoothing from interpolation would seem to validate the plane-wave assumption. A number of recent studies have looked into the validity of the plane-wave disturbance B-field assumption, particularly during geomagnetic storms[110,165–167]. Although a plane-wave approximation is representative locally in the context of magnetospheric ring current driving at mid-latitudes, there can be significant deviations from the plane-wave assumption during storm periods (seen through larger variation in mid-latitude variogram) and pulsations (seen measurement from the TVA network). The implication is that GIC or MT responses derived making use of this assumption may have associated error. Further, the mid-latitude scale lengths previously defined through SECS interpolation[152] should not be relied on and robust modelling is required that can absorb errors in the B-field estimation due to localised variations.

At mid-latitudes there is the further consideration that the divergence-free nodes assumed in SECS do not describe the dominant magnetospheric ring current system. In essence, the divergence-free current nodes are not able to describe what is more a curl-free equivalent current system locally. Rather than the traditional implementation, a representative line current or line element version is implemented. The resulting improved interpolation in Chapter 7 gives results similar to the previous incorrect implementation of SECS in southern Africa that saw success, but is physically accurate. With the further improvement of including variometers and dB/dt interpolation, it is feasible for a utility to get accurate B-field measurements within a network in real-time and without costly observatory grade magnetometers. The further inclusion of uncertainty and spatial characteristics for the first time in B-field interpolation allows for optimisation of magnetometer resources to reduce uncertainty and propagate uncertainty into GIC modelling.

Geophysical Considerations

An important consideration is related to the mapping between the B-field and either E-field or GIC in the frequency domain, where Fourier type approaches are most often used. These methods assume periodicity over a time series and are not designed to reproduce transient-like spikes. Although mathematically spikes or steps can be reproduced via FFTs using high frequency contributions (infinitely many for perfect resolution), the high frequencies are not associated with physical processes at these frequencies. A good example is the signal seen during a sudden impulse (SI). Here a shock-front interaction with the magnetosphere is the driving physical process and there are no particle motions at infinitely high frequencies. For GIC modelling, although most of the power sits in the lower frequencies, peak estimation is affected by lack of higher frequencies – similar in essence to reduced peak estimates from lower temporal sampling[174]. In an MT response sense, the higher frequencies link to geology nearer the surface, which is often complex or heterogeneous. Given a GIC spectrogram over the course of a geomagnetic storm, there are distinctly different spectral responses for different phases, such as higher frequency contributions from transients (a good example being sudden impulses). Regardless if they are physical or not, these different spectral components can drive the ‘tuning’ associated with the empirical network parameter variation seen – usually due to incorrect conductivity assumptions. During large geomagnetic disturbances induction effects from lateral contrasts in the ground conductivity may be larger[46], contributing to divergence away from the plane-wave assumption of the B-field. A typical example of such a contrast is in coastal areas, where the sea-land interface creates large E-field perturbations[166]. Deviations in the E-field are not confined to coastal regions alone, as similar or larger deviations are also seen inland – purely due to the 3D conductivity structure of Earth. Polarisation of the E-field has been seen to be more intense for areas where the E-field magnitude is higher[132].

Assuming well defined 3D MT responses across a network, the different spectral components due to different parts of a storm would be filtered by different conductivity profiles – the extent dependant on the variation of the geophysical environment. The resulting E-field is not the same as any single MT estimate but rather an averaged response integrated according to the power network. The TF approach achieves this in practice, and to a lesser degree so do empirical network parameters. Typically, the E-field is computed for an MT survey and then interpolated and integrated along transmission lines. Recent work by Kelbert and Lucas[140] has taken a similar approach, but rather integrated the MT response along transmission lines to map the B-field to GIC. The heterogeneity of the E-field makes even dense MT surveys susceptible to large interpolation errors. Both MT approaches, either estimating the E-field or transmission line response, would ultimately aim to use dense surveys to base a geophysical inversion on and compute surface impedance data along transmission lines with minimal interpolation error. Simple integration along the network does however not take into account the non-trivial network weighting on top of the heterogeneous E-field. For this, accurate network information is needed for the system at large and across voltage levels. Using a single E-field estimate or even a simple average may be misleading – as seen in Section 6.1 for the TVA network at PAR using high-fidelity data.

A further example is in the geologically complex region around Memanbetsu, Japan. In Section 6.4, using E-field and GIC data for the 14-16 December 2006 geomagnetic storm, the single site measured E-field and GIC frequency response slopes are not well matched[174], with the local single site E-field assumption not representative of the network effective E-field driving the measured GIC. GIC modelling using the single site E-field as such is expected to suffer. Due to the geophysical environment at MMB, the generalised approach of a global synthetic layered-Earth profile used for estimating the E-field similarly fails. The synthetic layered-Earth profile reflects the typical case of conductivity increasing with depth[66], but at Memanbetsu it has been shown that a shallow conductive layer sits atop a more resistive profile[84,85] and an alternative layered-Earth profile needs to be used. Making use of a general profile and empirically determining network parameters allows for relative comparison of risk and GIC magnitude between nodes, which includes both geophysical and network aspects if the assumptions are kept constant. Where assumptions are inaccurate, large modelling uncertainty would drive large uncertainty bounds.

Use of Representative Data

The variation of network parameters seen has direct implications for modelling. As has been shown in Chapter 6, noise-level GIC training cannot be used to estimate larger GICs that would impact the grid. Above noise-levels (roughly the 0.0-20.0 percentile range using an intense storm as base case, see Table 3), the network parameters show stability with the main change being in spread as SNR improves. The approach of training on GIC levels above median levels helps to ensure relevant training samples, but node-specific follow-up analysis is needed to determine what GIC magnitude should be defined as the noise-level. Operational modelling requires representative training that samples various possibilities of geomagnetic driving. In the transfer function (TF) approach that maps B-field to GIC, the geophysical aspects can be encoded but a representative spectrum needs to be sampled, i.e. SSC, main phase, pulsations and recovery phase need to be included in training. In the current study, the emphasis has been on probing the drivers of uncertainty in GIC modelling and only GRS uses multiple geomagnetic storms, mainly to increase ensemble size. In the TVA network, where data for multiple storms exist, the single June 2015 event that included high-fidelity local B-field data was favoured to determine model characteristics. The applicability of the ensemble methodology has however been shown across geomagnetic storms in the TVA network using remote B-field from FRD[188]. There is the caveat that due to the separation between magnetometer and network, significant uncertainty creeps in and geomagnetic storms with localised effects, such as long period pulsations during the June 2015 storm[194], may seem to generate different results. Remote B-field measurements from FRD in these cases would not suffice. When local B-field data becomes available for multiple events in the TVA network, it will be important to confirm the applicability of the different mappings across different geomagnetic storm types with similar high certainty.

Frequency Domain Modelling

Looking at the frequency response of GICs and considering the frequency weighting for discrete frequency driving (such as geomagnetic pulsations), the commonly used dB/dt proxy does not adequately describe active periods when the driving frequency is significantly different from the sampling frequency of the B-field. This is evident in the TVA network during the June 2015 storm, where a long-period pulsation interval (period $\approx$ 20 minutes) was not identified in either raw or rolling maximum 1 second cadence dB/dt proxies (see Section 5.2). As an alternative, a frequency weighted proxy that captures the appropriate low-frequency bias of the Earth's conductivity on dB/dt has been shown to identify discrete frequency driving.

Of the data-driven methods presented, the transfer function (TF) mapping between B-field and GIC is the most accurate and physically based. The addition of parameter ensembles (TF*) in the TF approach makes this method operational as it propagates uncertainty into the final GIC estimates, not otherwise done. The mapping is further only valid for a similar network state and a similar B-field disturbance spectrum as used for training. Although this work has focussed on nodal GIC modelling, there is the possibility of broadening the modelling results to the larger network, either as state estimation to calibrate conventional models using the same base E-field and network parameter assumptions, or as error scaling (using the network parameter uncertainties estimated) for these same conventional models. The frequency domain application does not allow for such extrapolation to the larger network, but can allow for very accurate validation. A further disadvantage of estimation of the TF in the frequency domain is that missing data may be an issue in FFT implementation. There are ways to overcome this, including an impulse response of the same TF mapping[110]. The ensemble estimation of network parameters provides an alternative empirical approach that, although based on simpler assumptions, can model similar complexities and do so more efficiently and robustly.

Ensemble Modelling Characteristics

Both the network parameter and TF approaches use ensemble estimation (either of parameters or components) and are probabilistic in nature. Taking the ensemble spreads into account, the error due to either measurement or deviations from base assumptions can be quantified. Unmodelled complexity arising from geological, network or current sources all contribute to the probabilistic spreads. A relevant example of this is seen again at MMB, where the lower voltage network introduced significant GICs, and in TVA, where the geophysical bias is seen in network effective directionality. Both characteristics are evident in the Australian network. For utilities, an accurate idea of the uncertainty associated with modelling is just as critical as the model output itself. In this case, the ensemble methodology explicitly includes uncertainty estimates. A good example is the network parameter ensemble, where the first-order physical approximations are built into the simplistic governing GIC equation and then extended to be much more powerful. Other characteristics uncovered and relevant to operational application are in terms of SNR, where dB/dt provides a better TF than the B-field at higher frequencies, and observed temporal lags between B-field and GIC data. Developing a hybrid TF estimation using both B-field and dB/dt, similar to the average of model outputs taken for PAR, may improve modelling with an optimal SNR throughout the GIC frequency response. Further, the temporal lags identified in measurement may drive additional error and spread in time domain ensembles if not corrected for. Using the TF approach, but instead mapping the E-field to GIC, it was found that there is no statistically significant deviation of the network away from the resistive assumption. This last point validates the traditional governing equation for nodal GIC modelling and explains why, when empirically tuned, it is so effective. Considering line GIC estimation, it is expected that similar empirical approaches can be applied, but validation would be needed.

Operational Context

For empirical methods to be operationally useful and effective, the whole network does not need to be instrumented. Rather, a network can be calibrated using the most physically informed model as a baseline. This approach is often done in initial risk assessment where damage and geomagnetic driving are correlated[87]. As long as the framework is kept consistent, relative susceptibility and risk can be computed[188]. For the network parameter approach, this entails an estimation of both B-field and E-field, whereas the TF approach only requires B-field. The methods presented show that remote magnetometers can be used, with the error introduced absorbed in the ensemble spreads. An alternative is the set up of multiple low-cost magnetometers or variometers within the network that can estimate an average network B-field, minimising uncorrelated noise and improving accuracy of the estimated disturbance B-field. In the case of network parameter ensembles, the spreads associated with uncertainty can further be used for stress testing and propagation of uncertainty to other network nodes. Once a network has online GIC measurement, the calibration can be extended into real-time.

The feasibility of empirical approaches has gained momentum with the availability of low-cost GIC monitoring equipment. The cost associated with GIC data logging can be very reasonable, i.e. less than $350 in a recent 2018 study[189]. In an operational sense, this allows a utility to instrument all transformers with previously identified risk, possibly through more traditional methods, with the resulting data in-house and readily accessible[155]. An added benefit is that empirical GIC measurements allow for accurate estimation at all times, and in regions where cultural noise can have large effects on MT studies or the measured B-field. What is measured is exactly the current state of the power system and no further network information needed. Data-driven models can be updated in real-time and in changing conditions, with limited previous data required for the methods presented. The fact that no further information is needed is important in the resilience and reliability of GIC modelling capability, with the utility ultimately independent from third party data providers or neighbouring networks. That said, data-driven approaches do not replace physics-based approaches but should rather aim to augment or calibrate such models. Physics-based models remain useful for theoretical or predictive modelling of the entire grid, which is needed in scenario or stress testing. At an operational level, analytical physics-based models can identify at-risk nodes that will allow for optimal instrumentation for data-driven methods. Besides real-time output from instrumented nodes, the data-driven methods can then feed back uncertainty estimates into baseline physics-based models.

Limitations

The data-driven methodology presented has three limitations, all stemming from the representativeness of the data available. The first limitation is whether the data-driven relations can be generalised to samples outside of the training set. As with all empirical methods, there is the distinct disadvantage that the mapping is only defined for a defined B-field (through a magnetometer, variometer or interpolation) and network node pair. The second limitation is that the research focuses on mid-latitude regions. In comparison to high-latitudes, mid-latitude current system dynamics are generally less complex and more homogeneous across a power network. It has been shown by Heyns et al.[194] that localised current systems occur within the data used in this work and, coupled with heterogeneous ground conductivity considerations, the methods presented are adequately robust. Validation is needed to confirm that the data-driven transforms can be extended to other regions. The third limitation is that there has been no analysis of extreme driving, whether in high- or mid-latitude regions. In the mid-latitude regions analysed for this report there are few coincident GIC and B-field data sets. Although high-latitude regions have more extensive data coverage, data from extreme events remain limited. From the datasets available, it cannot be conclusively stated that the B-field to GIC transforms derived scale linearly to all storms. Within the geophysical aspects, the B-field characteristics in extreme events are not well defined at high cadences since magnetometer measurements for such cases either saturate or are not readily available. Studies have attempted to assimilate higher frequency components using comparative Dst[212], but there is significant spread in estimates. From a network perspective, once a transformer saturates it becomes an active part of the network response which requires representative modelling, not covered in conventional GIC studies. Although the use of the data-driven transforms are not fully generalisable, their use on a growing number of datasets may give good indications of how general scaling would work.

Future Outlook

Looking toward the future, we ultimately want predictive capabilities with models that use solar wind data. In advance of such prediction, we need an idea of what will happen and simulate states of the network to generate mitigation strategies. Until we have confidence in our approaches to the full engineering problem, there is a risk that hard mitigation may cause more problems[142]. Concurrently, geophysical aspects are becoming better understood and modelled. The challenge is merging this understanding with real-world power systems and creating operational approaches that work in cases where the level of data fidelity is not adequate for state-of-the-art physics-based application.

8.1 Summary of Contributions to the Field

In analysing uncertainty in GIC modelling and looking at the interplay between the engineering and geophysical steps for operational modelling, several new contributions to the modelling and understanding of the geomagnetic field and GICs have been developed:

1. A robust empirical GIC modelling methodology has been developed in the time and frequency domains to improve accuracy and quantify uncertainty in real-world application (see Section 5.3).
    - The novel ensemble methodology has been developed independently from other work in the geophysics field, for both time and frequency domain modelling.
    - Uncertainty in both time and frequency domain GIC modelling has been quantified for the first time.
    - Useful operational results can be produced using limited and/or low-fidelity data.
    - The methods developed can be applied in real-time, with validation of the network state possible.
2. Network and GIC responses have been characterised, with new insights into drivers of uncertainty seen (see Chapter 6).
    - Different regimes of network parameter responses have been found for different GIC magnitudes.
    - Directionality and the impact of the geophysical environment and the network at large is seen as an effective response, without explicitly modelling these factors.
    - Single E-field measurements cannot always be used as representative driving across the larger network area, even if it is measured.
3. Frequency characteristics of GIC and B-fields were rigorously defined and related, with implications in terms of the proxies and methods often used (see Sections 5.1 and 5.2).
    - GIC spectral slopes and minimum sampling cadence for modelling have been defined (Section 5.1).
    - Using dB/dt training in the transfer function (TF) approach can improve SNR at higher frequencies (Section 5.3.2).
    - dB/dt has been shown to be an inaccurate proxy for frequencies significantly different from the sampling rate (Section 5.2).
    - Discrete frequency driving arising from localised B-field pulsations are evident at mid-latitudes and result in GIC modelling scale lengths more limited than previously thought (Section 4.3.3).
4. The SECS interpolation method has been improved upon for the mid-latitude context, with new methods proposed to include lower fidelity data and uncertainty while correcting an error in previous implementation in southern Africa (see Chapter 7).
    - Variometers and low-fidelity data can be included in interpolation through dSECS method, improving on previous results (Section 7.1).
    - The previous implementation of SECS in southern Africa is corrected, and an alternative more accurate mid-latitude effective equivalent current system interpolation using line elements has been developed (Section 7.3).
    - Uncertainty in B-field interpolation quantified in rigorous physics and inversion based methodology which includes measured data and spatial information encoded into the inversion method (Section 7.2).
    - The improvements in B-field interpolation have application within the wider research community, the implication being that these contributions can stand alone from GIC modelling.

9 Concluding Remarks

This chapter provides answers to the research questions, assesses the validity of the hypothesis proposed in Chapter 1 and identifies some of the implications of the hypothesis and research.

9.1 Answers to the Research Questions

Coming full-circle, we revisit the initial research questions from Section 1.6 with responses from the body of work presented.

RQ1: ***What measured GIC and geomagnetic data are available to utilities for operational modelling?***

Since we are linking geomagnetic data to GIC data, specifically what are the limitations of the data available? How large a dataset is needed to be representative? Does data cadence play a role? Does the data fidelity available inform the modelling methodology to be used? How are data sources calibrated and is there a significant issue of noise or poor data quality? Regarding the B-field driving GICs over the entire network, what type of spatial resolution is needed in B-field modelling for GIC studies? When this resolution is not available through measured data, what approaches are used to define the B-field needed?

Although there are cases of high data fidelity, most utilities face a challenge of limited GIC and geomagnetic data. For GIC data, there is limited temporal coverage due to the occurrence of significant geomagnetic disturbances, and limited coverage within a network due to instrumentation of only certain nodes. For B-field data, the main limitation is in the spatial coverage given sparse magnetometer arrays. In terms of GIC measurements, there is the added complication of noise or drift in measurements that needs to be corrected for or modelled robustly. Cadence also plays a large role in the ability to model GIC and B-field dynamics. Although most GIC power comes from periods greater than 1 minute, this data cadence does not show the result of SSC propagation across the globe. When considering the availability of E-field data or dense magnetotelluric transfer functions, few utilities have access to this level of data and in many cases the use of single E-field measurements or estimations can be misleading. For broad operational modelling, methods must be able to use synthetic profiles as a base assumption or else solely rely on mapping from the B-field to GIC. From the perspective of the GIC modelling methodology developed, limited data of the order of hours can provide model convergence and useful estimation. The inherent uncertainty is quantified, with low-fidelity cases simply having larger uncertainty bounds.

Regarding the B-field modelling required over a network, previous studies have found that the largest error comes from inaccurate B-field estimation – compounded by the fact that a magnetometer network is usually sparse. At mid-latitudes, there is a distinct advantage of the main driving currents systems being temporally and spatially more regular in comparison with the higher latitude auroral regions. This means that in general, utilities in mid-latitudes can get away with much sparser magnetometer coverage than those in high-latitudes. It has however been shown (Section 4.3.3) that local effects such as pulsations play a significant role in the driving disturbance B-field, with the implication that a sparse array does not always suffice. General approaches include interpolation of the magnetic field over the network, such as the SECS interpolation scheme, but there is no uncertainty estimate associated with the final interpolated field.

At mid-latitudes, SECS basis functions are not always representative for a sparse magnetometer grid. In this work, new basis functions that make use of Cartesian line current elements have been developed, while keeping the concept of an equivalent current system. A previous implementation of the SECS method in southern Africa was found to be incorrect and the new basis function implementation used instead. Further, a new methodology has been developed to include low-fidelity variometers and exploit the linearity of the interpolation scheme by interpolating dB/dt directly. This interpolation of dB/dt can then be used to improve standard B-field interpolation if required. Lastly, and keeping with the theme of quantifying uncertainty, a novel approach to quantifying uncertainty in B-field interpolation has been developed. In this approach, any basis functions can be used as long as a Backus-Gilbert inverse is applied. The use of a spatially aware inverse allows for inversion uncertainty to be quantified. To further define physical uncertainty that may be missed in interpolation, the novel use of an experimental variogram has been employed. In this step measured data defines a typical variation of the B-field that can be used to simulate synthetic B-fields. The inversion of synthetic B-field provides an indication of equivalent current variation that propagates to uncertainty in final B-field inversion.

RQ2: ***Can data-driven methods encode more complicated dynamics and do they improve on conventional modelling accuracy?***

Using the same base assumptions, do data-driven models result in more accurate models? In the case that base assumptions relating measured B-field and GIC are incorrect, do data-driven models remain representative? Typical cases of the latter are when the frequency dependence of the E-field is incorrectly defined or when network modelling assumes incorrect system parameters.

By allowing the fixed parameters in conventional modelling to become free parameters determined by data, the data-driven approaches have shown to encode more complicated dynamics of the GIC modelling chain. Within the frequency domain approach of transfer function mapping between the B-field and GICs, the mapping is fully representative and is able to encode complex geological and network responses. In the time domain, the network parameters require an E-field estimate which may be wrong. In this case, we see that the data-driven network parameters can encode geophysical variations not modelled conventionally in the input E-field and identify a network effective response. Explicitly this is seen through network parameter uncertainties and showing a directionality response not aligned to the local network. Using different conductivity profiles and B-field measurements gives different responses, showing that the network parameters are sensitive to input and can be used to probe the effects of different inputs. By using sub-sets of parameters given different GIC magnitudes there is further variation seen that may indicate more complex responses not explicitly modelled otherwise. When comparing the data-driven network parameter results to analytical network parameters, we see a significant improvement in accuracy.

RQ3: ***Do conventional models quantify the associated uncertainties in modelling?***

Dealing with operational modelling, are there any probabilistic or error bands associated with GIC models previously developed? Do we have an idea of where there are drivers of uncertainty in the modelling chain and how this uncertainty propagates? Understanding the drivers of error and the robustness of methods given these errors is critical to operational application.

In terms of operational GIC modelling, the gap between model output and real-world measurement of GIC has been identified as a source of significant risk. In previous studies, there has been no estimate of uncertainty in GIC modelling included. Using the ensemble approach estimation from statistical ensembles of free variables, the measured data defines spreads in the various relations that implicitly define uncertainty and unmodelled aspects. Propagating these spreads into a final model result, error bands are produced.

The nature of the parameters estimated through ensemble estimation is dependent on whether the calculation is done in the time or frequency domains, with the resulting distributions being either related to network parameters or transfer function components. Although relations between B-field, E-field and GIC have been explored in previous work, this new research is the first to apply a data-driven ensemble methodology that focuses on describing the gap between measurement and modelling. Other than providing a different perspective to modelling, the calculation method leverages simultaneous equations and provides an independent approach to network parameter and transfer function estimation. The robustness of the methods used allows for various levels of data fidelity to be used, without impacting the usefulness of the resulting estimates. Taking into account the uncertainty and calibrating analytical models using the empirical approaches further leverages what data is available, in contrast to state-of-the-art physics-based models that that require high-fidelity surveys and data to produce actionable results.

For a mid-latitude utility facing the decision of capital investment to enable full physics-based modelling or selective empirical modelling, the latter is definitely the most cost effective and operationally robust, being real-time and directly giving the state of the system. When the system is in a similar state and the same B-field and GIC measurement pair are used, then the empirical modelling is fully generalisable. Failing that, the spread of estimates is likely to give a good indication of the modelling result and relative comparisons are applicable. At its heart, the empirical network parameter ensemble and transfer function approaches proposed aim to augment general theoretical models that identify nodes of interest for real time operational modelling. The derived uncertainties can be propagated to other single estimate theoretical results, with the results serving as inputs for susceptibility and risk analysis.

RQ4: ***Are there any further characteristics of the modelling chain that can be inferred from the analysis of measured data?***

Besides the modelling of GIC time series, can we say anything about the drivers or network purely by looking at the measured data and empirical modelling? Using different datasets, can we infer the impact of different factors? Do any of these factors or characteristics inform operational applications?

Analysing the uncertainties further, factors that drive uncertainty in the final modelling result can be identified as separation between the B-field and network, conductivity assumptions and influences of multiple lines at a node (possibly from lower voltage networks). A result of the different errors is variation of network parameters. In the frequency domain using the TF approach it was found that SNR is a large factor in the stability of component estimation, with dB/dt being favoured for high frequencies (periods less than 1 minute). Expanding the TF approach to map the E-field to GIC through frequency dependent network parameters, no statistically significant deviation from a resistive approximation of the network was found. Purely from the GIC data, pulsation driving can be identified along with geophysical influences such as the coastal effect. The effective network averaging is non-trivial and dense E-field measurements are not sufficient for improved model accuracy. Taking all the modelling chain factors and variations into account together, it is doubtful that a full physics-based model would accurately describe all influences. Rather, simpler models can identify the vast majority of variation and should be used in a empirical sense. A key test for the appropriateness of a model can be defined by the slope of GIC spectrum, i.e. whether an assumed E-field is representative. Measuring the effective frequency response slope across network nodes should be able to calibrate a network for analytical models and identify where there are shortcomings in model assumptions.

RQ5: ***Are there any particular benefits or differences regarding modelling in the time and frequency domains?***

Since modelling can be approached from either perspective, are there any benefits to choosing a single domain? Are there operational considerations regarding either modelling approach? Can uncertainty estimates in the frequency domain be propagated to the time domain?

Making use of the empirical network parameter ensemble method developed, the time domain application is the more robust and flexible version given simple cases. Where the empirical transfer function approach in the frequency domain approach comes out on top is very much when there are complex geophysical conditions that are not encoded by a simple layered-Earth with conductivity variable with depth, or full 3D structure. There is however the shortcoming that the frequency domain calculations use an FFT, which means missing data becomes an issue. As modelling is required, and not only characterisation, approaches such as Lomb-Scargle or wavelet analysis are not suitable. The ensemble methodology in both cases can quantify the uncertainty and provide operational results. Unless an impulse response is used for the frequency domain application, there would be an additional issue around real-time modelling. The time domain ensembles do not have this shortcoming. It is important to make use of datasets that are as representative as possible in training. This is particularly the case of large GIC magnitudes in the time domain and discrete driving in the frequency domain such as pulsations. A consideration in both approaches is the use of Fourier decomposition in either the E-field or transfer function estimation. GICs in their nature are low-frequency phenomena, but the spike-like peaks, such as those seen during the SSC, are transient that mathematically cannot be fully reproduced using only periodic functions unless an infinite sum of frequency components is taken. Of course, this is impractical given limited sampling. Underestimation of transient spikes are common in GIC modelling in general as a result. Lastly, propagation of uncertainty in the frequency domain to time domain results is not possible without the inclusion of parameter ensembles, defined in a similar way to network parameter ensembles but using transfer function components instead of E-field components.

9.2 Validity of the Hypothesis

Having addressed the research questions posed to help guide research, we move on to the hypothesis itself. Considering the simplistic conventional GIC modelling approaches available to most utilities, a representative first-order approximation of GIC driving in these power networks is possible. A large part of the success of the simplistic representations is that the network can be assumed to be resistive and that the plane-wave assumption of disturbance B-field largely holds at mid-latitudes. Furthermore, the base assumption benefits from the network averaging out fine scale geophysical heterogeneities. There is still however a gap between real-world measurement and the output of conventional models. In operational terms, where decision-making is critical, such a gap may be dangerous. A data-driven methodology was developed to quantify the gap and probe where the base assumptions fall short, such as in the case of complex ground conductivity structures, large separation between B-field measurement and network node or unmodelled power network aspects. The resulting modelling encodes both the effective network response and the uncertainty associated with the various levels of data fidelity and allows for operationally useful estimates, even in cases where assumptions are violated or limited data is available. These results were validated through by applying the data-driven methodology developed to four different mid-latitude networks around the world across multiple geomagnetic storms. Different levels of data quality were used, both in terms of GIC data and geomagnetic data, ranging from low-fidelity data with data gaps, low-cadence, noise and offsets to high-fidelity data that has been calibrated and recorded at a high cadence. Further, different geological contexts have been used with either synthetic conductivity profiles, measured E-field or full 3D MT surface impedances. In all cases, the methodology results have been found to be consistent and robust, with remote magnetometers being useful.

Chains of analytical, physics-based models, although accurate in individual modelling aspects, are a product of the assumptions made and cannot link the multiple factors together in defining an effective response with uncertainty that is needed in real-world or operational application. Previously, the best option for such modelling has been the use of proxies that are general enough to be useful when calibrated. In this realm of operational modelling there are other shortcomings, particularly in the frequency domain given discrete frequency driving. Taking into account the correct frequency weighting of the different phenomena allows for identification of better proxies. In terms of B-field modelling for GIC studies when more accuracy is needed, improved mid-latitude specific interpolation has been defined, with the associated uncertainty in interpolation estimated.

Considering the research questions and body of work presented, we can state that the hypothesis,

> ***"Data-driven adaptations of conventional modelling of measured GICs from geomagnetic field disturbances can improve operational modelling application and accuracy."***

is not generally valid, but that it is has been shown to be valid given the mid-latitude regions studied. Further validation would be needed to extend the validity of hypothesis to low- and high-latitude regions where there may be more complex dynamics. There are further caveats that accuracy is improved when compared to analytical models using comparable datasets and that the results are only valid for a node. In terms of the operational requirement for GIC profile shape and uncertainty estimation possible in an online implementation, the proposed data-driven adaptations do allow for operational application. Taking these considerations into account, the hypothesis can be reworded as a valid statement as,

> ***"In mid-latitude regions as defined here, data-driven adaptations of conventional modelling of measured nodal GICs from geomagnetic field disturbances can improve modelling accuracy in comparable datasets and allow for operational application through uncertainty estimation."***

9.3 Implications of Hypothesis and Research Presented

Leveraging data-driven adaptations of conventional GIC modelling is not only feasible but also attractive for operational modelling. Aside from offering advantages of improved accuracy and uncertainty quantification, identified as objectives of operational application, the methodology presented is applicable to large regions of the world where many power systems are exposed to GICs. Utilities in these mid-latitude regions often face challenges of sparse magnetometer coverage or limited geophysical information, usually lagging in GIC awareness and resilience when compared to the more affected high-latitudes. In light of these challenges, the robustness of the methods proposed allow for optimal use of existing assets and modelling. Having identified at-risk nodes, little capital expenditure is required for instrumentation and real-time operational modelling compared to full physics-based approaches requiring large surveys. In terms of augmenting conventional modelling, the proposed data-driven adaptations provide a viable validation approach and state estimation within the network. Ultimately data-driven modelling includes the entire network response without any information about the network, making it ideal for complex or unknown parts of the network. Both the network parameter ensembles and transfer functions provide a benchmark for investigating and improving analytical models, which could extend GIC modelling to whole networks instead of only the nodes with GIC monitoring. Lastly, the development of uncertainty estimation due to B-field interpolation can be used both in operational model inputs and in planning for asset optimisation within a network. At mid-latitudes, the adapted basis functions which describe the driving current systems better provides an improved basis for B-field input into models and eventual model accuracy.

Acknowledgement of Data Sources

This work would not have been possible without the provision of data from different institutions, utilities and individuals. The datasets used come from various parts of the GIC modelling chain and are summarised below:

Geomagnetic Indices and Solar Wind Data
The author gratefully acknowledges the NASA/GSFC's Space Physics Data Facility's OMNIWeb (or CDAWeb or ftp) service and OMNI data for the SYM-H index and solar wind measurements. Further thanks goes to the Hermanus Geomagnetic Observatory, operated by SANSA, for the provision of local K-indices in South Africa.

Geomagnetic Data
The results presented in this work rely on data collected at magnetic observatories. The author thanks the national institutes that support them and INTERMAGNET for promoting high standards of magnetic observatory practice (`www.intermagnet.org`). The author also acknowledges the SuperMAG[213] collaborators (`http://supermag.jhuapl.edu/info/?page=acknowledgement`) regarding the use of geomagnetic data. Raw geomagnetic field data from magnetotelluric field units, part of the USArray Transportable Array, were used and are available through the The IRIS Data Management Center (IRISDMC) (doi:10.7914/SN/EM). Data from a legacy pulsation magnetometer operated by SANSA in Sutherland, South Africa, was also used along with other variometers, whether used for MT sites or pulsation studies in southern Africa. All SANSA geomagnetic data can be accessed through the SANDIMS data portal (`https://sandims.sansa.org.za/`).

Geoelectric Data
Measured geoelectric data has also been used, and the author thanks the Kakioka Magnetic Observatory of the Japan Meteorological Agency for making the data available (`www.kakioka-jma.go.jp/obsdata/metadata`).

Magnetotelluric Surface Impedances
Magnetotelluric transfer functions derived from magnetotelluric field units, part of the USArray Transportable Array, were used and are available through the SPUD EMTF repository (`ds.iris.edu/spud/emtf`), with thanks to A. Kelbert, G.D. Egbert and A. Schultz.

GIC Data
Of all the datasets, GIC data has in the past been the most difficult to access. As general and regulatory awareness grows, the sharing of data is becoming more and more common. For this work there are a number of individuals and utilities that have been ahead of the curve and should be acknowledged as such. For South African GIC data, the author acknowledges Eskom and the EPRI Sunburst project. In the USA, the Tennessee Valley Authority (TVA) has been a leader in instrumenting their network and sharing data, with special thanks to Ian Grant. On the other side of the world, Powerlink Queensland in Australia has similarly been very helpful with thanks to Greg Hesse. Further thanks goes to S. Watari who facilitated in the sharing of data from Hokkaido Electric Power in Japan.

Other
The benchmark geomagnetic and geoelectric field profiles for the March 1989 storm are available on the NERC GMD Task Force project webpage, `www.nerc.com/comm/PC/Pages/Geomagnetic-Disturbance-Task-Force-(GMDTF)-2013.aspx`.

Acknowledgement of Software Sources

By far the majority of the analysis done in this thesis has been in Python and Linux. Besides the typical packages for plotting and analysis, a number of packages specific to geomagnetic modelling have been particularly useful. These can be summarised with their functions as:

1. `apexpy`: geographic and geomagnetic coordinate conversion (`https://apexpy.readthedocs.io/en/latest/readme.html`)
2. `basemap`: map plotting in Python (`https://matplotlib.org/basemap/`)
3. `mtpy`: MT helper functions for reading MT files, basic visualisation and modelling (`https://github.com/MTgeophysics/mtpy`)
4. `rpy2`: R wrapper for Python (`https://rpy2.github.io/`)

The `rpy2` is specifically used to be able to use the variogram simulation capability of `gstat` R package in Python. Other software packages used include Octave to run geoelectric field estimation code for a layered-Earth using Wait's recursion formula, developed by Ari Viljanen (FMI/GEO), March 2001, and modified by A. Pulkkinen, December 2006, and C-based Enhanced Magnetic Model 2017 for main geomagnetic field estimation (`https://www.ngdc.noaa.gov/geomag/EMM/`). Finally, for illustrative purposes, Occam's 1D inversion of MT data was estimated using the OCCAM1DCSEM code (`https://marineemlab.ucsd.edu/Projects/Occam/index.html`) and `mtpy` wrapper. QGIS was used for various power network shapefiles and mapping outside of Python. The power network shapefiles were either obtained for the specific network (South Africa: `https://www.eskom.co.za/Whatweredoing/GCCAReport/Pages/GCCA2022Update.aspx`, USA: `https://hifld-geoplatform.opendata.arcgis.com/datasets/electric-power-transmission-lines`, Australia: `https://www.aemo.com.au/aemo/apps/visualisations/map.html`) and/or validated through OpenStreetMap (`https://www.openstreetmap.org/`).

References

[1] J. G. Kappenman and V. D. Albertson, "Bracing for the geomagnetic storms," *IEEE Spectrum*, vol. 27, no. 3, pp. 27–33, 1990.

[2] D. H. Boteler, R. J. Pirjola, and H. Nevanlinna, "The effects of geomagnetic disturbances on electrical systems at the Earth's surface," *Advances in Space Research*, vol. 22, no. 1, pp. 17–27, 1998.

[3] A. A. Pulkkinen, R. J. Pirjola, and A. Viljanen, "Statistics of extreme geomagnetically induced current events," *Space Weather*, vol. 6, no. 7, 2008.

[4] P. Riley, "On the probability of occurrence of extreme space weather events," *Space Weather*, vol. 10, no. 2, 2012.

[5] S. I. Lotz, M. J. Heyns, and P. J. Cilliers, "Regression-based forecast model of induced geoelectric field," *Space Weather*, vol. 15, no. 1, pp. 180–191, 2017.

[6] T. Maynard, N. Smith, and S. Gonzalez, "Solar Storm Risk to the North American Electric Grid - Lloyd's," *Lloyd's*, pp. 1–21, 2013. Available: http://www.lloyds.com/the-market/tools-and-resources/research/exposure-management/emerging-risks/emerging-risk-reports/business/solar-storm{%}5Cnhttp://www.washingtonpost.com/blogs/wonkblog/files/2013/07/Solar-risk-in-North-America.pdf

[7] E. J. Oughton, A. Skelton, R. B. Horne, A. W. P. Thomson, and C. T. Gaunt, "Quantifying the daily economic impact of extreme space weather due to failure in electricity transmission infrastructure," *Space Weather*, vol. 15, no. 1, pp. 65–83, 2017.

[8] V. D. Albertson and J. Van Baelen, "Electric and Magnetic Fields at the Earth's Surface Due to Auroral Currents," *IEEE Transactions on Power Apparatus and Systems*, vol. PAS-89, no. 4, pp. 578–584, 1970.

[9] V. D. Albertson, J. Thorson, and S. Miske, "The Effects of Geomagnetic Storms on Electrical Power Systems," *IEEE Transactions on Power Apparatus and Systems*, vol. PAS-93, no. 4, pp. 1031–1044, 1974.

[10] R. Ringlee and J. Stewart, "IEEE Power Engineering Society," *IEEE Power Engineering Review*, vol. 9, no. 7, 1989.

[11] L. Bolduc, "GIC observations and studies in the Hydro-Québec power system," *Journal of Atmospheric and Solar-Terrestrial Physics*, vol. 64, no. 16, pp. 1793–1802, 2002.

[12] D. H. Boteler, "A 21st Century View of the March 1989 Magnetic Storm," *Space Weather*, vol. 17, no. 10, pp. 1427–1441, 2019.

[13] M. Weiss and M. Weiss, "An assessment of threats to the American power grid," *Energy, Sustainability and Society*, vol. 9, no. 1, p. 18, 2019.

[14] J. G. Kappenman, "Storm sudden commencement events and the associated geomagnetically induced current risks to ground-based systems at low-latitude and midlatitude locations," *Space Weather*, vol. 1, no. 3, 2003.

[15] C. T. Gaunt and G. Coetzee, "Transformer failures in regions incorrectly considered to have low GIC-risk," in *2007 IEEE Lausanne Power Tech*. IEEE, 2007.

[16] N. Moodley and C. T. Gaunt, "Low Energy Degradation Triangle for power transformer health assessment," *IEEE Transactions on Dielectrics and Electrical Insulation*, vol. 24, no. 1, pp. 639–646, 2017.

[17] T. Divett, G. S. Richardson, C. D. Beggan, C. J. Rodger, D. H. Boteler, M. Ingham, D. H. Mac Manus, A. W. P. Thomson, and M. Dalzell, "Transformer-Level Modeling of Geomagnetically Induced Currents in New Zealand's South Island," *Space Weather*, vol. 16, no. 6, pp. 718–735, 2018.

[18] C. Liu, L. Liu, and R. J. Pirjola, "Geomagnetically Induced Currents in the High-Voltage Power Grid in China," *IEEE Transactions on Power Delivery*, vol. 24, no. 4, pp. 2368–2374, 2009.

[19] T. J. Overbye, K. S. Shetye, T. R. Hutchins, Q. Qiu, and J. D. Weber, "Power Grid Sensitivity Analysis of Geomagnetically Induced Currents," *IEEE Transactions on Power Systems*, vol. 28, no. 4, pp. 4821–4828, 2013.

[20] J. Hübert, C. D. Beggan, G. S. Richardson, T. Martyn, and A. W. P. Thomson, "Differential Magnetometer Measurements of Geomagnetically Induced Currents in a Complex High Voltage Network," *Space Weather*, vol. 18, no. 4, 2020.

[21] L. D. Borrill, H. K. Chisepo, and C. T. Gaunt, "Importance of core joints in GIC/dc studies with scaled down laboratory transformers," *International Journal of Electrical Power & Energy Systems*, vol. 120, 2020.

[22] H. K. Chisepo, C. T. Gaunt, and L. D. Borrill, "Measurement and FEM analysis of DC/GIC effects on transformer magnetization parameters," in *2019 IEEE Milan PowerTech*. IEEE, 2019.

[23] P. Jankee, H. K. Chisepo, V. Adebayo, D. T. O. Oyedokun, and C. T. Gaunt, "Transformer models and meters in MATLAB and PSCAD for GIC and leakage dc studies," in *2020 International SAUPEC/RobMech/PRASA Conference*. IEEE, 2020.

[24] R. Walling and A. Khan, "Characteristics of transformer exciting-current during geomagnetic disturbances," *IEEE Transactions on Power Delivery*, vol. 6, no. 4, pp. 1707–1714, 1991.

[25] H. Kirkham and D. White, "Reactive Power and GIC: the Problems of an Unrecognized Operationalist Measurement," in *2018 IEEE 9th International Workshop on Applied Measurements for Power Systems (AMPS)*. IEEE, 2018.

[26] M. Malengret and C. T. Gaunt, "Active Currents, Power Factor, and Apparent Power for Practical Power Delivery Systems," *IEEE Access*, 2020.

[27] V. D. Albertson, J. G. Kappenman, N. Mohan, and G. Skarbakka, "Load-Flow Studies in the Presence of Geomagnetically-Induced Currents," *IEEE Transactions on Power Apparatus and Systems*, vol. PAS-100, no. 2, pp. 594–607, 1981.

[28] T. S. Molinski, "Why utilities respect geomagnetically induced currents," *Journal of Atmospheric and Solar-Terrestrial Physics*, vol. 64, no. 16, pp. 1765–1778, 2002.

[29] A. A. Pulkkinen, S. Lindahl, A. Viljanen, and R. J. Pirjola, "Geomagnetic storm of 29-31 October 2003: Geomagnetically induced currents and their relation to problems in the Swedish high-voltage power transmission system," *Space Weather*, vol. 3, no. 8, 2005.

[30] "TPL-007-1: Transmission System Planned Performance for Geomagnetic Disturbance Events," https://www.nerc.com/pa/Stand/Reliability%20Standards/TPL-007-1.pdf, North American Reliability Corp., 2017.

[31] R. H. Khawaja and T. R. Blackburn, "Impact of high temperature on partial discharges in oil-impregnated insulation," *AUPEC'09 - 19th Australasian Universities Power Engineering Conference: Sustainable Energy Technologies and Systems*, 2009.

[32] D. J. Knipp, M. A. Hapgood, and D. Welling, "Communicating Uncertainty and Reliability in Space Weather Data, Models, and Applications," *Space Weather*, vol. 16, no. 10, pp. 1453–1454, 2018.

[33] T. E. Cravens, *Physics of Solar System Plasmas.* Cambridge, UK: Cambridge University Press, 1997.

[34] C. M. Ngwira, A. A. Pulkkinen, M. Leila Mays, M. M. Kuznetsova, A. B. Galvin, K. Simunac, D. N. Baker, X. Li, Y. Zheng, and A. Glocer, "Simulation of the 23 July 2012 extreme space weather event: What if this extremely rare CME was Earth directed?" *Space Weather*, vol. 11, no. 12, pp. 671–679, 2013.

[35] T. Saito, "Geomagnetic pulsations," *Space Science Reviews*, vol. 10, no. 3, 1969.

[36] S. V. Apatenkov, V. A. Pilipenko, E. I. Gordeev, A. Viljanen, L. Juusola, V. B. Belakhovsky, Y. A. Sakharov, and V. N. Selivanov, "Auroral Omega Bands are a Significant Cause of Large Geomagnetically Induced Currents," *Geophysical Research Letters*, vol. 47, no. 6, 2020.

[37] A. Kelbert, "The Role of Global/Regional Earth Conductivity Models in Natural Geomagnetic Hazard Mitigation," *Surveys in Geophysics*, vol. 41, no. 1, pp. 115–166, 2020.

[38] M. Lehtinen and R. J. Pirjola, "Currents produced in earthed conductor networks by geomagnetically-induced electric fields," *Annales Geophysicae*, vol. 3, no. 4, pp. 479–484, 1985.

[39] D. N. Baker, X. Li, A. A. Pulkkinen, C. M. Ngwira, M. L. Mays, A. B. Galvin, and K. D. C. Simunac, "A major solar eruptive event in July 2012: Defining extreme space weather scenarios," *Space Weather*, vol. 11, no. 10, pp. 585–591, 2013.

[40] M. G. Kivelson and C. T. Russell, *Introduction to Space Physics.* Cambridge, UK: Cambridge University Press, 1995.

[41] W. H. Campbell, *Introduction to Geomagnetic Fields.* Cambridge, UK: Cambridge University Press, 1997.

[42] K. M. Laundal and A. D. Richmond, "Magnetic Coordinate Systems," *Space Science Reviews*, vol. 206, no. 1-4, pp. 27–59, 2017.

[43] W. H. Campbell, *Earth Magnetism: A Guided Tour Through Magnetic Fields*, ser. Complementary science series. San Diego, California: Harcourt/Academic Press, 2001.

[44] W. D. Gonzalez, J. A. Joselyn, Y. Kamide, H. W. Kroehl, G. Rostoker, B. T. Tsurutani, and V. M. Vasyliunas, "What is a geomagnetic storm?" *Journal of Geophysical Research*, vol. 99, p. A4, 1994.

[45] R. J. Pirjola, "Electromagnetic induction in the Earth by a plane wave or by fields of line currents harmonic in time and space," *Geophysica*, vol. 18, no. 1-2, pp. 1–161, 1982.

[46] E. I. Tanskanen, A. Viljanen, T. I. Pulkkinen, R. J. Pirjola, L. Häkkinen, A. A. Pulkkinen, and O. Amm, "At substorm onset, 40% of AL comes from underground," *Journal of Geophysical Research: Space Physics*, vol. 106, no. A7, pp. 13 119–13 134, 2001.

[47] L. Juusola, H. Vanhamäki, A. Viljanen, and M. Smirnov, "Induced telluric currents play a major role in the interpretation of geomagnetic variations," *Annales Geophysicae Discussions*, no. 4, pp. 1–23, 2020.

[48] "Order 830: Reliability Standard for Transmission System Planned Performance for Geomagnetic Disturbance Events. Sep 2016, Washington DC." https://www.ferc.gov/whats-new/comm-meet/2016/092216/E-4.pdf, Federal Energy Regulatory Commission, 2016.

[49] C. J. Rodger, D. H. Mac Manus, M. Dalzell, A. W. P. Thomson, E. Clarke, T. Petersen, M. A. Clilverd, and T. Divett, "Long-Term Geomagnetically Induced Current Observations From New Zealand: Peak Current Estimates for Extreme Geomagnetic Storms," *Space Weather*, vol. 15, no. 11, pp. 1447–1460, 2017.

[50] R. A. Marshall, A. Kelly, T. Van Der Walt, A. Honecker, C. Ong, D. Mikkelsen, A. Spierings, G. Ivanovich, and A. Yoshikawa, "Modeling geomagnetic induced currents in Australian power networks," *Space Weather*, vol. 15, no. 7, pp. 895–916, 2017.

[51] P. A. Bedrosian and J. J. Love, "Mapping geoelectric fields during magnetic storms: Synthetic analysis of empirical United States impedances," *Geophysical Research Letters*, vol. 42, no. 23, pp. 10,160–10,170, 2015.

[52] K. Robertson, S. Thiel, and N. Meqbel, "Quality over quantity: on workflow and model space exploration of 3D inversion of MT data," *Earth, Planets and Space*, vol. 72, no. 1, p. 2, 2020.

[53] A. A. Pulkkinen, E. Bernabeu, J. Eichner, C. D. Beggan, and A. W. P. Thomson, "Generation of 100-year geomagnetically induced current scenarios," *Space Weather*, vol. 10, no. 4, 2012.

[54] A. W. P. Thomson, E. B. Dawson, and S. J. Reay, "Quantifying extreme behavior in geomagnetic activity," *Space Weather*, vol. 9, no. 10, pp. 1–12, 2011.

[55] G. M. Lucas, J. J. Love, A. Kelbert, P. A. Bedrosian, and E. J. Rigler, "A 100-year Geoelectric Hazard Analysis for the U.S. High-Voltage Power Grid," *Space Weather*, vol. 18, no. 2, 2020.

[56] J. Gannon, A. Swidinsky, and Z. Xu, *Geomagnetically Induced Currents from the Sun to the Power Grid*, ser. Geophysical Monograph Series. Wiley, 2019.

[57] A. A. Pulkkinen, E. Bernabeu, A. W. P. Thomson, A. Viljanen, R. J. Pirjola, D. H. Boteler, J. Eichner, P. J. Cilliers, D. Welling, N. P. Savani, R. S. Weigel, J. J. Love, C. Balch, C. M. Ngwira, G. Crowley, A. Schultz, R. Kataoka, B. Anderson, D. Fugate, J. J. Simpson, and M. MacAlester, "Geomagnetically induced currents: Science, engineering, and applications readiness," *Space Weather*, vol. 15, no. 7, pp. 828–856, 2017.

[58] D. H. Boteler and R. J. Pirjola, "Modeling geomagnetically induced currents," *Space Weather*, vol. 15, no. 1, pp. 258–276, 2017.

[59] J. J. Zhang, C. Wang, and B. B. Tang, "Modeling geomagnetically induced electric field and currents by combining a global MHD model with a local one-dimensional method," *Space Weather*, vol. 10, no. 5, 2012.

[60] D. H. Boteler, "Methodology for simulation of geomagnetically induced currents in power systems," *Journal of Space Weather and Space Climate*, vol. 4, p. A21, 2014.

[61] A. Viljanen, A. A. Pulkkinen, R. J. Pirjola, K. Pajunpää, P. Posio, and A. Koistinen, "Recordings of geomagnetically induced currents and a nowcasting service of the Finnish natural gas pipeline system," *Space Weather*, vol. 4, no. 10, 2006.

[62] A. W. P. Thomson, A. J. McKay, E. Clarke, and S. J. Reay, "Surface electric fields and geomagnetically induced currents in the Scottish Power grid during the 30 October 2003 geomagnetic storm," *Space Weather*, vol. 3, no. 11, 2005.

[63] I. Honkonen, A. Kuvshinov, L. Rastätter, and A. A. Pulkkinen, "Predicting Global Ground Geoelectric Field With Coupled Geospace and Three-Dimensional Geomagnetic Induction Models," *Space Weather*, vol. 16, no. 8, pp. 1028–1041, 2018.

[64] L. Cagniard, "Basic Theory of the Magneto-telluric Method of Geophysical Prospecting," *Geophysics*, vol. 18, no. 3, pp. 605–635, 1953.

[65] F. Simpson and K. Bahr, *Practical Magnetotellurics.* Cambridge: Cambridge University Press, 2005.

[66] A. D. Chave, A. G. Jones, R. Mackie, and W. Rodi, *The Magnetotelluric Method.* Cambridge: Cambridge University Press, 2012.

[67] C. M. Ngwira, A. A. Pulkkinen, F. D. Wilder, and G. Crowley, "Extended study of extreme geoelectric field event scenarios for geomagnetically induced current applications," *Space Weather*, vol. 11, no. 3, pp. 121–131, 2013.

[68] R. Tozzi, I. Coco, P. De Michelis, and F. Giannattasio, "Latitudinal dependence of geomagnetically induced currents during geomagnetic storms," *Annals of Geophysics*, vol. 61, 2018.

[69] N. C. Rogers, J. A. Wild, E. F. Eastoe, J. W. Gjerloev, and A. W. P. Thomson, "A global climatological model of extreme geomagnetic field fluctuations," *Journal of Space Weather and Space Climate*, vol. 10, 2020.

[70] A. A. Pulkkinen, E. Bernabeu, J. Eichner, A. Viljanen, and C. M. Ngwira, "Regional-scale high-latitude extreme geoelectric fields pertaining to geomagnetically induced currents," *Earth, Planets and Space*, vol. 67, no. 1, p. 93, 2015.

[71] C. M. Ngwira, A. A. Pulkkinen, E. Bernabeu, J. Eichner, A. Viljanen, and G. Crowley, "Characteristics of extreme geoelectric fields and their possible causes: Localized peak enhancements," *Geophysical Research Letters*, vol. 42, no. 17, pp. 6916–6921, 2015.

[72] R. Kataoka and C. M. Ngwira, "Extreme geomagnetically induced currents," *Progress in Earth and Planetary Science*, vol. 3, no. 1, p. 23, 2016.

[73] D. H. Mac Manus, C. J. Rodger, M. Dalzell, A. W. P. Thomson, M. A. Clilverd, T. Petersen, M. M. Wolf, N. R. Thomson, and T. Divett, "Long-term geomagnetically induced current observations in New Zealand: Earth return corrections and geomagnetic field driver," *Space Weather*, vol. 15, no. 8, pp. 1020–1038, 2017.

[74] G. S. Kelly, A. Viljanen, C. D. Beggan, and A. W. P. Thomson, "Understanding GIC in the UK and French high-voltage transmission systems during severe magnetic storms," *Space Weather*, vol. 15, no. 1, pp. 99–114, 2017.

[75] A. A. Pulkkinen, L. Rastätter, M. Kuznetsova, H. Singer, C. Balch, D. Weimer, G. Toth, A. Ridley, T. Gombosi, M. Wiltberger, J. Raeder, and R. S. Weigel, "Community-wide validation of geospace model ground magnetic field perturbation predictions to support model transition to operations," *Space Weather*, vol. 11, no. 6, pp. 369–385, 2013.

[76] A. Viljanen, "The Relation Between Geomagnetic Variations and Their Time Derivatives and Implications for Estimation of Induction Risks," *Geophysical Research Letters*, vol. 24, no. 6, pp. 631–634, 1997.

[77] A. Viljanen, H. Nevanlinna, K. Pajunpää, and A. A. Pulkkinen, "Time derivative of the horizontal geomagnetic field as an activity indicator," *Annales Geophysicae*, vol. 19, no. 9, pp. 1107–1118, 2001.

[78] A. Viljanen and E. Tanskanen, "Climatology of rapid geomagnetic variations at high latitudes over two solar cycles," *Annales Geophysicae*, vol. 29, no. 10, pp. 1783–1792, 2011.

[79] J. G. Kappenman, "An overview of the impulsive geomagnetic field disturbances and power grid impacts associated with the violent Sun-Earth connection events of 29-31 October 2003 and a comparative evaluation with other contemporary storms," *Space Weather*, vol. 3, no. 8, 2005.

[80] R. A. D. Fiori, D. H. Boteler, and D. M. Gillies, "Assessment of GIC risk due to geomagnetic sudden commencements and identification of the current systems responsible," *Space Weather*, vol. 12, no. 1, pp. 76–91, 2014.

[81] L. Trichtchenko and D. H. Boteler, "Modeling Geomagnetically Induced Currents Using Geomagnetic Indices and Data," *IEEE Transactions on Plasma Science*, vol. 32, no. 4, pp. 1459–1467, 2004.

[82] A. Viljanen, P. Wintoft, and M. Wik, "Regional estimation of geomagnetically induced currents based on the local magnetic or electric field," *Journal of Space Weather and Space Climate*, vol. 5, p. A24, 2015.

[83] S. Watari, M. Kunitake, K. Kitamura, T. Hori, T. Kikuchi, K. Shiokawa, N. Nishitani, R. Kataoka, Y. Kamide, T. Aso, Y. Watanabe, and Y. Tsuneta, "Measurements of geomagnetically induced current in a power grid in Hokkaido, Japan," *Space Weather*, vol. 7, no. 3, 2009.

[84] A. A. Pulkkinen, R. Kataoka, S. Watari, and M. Ichiki, "Modeling geomagnetically induced currents in Hokkaido, Japan," *Advances in Space Research*, vol. 46, no. 9, pp. 1087–1093, 2010.

[85] R. J. Pirjola, "Derivation of characteristics of the relation between geomagnetic and geoelectric variation fields from the surface impedance for a two-layer earth," *Earth, Planets and Space*, vol. 62, no. 3, pp. 287–295, 2010.

[86] R. A. Marshall, C. L. Waters, and M. D. Sciffer, "Spectral analysis of pipe-to-soil potentials with variations of the Earth's magnetic field in the Australian region," *Space Weather*, vol. 8, no. 5, 2010.

[87] R. A. Marshall, E. A. Smith, M. J. Francis, C. L. Waters, and M. D. Sciffer, "A preliminary risk assessment of the Australian region power network to space weather," *Space Weather*, vol. 9, no. 10, pp. 1–18, 2011.

[88] R. Tozzi, P. De Michelis, I. Coco, and F. Giannattasio, "A Preliminary Risk Assessment of Geomagnetically Induced Currents over the Italian Territory," *Space Weather*, vol. 17, no. 1, pp. 46–58, 2019.

[89] R. J. Pirjola, "Induction in power transmission lines during geomagnetic disturbances," *Space Science Reviews*, vol. 35, no. 2, 1983.

[90] V. D. Albertson, W. E. Feero, J. G. Kappenman, E. V. Larsen, D. E. Nordell, J. Ponder, F. S. Prabhakara, K. Thompson, and R. Walling, "Geomagnetic disturbance effects on power systems," *IEEE Transactions on Power Delivery*, vol. 8, no. 3, pp. 1206–1216, 1993.

[91] R. Lesher, J. Porter, and R. Byerly, "SUNBURST-a network of GIC monitoring systems," *IEEE Transactions on Power Delivery*, vol. 9, no. 1, pp. 128–137, 1994.

[92] E. Matandirotya, P. J. Cilliers, R. R. Van Zyl, D. T. O. Oyedokun, and J. de Villiers, "Differential magnetometer method applied to measurement of geomagnetically induced currents in Southern African power networks," *Space Weather*, vol. 14, no. 3, pp. 221–232, 2016.

[93] A. Viljanen and R. J. Pirjola, "Use of GIC's in Studies of Ionospheric-Magnetospheric Currents and the Earth's Structure," in *[Proceedings] IGARSS'91 Remote Sensing: Global Monitoring for Earth Management*, vol. 3. IEEE, 1991, pp. 1687–1690.

[94] A. Viljanen and R. J. Pirjola, "Geomagnetically induced currents in the Finnish high-voltage power system," *Surveys in Geophysics*, vol. 15, no. 4, pp. 383–408, 1994.

[95] D. H. Boteler and R. J. Pirjola, "Modelling geomagnetically induced currents produced by realistic and uniform electric fields," *IEEE Transactions on Power Delivery*, vol. 13, no. 4, pp. 1303–1308, 1998.

[96] D. H. Boteler and R. J. Pirjola, "Comparison of methods for modelling geomagnetically induced currents," *Annales Geophysicae*, vol. 32, no. 9, pp. 1177–1187, 2014.

[97] D. H. Boteler, A. J. C. Lackey, L. Marti, and S. Shelemy, "Equivalent circuits for modelling geomagnetically induced currents from a neighbouring network," in *2013 IEEE Power & Energy Society General Meeting*. IEEE, 2013.

[98] R. S. Weigel and P. J. Cilliers, "An Evaluation of the Frequency Independence Assumption of Power System Coefficients Used in Geomagnetically Induced Current Estimates," *Space Weather*, vol. 17, no. 12, pp. 1674–1688, 2019.

[99] D. H. Boteler, Q. Bui-Van, and J. Lemay, "Directional sensitivity to geomagnetically induced currents of the Hydro-Quebec 735 kV power system," *IEEE Transactions on Power Delivery*, vol. 9, no. 4, pp. 1963–1971, 1994.

[100] D. H. Boteler, "Assessment of Geomagnetic Hazard to Power Systems in Canada," *Natural Hazards*, vol. 23, no. 2/3, pp. 101–120, 2001.

[101] J. M. Torta, S. Marsal, and M. Quintana, "Assessing the hazard from geomagnetically induced currents to the entire high-voltage power network in Spain," *Earth, Planets and Space*, vol. 66, no. 1, p. 87, 2014.

[102] A. A. Pulkkinen, R. J. Pirjola, and A. Viljanen, "Determination of ground conductivity and system parameters for optimal modeling of geomagnetically induced current flow in technological systems," *Earth, Planets and Space*, vol. 59, no. 9, pp. 999–1006, 2007.

[103] S. Watari, "Estimation of geomagnetically induced currents based on the measurement data of a transformer in a Japanese power network and geoelectric field observations," *Earth, Planets and Space*, vol. 67, no. 1, p. 77, 2015.

[104] C. M. Ngwira, A. A. Pulkkinen, L.-A. McKinnell, and P. J. Cilliers, "Improved modeling of geomagnetically induced currents in the South African power network," *Space Weather*, vol. 6, no. 11, 2008.

[105] M. Wik, A. Viljanen, R. J. Pirjola, A. A. Pulkkinen, P. Wintoft, and H. Lundstedt, "Calculation of geomagnetically induced currents in the 400 kV power grid in southern Sweden," *Space Weather*, vol. 6, no. 7, 2008.

[106] E. Matandirotya, P. J. Cilliers, and R. R. Van Zyl, "Modeling geomagnetically induced currents in the South African power transmission network using the finite element method," *Space Weather*, vol. 13, no. 3, pp. 185–195, 2015.

[107] J. L. Gilbert, "Modeling the effect of the ocean-land interface on induced electric fields during geomagnetic storms," *Space Weather*, vol. 3, no. 4, 2005.

[108] B. Dong, D. W. Danskin, R. J. Pirjola, D. H. Boteler, and Z. Z. Wang, "Evaluating the applicability of the finite element method for modelling of geoelectric fields," *Annales Geophysicae*, vol. 31, no. 10, pp. 1689–1698, 2013.

[109] C. Liu, X. Wang, H. Wang, and H. Zhao, "Quantitative influence of coast effect on geomagnetically induced currents in power grids: a case study," *Journal of Space Weather and Space Climate*, vol. 8, p. A60, 2018.

[110] A. Kelbert, C. C. Balch, A. A. Pulkkinen, G. D. Egbert, J. J. Love, E. J. Rigler, and I. Fujii, "Methodology for time-domain estimation of storm time geoelectric fields using the 3-D magnetotelluric response tensors," *Space Weather*, vol. 15, no. 7, pp. 874–894, 2017.

[111] A. Viljanen and R. J. Pirjola, "Statistics on geomagnetically-induced currents in the Finnish 400kV power system based on recordings of geomagnetic variations." *Journal of Geomagnetism and Geoelectricity*, vol. 41, no. 4, pp. 411–420, 1989.

[112] D. H. Boteler and R. J. Pirjola, "The complex-image method for calculating the magnetic and electric fields produced at the surface of the Earth by the auroral electrojet," *Geophysical Journal International*, vol. 132, no. 1, pp. 31–40, 2002.

[113] R. J. Pirjola and A. Viljanen, "Complex image method for calculating electric and magnetic fields produced by an auroral electrojet of finite length," *Annales Geophysicae*, vol. 16, no. 11, pp. 1434–1444, 1998.

[114] A. T. Price, "The Induction of Electric Currents in Non-uniform Thin Sheets and Shells," *The Quarterly Journal of Mechanics and Applied Mathematics*, vol. 2, no. 3, pp. 283–310, 1949.

[115] G. Vasseur and P. Weidelt, "Bimodal electromagnetic induction in non-uniform thin sheets with an application to the northern pyrenean induction anomaly," *Geophysical Journal of the Royal Astronomical Society*, vol. 51, no. 3, pp. 669–690, 1977.

[116] D. M. McKirdy, J. T. Weaver, and T. W. Dawson, "Induction in a thin sheet of variable conductance at the surface of a stratified earth — II. Three-dimensional theory," *Geophysical Journal International*, vol. 80, no. 1, pp. 177–194, 1985.

[117] G. Fischer, "Electromagnetic induction effects at an ocean coast," *Proceedings of the IEEE*, vol. 67, no. 7, pp. 1050–1060, 1979.

[118] C. D. Beggan, D. Beamish, A. Richards, G. S. Kelly, and A. W. P. Thomson, "Prediction of extreme geomagnetically induced currents in the UK high-voltage network," *Space Weather*, vol. 11, no. 7, pp. 407–419, 2013.

[119] R. L. Bailey and R. Leonhardt, "Automated detection of geomagnetic storms with heightened risk of GIC," *Earth, Planets and Space*, vol. 68, no. 1, p. 99, 2016.

[120] T. Divett, M. Ingham, C. D. Beggan, G. S. Richardson, C. J. Rodger, A. W. P. Thomson, and M. Dalzell, "Modeling Geoelectric Fields and Geomagnetically Induced Currents Around New Zealand to Explore GIC in the South Island's Electrical Transmission Network," *Space Weather*, vol. 15, no. 10, pp. 1396–1412, 2017.

[121] F. E. M. Lilley, "Geomagnetic Field Fluctuations Over Australia in Relation to Magnetic Surveys," *Exploration Geophysics*, vol. 13, no. 3, pp. 68–76, 1982.

[122] A. J. McKay, "PhD Thesis: Geoelectric Fields and Geomagnetically Induced Currents in the United Kingdom," PhD, University of Edinburgh, 2003.

[123] T. Divett, D. H. M. Manus, G. S. Richardson, C. D. Beggan, C. J. Rodger, M. Ingham, E. Clarke, A. W. P. Thomson, M. Dalzell, and Y. Obana, "Geomagnetically Induced Current Model Validation from New Zealand's South Island," *Space Weather*, 2020.

[124] J. M. Torta, A. Marcuello, J. Campanyà, S. Marsal, P. Queralt, and J. Ledo, "Improving the modeling of geomagnetically induced currents in Spain," *Space Weather*, vol. 15, no. 5, pp. 691–703, 2017.

[125] L. H. Wei, N. Homeier, and J. L. Gannon, "Surface electric fields for North America during historical geomagnetic storms," *Space Weather*, vol. 11, no. 8, pp. 451–462, 2013.

[126] M. Myllys, A. Viljanen, Ø. A. Rui, and T. M. Ohnstad, "Geomagnetically induced currents in Norway: the northernmost high-voltage power grid in the world," *Journal of Space Weather and Space Climate*, vol. 4, p. A10, 2014.

[127] S. P. Blake, P. T. Gallagher, J. McCauley, A. G. Jones, C. Hogg, J. Campanyà, C. D. Beggan, A. W. P. Thomson, G. S. Kelly, and D. Bell, "Geomagnetically induced currents in the Irish power network during geomagnetic storms," *Space Weather*, vol. 14, no. 12, pp. 1136–1154, 2016.

[128] R. S. Weigel, "A comparison of methods for estimating the geoelectric field," *Space Weather*, vol. 15, no. 2, pp. 430–440, 2017.

[129] J. J. Love, A. A. Pulkkinen, P. A. Bedrosian, S. Jonas, A. Kelbert, E. J. Rigler, C. A. Finn, C. C. Balch, R. Rutledge, R. M. Waggel, A. T. Sabata, J. U. Kozyra, and C. E. Black, "Geoelectric hazard maps for the continental United States," *Geophysical Research Letters*, vol. 43, no. 18, pp. 9415–9424, 2016.

[130] J. J. Love, G. M. Lucas, A. Kelbert, and P. A. Bedrosian, "Geoelectric Hazard Maps for the Mid-Atlantic United States: 100 Year Extreme Values and the 1989 Magnetic Storm," *Geophysical Research Letters*, vol. 45, no. 1, pp. 5–14, 2018.

[131] J. J. Love, G. M. Lucas, A. Kelbert and P. A. Bedrosian, "Geoelectric Hazard Maps for the Pacific Northwest," *Space Weather*, vol. 16, no. 8, pp. 1114–1127, 2018.

[132] J. J. Love, G. M. Lucas, P. A. Bedrosian, and A. Kelbert, "Extreme-Value Geoelectric Amplitude and Polarization Across the Northeast United States," *Space Weather*, vol. 17, no. 3, pp. 379–395, 2019.

[133] L. Wang, A. P. Hitchman, Y. Ogawa, W. Siripunvaraporn, M. Ichiki, and K. Fuji-ta, "A 3-D conductivity model of the Australian continent using observatory and magnetometer array data," *Geophysical Journal International*, vol. 198, no. 2, pp. 1143–1158, 2014.

[134] L. Wang, A. M. Lewis, Y. Ogawa, W. V. Jones, and M. T. Costelloe, "Modeling geomagnetic induction hazards using a 3-D electrical conductivity model of Australia," *Space Weather*, vol. 14, no. 12, pp. 1125–1135, 2016.

[135] S. W. Cuttler, J. J. Love, and A. Swidinsky, "Geoelectric hazard assessment: the differences of geoelectric responses during magnetic storms within common physiographic zones," *Earth, Planets and Space*, vol. 70, no. 1, p. 35, 2018.

[136] J. L. Gannon, A. B. Birchfield, K. S. Shetye, and T. J. Overbye, "A Comparison of Peak Electric Fields and GICs in the Pacific Northwest Using 1-D and 3-D Conductivity," *Space Weather*, vol. 15, no. 11, pp. 1535–1547, 2017.

[137] R. Sun and C. Balch, "Comparison Between 1-D and 3-D Geoelectric Field Methods to Calculate Geomagnetically Induced Currents: A Case Study," *IEEE Transactions on Power Delivery*, vol. 34, no. 6, pp. 2163–2172, 2019.

[138] A. P. Dimmock, L. Rosenqvist, J. Hall, A. Viljanen, E. Yordanova, I. Honkonen, M. André, and E. C. Sjöberg, "The GIC and Geomagnetic Response Over Fennoscandia to the 7–8 September 2017 Geomagnetic Storm," *Space Weather*, 2019.

[139] G. M. Lucas, J. J. Love, and A. Kelbert, "Calculation of Voltages in Electric Power Transmission Lines During Historic Geomagnetic Storms: An Investigation Using Realistic Earth Impedances," *Space Weather*, vol. 16, no. 2, pp. 185–195, 2018.

[140] A. Kelbert and G. M. Lucas, "Modified GIC estimation using 3D Earth conductivity," *Space Weather*, pp. 1–42, 2020.

[141] L. Rosenqvist and J. O. Hall, “Regional 3-D Modeling and Verification of Geomagnetically Induced Currents in Sweden,” *Space Weather*, vol. 17, no. 1, pp. 27–36, 2019.

[142] R. L. Bailey, T. S. Halbedl, I. Schattauer, G. Achleitner, and R. Leonhardt, “Validating GIC Models With Measurements in Austria: Evaluation of Accuracy and Sensitivity to Input Parameters,” *Space Weather*, vol. 16, no. 7, pp. 887–902, 2018.

[143] M. Ingham, C. J. Rodger, T. Divett, M. Dalzell, and T. Petersen, “Assessment of GIC Based On Transfer Function Analysis,” *Space Weather*, vol. 15, no. 12, pp. 1615–1627, 2017.

[144] D. Beamish, T. Clark, E. Clarke, and A. W. P. Thomson, “Geomagnetically induced currents in the UK: geomagnetic variations and surface electric fields,” *Journal of Atmospheric and Solar-Terrestrial Physics*, vol. 64, no. 16, pp. 1779–1792, 2002.

[145] A. A. Pulkkinen, A. Viljanen, and R. J. Pirjola, “Estimation of geomagnetically induced current levels from different input data,” *Space Weather*, vol. 4, no. 8, 2006.

[146] A. A. Pulkkinen, L. Rastätter, M. Kuznetsova, M. Hesse, A. Ridley, J. Raeder, H. J. Singer, and A. Chulaki, “Systematic evaluation of ground and geostationary magnetic field predictions generated by global magnetohydrodynamic models,” *Journal of Geophysical Research: Space Physics*, vol. 115, p. A3, 2010.

[147] A. Viljanen, “Relation of geomagnetically induced currents and local geomagnetic variations,” *IEEE Transactions on Power Delivery*, vol. 13, no. 4, pp. 1285–1290, 1998.

[148] A. Viljanen, R. J. Pirjola, M. Wik, A. Ádám, E. Prácser, Y. Sakharov, and J. Katkalov, “Continental scale modelling of geomagnetically induced currents,” *Journal of Space Weather and Space Climate*, vol. 2, p. A17, 2012.

[149] A. Viljanen, R. J. Pirjola, E. Prácser, S. Ahmadzai, and V. Singh, “Geomagnetically induced currents in Europe: Characteristics based on a local power grid model,” *Space Weather*, vol. 11, no. 10, pp. 575–584, 2013.

[150] K. Zheng, L. Trichtchenko, R. J. Pirjola, and L. Liu, “Effects of Geophysical Parameters on GIC Illustrated by Benchmark Network Modeling,” *IEEE Transactions on Power Delivery*, vol. 28, no. 2, pp. 1183–1191, 2013.

[151] M. D. Butala, M. Kazerooni, J. J. Makela, F. Kamalabadi, J. L. Gannon, H. Zhu, and T. J. Overbye, “Modeling Geomagnetically Induced Currents From Magnetometer Measurements: Spatial Scale Assessed With Reference Measurements,” *Space Weather*, vol. 15, no. 10, pp. 1357–1372, 2017.

[152] C. M. Ngwira, L.-A. McKinnell, P. J. Cilliers, A. Viljanen, and R. J. Pirjola, “Limitations of the modeling of geomagnetically induced currents in the South African power network,” *Space Weather*, vol. 7, no. 10, 2009.

[153] O. Kozyreva, V. Pilipenko, R. Krasnoperov, L. Baddeley, Y. Sakharov, and M. Dobrovolsky, “Fine structure of substorm and geomagnetically induced currents,” *Annals of Geophysics*, vol. 62, 2019.

[154] S. P. Blake, P. T. Gallagher, J. Campanyà, C. Hogg, C. D. Beggan, A. W. P. Thomson, G. S. Richardson, and D. Bell, “A Detailed Model of the Irish High Voltage Power Network for Simulating GICs,” *Space Weather*, vol. 16, no. 11, pp. 1770–1783, 2018.

[155] R. A. Marshall, L. Wang, G. A. Paskos, G. Olivares-Pulido, T. Van Der Walt, C. Ong, D. Mikkelsen, G. Hesse, B. McMahon, E. Van Wyk, G. Ivanovich, D. Spoor, C. Taylor, and A. Yoshikawa, “Modeling Geomagnetically Induced Currents in Australian Power Networks Using Different Conductivity Models,” *Space Weather*, vol. 17, no. 5, pp. 727–756, 2019.

[156] A. A. Pulkkinen, A. W. P. Thomson, E. Clarke, and A. J. McKay, "April 2000 geomagnetic storm: ionospheric drivers of large geomagnetically induced currents," *Annales Geophysicae*, vol. 21, no. 3, pp. 709–717, 2003.

[157] E. H. Bernhardi, P. J. Cilliers, and C. T. Gaunt, "Improvement in the modelling of geomagnetically induced currents in southern Africa," *South African Journal of Science*, vol. 104, no. 7-8, pp. 265–272, 2008.

[158] O. Amm, "Ionospheric Elementary Current Systems in Spherical Coordinates and Their Application." *Journal of Geomagnetism and Geoelectricity*, vol. 49, no. 7, pp. 947–955, 1997.

[159] O. Amm and A. Viljanen, "Ionospheric disturbance magnetic field continuation from the ground to the ionosphere using spherical elementary current systems," *Earth, Planets and Space*, vol. 51, no. 6, pp. 431–440, 1999.

[160] A. A. Pulkkinen, O. Amm, and A. Viljanen, "Separation of the geomagnetic variation field on the ground into external and internal parts using the spherical elementary current system method," *Earth, Planets and Space*, vol. 55, no. 3, pp. 117–129, 2003.

[161] S. Marsal, J. M. Torta, A. Segarra, and T. Araki, "Use of spherical elementary currents to map the polar current systems associated with the geomagnetic sudden commencements on 2013 and 2015 St. Patrick's Day storms," *Journal of Geophysical Research: Space Physics*, vol. 122, no. 1, pp. 194–211, 2017.

[162] A. Viljanen, A. A. Pulkkinen, O. Amm, R. J. Pirjola, T. Korja, and BEAR Working Group, "Fast computation of the geoelectric field using the method of elementary current systems and planar Earth models," *Annales Geophysicae*, vol. 22, no. 1, pp. 101–113, 2004.

[163] S. A. McLay and C. D. Beggan, "Interpolation of externally-caused magnetic fields over large sparse arrays using Spherical Elementary Current Systems," *Annales Geophysicae*, vol. 28, no. 9, pp. 1795–1805, 2010.

[164] A. A. Pulkkinen, "Geomagnetic Induction During Highly Disturbed Space Weather Conditions: Studies Of Ground Effects," PhD, University of Helsinki, 2003.

[165] A. Neska, J. T. Reda, M. L. Neska, and Y. P. Sumaruk, "On the relevance of source effects in geomagnetic pulsations for induction soundings," *Annales Geophysicae*, vol. 36, no. 2, pp. 337–347, 2018.

[166] E. Marshalko, M. Kruglyakov, A. Kuvshinov, B. S. Murphy, L. Rastätter, C. M. Ngwira, and A. A. Pulkkinen, "Exploring the Influence of Lateral Conductivity Contrasts on the Storm Time Behavior of the Ground Electric Field in the Eastern United States," *Space Weather*, vol. 18, no. 3, pp. 1–25, 2020.

[167] F. Simpson and K. Bahr, "Nowcasting and validating Earth's electric-field response to extreme space-weather events using magnetotelluric data: application to the September 2017 geomagnetic storm and comparison to observed and modelled fields in Scotland," *Space Weather*, 2020.

[168] J. A. Wanliss and K. M. Showalter, "High-resolution global storm index: Dst versus SYM-H," *Journal of Geophysical Research*, vol. 111, p. A2, 2006.

[169] J. S. de Villiers, M. Kosch, Y. Yamazaki, and S. Lotz, "Influences of various magnetospheric and ionospheric current systems on geomagnetically induced currents around the world," *Space Weather*, vol. 15, no. 2, pp. 403–417, 2017.

[170] R. L. Evans, A. G. Jones, X. Garcia, M. Muller, M. Hamilton, S. Evans, C. J. S. Fourie, J. Spratt, S. Webb, H. Jelsma, and D. Hutchins, "Electrical lithosphere beneath the Kaapvaal craton, southern Africa," *Journal of Geophysical Research*, vol. 116, p. B4, 2011.

[171] R. J. Pirjola, D. H. Boteler, and L. Trichtchenko, "Ground effects of space weather investigated by the surface impedance," *Earth, Planets and Space*, vol. 61, no. 2, pp. 249–261, 2009.

[172] K. Takahashi and B. J. Anderson, "Distribution of ULF energy ($f < 80$ mHz) in the inner magnetosphere: A statistical analysis of AMPTE CCE magnetic field data," *Journal of Geophysical Research*, vol. 97, no. A7, p. 10751, 1992.

[173] A. G. Jones, "Geomagnetic Induction Studies in Southern Scotland," PhD, University of Edinburgh, 1977.

[174] D. T. O. Oyedokun, M. J. Heyns, P. J. Cilliers, and C. T. Gaunt, "Frequency Components of Geomagnetically Induced Currents for Power System Modelling," in *2020 International SAUPEC/RobMech/PRASA Conference*. IEEE, 2020.

[175] D. H. Boteler, R. J. Pirjola, and L. Marti, "Analytic Calculation of Geoelectric Fields Due to Geomagnetic Disturbances: A Test Case," *IEEE Access*, vol. 7, pp. 147 029–147 037, 2019.

[176] M. J. Heyns, S. I. Lotz, and C. T. Gaunt, "dSECS : Including Variometers in Geomagnetic Field Interpolation," in *The Proceedings of SAIP2018, the 63rd Annual Conference of the South African Institute of Physics*, J. Engelbrecht, Ed. Bloemfontein: SAIP, 2018, pp. 212–217.

[177] N. Fukushima, "Generalized theorem for no ground magnetic effect of vertical currents connected with Pedersen currents in the uniform-conductivity ionosphere," *Report of Ionosphere and Space Research in Japan*, vol. 30, no. 1-2, pp. 35–40, 1976.

[178] A. A. Pulkkinen, O. Amm, and A. Viljanen, "Ionospheric equivalent current distributions determined with the method of spherical elementary current systems," *Journal of Geophysical Research: Space Physics*, vol. 108, no. A2, pp. 1–9, 2003.

[179] R. Herman and C. T. Gaunt, "Probabilistic estimation of power system interruption impact using time element matrices," in *2016 IEEE Power and Energy Society General Meeting (PESGM)*. IEEE, 2016.

[180] E. J. Oughton, M. Hapgood, G. S. Richardson, C. D. Beggan, A. W. P. Thomson, M. Gibbs, C. Burnett, C. T. Gaunt, M. Trichas, R. Dada, and R. B. Horne, "A Risk Assessment Framework for the Socioeconomic Impacts of Electricity Transmission Infrastructure Failure Due to Space Weather: An Application to the United Kingdom," *Risk Analysis*, vol. 39, no. 5, pp. 1022–1043, 2019.

[181] N. Nishizuka, K. Sugiura, Y. Kubo, M. Den, and M. Ishii, "Deep Flare Net (DeFN) Model for Solar Flare Prediction," *The Astrophysical Journal*, vol. 858, no. 2, p. 113, 2018.

[182] H. Liu, C. Liu, J. T. L. Wang, and H. Wang, "Predicting Solar Flares Using a Long Short-term Memory Network," *The Astrophysical Journal*, vol. 877, no. 2, p. 121, 2019.

[183] A. Parsons, D. Biesecker, D. Odstrcil, G. Millward, S. Hill, and V. Pizzo, "Wang-Sheeley-Arge-Enlil Cone Model Transitions to Operations," *Space Weather*, vol. 9, no. 3, 2011.

[184] M. Kazerooni, H. Zhu, and T. J. Overbye, "Mitigation of Geomagnetically Induced Currents Using Corrective Line Switching," *IEEE Transactions on Power Systems*, vol. 33, no. 3, pp. 2563–2571, 2018.

[185] R. J. Redmon, D. B. Seaton, R. Steenburgh, J. He, and J. V. Rodriguez, "September 2017's Geoeffective Space Weather and Impacts to Caribbean Radio Communications During Hurricane Response," *Space Weather*, vol. 16, no. 9, pp. 1190–1201, 2018.

[186] Y. Minamoto, “Availability and Access to Data from Kakioka Magnetic Observatory, Japan,” *Data Science Journal*, vol. 12, pp. G30–G35, 2013.

[187] I. Fujii, T. Ookawa, S. Nagamachi, and T. Owada, “The characteristics of geoelectric fields at Kakioka, Kanoya, and Memambetsu inferred from voltage measurements during 2000 to 2011,” *Earth, Planets and Space*, vol. 67, no. 1, 2015.

[188] M. J. Heyns, S. I. Lotz, and C. T. Gaunt, “Probabilistic Analysis of Power Network Susceptibility to GICs,” in *2020 International Conference on Probabilistic Methods Applied to Power Systems (PMAPS).* IEEE, 2020, pp. 1–6.

[189] A. Muchinapaya, C. T. Gaunt, and D. T. O. Oyedokun, “Design of a Low-Cost System to Monitor Geomagnetically Induced Currents in Transformer Neutrals,” in *2018 IEEE PES/IAS PowerAfrica.* IEEE, 2018.

[190] J. Jankowski and C. Sucksdorff, *IAGA Guide for Magnetic Measurements and Observatory Practice.* Warsaw: International Association of Geomagnetism and Aeronomy, 1996.

[191] M. J. Heyns, C. T. Gaunt, S. I. Lotz, and P. J. Cilliers, “Data driven transfer functions and transmission network parameters for GIC modelling,” *Electric Power Systems Research*, vol. 188, no. PSCC, p. 106546, 2020.

[192] M. A. Grawe, J. J. Makela, M. D. Butala, and F. Kamalabadi, “The Impact of Magnetic Field Temporal Sampling on Modeled Surface Electric Fields,” *Space Weather*, vol. 16, no. 11, pp. 1721–1739, 2018.

[193] J. Sun, A. Kelbert, and G. D. Egbert, “Ionospheric current source modeling and global geomagnetic induction using ground geomagnetic observatory data,” *Journal of Geophysical Research: Solid Earth*, vol. 120, no. 10, pp. 6771–6796, 2015.

[194] M. J. Heyns, S. I. Lotz, and C. T. Gaunt, “Geomagnetic Pulsations Driving Geomagnetically Induced Currents,” *Space Weather*, pp. 1–26, 2020.

[195] C. Püthe and A. Kuvshinov, “Mapping 3-D mantle electrical conductivity from space: a new 3-D inversion scheme based on analysis of matrix Q-responses,” *Geophysical Journal International*, vol. 197, no. 2, pp. 768–784, 2014.

[196] A. Avdeeva, M. Moorkamp, D. Avdeev, M. Jegen, and M. Miensopust, “Three-dimensional inversion of magnetotelluric impedance tensor data and full distortion matrix,” *Geophysical Journal International*, vol. 202, no. 1, pp. 464–481, 2015.

[197] G. D. Egbert, N. Meqbel, and A. Kelbert, “Some results from ModEM3DMT, the freely available OSU 3D MT inversion code,” in *6th International Symposium on Three-Dimensional Electromagnetics*, Berkeley, California, USA, 2017.

[198] T. G. Caldwell, H. M. Bibby, and C. Brown, “The magnetotelluric phase tensor,” *Geophysical Journal International*, vol. 158, no. 2, pp. 457–469, 2004.

[199] R. Kataoka and A. A. Pulkkinen, “Geomagnetically induced currents during intense storms driven by coronal mass ejections and corotating interacting regions,” *Journal of Geophysical Research: Space Physics*, vol. 113, p. A3, 2008.

[200] C. Turbitt, “INTERMAGNET Technical Note TN6: INTERMAGNET Definitive One-second Data Standard,” https://intermagnet.org/publications/im_tn_06_v1_0.pdf, 2014.

[201] J. J. Zhang, C. Wang, T. R. Sun, and Y. D. Liu, “Risk assessment of the extreme interplanetary shock of 23 July 2012 on low-latitude power networks,” *Space Weather*, vol. 14, no. 3, pp. 259–270, 2016.

[202] N. I. Fisher, *Statistical Analysis of Circular Data.* Cambridge University Press, 1993.

[203] M. J. Heyns, S. I. Lotz, P. J. Cilliers, and C. T. Gaunt, "Ensemble Estimation of Network Parameters: A Tool to Improve the Real-time Estimation of GICs in the South African Power Network," in *The Proceedings of SAIP2017, the 62nd Annual Conference of the South African Institute of Physics*, J. Engelbrecht, Ed. Stellenbosch: SAIP, 2017, pp. 270–275.

[204] J. Koen, "Geomagnetically Induced Currents in the Southern African Electricity Transmission Network," PhD, University of Cape Town, 2002.

[205] J. Koen and C. T. Gaunt, "Disturbances in the Southern African Power Network Due To Geomagnetically Induced Currents," in *Cigre Session*, Paris, 2002.

[206] B. A. Carter, E. Yizengaw, R. Pradipta, J. M. Weygand, M. Piersanti, A. A. Pulkkinen, M. B. Moldwin, R. Norman, and K. Zhang, "Geomagnetically induced currents around the world during the 17 March 2015 storm," *Journal of Geophysical Research: Space Physics*, vol. 121, no. 10, pp. 10,496–10,507, 2016.

[207] S. Nakamura, Y. Ebihara, S. Fujita, T. Goto, N. Yamada, S. Watari, and Y. Omura, "Time Domain Simulation of Geomagnetically Induced Current (GIC) Flowing in 500-kV Power Grid in Japan Including a Three-Dimensional Ground Inhomogeneity," *Space Weather*, vol. 16, no. 12, pp. 1946–1959, 2018.

[208] M. J. Heyns, "Ensemble Estimation and Analysis of Network Parameters," M.Phil, University of Cape Town, 2017.

[209] W. Menke, *Geophysical Data Analysis: Discrete Inverse Theory*, 2012.

[210] A. Tarantola, *Inverse Problem Theory and Methods for Model Parameter Estimation.* Society for Industrial and Applied Mathematics, 2005.

[211] P. K. Kitanidis, *Introduction to Geostatistics.* Cambridge University Press, 1997.

[212] L. M. Winter, J. Gannon, R. Pernak, S. Huston, R. Quinn, E. Pope, A. Ruffenach, P. Bernardara, and N. Crocker, "Spectral scaling technique to determine extreme Carrington-level geomagnetically induced currents effects," *Space Weather*, vol. 15, no. 5, pp. 713–725, 2017.

[213] J. W. Gjerloev, "The SuperMAG data processing technique," *Journal of Geophysical Research: Space Physics*, vol. 117, p. A9, 2012.